

Environmental Science and Engineering
Subseries: Environmental Science

Series Editors: R. Allan • U. Förstner • W. Salomons

Xiaojing Zheng

Mechanics of Wind-blown Sand Movements

Prof. Xiaojing Zheng
Lanzhou University
222 South Tianshui Rd.
730000 Lanzhou, Gansu
People's Republic of China
xjzheng@lzu.edu.cn

ISSN 1863-5520
ISBN 978-3-540-88253-4
DOI 10.1007/978-3-540-88254-1
Springer Dordrecht Heidelberg London New York

e-ISBN 978-3-540-88254-1

Library of Congress Control Number: 2009920947

© Springer-Verlag Berlin Heidelberg 2009

This work is subject to copyright. All rights are reserved, whether the whole or part of the material is concerned, specifically the rights of translation, reprinting, reuse of illustrations, recitation, broadcasting, reproduction on microfilm or in any other way, and storage in data banks. Duplication of this publication or parts thereof is permitted only under the provisions of the German Copyright Law of September 9, 1965, in its current version, and permission for use must always be obtained from Springer. Violations are liable to prosecution under the German Copyright Law.

The use of general descriptive names, registered names, trademarks, etc. in this publication does not imply, even in the absence of a specific statement, that such names are exempt from the relevant protective laws and regulations and therefore free for general use.

Cover design: Integra Software Services Pvt. Ltd., Pondicherry

Printed on acid-free paper

Springer is part of Springer Science+Business Media (springer.com)

Foreword

Ever since 1930s, human beings have been plagued by disasters caused by desertification and accompanying dust storms. Although basically a result of the evolution of the local inherent environmental conditions, all forms of desertification are also related to the economic development and influenced by global climate changes. Damages caused by desertification not only hinder the economic development, but also aggravate man's living condition. Therefore, the United Nations passed the 3337 General Assembly Resolution on 'Plan of Action to Combat Desertification' in 1975, and desertification has become one of the major concerns of all nations since 1970s. In China, the government has also attached great importance to studies on desertification and ways to control desertification. Since the establishment of the Sand Control Team by Chinese Academy of Sciences (CAS) in 1950's, disciplines involved have been extending from merely physical geography to multi-disciplinary combination of atmospheric science, ecology and mechanics, etc. Nowadays, many scientists and technologists plunge into the multi-disciplinary studies on desertification, they are from various national and provincial research institutions, Universities, and China Meteorological Administration (CMA). In the past 50 years, they have accumulated many experiences on monitoring and controlling of desertification, and also achieved a lot laudability progresses in theoretical researches on desertification.

The physics of wind-blown sand is an issue of basic researches in desertification controlling and sand and dust storm prediction. As early as the 1930s, Bagnold, the British scientist, summarized and classified his field measurements and wind tunnel experiments. In his *The Physics of Blown Sand and Desert Dune* (1941), he established an initial system of wind-blown sand research, laying a foundation in related studies and the engineering application in the controlling of soil wind erosion and desertification. Theoretically speaking, desertification or wind-induced soil erosion is a dynamic process of spatial-temporal evolution manifested by the group behavior of wind-forced sand movement, in which many factors are involved. These factors, to name just a few of them, are the granular characteristic of sand particles, the coupling effect among sand motions, the driving wind field and moving boundary of the landforms, the trans-scale

(from micrometer-scale sand particles to centimeter-scale sand ripples, and even to ten-meter sand dunes) characteristics, the nonlinearity (the turbulent characteristics in the near-surface layer, the interaction among wind field, sand motions and thermal effect, and the nonlinearity caused by moving boundary, etc.), and the randomness (the random size distribution of sand particles, the spatial and temporal randomness of wind field, and the stochastic of turbulence, etc.). Due to the extreme complex nature of sand transportation, it remains a most challenging task to scientists, and we still have a long way to go before asserting that we have fully understood its mechanism and rules. Fortunately, achievements in non-linear science and computing technology render further in-depth studies of these complex issues possible with the rapid advancement of science and technology. Moreover, the urgent demand to increase the efficiency of desertification controlling and to vouch for the accuracy of sand (dust) storm monitoring and forecasting also promote studies on the mechanism of wind-blown sand movement in a more quantitative and more profound way.

In the last decade, Professor Xiaojing Zheng, the author of this book, with her team has been working painstakingly on wind-blown sand movement. They started with a basic analysis of its underlying mechanical processes, and then undertook systematical and thorough studies on the formation and evolutional processes of the wind-blown sand flux in the near-surface boundary layer. They have made some remarkable progresses which evolve and renew the extant theories of the physics of wind-blown sand forward to be more reasonable and sophisticated. Based on a summary of the major achievements since Bagnold, the author, in this book, elaborates her with her team's latest researches into the mechanism of wind-blown sand movement. Professor Zheng with her team's main achievements include establishing the kind of statistical method and the stochastic particle-bed collision model to obtain the lift-off velocity distribution function of sand particles, promoting the quantitative investigation on the phenomenon of wind-blown sand electrification and its impact by their experimental measurements and theoretical estimations, realizing the quantitative simulations on the formation and evolution of wind-blown sand flux relating to wind erosion, dust devil, sand ripples and sand dune fields. Furthermore, they formulated some analytical methods and presented experimental results from the mechanical approach, regarding the erecting of straw checkerboard barriers and sand fences, and the formation of soil crust. These remarkable achievements have not only profoundly revealed the underlying dynamic mechanism of wind-blown sand movement but also provided a kind of essential methods for effective design of sand-control engineering, which makes a very significant contribution to the physics of wind-blown sand.

Frequently plagued by raging disastrous sand and dust storms, China vigorously facilitates studies on the controlling of desertification, incubating national projects dedicating to the monitoring, the understanding and forecasting of dust storms. Scientists from CAS, CMA and some universities have made joint efforts to approach related issues from the perspective of atmospheric dynamics, such as the weather system dynamics, climatological statistics, monitoring method and predicting model of dust storms. They have established a comprehensive system, from dust monitoring to predicting, and applied it to operational service.

It is worth mentioning that dust emission scheme is one of the key factors in dust storm forecast and closely related to the fashion of wind-blown sand movement in the near surface layer, which, in turn, is based on the analytic methods and corresponding studies on sand transportation illustrated in this book. Therefore, Professor Zheng's work is also very instructive for investigation on dust storms. In my own research on the dust storm, especially on the dust emission scheme, I have probed into similar issues that Professor Zheng discusses in her work. Professor Zheng and I exchanged ideas on several occasions, and have reached an understanding out of those elaborate talks that both of us are trying to find a solution to an identical problem. Our approaches may differ, but we do share same ideas and benefit from each other's research. We have also been more than once enlightened by Professor Zheng's work.

Last but not least, I have to point out that the complex scientific issues involved in mechanics of wind-blown sand movement, such as multi-scale process, multi-physics field coupling effect, randomness, nonlinearity, and so on, are also paramount concerns shared by scientists working in some other fields. The solution to these problems calls for joint efforts of scientists from different disciplines. Professor Zheng's work is a rewarding attempt to provide answers to some of those questions, and certainly sets, as we have realized, a valuable example for the study of other perplexing dynamical systems, aside from solving these intractable scientific issues in mechanics of wind-blown sand movement.

Qingcun Zeng



Academician of CAS

Institute of Atmospheric Physics, CAS

December 2008

Preface

Sand (dust) movement driven by wind force as a natural phenomenon can be seen everywhere in arid desert, farmland, seashore or even broader regions on the earth and other planets including the Mars, Venus, Titan and so on. This kind of aeolian process is usually constituted by three parts including the uplifting from the surface of the earth, atmospheric dispersion, and deposition back to the surface. Whilst wind-blown sand (dust) movement contributes to the formation of the Loess Plateau and the growth of marine fauna and flora, it also causes a series of disasters such as soil nutrient loss, physical damage to farmland, deterioration of air quality, abrasion of engineering facility, etc. These above-mentioned disasters and environmental problems arising from wind-blown sand (dust) movement, to which scholars from many scientific fields other than geographers have paid more and more attention, have always been a governmental as well as a public concern since the 20th century. Despite great achievements have been made in controlling and managing the wind-blown sand hazard in some developed countries, for example, in the United States and Canada, desertification and pollution caused by wind-blown sand movement still remain to be the most serious, most urgent issues in developing countries, especially in China, as the global climate changes.

The transportation of sand (dust) materials by wind force is influenced by a lot of factors: climate, soil type, vegetation cover and soil utilization, to name just a few. Due to its critical dependency, hysteretic nature and high spatial-temporal discontinuity, it is a typical complex natural flow of multi-phases, multi-component media, multi-scale nonlinearity under complex boundaries as well as a comprehensive dynamical system presenting multiple characteristics such as non-linearity, statistical property, diversity, self-similarity, criticality, etc., in which the multi-physics field coupling (wind field, temperature field, wind-blown sand electric field caused by charged sand particles) and multi-processes interaction (atmospheric, ecological, chemical, human activity, and so on) co-exist. Scientific research concerning the transportation of sand (dust) materials by wind force involves issues like multi-scale and multi-field coupling, stochastic and nonlinear process, and complex system, etc., which are also crucial issues confronted by other disciplines. Despite the large amount of progress

achieved through long-period field observations, wind-tunnel experiments and theoretical analysis as well as some famous monographs (i.e. Bagnold, 1941; Greeley and Iversen, 1985; Pye and Tsoar, 1990; Shao, 2000; Zeng, et al., 2006, etc.) published, there is still a long way to travel before we arrive at a comprehensive and profound understanding on the mechanism of sand (dust) movement and form a precise prediction of its real physical process; further still, a lot more obligations need to fulfill before we realize an effective simulation and reproduction of the evolution of wind-blown sand flux and aeolian landforms.

Hence, the research approach which combines experiments, modelling and quantitative analysis, as a predominance of mechanics, is probably to the advantage of a deeper understanding of the physical process and basic rules of wind-blown sand environmental problems. Taking this advantage of mechanics into consideration, my team and I have devoted to the research of several typical issues related to aeolian processes during the past decade from a mechanical perspective. Apart from a summary of recent considerable achievements, this book mainly intends to introduce our recent research on the wind-blown sand movement through theoretical modelling, quantitative analysis and computer simulation. The first chapter of this book briefly introduces the situation of desertification and wind-blown sand disasters in China, especially North-western China. Chapter 2 summarizes the characteristics of the wind field in the atmospheric boundary layer with a particular emphasis on the turbulent property of the wind field. Chapter 3 devotes to the introduction of researches on sand's lifting off the sand bed surface, including the linear and angular velocity of sand particles lifting from the bed, their distribution and the representation of the particle-bed collision process. Chapter 4 is a description of the wind-blown sand electrification and its effect on sand saltation movement. Chapter 5 is dedicated to an analysis of the forces on sand particles and their trajectories, and is also an introduction to the experiment and theoretical prediction of sand transport rate, and in particular, the electric and thermal effect on the development of wind-blown sand flux, as well as the prediction of sand movement and transport intensity under a fluctuating wind field. Chapter 6 and 7 are devoted to the introduction of the formation and evolution of some typical aeolian landforms like ripples and dunes. Chapter 8 presents the mechanical analysis method to estimate the efficiency of sand prevention methods.

This book aims at serving as a reference for researchers and graduate students who major in geo-related sciences, such as physics of wind-blown sand, environmental science, geophysics, atmospheric science, etc., mechanics as well as applied mathematics, broadening the readers' horizon on the latest development of the quantitative research on wind-blown sand

movement and enhancing their competence to apply basic methods in this field. What I strive for is provide some methods and principles which may be helpful to researchers interested in the wind-blown sand movement and other environmental issues via this book, which, on one hand, may help researchers and students of geology and atmospheric science understand what can be absorbed from mechanics to push investigations on wind-blown sand movements in a more rational and quantitative manner and on the other hand, provide researchers and students expertise in mechanics, mathematics, physics and environment-related engineering with a smooth access to the research field of wind-blown sand movement. In this case, both parties mentioned above can unit their efforts to promote an understanding of the mechanism of wind-blown sand (dust) movements and push forward the development of this interdisciplinary research. By the way, with the publication of this book, I would also hope that more and more scholars and experts in the world will pay their attention, further their professional suggestions and actions to aeolian environmental problems in China.

Since the first day I set foot in the field of wind-blown sand movements, I have been inspired by some scholars in Geosciences and atmospheric sciences as follow: Prof. D. A. Gillette of National Oceanic and Atmospheric Administration (USA), Prof. Y. P. Shao of the Institute of Geophysics and Meteorology, University of Cologne, Academician H. L. Sun and D. H. Qin, Dr. P. Cui, Dr. Z. H. Lin, Dr. T. Wang, Dr. J. J. Qu, Dr. Y. Q. Ling, Dr. Z. B. Dong of Chinese Academy of Sciences (CAS) and Academician Y. T. Chen of China Earthquake Administration as well as Dr. X. Y. Zou of Beijing Normal University. Besides, some scholars in Mechanics like Prof. K. Moffat, ex-President of the International Union of Theoretical and Applied Mechanics (IUTAM, 2000-2004), Prof. F. Hussain (Member of the National Academy of Engineering and the Academy of Sciences for the Developing World) of the University of Houston, and several ex-Presidents of the Chinese Society of Theoretical and Applied Mechanics (CSTAM), including Academician Z. M. Zheng, Y. L. Bai, and E. J. Cui, etc., also offered me very important assistance. I would like to take the opportunity to express my gratitude to them. In particular, I would like to appreciate Academician H. Zhou of Tianjin University, Academician Q. C. Zeng of the Institute of Atmospheric Physics, CAS, and Academician J. C. Li, President of CSTAM, who not only provided much important and detailed guidance, but also paid much attention to my research work. All these concern and encouragement have been urging me keep going forward.

The research work in this book is co-financed by the project of the Ministry of Science and Technology of China (No.2009CB421304,

No.2006DFA03640), the Natural Science Foundation of China (NSFC, No.10532040, No.10872082) and the Science Foundation of Ministry of Education of China (No.308022). I would like to express my acknowledgement on these supports and also would like to thank Dr. P. W. Ji, Dr. Q. G. Meng, Dr. S. G. Zhan, and Dr. Q. Q. Liu of NSFC.

Besides, sincere thanks are due to my students as follows: N. Huang, L. Xie, T. L. Bo, J. H. Zhang, P. Wang and W. Zhu, etc., who assisted me to collect relevant materials. I appreciate Mr. M. Lion from Canada and Mr. N. Virgo from the United Kingdom for the proofreading of this book, and due to Dr. Agata Oelschläger from Springer-Verlag, Germany for the publishing work and Mr. N. Cheng for the typesetting of this book. Finally, I would like to express my sincere thanks to Prof. Y. H. Zhou, Director of the Key Laboratory of Mechanics on Western Disaster and Environment (Lanzhou University) for his long-term support.

Lanzhou University
Lanzhou, P. R. China
January 2009


Xiao Jing Zheng

Contents

| | |
|--|-----------|
| Chapter 1 Wind-Blown Sand Environment | 1 |
| 1.1 Desert and Desertification | 1 |
| 1.1.1 Desert..... | 1 |
| 1.1.2 Desertification | 4 |
| 1.2 Harms of Wind-Blown Sand Environment..... | 6 |
| 1.2.1 Wind Erosion..... | 7 |
| 1.2.2 Sand (Dust) Storm | 8 |
| 1.3 Examples: Dunhuang, Minqin, Maqu..... | 12 |
| 1.3.1 Dunhuang | 12 |
| 1.3.2 Minqin | 14 |
| 1.3.3 Maqu..... | 16 |
| Chapter 2 Flows of the Near-Surface Boundary Layer..... | 19 |
| 2.1 An Introduction to Fluid Mechanics..... | 19 |
| 2.1.1 Viscosity of a Fluid..... | 20 |
| 2.1.2 Properties of Flow | 20 |
| 2.2 Basic Equations of Fluid Mechanics | 22 |
| 2.2.1 Conservation of Mass (Continuity Equation)..... | 23 |
| 2.2.2 Conservation of Momentum | 23 |
| 2.2.3 Conservation of Energy | 24 |
| 2.2.4 Basic Equations of Turbulence..... | 25 |
| 2.2.5 Models of Turbulence..... | 25 |
| 2.2.6 Approaches of Turbulent Numerical Simulation..... | 27 |
| 2.3 Basic Characteristics of the Atmospheric Boundary Layer | 28 |
| 2.4 Observations of the Atmosphere Boundary Layer | 32 |
| 2.5 Basic Equations of the Atmospheric Boundary Layer..... | 38 |
| 2.5.1 Basic Equations | 38 |
| 2.5.2 Aerodynamic Roughness | 41 |
| 2.5.3 Characteristics of the Flow Field on the Wind-Blown Sand Boundary Layer | 42 |
| 2.5.4 Effect of Sand Dunes on the Flow Field..... | 44 |
| 2.6 Wind Gusts near the Earth's Surface..... | 46 |
| 2.6.1 Analysis of the Wind Gusts | 47 |

| | |
|---|------------|
| 2.6.2 Prediction Model I: Wind Gusts Vary with Time | 55 |
| 2.6.3 Prediction Model II: Wind Gusts Vary with Height..... | 58 |
| Chapter 3 Sand Motion near the Sand Bed Surface..... | 61 |
| 3.1 Threshold Wind Velocity for Sand Motion | 62 |
| 3.1.1 Mechanism of the Entrainment of Sand Particles..... | 62 |
| 3.1.2 Threshold Wind Velocity of Sand Motion | 63 |
| 3.1.3 Factors Affecting the Threshold Wind Velocity | 65 |
| 3.2 Experimental Research on the Lift-off of Sand Particles | 67 |
| 3.2.1 Experiments on Particle-Bed Collision with ‘Artificial’ Sand | 67 |
| 3.2.2 Measurements of the Linear Velocities of Lift-off Particles .. | 68 |
| 3.2.3 Measurement of the Angular Velocities of Saltating Particles | 72 |
| 3.3 Stochastic Model of Particle-Bed Collision | 76 |
| 3.3.1 Stochastic Model | 76 |
| 3.3.2 Soft-Particle Approach for Collision Process..... | 79 |
| 3.3.3 Hard-Particle Approach for Collision Process | 81 |
| 3.3.4 Analytical Solution of Lift-off Velocity | 84 |
| 3.4 Probability Distribution of Lift-off Velocities..... | 86 |
| 3.5 Splash Function | 94 |
| 3.5.1 Splash Function for ‘Uniform’ Sands..... | 94 |
| 3.5.2 Splash Function for ‘Mixed’ Sands | 98 |
| Chapter 4 Wind-Blown Sand Electrification | 105 |
| 4.1 Charged Sand Particles and their Charging Mechanisms | 106 |
| 4.1.1 Observations and Measurements | 106 |
| 4.1.2 Charging Mechanisms of Sand Particles | 109 |
| 4.2 Measurements of Wind-Blown Sand Electric Field | 111 |
| 4.2.1 Atmospheric Electric Field..... | 111 |
| 4.2.2 Field Observation of Wind-Blown Sand Electric Field..... | 112 |
| 4.2.3 Wind Tunnel Measurement of Wind-Blown Sand Electric Field..... | 115 |
| 4.3 Theoretical Calculation of Wind-Blown Sand Electric Field | 120 |
| 4.3.1 Electric Field Due to Sand Particles Moving in Air..... | 121 |
| 4.3.2 Electric Field Due to Sand Particles in Sand Bed..... | 122 |
| 4.3.3 Total Electric Field Due to Charged Sand Particles in Wind-Blown Sand Flux | 123 |
| 4.4 Effects of Charged Sand Particles | 126 |
| 4.4.1 Effects on the Entrainment of Sand Particles’ | 126 |
| 4.4.2 Effects on Electromagnetic Wave Propagation | 128 |

| | |
|--|------------|
| Chapter 5 Wind-Blown Sand Flux and its Prediction | 133 |
| 5.1 Forces on Saltating Sand Particles..... | 134 |
| 5.2 Sand Saltation | 139 |
| 5.2.1 The Effect of Wind-Blown Sand Electric Field on Sand Saltation..... | 139 |
| 5.2.2 The Effects of Particle's Mid-Air Collisions on Sand Saltation Trajectories | 144 |
| 5.2.3 Saltation Trajectory and Saltation Activity in a Fluctuating Wind Field..... | 148 |
| 5.2.4 The Criterion of Saltation and Suspension | 152 |
| 5.3 Experiments and Observations on Sand Transport Rate | 155 |
| 5.4 Theoretical Simulations on the Evolution of Wind-Blown Sand Flux..... | 160 |
| 5.5 Dust Devil..... | 171 |
| | |
| Chapter 6 Aeolian Geomorphology and its Simulation – Aeolian Sand Ripples..... | 181 |
| 6.1 Observations of Aeolian Sand Ripples | 183 |
| 6.1.1 The Basic Characteristics of Aeolian Sand Ripples | 183 |
| 6.1.2 The Formation Mechanism of Aeolian Sand Ripples..... | 187 |
| 6.2 Continuous Models for Aeolian Sand Ripples | 189 |
| 6.2.1 The Anderson's Continuous Model..... | 189 |
| 6.2.2 The Granular Surface Flow Model..... | 192 |
| 6.3 Discrete Models for Aeolian Sand Ripples..... | 196 |
| 6.3.1 Cellular Automata Model (Anderson-Bunas Discrete Model) | 196 |
| 6.3.2 Discrete Element Model (Landry-Werner Model) | 199 |
| 6.3.3 Coupled Mapping Lattice Model (Nishimori-Ouchi Model) | 202 |
| 6.4. Discrete Particle Tracing Method (DPTM) Model..... | 205 |
| 6.4.1 Basic Method..... | 205 |
| 6.4.2 Major Simulation Results | 207 |
| | |
| Chapter 7 Aeolian Geomorphology and its Simulation – Aeolian Sand Dunes | 219 |
| 7.1 Aeolian Sand Dunes and Observation Results | 220 |
| 7.1.1 Classification of Sand Dunes..... | 220 |
| 7.1.2 The Observation of Sand Dune Migration..... | 225 |
| 7.1.3 Observation on the Dynamical Behavior of Sand Dunes | 229 |
| 7.1.4 Influence Factors | 231 |
| 7.2 Continuum Sand Dune Model | 232 |

| | |
|--|------------|
| 7.3 Simulation of Sand Dune Field | 235 |
| 7.3.1 Coupled Mapping Lattice Method..... | 235 |
| 7.3.2 Cellular Automaton Method..... | 236 |
| 7.4 Numerical Simulation of Sand Dune Field..... | 238 |
| 7.4.1 Discrete Numerical Simulation of Sand Dune Field | 238 |
| 7.4.2 Simulation Results..... | 243 |
| Chapter 8 Mechanical Analysis on the Efficiency of Sand Prevention Methods..... | 261 |
| 8.1 Sand Fence..... | 262 |
| 8.2 Straw Checkerboard Barriers..... | 268 |
| 8.3 The Mechanical Properties of Crust | 272 |
| 8.3.1 The Survey on the Mechanical Properties of Crust..... | 274 |
| 8.3.2 The Destruction of Saltating Sand to Crust | 280 |
| References..... | 287 |
| Author Index | 301 |
| Subject Index..... | 305 |

Symbols

In this text, hundreds of different physical quantities are included in various formulations. Use of the same letters or symbols for different concepts has been unavoidable. Choice of notation was affected by the desire to retain commonly used notations familiar in each field of study, while at the same time avoiding ambiguity by making a single choice where two or more symbols for the same quantity are known to exist in the literature.

Main symbols commonly used in this text are listed below, unless otherwise defined in the text, the meaning of symbols, are understood:

| | | | |
|-----------------------|--|--------------------|--|
| x, y, z | Cartesian coordinates | S_T | viscous dissipation term |
| $\mathbf{u}(u, v, w)$ | velocity vector of fluid (velocity component in coordinates x, y, z) | λ_T | thermal conductivity |
| x_i | i th coordinate ($i = 1, 2, 3$) | γ_d | atmospheric dry adiabatic lapse rate |
| \mathbf{e} | the unit vector of the coordinates with \mathbf{e}_i in the direction of x_i | k_T | thermal diffusivity |
| μ | viscosity of fluid | e | internal energy |
| μ_t | turbulent viscosity or eddy viscosity coefficient | c_p | heat capacity at constant pressure of fluid phase |
| v | kinetic viscous of fluid | g | gravity acceleration |
| Re | Reynolds number | R | Molar gas constant |
| ρ | density | t | time |
| ν | kinetic viscous of fluid | Δt | time interval |
| U | characteristic velocity of fluid or velocity | l_m | Prandtl mixing length |
| L | length | k | Karman constant |
| H | height | σ_k | Prandtl number of the turbulent fluctuation momentum |
| P | thermodynamics pressure | ε | turbulent dissipation rate |
| T | temperature | c | concentration of solid phase in two phase flow |
| \mathbf{f} | body force vector | P^0, ρ_0, T^0 | pressure, density and temperature of static atmosphere |
| \mathbf{T} | surface force tensor | | |
| q_T | heat flux | | |

XVIII Symbols

| | | | |
|-----------------|--|-----------------------------|---|
| p, ρ', T^d | variation of thermodynamic quantities caused by flow | N_s | number flux of saltation particle from surface bed |
| u_{*t} | threshold friction velocity for bare-sand(soil) surface | N_a | number flux of particles entrained directly by the aerodynamic force of air flow |
| u_{*0} | surface friction velocity | σ | standard deviation or basal-to-frontal area ratio of vegetation |
| u_* | friction velocity of fluid | S_k | skewness |
| $(u_{*t})_v$ | threshold friction velocity for vegetated surface | K_x | kurtosis |
| u_t | threshold fluid velocity at height z | I | turbulence |
| u_{*a} | friction velocity of wind in saltation layer in wind-blown sand | T_g | wind gusts period |
| z_0 | aerodynamic roughness length | D | particle diameter |
| z_s | equivalent roughness or movable bed roughness in wind blown sand | ρ_s | density of sand particle |
| τ_0 | shear stress at the upper boundary of the saltation layer in wind-blown sand | D_s | diameter of sand particle |
| τ_a | shear stress in the saturation layer | m_s | mass of sand particle |
| τ_c | critical fluid shear stress | V_s | volume of sand particle |
| τ_s | vertical momentum flux produced by sand movement | $\dot{x}, \dot{y}, \dot{z}$ | resultant velocity vector of sand particle (velocity component in coordinates x, y, z) |
| H_s | thickness of mean saltation | θ | angle of sand velocity to the horizontal or potential temperature |
| | | η | porosity of the sand bed or fence |
| | | E | kinetic energy of moving particle or Young's modulus of crust |
| | | α_{dune} | velocity acceleration factor on the dune |
| | | u_{*crest} | friction velocity on dune top |

| | | | |
|------------------------------------|---|-----------------------------------|---|
| $u^*_{-\infty}$ | friction velocity of the inflow far away from dune | β, α_k | impact and contact angle of sand in the process of impact with bed surface |
| \mathbf{F}_D | aerodynamic drag force | ω | spin angular velocity |
| \mathbf{F}_g | gravity force | N_r, N_e | numbers of rebound and ejected sand particles |
| \mathbf{F}_L | aerodynamic lift force | | |
| \mathbf{F}_M | Magnus force | | |
| \mathbf{F}_E | electric force | V_{im} | Impact velocity of sand particle |
| \mathbf{F}_s | Saffman force | \bar{N}_{ej} | mean number of sand particles jumping from the bed per impact |
| \mathbf{F}_B | Basset force | | |
| \mathbf{F}_i | inter-particle force | | |
| \mathbf{F}_{pn} | normal contact force in the process of particle colliding | | |
| \mathbf{F}_{fr} | tangential friction force in the process of particle colliding | V_r, V_e | rebound velocity and ejected velocity of sand particle from bed, respectively |
| $\mathbf{F}_{rn}, \mathbf{F}_{rt}$ | normal and tangential damping forces in the process of particle colliding | V | resultant lift-off velocity of sand particle from bed |
| \mathbf{F}_x | force acting on the wind per volume resulted from sand transport | \mathbf{E}_s E_x, E_y, E_z | wind sand electric field vector |
| C_D | aerodynamic drag coefficient | E_a | atmospheric electric field |
| C_L | aerodynamic lift coefficient | E_{a0} | atmosphere electric field at ground level |
| λ_V | roughness density, frontal area index of vegetation roughness | δ_e | density of surface charges at ground level |
| σ_V | basal-to-frontal area ratio of roughness element or vegetation | ε_0 | electrical permittivity of air |
| χ | angle between the wind direction and the normal line of the bed surface | ε_s | permittivity of sand particle |
| α | surface slope angle | C_q | charge-to-mass ratio of charged sand particle |
| | | q^c | particle charge |

| | | | |
|----------------------|--|----------------------------|--|
| ρ_q | volume charge density | RSI | ripple symmetry index |
| σ_q | surface charge density | RI | ripple index |
| E_{sz}^1, E_{sz}^2 | electric field produced by saltating and suspending particle, respectively | λ | wavelength of sand ripple |
| E_{cz} | electric field produced by sand particles in sand bed | α_{ss}, α_{ls} | stoss and lee slope angle of sand ripple |
| E_i | electric field of incident electromagnetic wave penetrating in the spherical sand particle | V_d | migration velocity of sand dune |
| σ_w | vertical velocity standard deviation of air parcel | H_{supply} | thickness of sand supply |
| w_{st} | terminal settling velocity of sand particle | h_{tun} | height of wind tunnel |
| P_{sal} | saltation parameter | u_{ax} | axial wind velocity of wind tunnel |
| σ_w^s | vertical velocity standard deviation of sand particle | h_0 | straw height of straw checkerboard barrier |
| τ_L | Lagrangian time scale of air parcel | l_{max} | maximum distance of two adjacent straw grids of straw checkerboard barrier |
| T_L^* | modified Lagrangian time scale of air parcel along the sand particle trajectory | w_e | elastic deflection of crust because of saltation impact |
| I_s | processional moment of sand particle | $W(t)$ | creep deflection function of crust |
| | | $p(\cdot)$ | collision probability of saltating particle |
| | | $f(\cdot)$ | distribution function |
| | | Q | sand transport rate |
| | | q | mass flux of sand |

Subscripts

ij tensor
 s sand
 f fluid

Unsuperscripted or Superscripts

($\bar{\cdot}$) mean of the physical quantity
 $(')$ fluctuation of the physical quantity
 (\cdot) time rate
 $(\cdot\cdot)$ second derivative with respect to time

Chapter 1 Wind-Blown Sand Environment

The surfaces of the earth and some other planets are permeated with sand (dust) particles entrained by airflow, which constitute the wind-blown sand environment to be discussed in the book. Deserts and desertified lands are one of the major material sources of the wind-blown sand environment. Researchers devote their major attention to the evolution mechanism of the wind-blown sand environment, while the government and the public cast more of their eyes on its harm to human beings. Consequently, in this chapter, Sect. 1.1 makes a brief introduction on the situation of deserts and desertification of lands in the world, especially, in the inland China; Sect. 1.2 expounds the major harms brought by the wind-blown sand environment with wind erosion and sand (dust) storm as examples. To make our point more clearly; Sect. 1.3 devotes to a brief introduction of the situations of three typical desertified areas in Gansu, China, where the author comes from, so as to illustrate the disastrous consequences of wind-blown sand. The three areas are Dunhuang, a site of world cultural heritage in an arid region which is severely threatened by wind-blown sand, Minqin, a county situated between the two great deserts of Tengger and Badain Jaran, and Maqu, a county located in a natural meadow of the alpine humid region respectively.

1.1 Desert and Desertification

1.1.1 Desert

The global arid region is over 55.5 million km², covering a third of the total land area (Ci 2005). Deserts, taking up some 7 million km², are mainly located in the six regions along the equatorial, i.e., North Africa, the middle part of Central Asia, Southwest Africa, the Midwest part of North America, the southwest part of South America and Australia. There lie the great deserts of the world, including the Sahara Desert (1.8 million km²) in North Africa, the Rub Al Khal Desert (0.56 million km²) in Arabia, the Great Sandy Desert (0.36 million km²), the Simpson Desert (0.312 million km²) and the Gibson Desert (0.221 million km²) in Australia, the Kara-Kum

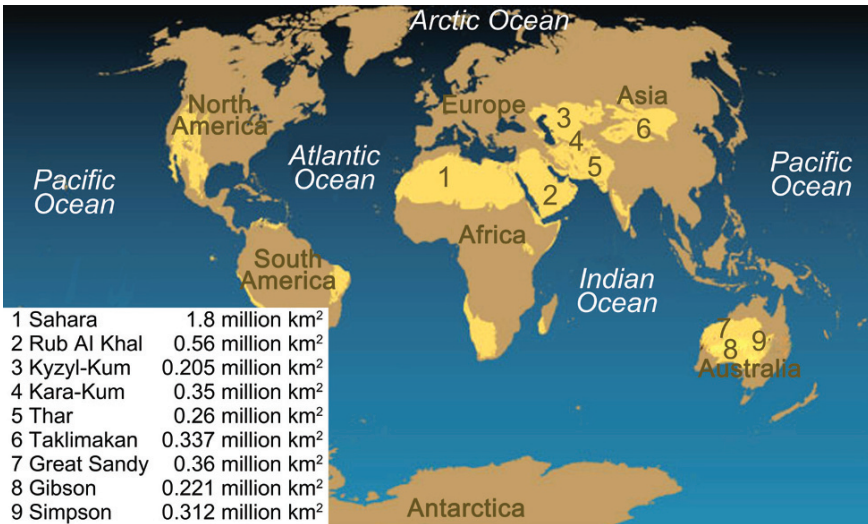


Fig. 1.1. Distribution of world arid and desert area (modified from National Geographic)

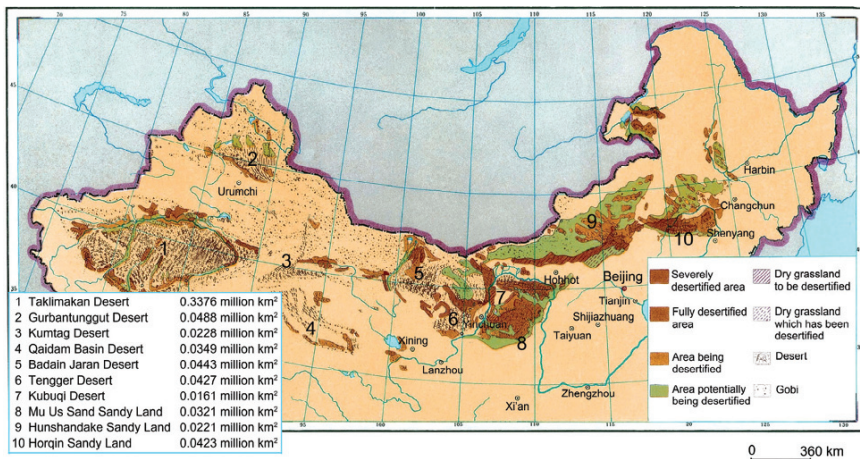


Fig. 1.2. Distribution of desert and desertification region in the Northern of China (modified from Wang 2003)

Desert (0.35 km^2) and the Kyzyl-Kum Desert (0.205 km^2) in mid Asia, the Thar Desert (0.26 km^2) in India and Pakistan and the Taklimakan Desert (0.337 km^2) in China (see Fig. 1.1). As far as China is concerned, deserts are mainly in the Northwest China, north of North China and west of Northeast China, forming an area of 600 km in width and 4,000 km in

length and covering an area of 865,100 km² (Zhong 1998). China has the largest area of deserts except Australia and Saudi Arabia (see Fig. 1.2).

Arid climate, characterized by drought and lack of precipitation, is prerequisite to the formation of deserts, which is also significantly affected by the latitude, atmospheric circulation, land-sea distribution and topography. Globally speaking, zones between 15°–35° N/S are predominated by the subtropical anticyclone. Due to the dry and cold wind blowing from high latitudes all the year round, the climate there is featured by rarity of precipitation and cloud, long sunshine duration, strong evaporation and extreme drought, all of which are vital to the formation of deserts. Therefore, like Sahara, most of the largest deserts are situated in these two zones. However, it is not the case in China. Because of the influence of the Qinghai-Tibetan Plateau on atmospheric circulation, the subtropical zone in China is dominated by the monsoon, which brings sufficient precipitation and pleasant temperature. Concurrence of warm and rainfall makes this area home to diversified subtropical vegetation and a fully developed agrarian region rather than a desert (McKee 1980). In China, deserts are mainly situated in the temperate zone of 35°–50° N and 75°–125° E. For example, deep in the inland, far from the sea and under the control of the continental air mass all the year round, the Taklimakan Desert becomes the largest temperate inland arid area, with an annual precipitation less than 50 mm and in some parts even below 20 mm.

The material basis of desert formation is the abundance of sand supplies which is closely related to the ancient geography. In the arid region, there are mainly two landform structures that could possibly become the material source of sands: one is the vast inland basin like the Tarim Basin and the Junggar Basin in China and the Turan Plain in the former Union of Soviet Socialist Republics (USSR) where the Taklimakan Desert, the Gurbantunggut Desert and the Karakum Desert are respectively located, and the other is the arid scabrock, especially its piedmont plain and partial depression. For example, due to the alpine climate, ample precipitation and great diurnal temperature variation, rocks on the piedmont plains in the Saharan Atlas and the Tademait Plateau in the middle of Algeria are apt to weathering and peeling. In summer, rock chips are transported by melted ice and snow to the basin and form a thick deposition-alluvium. In arid climate, these sandy sediments, once deflated by wind, will soon yield ample sand materials for deserts, large or small, in the Sahara.

1.1.2 Desertification

‘Desertification’ was first proposed by the French scholar Aubreville in 1949 (Zhu 1999) and became a standard term after the United Nations (UN) Conference on Desertification in 1977. It was originally merely applied to the migration of dunes, activation of fixed dunes and sandy lands and expansion of deserts, etc. Not until 1992 did United Nations Conference on Environment and Development (UNCED) propose a more comprehensive and more precise definition, that is, ‘Desertification is land degradation in arid, semi-arid and dry sub-humid areas resulting from various factors, including climatic variations and human activities’ (United Nations General Assembly 1994). It was noted that ‘land’ means the terrestrial bio-productive system that comprises soil, vegetation, other biota, and the ecological and hydrological processes that operate within the system; ‘land degradation’ means reduction or loss, in arid, semi-arid and dry sub-humid areas, of the biological or economic productivity and complexity of rainfed cropland, irrigated cropland, or range, pasture, forest and wood-lands resulting from land uses or from a process or combination of processes, including processes arising from human activities and habitation patterns, such as: (1) soil erosion caused by wind and/or water; (2) deterioration of the physical, chemical and biological or economical properties of soil; and (3) long-term loss of natural vegetation. With the rapid economic development, desertification, as a crucial global issue, becomes more and more a common concern of the entire international community.

At present, the total area of desertification in the world is 35.92 million km², about a fourth of the world’s land area, and is increasing at a rate of 50,000–70,000 km²·year⁻¹ (United Nations Environment Programme 1992). Desertification is a common phenomenon of all continents, but especially conspicuous in Asia and Africa with the total area of desertification accounts for 66.65% of the world’s. China is unfortunately one of the countries under the fiercest attack of desertification. By the end of 2004, the area of desertification is 2.6362 million km², taking up 27.64% of the total territory and 79.47% of the area prone to desertification, which is higher than the world’s average of 69% (United Nations Secretariat of China to the Convention to Combat Desertification 2006). Besides, 80.5% of the area of desertification is in the arid or semi-arid regions. The heavy and extreme areas of desertification are respectively 0.4334 million km² and 0.5864 km², accounting for 16.44% and 22.24% of the total area of desertification. What is more appalling is the fact that the area prone to desertification in China has reached 3.317 million km², i.e., 34.6% of the total land area (State Forestry Administration 2005).

Desertification is the combined effect of climate changes and human activities. Climate changes, especially those concerning humidity, are the determinant of desertification. The ecological environment is made more apt to desertification by global climate changes, especially the warm-dry trend in mid latitudes. Meanwhile, desertification is rapidly accelerated by arid climate, great precipitation variability, high loose-sand content in soil as well as strong and frequent sand-moving wind. For example, in most of the areas of desertification in China, the number of days with wind velocity exceeding $17 \text{ m}\cdot\text{s}^{-1}$ is about 30 days per year and even more than 50 days per year in some parts, most of which take place in spring.

The impact of human activities on desertification is by no means to be neglected. In arid regions, desertification is accelerated by mainly overgrazing, extensive farming, irrational utilizing of water resource, excessive deforestation, unscientific mining, road building, industrial construction and transportation by motor vehicle, etc. In those areas, the fragile ecosystem has a very limited bearing capacity of population and human activities. Even a slight human interference would break its ecological balance and destroy primary surface soil, intensifying wind-blown sand movements and finally leading to desertification.

The damage of desertification is both longer in duration and higher in intensity than that of other natural disasters. Land degradation, biocoenotic degeneration, hydrological deterioration and environmental pollution would destroy the living environment of human beings. Its resultant natural disasters, such as the sand (dust) storm, often threaten human life, property, living facilities and construction projects. In areas of desertification, the wind-blown sand not only damages transportation constructions like highways, railways, road beds and bridges, but also impedes communication and transportation. For example, due to the intense sandstorm in Northwest China on May 5, 1993, the Lanzhou-Xinjiang Railway was disrupted for 31 hours and the Wuda-Jielantai Railway for 4 days; 37 trains were canceled or delayed; the Lanzhou Airport was closed for 2 days and the Dunhuang Airport 7 days. China suffers from a direct economic loss of ¥ 54 billion per year because of desertification (State Forestry Administration 1997). Therefore, the financial appropriation from the Chinese government used for desertification monitoring has risen from over US \$ 600 thousand per year to over US \$ 1.2 million per year. Since 2001, the central and local governments allocated about US \$ 6 billion to US \$ 8.5 billion per year for forestry ecological projects, US \$ 42 million per year for comprehensive agricultural development and desertification combating, US \$ 200 million per year for control of soil and water erosion, US \$ 1.2–2.4 million per year for sand control along railways, US \$ 76 million per year for greening along highways, and US \$ 70 million per year as dis-

count loan for sand control. Besides, a large amount of funds is used for grassland improvement, poverty alleviation, scientific research, and farmland reclamation in desertified areas (United Nations Secretariat of China to the Convention to Combat Desertification 2006).

1.2 Harms of Wind-Blown Sand Environment

The wind-blown sand environment is mainly characterized by wind-forced movements of sand (dust) particles on and above the ground surface, which are mainly in the form of creeping of sand particles on the ground surface, saltating within the wind-blown sand flow of the near-surface layer and suspending of dust in high altitudes (see Fig. 1.3). The book will focus on harms of wind-blown sand environment, wind erosion and sand (dust) storm in particular, though the transportation and deposition of sand (dust) particles do have some positive effects, such as serving as a shaping force of some certain landforms, providing nourishment for sea lives and neutralizing arid rain.

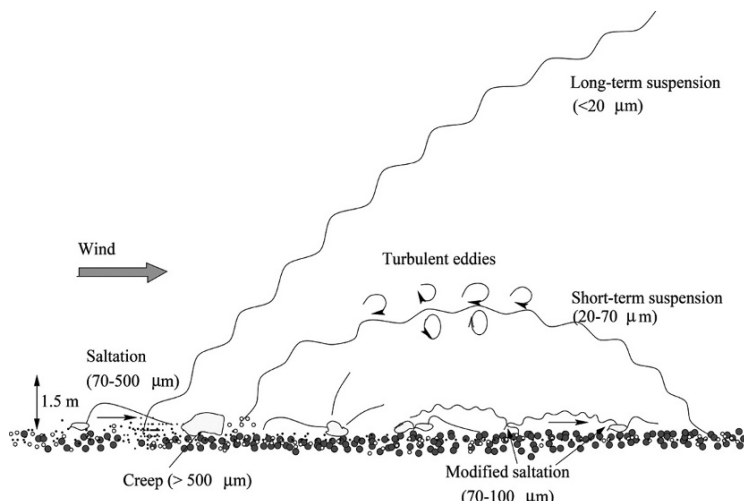


Fig. 1.3. An illustration of sand particle transport mode: creeping ($> 500 \mu\text{m}$), saltation (pure saltation 500–100 μm and modified saltation 100–70 μm) and suspension (short-term suspension 20–70 μm and long-term suspension $<20 \mu\text{m}$) of sand particles during wind erosion (from Shao 2000)

1.2.1 Wind Erosion

Wind erosion is a process of wind-forced movement of soil particles (Shao 2000). In arid and semi-arid regions, it is fundamental in the land-surface process and is itself one of the basic geomorphological processes. Meanwhile, it is not only a major cause of loss of soil and nourishment essential to vegetation, evaporation, surface desertification and dust emission, but also cause of mechanical damages to soil crusts, crops and engineering constructions by hitting, shearing and sapping. As a primary type, desertification caused by wind generally works in two ways, that is, wind erosion and wind deposition. Macroscopically speaking, if lack of vegetation cover, the foremost land on the path of wind-blown sand movement will be severely eroded into dust and sand materials, like silts and fine sand particles, which then will be transported by airflow and deposit far away. After years of wind erosion, various landforms, like the Gobi, monadnock and Yardang, will be formed on the ground. These eroded areas become the first sand supplies and are called the wind erosion areas. As it goes deeper into the land, the airflow will become less intense and drifting sands will deposit, finally form dunes and sandy lands of various shapes and heights, according to local topography and vegetation situations. The latter area is just the so-called wind deposition area.

According to the global desertification assessment made by the United Nations Environment Programme (UNEP) in 1991, 41.4% of the degraded land in arid regions resulted from water erosion, 45.9% from wind erosion and the rest from chemical erosion. Report on the State of Desertification and Sandification in China (State Forestry Administration, China 2005) announced that, the areas of desertified land as a result of wind erosion, water erosion, freeze-thawing erosion and salinization total respectively 1.8394 km^2 , 0.2593 km^2 , 0.3637 km^2 , 0.1738 km^2 , taking up respectively 69.77%, 9.84%, 13.80% and 6.59% of total desertified land. Wind erosion in the oasis-desert transition zone is particularly crucial in the process of eco-system degradation. What happens in Minqin, a county in an oasis-desert transition area of the northwest arid region, is exemplary. The Minqin oasis is an essential part of the ecological barrier of China, but under the combined influence of human activities and global climate changes, intensified wind erosion and its resultant wind-blown sand disaster lead to the severe deterioration of the oasis-desert eco-system, drastic sinking of its underground water level, rapid shrinking of the oasis area as well as the gradual merging of the Tengger Desert and the Badain Jaran Desert. All these seriously threaten the living environment of local residents. Moreover, with the advancement of West Development Programme in China, a series of large-scale projects conducted in arid regions disturb the typical

desert eco-system and result in destruction of desert vegetations and intensification of wind erosion. The erosion caused by wind makes the oasis-desert transition zone a potential or even another newly formed desert. Dusts emitted from this zone will lead to pollution problems in broader area if being transported and suspending in the troposphere. The dust flow of high density will disturb communication signals and reduce visibility, which will lead to traffic and aircraft accidents as well as casualty and economic loss. Besides, diffuse air pollution will do great harm to health and welfare of human beings.

1.2.2 Sand (Dust) Storm

Sand (dust) storm, a general term for both sand storm and dust storm, is a typical disastrous weather phenomenon harassing desert and its surrounding areas. The four regions in the world most frequented by sand (dust) storms are the Central Asia, North America, Central Africa, and Australia (Lu 2001). In the United States, due to lack of vegetation cover, Colorado, Kansas, Oklahoma and Texas are more apt to be visited by sand (dust) storm. Sahara in Africa is the largest arid region in the world and often falls into a victim to sand (dust) storm brought by the Inter-Tropical Convergence Zone (ITCZ) in its northward advance. In Australia also lie several areas of high sand (dust) storm risk: central Australia, central Queensland, east of Nullarbor Plain and the west coast of Australia etc. Iraq and Kuwait in the Middle East are no exception. As a part of the central Asian high risk region, areas of high sand (dust) storm risk in China are mainly situated in the arid north China, namely between 35° – 49° N and 74° – 119° E, forming a zone of 4,500 km long east-to-west and 600 km wide north-to-south. Major sand sources are centered on Minqin, stretching from the Taklimakan Desert and the Badain Jaran Desert, the north part of Gansu province, the Tengger Desert, the Ulan Buh Desert and finally to the Mu Us sandy land. Other areas of intense sand (dust) storm are the Turpan basin, the north piedmont of the Yinshan Mountain, the Otindag sandy land and their surrounding areas.

Powered by strong gale, sand and dust particles emitted from dry and bare land surface will be driven to surge forward and form a formidable wall of sand (see Fig. 1.4). If they are obstructed or the wind velocity slows down, a great number of particles will deposit, burying farmlands, villages, railways, highways and water sources (see Fig. 1.5 and 1.6) with sand piles and dunes. Passing over arid regions, the strong wind will blow away the surface layer of soil together with its organic matter, leaving the land sterile and apt to sandification. Sometimes, it even uproots trees and



Fig. 1.4. A photograph of dust storm near to Khartoum international airport, Sudan, on April 2008 (photo by Hou FD)



Fig. 1.5. A photo of the Jining-Erlianhot railway threatened by the invaded shifting sand On May 29, 2002, an international train from Beijing to Ulan Bator, Mongolia, driving on the railway threatened; the Jining-Erlianhot railway is a important component of Eurasian Continental Birdge, but the shifting sand threaten the transportation safety (Xinhua News Agency)



Fig. 1.6. On April 17, 2006, vehicles parked by the road of Ma Liandao in Beijing are covered with dust. Beijing encountered a dusty weather on that day (photo by Xinhua News Agency)



Fig. 1.7. On 28th Feb. 2007, the train 5807 head for Aksu from Urumuchi encountered a sandstorm with gale of 13th grade, 11 carriages are turned over, 32 passengers are wounded, 2 heavily injured and 3 persons are dead, the South Xinjiang railway are blocked (CNSPHOTO)

houses, blows over trains (see Fig. 1.7), destroys agricultural facilities and causes casualty of human lives and livestock. Fine particles entrained by sand (dust) storms may be transported to places far away from the source region and lead to air and water pollution. If transported to the troposphere

and suspending there for long, they will affect the long wave radiation of the sun and local climate, especially radiation budget and energy balance. Besides, low visibility in a sand (dust) storm will disturb the communication and transportation in urbane areas and even on expressways. The world has suffered great ecological and economical losses because of this. For instance, the Black Storm sweeping the Great Plain in 1930s was such an unprecedented sand storm in the history of the United States that the losses it caused remained uncountable even decades after its outbreak. Millions of hectares of farmland were destroyed; up to 1940, 2.5 million people had been forced to desert their homes in the sand (dust) storm stricken states. On May 5, 1993, the black storm hurtling through the west China cost 85 human lives, with another 264 injured and 31 missing, 120,000 livestocks, dead or missing, over 3,700 km² farmland and over 2,000 miles of penstocks. The direct economic loss amounted to ¥ 560 million. In 1993 and 1994, the most intense sand storms in Australia were no less than a catastrophe to the east coastal cities and surrounding towns. The 1993 sand storm was a large scale one, deflating a tremendous amount of soil, the depositions of which spread far and wide over the east Australia and New Zealand for over 1800 miles. Fine soil particles were driven into the atmosphere and revolved around the earth three times with atmospheric currents. In 1994 the tragedy repeated itself: a sand storm swept over the West Australia, South Australia and west of the New South Wales. It was estimated that 100–150 million tons of surface soil was blown away, intensifying the sand storm and afflicting disaster upon most of the continent. In the South Australia, the average number of dust weather days is 8.5 per year, when the floating dust in air is dense enough to trigger a break-out of asthma. It is reported that 20% cases of asthma there are related to floating dust.

The numerical prediction and early warning are essential to alleviate disastrous impact of sand (dust) storm and guide the state in its decision-making concerning sand storm control. For instance, in China, the satellite remote sensing technology was first applied to sand (dust) storm monitoring in 1993 and a satellite remote sensing system was put into operational application in 2002. It was in the same year that 12 sand storms of various intensities were inspected. Since March 1, 2003, the short term forecast of sand storm has been officially released on TV by the state meteorological department.

1.3 Examples: Dunhuang, Minqin, Maqu

1.3.1 Dunhuang

Dunhuang is a historic place famous for its Mogao Grottoes, which are regarded as the gem of Chinese culture. The treasure house of exquisite frescos and painted sculptures (see Fig. 1.8), which could be traced back to the 4th–14th century, was inscribed on the World Heritage List by United Nations Educational, Scientific and Cultural Organization (UNESCO) in 1987. The climate of its location, an extremely arid inland desert (see Fig. 1.9), is both a blessing and a curse of those extraordinary artistic works: its aridity serves as a preserver, while its severe wind-blown sand poses constant threats in three forms: wind erosion, sand deposition and dust (Qu et al. 1997). Here, wind erosion is of two types: deflation and ablation of open-air frescos and rocks around grottos by the wind-blown sand

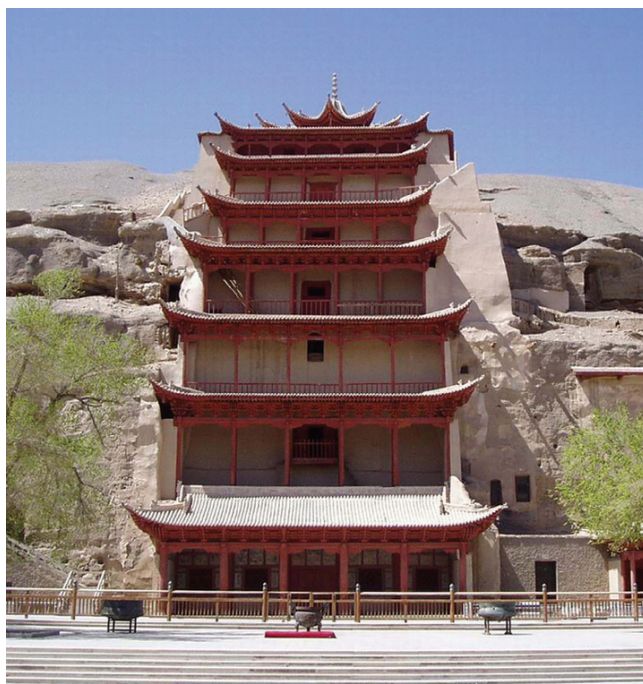


Fig. 1.8. A photo of Nine-Storey Pavilion – the symbol of Mogao Grottoes, and Mogao Grottoes are regarded as the gem of Chinese culture which are the richest treasure house of Buddhist art in the world. Today, 492 caves still stand, containing some 2,100 colored statues and 45,000 square meters of murals



Fig. 1.9. A photo of Mogao Grottoes of Dunhuang located in the acutely arid inland desert in Gansu, Northwest of China, which have been treated by wind-blown sand constantly (Wang 2003; photo by Stainmetz G)

flow. The impact and ablation of the Gobi wind-blown sand not only fade and change the color of frescos, but also weaken the upper rocks and tear off the top gravels, leaving the upper part dilapidated or even penetrated and frescos ruined. As to sand deposition, if the grotto top is steep, the wind-blown sand will be obstructed and forced to deposit in front of the grotto. It is reported by Dunhuang Research Institute that some $3,000 \text{ m}^3$ sand deposition needs to be cleaned up every year. The damage caused by dust is also not to be neglected. Dusts permeating into grottos are mainly quartz and feldspar particles in size of 0.05–0.005 mm, 83% of which are angular or sub-angular. Those quartz particles of high hardness, moved by turbulence, will ablate frescos as well as sculptures and infiltrate into tiny gaps of the paint. Not only does this weaken their artistic beauty, but also makes their surface cracked. As more and more dusts gather up, an outward pressure will accumulate and finally scale off pieces of frescos.

Dunhuang city itself is also under a severe threat of desertification. Out of its total area of $31,200 \text{ km}^2$, only $1,400 \text{ km}^2$, i.e. 4.5%, is covered with oasis. The area of oasis decreases from $2,870 \text{ km}^2$ at the early stages after

the foundation of the PRC to 1,400 km² at present. The area of the natural grassland at the verge of the oasis decreases from 1840 km² before the foundation of the PRC to present 900 km². In contrast, the area of sandification increases by 13 km² per year and the desert advances 2–3 m deeper into the oasis per year. Members of the joint Kumtag Desert expedition team discovers that the desert is expanding eastward at a speed of 1–4 m per year, gradually taking into its relentless grasp the historic city, together with its grassland, farmland and its cultural heritage.

1.3.2 Minqin

Minqin County in Gansu is an oasis in the lower reaches of the Shiyang River. With an altitude of 1,300–1,500 m, the oasis wedges itself between the Badain Jaran Desert and Tengger Desert, preventing the two great deserts from merging (see Fig. 1.10). It is of a typical continental desert climate with an average annual precipitation as low as 110 mm and an average annual evaporation up to 2,644 mm. The fact that, within an area of 16,000 km², desert and desertified land already reach to 14,450 km², taking up 91% of the total area, makes the county one of the most seriously desertified areas in China. In Minqin, the annual water demand is 772 million m³,

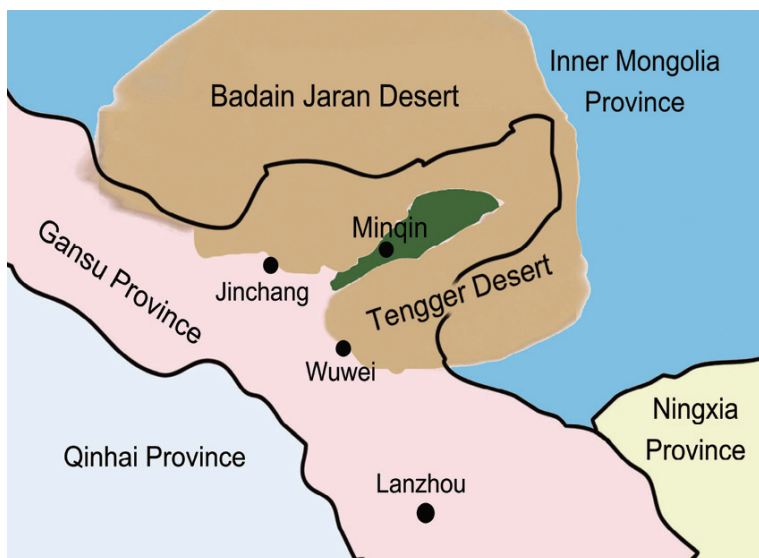


Fig. 1.10. A sketch topographic map of Minqin oasis, which is situated between the Badain Jaran Desert and the Tengger Desert, wedging the two great deserts away and preventing them from merging (— the province boundary)

but the average annual water runoff of the Shiyang River through Minqin decreases drastically: it dropped from 573 million m³ in 1950s, 229 million m³ in 1980s to mere 70 million m³ in 2002. The lack of surface water supplement forces local people to pump underground water for irrigation and drinking, which reduces the under-ground water level by 0.3–0.8 m per year and rapidly worsens the local ecological environment.

A sandification monitoring of this area carried out from 1998 to 2003 displays that, within those five years, another 110.35 km² of its farmland was sandified; the originally light or moderate desertification deteriorated to the heavy and extreme; the verge of desert was approaching the oasis by a speed of 3–4 m per year and made Minqin one of the four great sand (dust) storm sources (see Fig. 1.11). The analysis of long-term meteorological records since 1953 made by the Minqin State Meteorological Observatory shows that the days of sand (dust) storm events reaches up to an average of 27 per year. From early 1950s to early 1960s, a large number of sand (dust) storms attacked the area; from late 1960s to mid 1970s, the annual number of sand (dust) days declined a little; but from 1970s to the end of 1980s, the sand (dust) storm frequency worked up to a peak; within the year of 2006, Minqin was attacked by 14 sand (dust) storms, among which 4 were quite severe with the most intense one on April 10, when visibility was merely 100 m and the maximum instantaneous wind velocity was 17.1 m·s⁻¹.



Fig. 1.11. A photograph of sandification status in Minqin area as one of the four great sandstorm sources in China (photo by the author et al. on September 27, 2006)

At present, the serious desertification situation in Minqin has drawn great attention from the local and central governments. Between 2001 and March, 2008, the Chinese premier, Wen Jiabao had made fourteen instructions addressing the ecological problems in Minqin. The most well-known one was ‘Never let Minqin become another Lop Nur.’ All these facts demonstrate the unswerving determination of the Chinese government to prevent and control desertification.

1.3.3 Maqu

On the first bend of the Yellow River, Maqu County is located in southwest of the Tibetan Autonomous Region in the south of Gansu province and at the east end of the Qinghai-Tibetan Plateau. The Yellow River flows through Qinghai province into Maqu with an inflow of 13.7 billion m^3 , that is, 20% of its total water volume, and an outflow of 16.41 billion m^3 annually, 65% of its total water volume. The great excess of output over input makes the area an important water supplier of the Yellow River. Typical of the alpine humid region on a continental plateau, the climate there is characterized by abundance in alpine wind and rain/snow, indistinct division between seasons but difference in temperature, concentrated

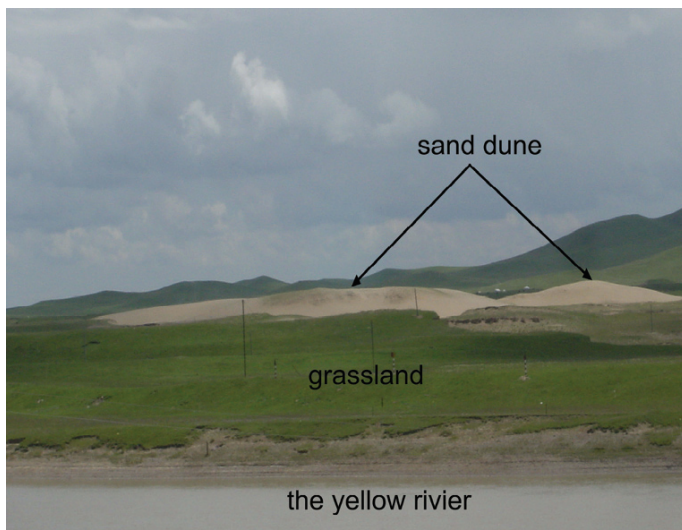


Fig. 1.12. A photograph of a sand dune lying on grassland beside the Yellow River in Maqu county, which located in southwest of the Tibetan Autonomous Region in south Gansu province, China (photo by the author et al. on Aug. 11, 2007)

precipitation, profuse sunshine and strong radiation. Such favorable natural averagely bring Maqu 611.9 mm precipitation per year and enable it develop into a vast pasture, home to various fine livestock animals. This pasture is a part of the plateau scrubby meadow region in west of Sichuan and east of Tibet. The fact that 8,586.79 km², 89.54% of the county's total area, is grassland and 96.70% of the grassland is utilizable makes this area the largest and best pasture in Asia and one of the important husbandry bases in Gansu.

For over a decade, however, grassland in Maqu has been suffering from severe sandification. In the entire area, there are 36 major sandified sites and 530 km² sandified grassland (see Fig.1.12). Along the Yellow River, dunes stretch for over 220 km and the area of sandified land reaches 61.33 km², 40.60 km² of which is covered with fixed dunes and the rest with mobile ones, all reaching up to 12–15 m in height. Comparison between satellite remote sensing images of 1976 and 2000 shows that spot-like distributed individual dunes in this area are inclined to join up and to form mobile dunes. From 1995 to 2000, sandified land averagely increased by 2.99 km² per year with an ascending rate. Grassland sandification did great harm to biological diversity. The habitation of a large number of rare wild animals was destroyed, driving many national protection species onto the verge of extinction. Even worse, some of the original human habitations also gave way to desertification and herdsmen in afflicted areas were under the threat of poverty because of gradual decrease of utilizable grassland.

Chapter 2 Flows of the Near-Surface Boundary Layer

Wind shear near the surface is responsible for the entrainment of sand particles, the formation and evolution of aeolian landforms, and the disasters induced by wind-blown sand movement. Therefore, many studies of the wind-blown sand movement are focused on understanding, representing and depicting the characteristics of air flows in the near-surface boundary layer where the wind-blown sand movement mainly takes place. The content of this chapter is arranged as follows. In Sects. 2.1 and 2.2, some basic definitions and equations, including the turbulent model, relevant to the wind-blown sand movement, are introduced in the light of fluid dynamics; Sects. 2.3 and 2.4 provide a brief summary of the characteristics and major observation methods of the atmospheric boundary layer, especially the near-surface boundary layer; Sect. 2.5 gives the basic equations governing air flow and their simplified forms for the near-surface layer and the wind-blown sand movement; Based on field observational results on the surface wind gusts, Sect. 2.6 devotes to the analysis on the statistical characteristics of fluctuating wind fields and resultant saltation activity near the surface, and then to establish two wind velocity prediction models to describe variations of fluctuating wind velocity at different heights and times.

2.1 An Introduction to Fluid Mechanics

As a rigorous discipline, fluid mechanics, especially fluid dynamics, came into being based on basic concepts and equations of velocity, acceleration, force, fluid field etc. and the fundamental laws which relate to the conservations of mass, momentum and energy. A fluid is usually assumed to be composed of (fluid) volume elements, which are assumed to be infinitely small from a macroscopic view and enormous from a microscopic view and among which no static friction exists. In this manner, the influence of molecular motions could be ignored and the property of a fluid could be regarded as continuous and isotropic. There are two ways to describe the fluid motion: the Euler and the Lagrange method. The former describes the

fluid motion within a given space or at a fixed point, while the latter traces the motion of specific particles of fluid. In the following part, without further specification, the Euler description of fluid motion is employed.

2.1.1 Viscosity of a Fluid

The viscosity of a fluid behaves like a drag effect caused by internal friction between two adjacent fluid layers where relative motion happens. It is a property that connects the shear stress and the velocity gradient of a fluid, and is one of the reasons for energy dissipation in a moving fluid. Viscosity can be denoted by the viscosity coefficient μ (measured in Pa·s). For gas, it is usually taken as 1.81×10^{-5} Pa·s, which increases with temperature increases but is almost unaffected by air pressure. Another important indicator for the effect of fluid viscosity is the Reynolds Number which is defined as the ratio of inertial force to viscous force: $Re = \rho U L / \mu$, where ρ , U and L are fluid density, characteristic velocity and characteristic length respectively. The smaller the Reynolds number is, the greater the viscous force's influence will be.

According to the magnitude and importance of viscosity in the problem under discussion, a fluid can be considered as an ideal fluid or a viscous fluid. A fluid is said to be ideal in the case that viscosity or relative velocity of the fluid motion is comparatively small, so its viscous stress could be ignored in comparison with other forces. It is notable that the ideal fluid is merely an approximation model of the real fluid under these conditions. In contrast, if its viscous stress cannot be ignored, it is a viscous fluid.

Viscous fluids can be further classified into Newtonian fluids and non-Newtonian fluids. A fluid is called Newtonian when it meets Newton's law of viscosity, that is, the internal friction shear stress between two fluid layers is in proportion to the relative velocity of the two layers where the ratio μ is a constant. Otherwise, it is a non-Newtonian fluid. In general, air and water are both considered as Newtonian fluids; while fluid, suspensions, liquid, polymer solution, blood and mud-rock flow in nature should be considered as non-Newtonian fluids. Air flow in the wind-blown sand flow can be regarded as Newtonian fluid.

2.1.2 Properties of Flow

Fluid mechanics deals with both incompressible and compressible fluids, that is, with fluids of either constant or variable density. Although there is no such thing in reality as an incompressible fluid, this term is applied

where the change in density with pressure is so small as to be negligible. This is usually the case with liquids. Gases, too, could be considered incompressible when the pressure variation is small in comparison with the absolute pressure. So air flow in the wind-blown sand flow can also be regarded as incompressible flow.

Fluid flow can also be divided into steady and unsteady. A steady flow is the one in which physical quantities, such as velocity, pressure, temperature and density could vary from point to point but do not change with time. At a given point, if conditions do change with time, the flow is described as unsteady. In practice, there will always be slight local variations of velocity and pressure, but if the average of these quantities is constant, the flow is considered to be steady, such as flow in the pipe or the boundary layer.

According to the state of fluctuation of physical quantities during the fluid's motion, the flow could be divided into turbulent and laminar flow. The fundamental characteristic of turbulence is the randomness of the motion of fluid volume elements. For turbulence, the instantaneous value of every local quantity, such as velocity u , pressure P , temperature T , concentration c and so on, can be expressed as the sum of a mean component and a fluctuating component due to turbulence while the mean of fluctuating component is zero. The flow is laminar flow if the viscous fluid travels smoothly or in regular paths. Laminar flow occurs only when the Reynolds number is small. When the Reynolds number exceeds a certain critical value (the turning point), laminar flow begins to transit into turbulence. In general, the analysis of laminar flow is far easier than turbulent since the equations of laminar flow have exact or approximate solutions.

Turbulence predominates in most flows in nature and engineering applications, whose major effects are an intensive transportation of momentum, heat and mass caused by random fluctuations. Turbulence contains eddies of diversified scales. The unstable large eddies give birth to smaller ones and the process repeats itself. This is called 'cascade' process. Since there are large eddy structures within it, turbulence is often regarded as irregular fluid motions with structures of diversified sizes. Though the turbulent value is spatially and temporally random, turbulent quantities still behaves as a physical continuum and is governed by the basic equations of fluid motion.

The turbulence is characterized by diffusion, dissipation, correlation, self-similarity and intermittency. Here, correlation indicates the interdependence between turbulent motions at different point of time or space. This degree of interdependence is inclined to decrease to zero as the temporal or spatial distance increases. Turbulent self-similarity indicates the self-similarity between eddies of different scales. These self-similar struc-

tures obey a scaling law; that is, in some certain areas of wave number space or on some physical scales, some quantities, such as the velocity structure function, are in direct proportion to fixed powers of other physical quantities. It is notable that the Navier-Stokes equations also meet scale invariance law. Turbulent intermittency makes the geometrical image of the turbulent movement fragile, for example, when the turbulent flow is confined, the boundary between the turbulent area and the non-turbulent area is irregular and is susceptible to fractals at any time. Moreover, the turbulence is a ‘burst’ process and has a large-scale eddy structure. The ‘burst’ process usually occurs in the viscous layer and buffer layer. Kline et al. (1967) found that, in the direction of flow, there naturally exist alternatively distributed low and high velocity stripes in the near wall area. The low velocity stripes gradually move downstream, moving further away from the wall and upward. Having reached the buffer layer, the stripes vibrate violently and eventually break into small-scale structures. This process is the so called ‘burst’ process. After the upcast of the low velocity stripes, the upper high velocity fluid volume elements subside rapidly. Large eddies in the boundary layer causes this burst to subsidence process, which is named by Kline et al. (1967) as coherent structure exhibit this process.

For atmospheric boundary layer flows, $Re \approx 10^8$ (Wyngaard 1992). Hence the atmospheric boundary layer flows are almost always turbulent. When the wind velocity in the open air exceeds $1 \text{ m}\cdot\text{s}^{-1}$, the air movement must be turbulent, no matter how smoothly the wind seems to pass by (Bagnold 1941). Therefore, the air flows which cause moving sand in the near surface layer are nearly all turbulent (Pettijohn et al. 1972) and exert a great influence on the material transportation and deposit. A detailed and comprehensive description of the irregularity and complexity of the turbulent movement is always the object scientists strive for. Any interested reader may be better informed by Frisch (1995).

2.2 Basic Equations of Fluid Mechanics

In this section, the three basic conservation laws of mass, momentum and energy are given first. Then, due to the importance of turbulence in the studies of wind-blown sand movement, basic governing equations, major patterns and several numerical simulation approaches to turbulence are briefly introduced. Due to the complexity of fluid motion and the limited space of this book, the theories of fluid mechanics could only be sketched; interested readers may refer to Landau and Lifshitz (1987).

2.2.1 Conservation of Mass (Continuity Equation)

Any closed flow system must satisfy the conservation of mass, that is, the rate of change of the mass of the fluid (with density ρ and volume V) with time t is equal to the total mass of the fluid passing through the boundary S , i.e.,

$$\frac{\partial}{\partial t} \int_V \rho dV = - \oint_S \rho \mathbf{u} \cdot d\mathbf{S} \text{ or } \frac{\partial \rho}{\partial t} = - \nabla \cdot (\rho \mathbf{u}). \quad (2.1)$$

For steady flow, the density ρ is unaffected by time, namely,

$$\nabla \cdot (\rho \mathbf{u}) = 0. \quad (2.2)$$

For incompressible flow, the density ρ is a constant, and then the above equation takes the following form,

$$\nabla \cdot \mathbf{u} = 0 \text{ or } \frac{\partial u_i}{\partial x_i} = 0, \quad (2.3)$$

where, $\nabla = (\partial/\partial x_i) \mathbf{e}_i$ is the divergence operator; $\mathbf{u} = u_i \mathbf{e}_i$ is the velocity vector of fluid material elements; \mathbf{e}_i is the unit vector of the coordinates $Ox_1 x_2 x_3$ and u_i is the component of the velocity vector in direction \mathbf{e}_i . According to Einstein's summation convention, when a subscript occurs more than once in the same expression, the expression is implicitly summed over all possible values for that index, so $i = 1, 2, 3$ or $x_i = x_1, x_2, x_3$.

2.2.2 Conservation of Momentum

Any closed flow system must also conserve momentum, that is, the rate of change of the momentum of the fluid (with density ρ and volume V) with time is equal to the sum of momentum of fluid passing through boundary S , the total power of the body force \mathbf{f} acting on unit mass and the surface force \mathbf{T}_n acting on S , that is,

$$\frac{\partial}{\partial t} \int_V (\rho \mathbf{u}) dV = - \oint_S \rho \mathbf{u} (\mathbf{u} \cdot \mathbf{n}) dS + \int_V \rho \mathbf{f} dV + \oint_S \mathbf{T}_n dS. \quad (2.4)$$

The corresponding differential equation is

$$\frac{d\rho \mathbf{u}}{dt} = \frac{\partial \rho \mathbf{u}}{\partial t} + \nabla \cdot (\rho \mathbf{u}) = \rho \mathbf{f} + \nabla \cdot (T_{ij} \mathbf{e}_i \mathbf{e}_j), \quad (2.5)$$

where \mathbf{n} is the unit vector in the normal direction of the boundary S , and $T_{ij} = (-P + \mu' S_{kk})\delta_{ij} + \tau_{ij}$ is the surface stress tensor acting on the fluid volume element. Here P is the pressure on the fluid volume element, δ_{ij} is the unit tensor, $\mu' S_{kk}\delta_{ij}$ is the stress tensor caused by volume change; viscous stress tensor $\tau_{ij} = \mu S_{ij}$, $S_{ij} = \partial u_i / \partial x_j + \partial u_j / \partial x_i$ is the deformation rate caused by the fluid motion, μ' is the second viscosity coefficient, generally taken as $\mu' = -2\mu/3$. Substituting the expression T_{ij} (the constitutive relation of Newton's fluid) into the differential equation of the momentum conservation (i.e., Eq. 2.5), the N-S equation can be written as

$$\rho \left(\frac{\partial u_i}{\partial t} + u_j \frac{\partial u_i}{\partial x_j} \right) = - \frac{\partial P}{\partial x_i} + \mu \frac{\partial}{\partial x_k} \left(\frac{\partial u_i}{\partial x_j} + \frac{\partial u_j}{\partial x_i} \right) - \frac{2}{3} \mu \frac{\partial^2 u_k}{\partial x_i \partial x_k} + \rho f_i. \quad (2.6)$$

For incompressible flow, it reduces to the following form

$$\rho \left(\frac{\partial u_i}{\partial x_i} + u_j \frac{\partial u_i}{\partial x_j} \right) = - \frac{\partial P}{\partial x_i} + \mu \nabla^2 u_i + \rho f_i. \quad (2.7)$$

2.2.3 Conservation of Energy

The conservation of energy is also a basic law that a flow system of heat exchange must satisfy. It is actually the first law of thermodynamics which can be expressed as: the increase rate of the volume element's energy is equal to the sum of the net heat flux entering the element, or q_T , and the power of the body force and surface force acting on the volume element, namely,

$$\rho \frac{\partial}{\partial t} \left(e + \frac{u^2}{2} \right) + \rho u_j \frac{\partial}{\partial x_j} \left(e + \frac{u^2}{2} \right) = \rho f_i u_i + \frac{\partial}{\partial x_i} (T_{ij} u_j) + \rho \dot{q}_T + \lambda_T \nabla^2 T, \quad (2.8)$$

where, e is the internal energy of unit mass, the first two terms in the right part are power made by body force and surface force respectively, \dot{q}_T is the heat source term, $\lambda_T \nabla^2 T$ is the heat conduction term, in which T is Kelvin temperature and λ_T is the thermal conductivity. Since the internal energy is related to temperature, $e = c_p T$, where c_p is the heat capacity at constant pressure, for incompressible flow, the energy conservation equation with respect to T is expressed in the following form

$$\rho \left(\frac{\partial T}{\partial t} + u_j \frac{\partial T}{\partial x_j} \right) = \frac{\lambda_T}{c_p} \nabla^2 T + S_T, \quad (2.9)$$

where S_T is the viscous dissipation term which includes the inner thermal source and the thermal energy, into which the mechanical energy turns due to the viscous effect. To make the equations closed, a state equation connecting pressure P and density ρ , $P=P(\rho, T)$, is required. For an ideal gas, $P=\rho RT$, where R is the Molar gas constant.

2.2.4 Basic Equations of Turbulence

It is generally assumed that no matter how complicated turbulence is, its instantaneous motion is still subject to unsteady conservation of mass equation (i.e., Eq. 2.1) and the N-S equation (i.e., Eq. 2.5). The popular approach to studying turbulent motion is the time-averaged method, that is, the turbulence is considered as a combination of two flow movements, the time-averaged flow and instantaneous turbulent flow. The most widely used time-averaged method is the Reynolds-averaged method. Here, the superscript ‘-’ stands for the mean of a physical quantity within a time period Δt ; ‘’ stands for a physical quantity’s fluctuation. Ignoring the density fluctuation but taking into consideration the change of the mean density, the averaged control equations for turbulence could be obtained from Eqs. 2.1 and 2.5. These are respectively the time-averaged continuity equation and the N-S equation for compressible flow, namely,

$$\frac{\partial \rho}{\partial t} + \frac{\partial (\rho \bar{u}_j)}{\partial x_j} = 0, \quad (2.10)$$

$$\rho \left(\frac{\partial \bar{u}_i}{\partial t} + \bar{u}_j \frac{\partial \bar{u}_i}{\partial x_j} \right) = - \frac{\partial \bar{P}}{\partial x_i} + \mu \frac{\partial^2 \bar{u}_i}{\partial x_j^2} - \rho \frac{\partial \bar{u}_i u'_j}{\partial x_j} + \rho \bar{f}_i. \quad (2.11)$$

As the Reynolds averaged method is employed, Eq. 2.11 is also called the Reynolds time-averaged Navier-Stokes equation. In which $-\rho \bar{u}_i u'_j$ is called the Reynolds stress, a new quantity relevant to turbulent fluctuation which changes the original closed equation into a non-closed one. Therefore, it is necessary to make some assumptions for the Reynolds stress, i.e., constructing an expression for the stress or introducing a new turbulent model equation, so as to connect the turbulent fluctuation value with its time-averaged value and hence close the equations.

2.2.5 Models of Turbulence

According to the assumptions made for the Reynolds stress, the turbulent model can be divided into the Reynolds stress model and the eddy viscos-

ity model. In the former case, the function indicating the Reynolds stress is directly constructed and then solved together with the averaged control equations for turbulence (i.e., Eqs. 2.10 and 2.11). In the latter case, a quantity of turbulent viscosity or eddy viscosity coefficient μ_t is introduced as a spatial coordinate function related to flow state rather than as a physical parameter, and is connected with the time-averaged turbulence parameters. This relationship is called the eddy viscosity model. According to Boussinesq's eddy viscosity model, the relationship between the Reynolds stress and the mean velocity gradient is written as

$$-\rho \overline{u'_i u'_j} = \mu_t \left(\frac{\partial \bar{u}_i}{\partial x_j} + \frac{\partial \bar{u}_j}{\partial x_i} \right) - \frac{2}{3} \left(\rho K + \mu_t \frac{\partial \bar{u}_k}{\partial x_k} \right) \delta_{ij}, \quad (2.12)$$

with $K = \overline{u'_i u'_i} / 2$. The key point of calculating a turbulent flow is to determine the turbulent kinetic viscosity μ_t . Several modes have been proposed and according to the number of differential equations required to determine μ_t , the eddy viscosity models were divided into the zero-equation model, the one-equation model and the two-equation model.

The zero-equation model employs algebraic relations, rather than differential equations to connect the turbulent kinetic viscosity and the time-averaged turbulent parameters. The most well-known zero-equation model is Prandtl's mixing length theory, from which calculated results agree well with experiments for simple flow cases, but seemingly not so well for complex flow. To compensate for the limitations of the zero-equation model, the one-equation model is proposed. It works like this: on the basis of the averaged control equation for turbulence equation (see Eq. 2.11), a turbulent kinetic energy transport equation is constructed to represent μ_t as a function of the turbulent kinetic energy K , $\mu_t = \rho C_\mu \sqrt{Kl}$, where C_μ is a empirical constant and l is the proportional length of the turbulent fluctuation. In this manner, the equations are closed. The turbulent kinetic energy transport equation can be expressed as

$$\frac{\partial K}{\partial t} + \bar{u}_j \frac{\partial K}{\partial x_j} = \frac{1}{\rho} \frac{\partial}{\partial x_j} \left[\left(\mu + \frac{\mu_t}{\sigma_k} \right) \frac{\partial K}{\partial x_j} \right] + \frac{\mu_t}{\rho} \frac{\partial \bar{u}_i}{\partial x_j} \left(\frac{\partial \bar{u}_i}{\partial x_j} + \frac{\partial \bar{u}_j}{\partial x_i} \right) - \frac{\rho}{l} C_d K^{\frac{3}{2}}, \quad (2.13)$$

where σ_k is the Prandtl number of the fluctuation momentum; the values of σ_k and C_μ will be given in the following part. As to the value of C_d , one can refer to Launder and Spalding (1972).

To solve Eq. 2.13, l should be determined in advance, but this is not an easy task. Therefore, the one-equation model is not widely used in practice. To solve this problem, the K - ε model is put forward. Based on the one-equation model, a new equation with the turbulent dissipation rate

$\varepsilon = \nu \overline{(\partial u'_i / \partial x_j)^2}$ is introduced where $\nu = \mu / \rho$ as the kinetic viscous coefficient. In this way, the turbulent kinetic viscosity μ_t can be expressed as a function of the turbulent kinetic energy K and the turbulent dissipation rate ε : $\mu_t = \rho C_\mu K^2 / \varepsilon$. Therefore, the transport equations relative to K and ε can be expressed as

$$\frac{\partial K}{\partial t} + \bar{u}_j \frac{\partial K}{\partial x_j} = \frac{1}{\rho} \frac{\partial}{\partial x_j} \left[\left(\mu + \frac{\mu_t}{\sigma_k} \right) \frac{\partial K}{\partial x_j} \right] + \frac{1}{\rho} \mu_t \frac{\partial \bar{u}_i}{\partial x_j} \left(\frac{\partial \bar{u}_i}{\partial x_j} + \frac{\partial \bar{u}_j}{\partial x_i} \right) - \varepsilon, \quad (2.14)$$

$$\frac{\partial \varepsilon}{\partial t} + \bar{u}_j \frac{\partial \varepsilon}{\partial x_j} = \frac{1}{\rho} \frac{\partial}{\partial x_j} \left[\left(\mu + \frac{\mu_t}{\sigma_\varepsilon} \right) \frac{\partial \varepsilon}{\partial x_j} \right] + \frac{\mu_t c_{1\varepsilon} \varepsilon}{\rho K} \frac{\partial \bar{u}_i}{\partial x_j} \left(\frac{\partial \bar{u}_i}{\partial x_j} + \frac{\partial \bar{u}_j}{\partial x_i} \right) - \frac{c_{2\varepsilon} \rho \varepsilon^2}{K}, \quad (2.15)$$

where $C_{1\varepsilon} = 1.44$, $C_{2\varepsilon} = 1.92$, $C_\mu = 0.09$, $\sigma_k = 1.0$, $\sigma_\varepsilon = 1.3$ recommended by Launder and Spalding (1972) and proved by later experiments. Eqs. 2.14 and 2.15 are called the standard K - ε model. This is currently the most widely used turbulent model.

The standard K - ε model is much more advanced than the zero- and one-equation models and it is widely and successfully used in scientific studies and engineering applications. However, it suffers distortions to some extent when treating flows with strong swirling, the flows near curved wall or flows with curved streamlines. Therefore, some improved versions of the K - ε model, such as the renormalization group (RNG) K - ε model, and the Realizable K - ε model have been derived. Generally speaking, either the mixing length or one-equation model is advisable for simple flow cases, such as flow in the boundary layer, jet flow, pipe flow or flow in a channel without rotation, recirculation or buoyancy; while the K - ε model or the other two-equation models may be more suitable to non-buoyancy recirculating, irrotational or weakly rotational flow. A more sophisticated model (see Yakhot and Orzag 1986; Moin 1997) is needed to tackle flows with strong swirling and buoyancy or compressible flows. In short, the selection of model depends on the characteristics of the specific problem under discussion.

2.2.6 Approaches of Turbulent Numerical Simulation

Though basic equations describing the turbulent motion have been established, it's not an easy task to solve them analytically. Therefore, at present numerical approaches are generally employed. Some sophisticated numerical models have been proposed to understand the physical properties of turbulence. Among which, the Direct Numerical Simulation (DNS)

model is of the most accuracy. It solves the instantaneous turbulent control equations (i.e., Eqs. 2.1 and 2.6) directly. When only the statistical quantities of turbulence are concerned, the numerical calculation can be accomplished by introducing the corresponding closed form model into the turbulent averaged control equation (i.e., Eq. 2.11), to form the so-called Reynolds-Averaged Navier-Stokes (RANS) model. Though practical, the closed RANS model is not universal since Reynolds stress mainly originates from the large-scale fluctuation and its properties are closely related to the boundary condition of the flow. In other words, there does not exist a uniform model which can be applied to all complex flows. As far as computational complexity is concerned, the Large Eddy Simulation (LES) model lies between the DNS and the RANS model. It works like this: the large-scale fluctuation or turbulent eddies are calculated through numerical simulation and the impact of the small-scale eddies on the large-scale ones is modeled on the basis of some conceptual, for example, the sub-grid scale (SGS) model. The Large Eddy Simulation model was first put forward by Smagorinsky (1963) and was then developed by other researchers into more sophisticated versions, such as the Lagrange dynamical model proposed by Meneveau et al. (1996) for non-isotropic turbulence. The main motivation behind the LES model stems from local balance of small scale fluctuation which may be subjected to some kind of locally applicable laws, such as local isotropy or local similarity.

The three numerical models mentioned above require substantially different resolutions of the flow field. The DNS model calculates turbulent fluctuations of all scales and the minimum resolution in algorithm must be smaller than the dissipation scale. The RANS gives an average of the Reynolds stresses generated by fluctuation of all scales, and the grid scale must be larger than the fluctuation integral scale or the length scale of energy containing eddies, and its minimum grid scale is also determined by the properties of mean flow. The resolution of LES lies between those of DNS and RANS. Its grid scale should be of the same order of magnitude of the scale of the inertial sub-region, since only the fluctuations smaller than the scale of the inertial sub-region may possibly be subjected to a locally applicable law.

2.3 Basic Characteristics of the Atmospheric Boundary Layer

The atmosphere is a layer of gases covering the Earth's surface, which is composed of nitrogen, oxygen and suspension particles (aerosol). It re-

volves together with the Earth and its density decreases with height. Energy needed for atmospheric motion mainly comes from solar radiation. The latitudinal heat imbalance drives global large-scale atmospheric motion – the global atmospheric circulation; meanwhile, in a localized area the heat imbalance causes regional atmospheric convection and turbulence. The latter is characterized by a high Reynolds Number, which can be decomposed into multi-scale fluctuations or eddies of various scales down to the viscous dissipation scale. Consequently, atmospheric motion is characterized by temporal and spatial multi-scale and dissipation, and thus, generally speaking, the atmospheric system is a system of dissipative structure.

According to the characteristics of temperature distribution with height, the atmosphere can be divided into four layers: the troposphere, the stratosphere, the mesosphere and the thermosphere (see Fig. 2.1). Generally speaking, the troposphere layer over equatorial and tropical areas is of 15–20 km in depth, while that over polar and middle latitudes is of 8–14 km in depth. Compared with the whole atmosphere, the troposphere is very thin but contains 75% of the atmospheric mass and nearly all moisture, cloud and precipitation. Most synoptic events, such as cold waves, typhoon,

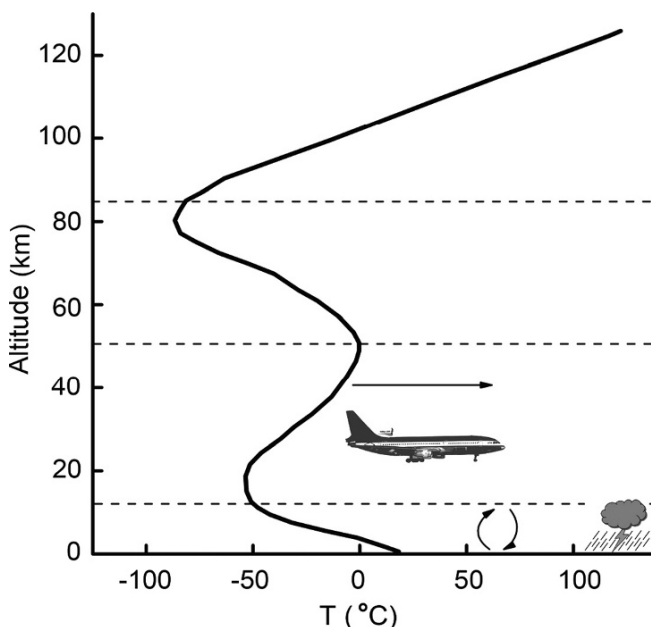


Fig. 2.1. Stratification of the atmosphere, the layers are respectively called troposphere, stratosphere, mesosphere and thermosphere with increasing altitude

thunder storms and lightning take place in the troposphere layer. It has the following features:

- (1) Decrease of temperature with height at a mean rate of about $6.5 \text{ K}\cdot\text{km}^{-1}$. The atmosphere absorbs heat through long-wave radiation, convection and turbulence from the ground and so the closer it is to the ground, the more heat it absorbs. This property gives birth to intensive convective motions within the troposphere and will facilitate the vertical transport of atmospheric components, such as vapor and aerosol.
- (2) Strong vertical mixing. Because of the influence of heating at the Earth surface, the warmer air at low altitudes rises while the colder air at high altitude sinks. This produces strong vertical mixing in the troposphere layer, and the maximum upward-velocity can reach up to $20\text{--}30 \text{ m}\cdot\text{s}^{-1}$. This is always associated with severe convection weathers, such as thunder storm, tornados, hail or squall lines.
- (3) Unbalanced horizontal distribution of meteorological elements. Due to the diversity in latitude and characteristic of the land surface, air over the ground is of different physical properties. The horizontal imbalance of pressure, temperature, humidity etc., in turn, produces various synoptic events.

The bottom of the troposphere ranging from the ground surface to an altitude of 1000 m has a sustained wind and temperature vertical gradient in response to the Earth's surface friction and surface heating. This is the so-called atmospheric boundary layer (ABL). Above it, the effect of earth's surface friction on air motion is negligible and that is where the free atmosphere performs. In the free atmosphere, the pressure gradient and the Coriolis forces dominate the behaviour of the flow field and induce the geostrophic wind, which is at an angle ($<30^\circ$) to the wind in the ABL. It should be pointed out that the atmospheric boundary layer is different from the boundary layer fluid mechanics. The concept of 'boundary layer' was first introduced by Prandtl to study the fluid motion with a large Reynolds number. He believed that in a thin layer near the wall the fluid's viscous force is of a large gradient in the direction perpendicular to the wall, and its effects cannot be ignored in comparison with the inertial force. Since the velocity of flow gradually changes from the boundary layer to the external layer, the thickness of the boundary layer is defined as the vertical distance from the wall to the place where the fluid velocity can reach 99% of the free velocity. Additionally, since there is exchange of momentum and mass between the atmospheric boundary layer flow field and the external non-viscous flow field, the flow velocity in the atmospheric boundary layer is related to both the horizontal coordinate x and the vertical z .

For different underlying surfaces, like desert, soil, vegetation, cities, water, etc. It has different physical properties, such as different radiation properties, thermal capacities, moisture content and roughness, all of which will exert different influences on the atmospheric motion and cause different stratifications and atmospheric boundary layer conditions.

The atmospheric boundary layer can be divided into the viscous subsidiary layer, the surface layer and the upper friction layer (or Ekman layer). The viscous subsidiary layer is a thin layer close to the surface, where the molecular viscosity is much larger than the turbulent shear stress. The viscous subsidiary layer includes the laminar flow region and transitional region. As it approaches to the wall, the viscous stress gradually dominates the flow. However, in practice its typical thickness is less than 1 cm and can be ignored. The space from the viscous subsidiary layer to 50–100 m height above the Earth's surface is the surface layer, where the atmospheric motion is typically turbulent and the turbulent momentum flux is approximately constant. So the layer is also called the constant flux layer. In the surface layer, the wind direction is unchangeable with height, while above it wind velocity increases with height and wind direction deflects constantly because of the weakening of the surface friction effect, until the flow field is completely dominated by the pressure gradient and the Coriolis force, and the combined actions of which result in the wind direction tending towards the direction of the geostrophic wind, and thus forming the famous 'Ekman spiral'. Wind direction changes continually to the top of the Ekman layer. Moreover, the atmospheric layer below 2 m is the near-surface layer. It is characterized by a large velocity gradient and a logarithmic wind profile, for the flow field is greatly influenced by the wall surface and the influence of thermal factors is negligible compared with dynamic factors. As far as the wind-blown sand movement is concerned, the motion of saltating sand takes place within 10 cm above the surface, therefore, the wind field in the near-surface layer plays a crucial role in sand particles' movement.

The air motion in the ABL is almost always turbulent (above 5–10 cm). The turbulence intensity could reach up to 20%. Due to surface radiation, air stratification alternates between stable and unstable states, causing the diversified mean wind velocity profiles and turbulent characteristics to vary. Moreover, the non-uniform topography and covering condition also complicate the air flow in the boundary layer, especially the surface layer. Under the influence of the temporal and spatial changes of wind field and its strong turbulent characteristics, the state of erosion and deposit of the surface material vary with wind field and topography accordingly. Therefore, the quantities indicating material transportation in different experi-

ments differ greatly, which poses tremendous obstacles to the wind-blown and movement studies.

2.4 Observations of the Atmosphere Boundary Layer

The knowledge of atmospheric boundary layer is mainly obtained from experimental observation, which includes field measurement and laboratory simulation. The former can be performed with the help of ground measurement, tower (Fig. 2.2a), released or tethered balloon (Fig. 2.3), aerial photography and remote sensing technology, while the latter mostly use wind tunnels. In recent years, the development and application of turbulent fluctuation metering equipment has made field measurements

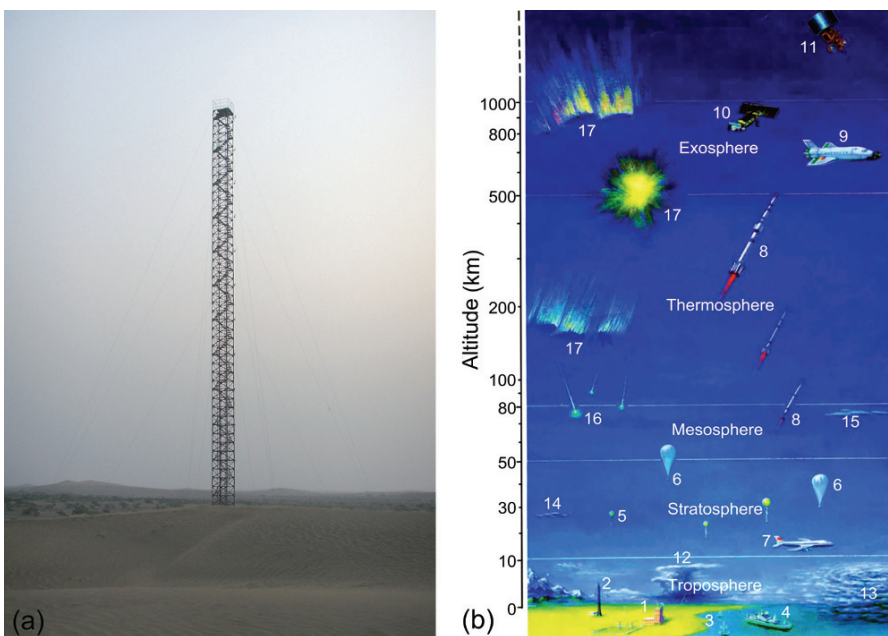


Fig. 2.2. Meteorological Observing System; (a) weather observation tower (photo by the author et al. in Minqin, China); (b) comprehensive meteorological measurement system, including: 1 weather observation stations, 2 meteorological tower, 3 buoy station, 4 marine weather ship, 5 sounding balloons, 6 high-altitude balloon, 7 weather aircraft, 8 meteorological rocket, 9 space shuttle, 10 polar orbit meteorological satellite, 11 geostationary meteorological satellite, 12 cumulonimbus, 13 typhoon, 14 nacreous clouds, 15 luminous cloud, 16 meteor, 17 Aurora (from Beijing geography teaching resources network)



Fig. 2.3. Released balloon (from Liu 2006)

become more and more sophisticated. The predominate physical processes taking place in the atmospheric boundary layer are exchanges and transports of momentum, energy, vapor and other materials due to turbulence. The exchange and transport processes determine the physical distribution and variance with time of physical quantities and the result is that the physical quantities will be transported from high-value area to low-value areas. Therefore, the subjects of interest in the observations of the boundary layer mainly include the following aspects: (1) the heat flux (such as latent heat flux, sensible heat flux): the heat arises from the solar radiation transported by turbulence from the ground to the boundary layer or from high temperature areas to low temperature areas; (2) the momentum flux: the momentum transferred from high wind power areas to low wind power areas, and mass of aerosol such as vapor and pollutants from high concentration area to low concentration area; and (3) fluctuating information of wind velocity and direction, correlation, flux and temporal and spatial distribution of the turbulence spectrum. This is required, on one hand, to reflect the strength of turbulence, and thus the intensity of turbulent transport, and on the other hand to describe the effect of frictional dissipation of the turbulence in the boundary layer on the atmospheric motion. The observations of those quantities mentioned above are primarily conducted 1.5 m above the human action space (see Fig. 2.2b, Fig. 2.4), while few results below 1 m are obtained.



Fig. 2.4. Tower measuring instruments including CSAT3 3-D Sonic Anemometer and LI7500 Open-gas Analyzer (from College of Atmospheric Sciences, Lanzhou University)



Fig. 2.5. The synchronization multipoint measurement system equipped with high sensitivity cup anemometer, which can be used to obtain the 1 Hz turbulence information of the near surface boundary flow (placed in Minqin, China by the author et al.)



Fig. 2.6. The piezoelectric kinetic sensor for impact events measurement, with a frequency of 1 Hz which can be used to measure sand saltation activity (placed in Minqin, China by the author et al.)

The equipment for field observation usually includes a cup anemometer (uniaxial and triaxial paver), a propeller anemometer, an ultrasonic velocimeter, a unidirectional weathercock, and a bidirectional weathercock. Both the cup anemometer and the ultrasonic velocimeter can be equipped on a rod, support or multilayer elevated tower (see Fig. 2.4). Cup anemometers are more widely adopted in meteorological observation for their low cost, in spite of the fact that their measurable frequency is 1 Hz, the measurable wind velocity is not zero and its own inertia affects its precision. Ultrasonic velocimeters can discern a wind of nearly $0 \text{ m}\cdot\text{s}^{-1}$, have no inertia and their measurable frequency is up to 50 Hz (some even up to 100 Hz). Its precision is high enough to measure the ground surface turbulence. Fig. 2.5 shows a synchronized multipoint measurement system equipped with a high sensitivity cup anemometer to measure the ground surface wind-blown sand flux in Minqin, Gansu. Fig. 2.6 is the system's piezoelectric kinetic energy sensor, which is used to count impacts of sand particles. The output data represents the number of impacting particles during a time period which can indirectly reflect the intensity of wind-blown sand flux (Stout and Zobeck 1997).

A hot-wire (hot-film) anemometer is usually used to measure high frequency wind fluctuation. There are two types: the constant-flow type and the constant-temperature type. Before the 1950s, the constant-flow hot wire anemometer was widely employed to measure low turbulent flows.

However, after the 1950s, it has been gradually replaced by the constant-temperature hot-wire anemometer. The latter can be used to measure turbulent flows of diversified intensity with the following advantages: (1) small volume and little disturbance to the flow field; (2) capability of measuring high frequency fluctuating velocities of turbulence; (3) simultaneous measuring of velocity components in multiple directions; (4) high response frequency (up to 1 MHz). The disadvantages of the constant-temperature hot wire anemometer include: (1) the sensor is susceptible to damage during the experiment; (2) incapable of measuring reverse flow; (3) calibrations required before measuring.

In the last twenty years, hot wire (film) anemometer has been widely used in the turbulent measurement of wind-blown sand dynamics for its ability to measure the characteristics of flow inside the wind-blown sand flux (below 5 cm). For example, Butterfield (1991) measured the wind velocity of the windblown sand flux 2 cm above the ground with a hot-wire meter with stainless thimbles. However, most commercial probes or sensors are susceptible to damage by the sand and wind, unless a shield is used, though this interferes with the measurement of frequency reducing it to below 10 Hz.

In the laboratory, a wind tunnel is used to drive a controllable piped air flow over a static mould or sand bed to measure the aerodynamical force acting on the mould or the flow near the sand bed. Based on the similarity theory, experimental data statistics can be converted into dimensionless coefficients for the corresponding practical object. In a wind tunnel experiment, it requires not only that model should be in a similar mode as the practical application, but also that these parameters of the flow field should be the same as the practical ones. These parameters are dimensionless resultant quantities derived from several parameters, which can be deduced from the basic dimensionless equations, to ensure the similarity. However, in practice, due to the limitation of the size and drive force of the wind tunnel, only the major similarity criteria such as the Reynolds number and Mach number can be satisfied. The experimental section is in the central part of the wind tunnel, where the mould is placed. Therefore, the quality of air flow, such as uniformity, stability and intensity of turbulence, should meet a certain standard. The advantage of a wind tunnel lies in the fact that the experimental conditions, including the air flow and mould state, are easily controlled; individual parameters can be changed independently; the experiment is not affected by the atmospheric environment; the experimental period is short and the cost is relatively low. But it also has disadvantages, such as the inability to meet all similarity principles and the susceptibility to air flow boundaries. As far as wind-blown sand movement is concerned, a low-speed (less than $100 \text{ m}\cdot\text{s}^{-1}$) blow down wind tunnel as

shown in Fig. 2.7 is required. This kind of wind tunnel can measure the lift-off velocities of sand particles, the saltation activity of the wind-blown sand flux, the evolution of aeolian landforms, the validity of sand breaking measures, the intensity of wind-blown sand electric fields and the degree of wind erosion.

Flow fields in the wind tunnel are usually measured by pitot tube, hot wire (film) anemometer, laser doppler velocimeter, phase doppler anemometer (PDA) and particle image velocity (PIV). Among these, PIV developed from the speckle methods in solid mechanics in 1970s and can be used for measuring turbulent fluctuations with high precision. As a piece of non-contact optical equipment, it can provide comprehensive instantaneous information about unsteady flow without disturbing the flow field.



Fig. 2.7. Low-speed blow down wind tunnel (Multi-function environmental wind tunnel of Lanzhou University), which contains four sections: the power part, the rectifier part, the experimental part and the proliferation part. The total length of the wind tunnel is 85 m, the experimental section is up to 20 m, the cross-sectional area is about $1.3 \text{ m} \times 1.45 \text{ m}$, wind velocity is adjustable from $4 \text{ m}\cdot\text{s}^{-1}$ to $40 \text{ m}\cdot\text{s}^{-1}$

2.5 Basic Equations of the Atmospheric Boundary Layer

In this section, we first introduce the basic equations of flows in the atmospheric boundary layer, which are the specific forms stemming from the equations introduced in Sect. 2.2 for atmospheric motions, then the concept of aerodynamic roughness and finally the influence of sand saltation and sand dunes on the flow field are given.

2.5.1 Basic Equations

Based on the Boussinesq assumption (Haugen 1973), the pressure, density and temperature of the fluid can be expressed as $P = P_0 + p$, $\rho = \rho_0 + \rho'$ and $T = T_0 + T_d$ respectively, it is known that the gradient of T_0 and P_0 , can be expressed as $\partial T_0 / \partial x_3 = -g/c_p = -\gamma_d$ and $\partial P_0 / \partial x_3 = -g\rho_0$ in direction x_3 respectively. Compared to the static atmosphere (P_0 , ρ_0 , T_0), variation of thermodynamic quantities (p , ρ' , T_d) caused by the flow is very little. Furthermore, besides gravity, pressure gradient force and viscous force, Coriolis force $2\Omega(\boldsymbol{\eta} \times \mathbf{u})$ caused by the Earth's rotation also acts on the atmosphere boundary layer, so the body force in the basic equations of incompressible flow (see Eqs. 2.7 and 2.11) is now the sum of gravity and the Coriolis force, with $\boldsymbol{\eta}$ is unit vector which parallels the Earth axis of rotation; Ω is the Earth's angular velocity of rotation. Neglecting the variation of heat energy caused by atmospheric radiation and molecular viscous dissipation, the equations for the atmospheric boundary layer can be written as:

$$\text{continuity equation} \quad \frac{\partial u_i}{\partial x_i} = 0, \quad (2.16)$$

$$\text{momentum equation} \quad \frac{\partial u_i}{\partial t} + u_j \frac{\partial u_i}{\partial x_j} = -\frac{1}{\rho} \frac{\partial P}{\partial x_i} - g\delta_{3i} + \nu \frac{\partial^2 u_i}{\partial x_j^2} - 2\Omega\varepsilon_{ijk}\eta_j u_k, \quad (2.17)$$

$$\text{heat energy equation} \quad \frac{\partial T}{\partial t} + u_j \frac{\partial T}{\partial x_j} = -\frac{g}{c_p} + k_T \frac{\partial^2 T}{\partial x_j^2}, \quad (2.18)$$

$$\text{and state equation} \quad P = \rho RT, \quad (2.19)$$

where $k_T = \lambda_T / \rho c_p$ is thermal diffusivity.

According to atmosphere boundary theory (see Haugen 1973), the Coriolis force in the surface layer below 20–80 m can be neglected. In this

manner, the equations of atmospheric flow in the surface layer can be obtained through equations of the atmospheric boundary layer (i.e., Eqs. 2.16–2.19). Using the Boussinesq assumption that ν and k_T are constants and the flow is incompressible, the heat energy equation can be simplified to $\rho'/\rho_0 = -T_d/T_0$. For the sake of convenience, the equations of atmospheric flow are expressed with components (u, v, w) of velocity vector (\mathbf{u}) under the Cartesian coordinate system $Oxyz$.

$$\frac{\partial u}{\partial x} + \frac{\partial v}{\partial y} + \frac{\partial w}{\partial z} = 0, \quad (2.20)$$

$$\frac{\partial u}{\partial t} + u \frac{\partial u}{\partial x} + v \frac{\partial u}{\partial y} + w \frac{\partial u}{\partial z} = -\frac{1}{\rho_0} \frac{\partial p}{\partial x} + \nu \left(\frac{\partial^2 u}{\partial x^2} + \frac{\partial^2 u}{\partial y^2} + \frac{\partial^2 u}{\partial z^2} \right), \quad (2.21a)$$

$$\frac{\partial v}{\partial t} + u \frac{\partial v}{\partial x} + v \frac{\partial v}{\partial y} + w \frac{\partial v}{\partial z} = -\frac{1}{\rho_0} \frac{\partial p}{\partial y} + \nu \left(\frac{\partial^2 v}{\partial x^2} + \frac{\partial^2 v}{\partial y^2} + \frac{\partial^2 v}{\partial z^2} \right), \quad (2.21b)$$

$$\frac{\partial w}{\partial t} + u \frac{\partial w}{\partial x} + v \frac{\partial w}{\partial y} + w \frac{\partial w}{\partial z} = -\frac{1}{\rho_0} \frac{\partial p}{\partial z} + g \frac{T_d}{T_0} + \nu \left(\frac{\partial^2 w}{\partial x^2} + \frac{\partial^2 w}{\partial y^2} + \frac{\partial^2 w}{\partial z^2} \right), \quad (2.21c)$$

$$\frac{\partial T_d}{\partial t} + u \frac{\partial T_d}{\partial x} + v \frac{\partial T_d}{\partial y} + w \frac{\partial T_d}{\partial z} = k_T \left(\frac{\partial^2 T_d}{\partial x^2} + \frac{\partial^2 T_d}{\partial y^2} + \frac{\partial^2 T_d}{\partial z^2} \right), \quad (2.22)$$

$$\frac{\rho'}{\rho_0} = -\frac{T_d}{T_0}. \quad (2.23)$$

Considering the neutral situation (i.e., the gradient Richardson number, R_i , is close to zero), and the viscous term is two orders smaller than the corresponding turbulence term and thus can be neglected at the height more than 10 cm above the ground surface (Haugen 1973), the equations can be simplified by applying the Reynolds averaged treatment to Eqs. 2.20–2.21 as

$$\frac{\partial \bar{u}}{\partial x} + \frac{\partial \bar{v}}{\partial y} + \frac{\partial \bar{w}}{\partial z} = 0, \quad (2.24)$$

$$\frac{\partial \bar{u}}{\partial t} + \bar{u} \frac{\partial \bar{u}}{\partial x} + \bar{v} \frac{\partial \bar{u}}{\partial y} + \bar{w} \frac{\partial \bar{u}}{\partial z} = -\frac{1}{\rho_0} \frac{\partial \bar{p}}{\partial x} - \frac{1}{\rho_0} \left(\rho_0 \frac{\partial \bar{u}'^2}{\partial x} + \rho_0 \frac{\partial \bar{u}' \bar{v}'}{\partial y} + \rho_0 \frac{\partial \bar{u}' \bar{w}'}{\partial z} \right), \quad (2.25a)$$

$$\frac{\partial \bar{v}}{\partial t} + \bar{u} \frac{\partial \bar{v}}{\partial x} + \bar{v} \frac{\partial \bar{v}}{\partial y} + \bar{w} \frac{\partial \bar{v}}{\partial z} = -\frac{1}{\rho_0} \frac{\partial \bar{p}}{\partial y} - \frac{1}{\rho_0} \left(\rho_0 \frac{\partial \bar{u}' \bar{v}'}{\partial x} + \rho_0 \frac{\partial \bar{v}'^2}{\partial y} + \rho_0 \frac{\partial \bar{v}' \bar{w}'}{\partial z} \right), \quad (2.25b)$$

$$\frac{\partial \bar{w}}{\partial t} + \bar{u} \frac{\partial \bar{w}}{\partial x} + \bar{v} \frac{\partial \bar{w}}{\partial y} + \bar{w} \frac{\partial \bar{w}}{\partial z} = -\frac{1}{\rho_0} \frac{\partial \bar{p}}{\partial z} - \frac{1}{\rho_0} \left(\rho_0 \frac{\partial \bar{u}' \bar{w}'}{\partial x} + \rho_0 \frac{\partial \bar{v}' \bar{w}'}{\partial y} + \rho_0 \frac{\partial \bar{w}'^2}{\partial z} \right). \quad (2.25c)$$

It can be seen that the Reynolds averaged equations of the flow are not closed. Therefore, any of the turbulence models mentioned in Sect. 2.2.5 can be involved to make them closed so as to solve them analytically or numerically.

Supposing that x is in the direction of the mean horizontal velocity and z the mean vertical velocity, on a homogeneous ground of even roughness, since the pressure gradient force and the molecular viscous force are of the same order, the two forces can be neglected. So the Eqs. 2.25 can be simplified to

$$\frac{\partial \bar{u}}{\partial t} = \frac{1}{\rho_0} \frac{\partial}{\partial z} (-\rho_0 \bar{u}' \bar{w}'), \quad 0 = \frac{1}{\rho_0} \frac{\partial}{\partial z} (-\rho_0 \bar{v}' \bar{w}'), \quad 0 = \frac{1}{\rho_0} \frac{\partial}{\partial z} (-\rho_0 \bar{w}'^2). \quad (2.26)$$

In a steady situation, the Eq. 2.26 can be simplified to

$$\frac{\partial}{\partial z} (-\rho_0 \bar{u}' \bar{w}') = \frac{\partial \tau}{\partial z} = 0, \quad (2.27)$$

where $\tau = -\rho_0 \bar{u}' \bar{w}'$ is the turbulence shear stress. According to Prandtl's mixing length theory, $\tau = \mu_t \frac{\partial \bar{u}}{\partial z}$, $\mu_t = \rho_0 l_m^2 |\frac{\partial \bar{u}}{\partial z}|$, and the mixing length l_m is in direct proportion to the distance from the wall. That is, $l_m = kz$, where $k=0.4$ is Karman constant. Then $\tau = \rho_0 k^2 z^2 (\frac{\partial \bar{u}}{\partial z})^2$, and the following equation can be inferred from Eq. 2.27.

$$\tau = \rho_0 k^2 z^2 \left(\frac{\partial \bar{u}}{\partial z} \right)^2 = \tau_0. \quad (2.28)$$

where τ_0 is the friction stress of the surface. If $u_{*0} = \sqrt{\tau_0 / \rho_0}$ is defined as the surface friction velocity and substituted into the above equation, then

$$\frac{\partial \bar{u}}{\partial z} = \frac{u_{*0}}{kz}. \quad (2.29)$$

After integration of the above equation, the logarithmic velocity profile is

$$\bar{u} = \frac{u_{*0}}{k} \ln \frac{z}{z_0} \quad \text{or} \quad u = 5.75 u_{*0} \lg \frac{z}{z_0}, \quad (2.30)$$

where z_0 is usually called the aerodynamic roughness, and should be determined through experiments.

Since Eq. 2.27 is applicable within the layer ranging from 10 cm to 20–80 m above the ground surface, the friction velocity u_* in this layer equals to the surface friction velocity u_{*0} . In our following discussion, we will use u_* instead of u_{*0} . In addition, in the neutral situation, we can further use ρ to replace ρ_0 and neglect the small variation of air density.

2.5.2 Aerodynamic Roughness

Aerodynamic roughness z_0 indicates the abated effect of the ground surface on the wind velocity at a certain height above the ground where wind velocity is zero. It is an important parameter in the parameterization of fluid mechanics and atmospheric boundary layer turbulent characteristics. Different landforms have different influences on the fluid flow over them. Roughness of the ground surface changes not only the flow velocity gradient but also its range, and thus forms boundary layer flow with various properties. Therefore, a correct understanding and description of aerodynamic roughness is helpful to model and predict fluid movement.

Since the complex land surface causes local imbalance in air current, roughness is divided into the effective roughness and the local roughness. The effective roughness is the large scale aerodynamic roughness and corresponds to the total ground surface stress, i.e., total momentum flux, while local roughness is the small scale aerodynamic roughness and corresponds to local ground surface stress. According to the properties of the fluid flow over the ground, roughness is divided into isotropic roughness and anisotropic roughness and the latter is the reason for the eddy turbulence. A roughness element is the smallest unit producing surface roughness and a crucial element of ground roughness. Its type, size, shape, arrangement and movement all exert influence on ground roughness. In terms of type, there are sandy roughness, snowy roughness, watery roughness, gravel roughness and vegetation roughness, and in terms of movement type, there are fixed bed roughness, transitional type roughness (water surface roughness) and movable bed roughness. Movable bed roughness is related to the particle size distribution and movement. Since roughness z_0 is closely related to the threshold friction velocity u_{*t} (Greeley

and Iversen 1985), z_0 also affects the absolute and relative sediment discharge. Therefore, aerodynamic roughness plays a crucial role in the wind-blown sand transport, and migration of sand dunes and the evolution of the Gobi deflation planes.

There are four methods to obtain aerodynamic roughness: logarithmic profile fitting method, mass conservation method, center of pressure method and resistance method. The first method is the most used in practice under the prerequisite that the wind velocity obeys a logarithmic law. Through fitting all results of Eq. 2.30 for wind velocity measured at three or more than three heights with the least square method, the roughness z_0 can be obtained. However, in reality, the wind profile close to the surface only roughly satisfies logarithmic law, as is shown in Sect. 2.5.1. Therefore, it's reasonable to seek the roughness in the view of the air turbulent structure. More and more relevant studies are available and interested readers may consult Raupach et al. (1991).

2.5.3 Characteristics of the Flow Field on the Wind-Blown Sand Boundary Layer

For the near surface layer (less than 2 m), the turbulence is mainly influenced by the horizontal wind shear and frictional resistance of the rough surface. Since the velocity profile is little affected by the thermal turbulence, it can be expressed approximately with the logarithmic wind profile (see Eq. 2.30). However, due to the wind force, a saltation layer will be formed above the sandy surface. The density of sand particles is not uniform in the saltation layer but decreases drastically as the height increases. Generally speaking, the saltation height is no more than 0.5 m and thus the saltation layer is very thin compared with the surface layer. Those moving sand particles will in turn exert an effect on the wind velocity, which is actually the reaction force of sand particles on the flow field according to Newton's Third Law. The force acting on the wind per volume is denoted as $F_x(z)$. In Eq. 2.26, taking the effect of $F_x(z)$ into consideration while neglecting the influence of viscosity, the flow equation of air in the saltation layer in the case of a flat and homogeneous surface can be obtained,

$$\rho_0 \frac{\partial \bar{u}}{\partial t} = \frac{\partial \tau_a}{\partial z} + F_x(z), \quad (2.31)$$

where $\tau_a = \rho u_*^2$ is the turbulence shear stress. According to Prandtl's mixing length theory, it can be rewritten as

$$\rho_0 \frac{\partial \bar{u}}{\partial t} = \frac{\partial}{\partial z} \left[\rho_0 k^2 z^2 \left(\frac{\partial \bar{u}}{\partial z} \right)^2 \right] + F_x(z). \quad (2.32)$$

In the steady situation, the above equation can be expressed as

$$\frac{\partial \tau_a}{\partial z} + F_x(z) = 0. \quad (2.33)$$

If the vertical momentum flux τ_s produced by sand movement in the thin layer $[z - dz/2, z + dz/2]$ at the height z is considered, it can be seen that

$$F_x(z) = \frac{\partial \tau_s}{\partial z}. \quad (2.34)$$

At the upper boundary of the saltation layer, the turbulence shear stress is determined by the outer flow field, and is generally taken as τ_0 . It can be inferred from Eqs. 2.33 and 2.34 that $\tau_a + \tau_s = \tau_0$, so

$$\frac{\partial \bar{u}}{\partial z} = A \frac{u_{*a}}{z} = \frac{1}{kz} \sqrt{\frac{\tau_0 - \tau_s}{\rho}}. \quad (2.35)$$

According to the contribution of the Sauermann et al. (2001), the above equation can be adapted into

$$\frac{\partial \bar{u}}{\partial z} = A \frac{u_{*a}}{z} = \frac{u_{*0}}{kz} \sqrt{1 - \frac{\tau_{s0}}{\tau_0} \exp\left(-\frac{z}{H_s}\right)}, \quad (2.36)$$

where H_s is the thickness of mean saltation. If the value of z_0 is properly attained, the continuity of the flow field's velocity outside the saltation layer can be assured. In addition, the analytic expression of the velocity in the wind-blown sand flux was also given by Raupach (1991).

Since the transport of sand particles and the turbulent fluctuation near the surface are both mainly horizontal (for the latter, the horizontal fluctuation is about 10 times larger than the vertical fluctuation), the turbulent stress in the saltation layer must be greatly reduced by the resistance of moving sand particles on the turbulent fluctuation, but the turbulent stress outside the saltation layer is unaffected. However, since the turbulent stress changes the velocity gradient, the velocity of the air flow outside the saltation layer will also be reduced. Owen (1964) considered the influences of the saltation layer and the ground friction as equal to another ground roughness and calculated wind profile outside the saltation layer using this train of thought. Owen (1964) believed that the wind profiles outside the saltation layer also obeys the logarithmic distribution on the condition that

the aerodynamic roughness z_0 is changed into equivalent roughness or movable bed roughness z_s , which is a physical quantity in wind-blown sand physics as important as the aerodynamic roughness.

2.5.4 Effect of Sand Dunes on the Flow Field

Erosion and deposit caused by wind erosion will change the landforms and give birth to complicated geomorphological patterns, such as sand dunes, sand ridges and sand ripples. When it flows over these complex landforms, the air flow will also become complicated under the influence of the landforms. In the following part, a simple case of changes in the flow field when the air flow perpendicularly passes an isolated traverse dune is studied.

According to the theory of Hunt, Leibovich and Richards (HLR) (Hunt et al. 1988), the flow field is divided into the inviscid outer region and the thin inner region. The average velocity in the latter still meets the wall law, while the velocity variance in the former is caused by pressure fluctuation. The two flow layers can further be divided into two sub-layers, respectively as shown in the Fig. 2.8.

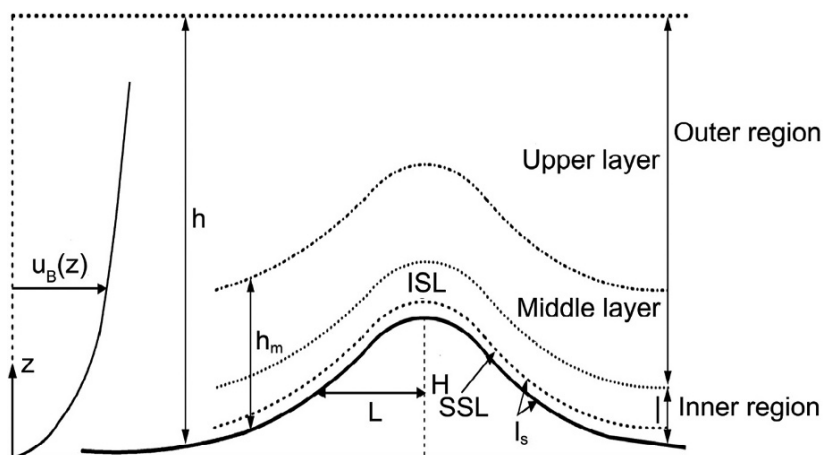


Fig. 2.8. Division of the flow field passing a two-dimensional terrain: upper layer, mid-layer, inner surface layer (ISL) and shear surface layer (SSL), where H is the terrain height, L is the horizontal distance from the top of the sand dune to the mid-point of the windward slope, the terrain surface shape is $z = h_{dune}(x)$, u_B is the flow velocity corresponding to h_m , which is the height of the mid-layer, besides, the surface roughness z_0 is a constant

According to the HLR theory, the inner layer depth l_{inner} which can be calculated from $l_{inner} = 2k^2 L / \ln(l_{inner} / z_0)$, is usually much higher than the saltation layer. The velocity profile in this layer follows logarithmic law, while the friction velocity u_* is not equal to the inflow friction velocity u_{*0} , but substituted by another value with taking into account of the local disturbance instead. According to HLR's assumption, the disturbance of the friction stress is linear, so it follows the following equation

$$\tau(x) = \tau_0(1 + \hat{\tau}(x)). \quad (2.37)$$

Based on the friction stress expression of Weng et al. (1991), Sauermann et al. (2001) made a simplification of $\hat{\tau}(x)$ which can be expressed as

$$\hat{\tau}(x) = A \left(\frac{1}{\pi} \int_{-\infty}^{\infty} \frac{\dot{h}_{dune}}{x - \xi} d\xi + B \dot{h}_{dune} \right), \quad (2.38)$$

where $A \approx 3.2$, $B \approx 0.25$.

Except for the HLR theory, it is also feasible method to determine velocity variation on the dune slope through experiments. From field observations and wind tunnel experiments, Mulligan (1988) and Lancaster et al. (1996) found that the shear velocity u_* is in a linear relation with the height from the bed,

$$u_* = u_{*-\infty} + k_* h_{dune}, \quad (2.39)$$

where h_{dune} is the height from the bed, $u_{*-\infty} = u_{*0}$ is the friction velocity of the inflow at the infinite distance, k_* is the velocity increment which is related to the dune height H . Because the shear velocity u_* is in a linear relation to the height h_{dune} , the velocity acceleration factor α_{dune} ($= u_{*crest} / u_{*-\infty}$, u_{*crest} is the wind velocity on the dune top) can be used to describe the evolution of the wind velocity acceleration on the windward slope of the dune. According to the relationship between the wind velocity acceleration factor α_{dune} and the angle of the windward slope (Lancaster 1985) and the relationship between the angle and the dune height, the following expression can be obtained

$$k_* = \frac{(\alpha_{dune} - 1)u_{*-\infty}}{H} = \frac{u_{*-\infty}}{H} \left[\alpha_0 - 1 + 2k_1 \tan \left(A + \ln \frac{H - B}{C} \right) \right], \quad (2.40)$$

where A , B , C , α_0 and k_1 are empirical parameters varying for different regions, which should be determined by observations and measurements conducted in the regions concerned.

Because of flow separation, an eddy current is usually formed on the leeward slope. The downwind velocity may decrease quickly to zero and even become negative. When the along-wind velocity is at an angle with the transverse dune, secondary flow along the dune will appear. The studies of Walker and Nickling (2002) showed that secondary flow is the reason for the appearance of sand ripples on the leeward side of sand dunes.

2.6 Wind Gusts near the Earth's Surface

Here wind gusts represent the wind fluctuations near the surface which are not the same as the definition of Cheng et al. (2007). Wind gusts affect the transfer of momentum, heat and material there. Their effects are embodied not only in the transmission of momentum through the Reynolds stress which makes erosion and deposition occur, but also in making the erosion process unstable and intermittent because of large turbulent intensity. Although wind gusts play an important role in the transport of particles from an erodible surface, most previous researches focused on steady state sediment transport, which means that both turbulence stress and wind velocity are time-averaged. In this case, although more and more factors (various aerodynamic forces exerted on a sand particle, the effects of particle size, particle shape, moisture level, heterogeneous saltation, collisions between particles in air, etc.) are taken into account in the prediction models, the simulated mass-flux relations show only moderate mutual agreement. According to the results of Anderson and Haff (1991), the responding time of mass flux to wind variations is no less than one second, so the wind fluctuations in this time scale should be considered in detail.

So the research of erosion processes should include wind gusts rather than mere steady flow (Zeng et al. 2007). The effects of wind gusts can be seen from the measured results of wind velocity and dust entrainment in a dust storm in Beijing, shown in Fig. 2.9 (Zeng et al. 2006).

It is known that the atmospheric turbulence spectrum contains three independent regions: the weather-scale region, the spectrum window and the turbulence scale region, and two peaks: one appears at a rate of 10^{-2} per hour, which belongs to weather scale, the other appears at 50 per hour. The latter results from turbulence fluctuations which can be affected by surface friction and dynamical interactions of turbulence eddies or thermal instability, so it belongs to the turbulence scale region. The near surface wind gusts, which show evident turbulent characteristics (instability, randomness, multi-scale characteristics, and intermittency), are contained in the second scale (see Kaimal et al. 1972).

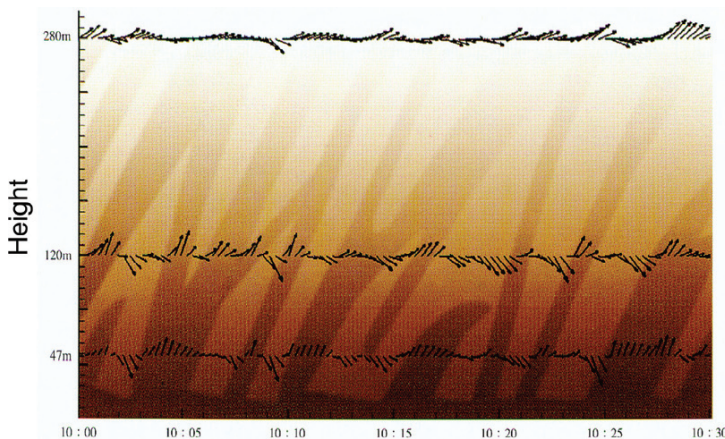


Fig. 2.9. Variations of the velocity vector and the concentration of dust with time, the data has been smoothed by 1 minutes interval (from Zeng et al. 2006)

In the following discussion, wind velocity and saltation activity measured at different heights from bare ground and dune crest are given out. It is found through calculating the correlation dimensions of the experimental data that both the wind gusts and the sand transport variations should be regarded as a dominant random behavior rather than chaos. Based on an analysis of the stochastic characteristics of the sand flux and turbulence, we discover that the sand transport is a highly intermittent process and may be mainly correlated with wind gusts in a time scale of about 3 min. Finally, a wind prediction model which can be used to define the wind velocity variations with time and height is proposed according to the characteristic analysis of the near-surface wind turbulence.

2.6.1 Analysis of the Wind Gusts

Experiments were performed to measure the wind profile (and sand transport flux) on bare inter-dunes and a 8 m high sand dune crest on the edge of the Badain Jaran desert and the Tengger Desert in Minqin, China. Using fast response instruments (a lightweight fast-responding cup anemometer, a micro wind vane and a piezoelectric saltation sensor (Sensit), CR-3000 Micrologger, all of which were sampled at a rate of 1 Hz, shown in Figs. 2.5 and 2.6), continuous and synchronous measurements of turbulent velocity fluctuations, wind direction and saltation activity at several heights were made. Figs. 2.10–2.12 show the variations of wind velocity with time for different time scales, from which it can be seen that even in one second scale the velocity still changes violently.

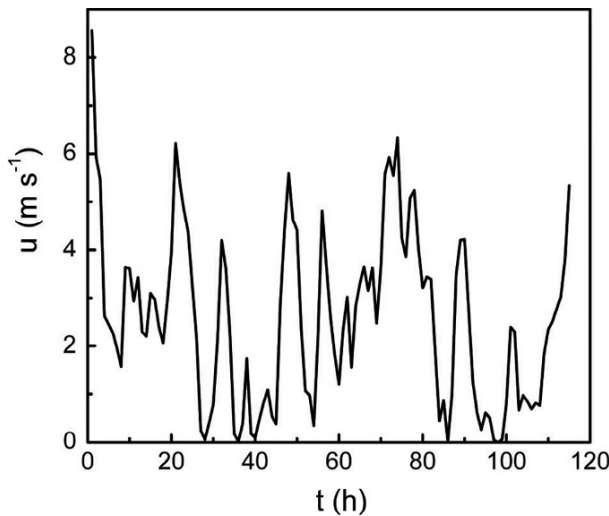


Fig. 2.10. The variations of wind velocity for the time scale of 1 hour at 2 m (measured by the author et al. on a flat ground in Minqin, China, during the period from October 28 to November 2, 2007)

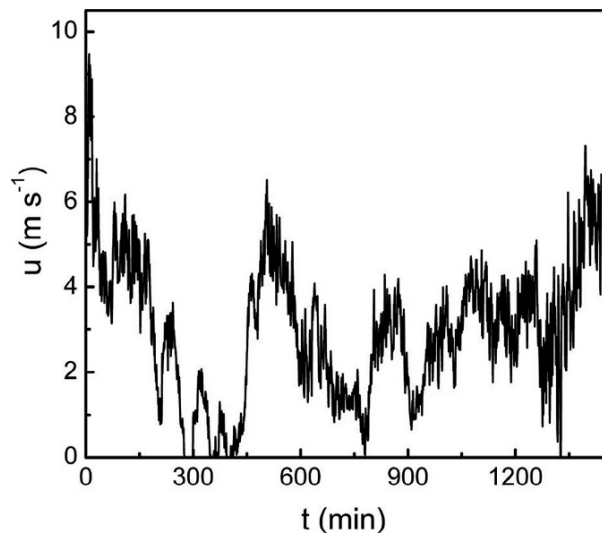


Fig. 2.11. The variations of wind velocity for the time scale of 1 min at 2 m (measured by the author et al. on flat ground in Minqin, China, during the period from October 28 to November 2, 2007)

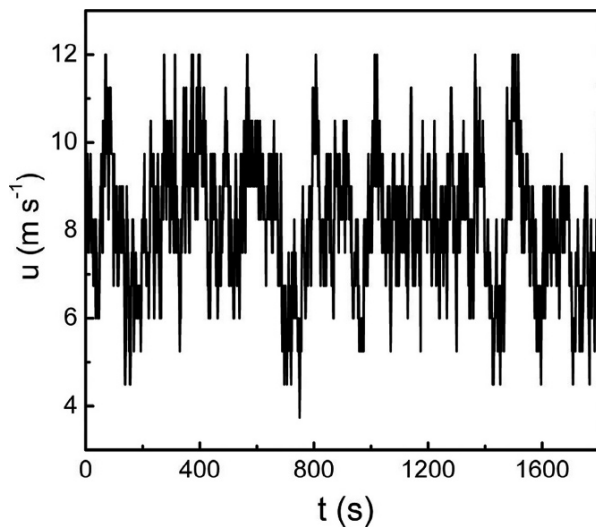


Fig. 2.12. The variations of wind velocity for the time scale of 1 second at 2 m. (measured by the author et al. on flat ground in Minqin, China, during the period from October 28 to November 2, 2007)

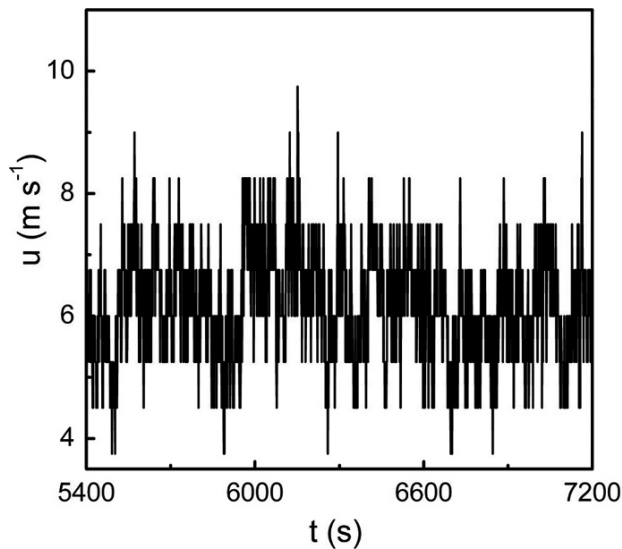


Fig. 2.13. The wind velocity at height of 0.15 m (measured by the author et al. on a dune crest in Minqin, China during the period from October 27 to October 28, 2007 with equipment shown in Fig. 2.5 and Fig. 2.6)

The wind velocity, wind direction and saltation activity on the dune crest were measured over a 2 hours period, part of the experimental results are presented in Figs. 2.13–2.15, which reveals evident fluctuations of the sediment transport flux as well as the flow velocity.

In order to analyze the nature of the random experimental signal, i.e., to see whether it belongs to a chaotic system or is just stochastic, the correlation dimension of the wind velocity and the saltation activity data are calculated. The experimental data are time series, which can be denoted by $\{x(t_i), t_i = t_0 + i\Delta t\}$, where $\Delta t = 1\text{s}$, and $x(t_i)$ represents the physical quantity measured at t_i , such as wind velocity, saltation activity, etc. Before the calculation, an m -dimensional phase space should be formed from $x(t_i)$, which can be represented by $\{\mathbf{X}_i, i = 1, 2, \dots, m\}$, where \mathbf{X}_i is a point in an m -dimensional phase space, which can be denoted as:

$$\mathbf{X}_i = (x_i, x_{i+\Delta\tau}, x_{i+2\Delta\tau}, \dots, x_{i+(m-1)\Delta\tau}) \quad i = 1, 2, \dots, N_0, \quad (2.41)$$

where $N_0 = N - (m-1)\Delta\tau$, $\Delta\tau$ is delay time lag and N is the total data number. Then, the correlation dimension of $x(t_i)$ can be defined in the following way:

$$d_c(m) = \lim_{\varepsilon_d \rightarrow 0} \frac{\ln C(\varepsilon_d, m)}{\ln \varepsilon_d}, \text{ while } C(\varepsilon_d) = \frac{N(i, j)}{N_0(N_0 - 1)}, \quad (2.42)$$

where $N(i, j)$ is the number of the pairs $(\mathbf{X}_i, \mathbf{X}_j)$ which satisfies $\|\mathbf{X}_i - \mathbf{X}_j\| < \varepsilon_d$. So we have:

$$C(\varepsilon_d, m) = \frac{1}{N_0(N_0 - 1)} \sum_{i=1, j=0, i \neq j}^{N_0} s(\varepsilon_d - \|\mathbf{X}_i - \mathbf{X}_j\|), \quad (2.43)$$

where $s(z)$ is Heaviside step function, and is expressed as

$$s(z) = \begin{cases} 0, & \text{if } z < 0 \\ 1, & \text{if } z \geq 0 \end{cases}. \quad (2.44)$$

If there exists a m_0 making $d_c(m)$ ($m \geq m_0$) approach a fixed value when $\varepsilon_d \rightarrow 0$, namely,

$$d_c(m_0) = d_c(m_0 + 1) = d_c(m_0 + 2) = \dots = d_c. \quad (2.45)$$

We can conclude that the mechanical system which produces the experimental data exhibits the characteristics of chaos. If the above condition is not satisfied, the system is dominated by stochastic features (see Grassberger and Procaccia 1983). Because of the multi-scale characteristic of the wind turbulence, the experiment data are decomposed to multi-scales by the discrete wavelet transform method.

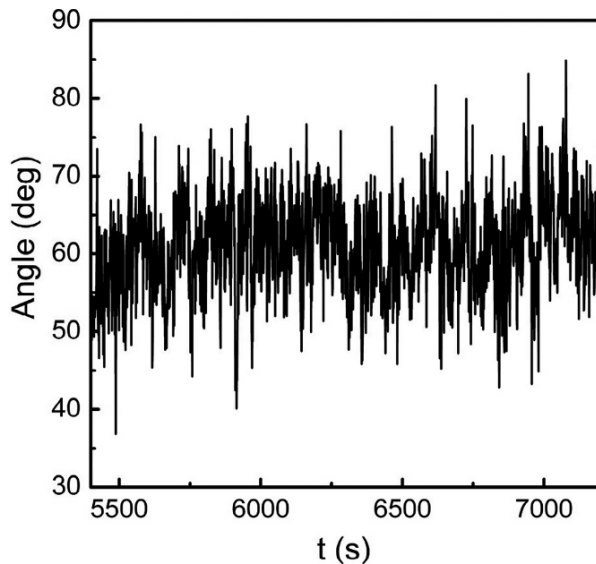


Fig. 2.14. Wind direction data at height of 2.0 m (measured by the author et al. on a dune crest in Minqin, China during the period from October 27 to October 28 in 2007 with equipment shown in Fig. 2.5 and Fig. 2.6)

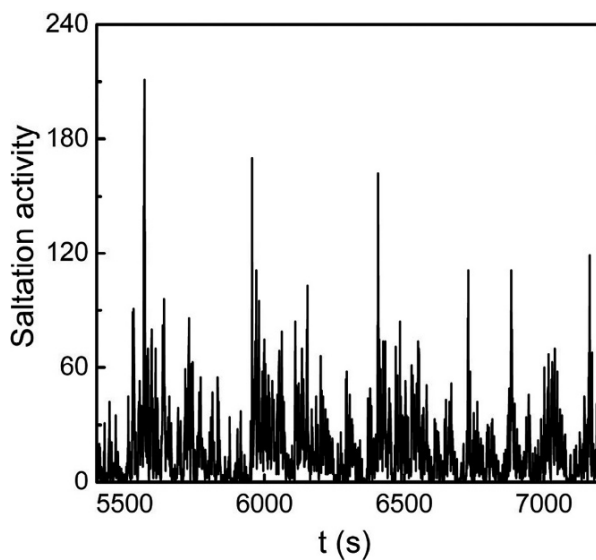


Fig. 2.15. Saltation activity at height of 0.04 m (measured by the author et al. on a dune crest in Minqin, China during the period from October 27 to October 28 in 2007 with equipment shown in Fig. 2.5 and Fig. 2.6)

Based on the wavelet theory, a signal $f(x)$ which belongs to real-space $L^2(R)$ can always be decomposed as the sum of a low-resolution part and several high-resolution parts in order to analyze the multi-scale characteristics. Suppose the scaling function is taken as the Daubechies scaling function $\phi(x)$, for example, which satisfies the following so-called ‘two-scale equation’,

$$\phi(x) = \sum_k p_k \phi(2x - k), \quad (2.46)$$

where $\{p_k\}$ is called the two-scale sequence for the scaling function. Corresponding to $\phi(x)$, the wavelet function $\psi(x)$ also satisfies its two-scale equation

$$\psi(x) = \sum_k q_k \phi(2x - k). \quad (2.47)$$

$\{q_k\}$ is called the two-scale sequence for the wavelet function. $\{p_k\}$ and $\{q_k\}$ are also called the low pass filter coefficient and the band-pass filter coefficient, respectively. If ‘expansion’ and ‘translation’ are performed to the scaling function and the wavelet function, the new functions can be defined by:

$$\begin{cases} \phi_{j,k}(x) = 2^{-j/2} \phi(2^{-j}x - k) \\ \psi_{j,k}(x) = 2^{-j/2} \psi(2^{-j}x - k) \end{cases} \quad j, k \in N. \quad (2.48)$$

Then for a given integer j , the functions sequences $\{\phi_{j,k}(x), k \in N\}$ and $\{\psi_{j,k}(x), k \in N\}$ can form two groups of linear subspace of $L^2(R)$, which can be expressed as:

$$\begin{cases} V_j = \text{span}\{\phi_{j,k}(x), k \in N\} \\ W_j = \text{span}\{\psi_{j,k}(x), k \in N\} \end{cases}. \quad (2.49)$$

These subspaces meet the nested relations: $V_0 \subset V_1 \subset \dots \subset V_j \subset \dots \subset L^2(R)$, and $V_{j+1} = V_j + W_j$, so the function $f(x) \in L^2(R)$ can be decomposed as:

$$f^{j+1} = \sum_k c_k^{j+1} \phi_{j+1,k}(x) = \sum_k c_k^j \phi_{j,k}(x) + \sum_k d_k^j \psi_{j,k}(x) = f^j + \delta^j, \quad (2.50)$$

where $c_k^j = \sum_s \langle \phi, \phi_{-1,s-2k} \rangle c_s^{j-1}$, $d_k^j = \sum_s \langle \psi, \phi_{-1,s-2k} \rangle c_s^{j-1}$, $c_k^0 = \langle f^0, \phi_{0,k} \rangle$. Here

$$f^j = \sum_k c_k^j \phi_{j,k}(x), \quad \delta^j = \sum_k d_k^j \psi_{j,k}(x)$$

are respectively called the approximate part and the detailed part of the signal. Following the above method, the original signal is decomposed to multi-scale signals, and the numbers of the data of all levels are equal.

Therefore, for the experimental data $\{x(t_i), t_i=t_0+i\Delta t\}$, we measured in the field (the wind velocity and saltation activity), c_k^0 can be calculated using:

$$c_k^0 = \Delta t \sum_l x(t_l) \phi_{0,k}(t_l). \quad (2.51)$$

Here in, the approximate part and the detailed part of the original signal can be computed through Eq. 2.50.

It is found that the correlation dimension grows with the increasing of embedding dimension of phase space for different levels and different heights, so it can be concluded that the boundary turbulence beneath 2 m should be considered as a predominant random behavior rather than chaos.

In order to further analyze the fluctuating profile of the flow velocity and the saltation activity, some statistic of the experimental data $\{x(t_0+i\Delta t)=\{x(i)\}\}$ are calculated.

average: $\bar{X} = \frac{1}{t_a} \sum_{i=1}^N x(t_i) = \frac{1}{N} \sum_{i=1}^N x(i), \quad (2.52)$

standard deviation: $\sigma = \sqrt{\frac{1}{N-1} \sum_{i=1}^N [x(i) - \bar{X}]^2}, \quad (2.53)$

skewness: $S_k = \frac{1}{\sigma^3 N} \sum_{i=1}^N [x(i) - \bar{X}]^3 \quad (2.54)$

kurtosis: $K_x = \frac{1}{\sigma^4 N} \sum_{i=1}^N [x(i) - \bar{X}]^4, \quad (2.55)$

and turbulence: $I = \sigma / \bar{X}. \quad (2.56)$

Generally the total time length, $t_a=N\Delta t$, can be selected as 10 minutes to one hour and in our calculations $t_a=30$ min. The statistics of the measured velocity data (including the data measured on the bare ground and on the dune crest) are listed in Table 2.1, and the same statistic for the wind velocity and the saltation activity are listed in Table 2.2, in which the measuring heights of the wind velocity and the saltation activity are 0.15 m and 0.04 m, respectively. The total data for two hours is divided into four groups according to the time period.

It can be shown from Table 2.1 that the mean wind gusts obey the logarithmic law, and they almost approach standard normal distribution at all heights ($S_k \approx 0$, $K_x \approx 3$). Also revealed by this table is that the Standard Deviation (STD) increases and the other parameters, such as the turbulence, the skewness and the kurtosis, all reduce as the height increases. Compared to the bare interdune results, the skewness and the kurtosis deviate more from normal distribution, which shows that the wind profile is more intermittent on the dune crest. From Table 2.2 we can see that the skewness and the kurtosis of the saltation activity get far away from a Gaussian distribution, indicating strong intermittent characteristics. The above analysis leads to the conclusion that although the wind in the period of the weather scale has important effects on the sediment transport (for example, it may be the dynamical cause of sand storms), the wind gusts in the turbulence scale directly affect the wind-blown sand transport process

Table 2.1. The statistics of the wind velocity

| | Height [m] | Average [m s ⁻¹] | STD | Turbulence | Skewness | Kurtosis |
|--------|---------------|---------------------------------|------|------------|----------|----------|
| Dune | 0.15 | 6.02 | 1.08 | 0.179 | 0.250 | 2.77 |
| | 0.55 | 7.81 | 1.34 | 0.172 | 0.262 | 2.60 |
| | 1.00 | 8.12 | 1.38 | 0.170 | 0.229 | 2.57 |
| | 2.00 | 8.52 | 1.42 | 0.167 | 0.212 | 2.34 |
| Ground | 0.12 | 5.38 | 1.10 | 0.204 | 0.129 | 2.76 |
| | 0.55 | 6.97 | 1.32 | 0.190 | 0.104 | 2.68 |
| | 1.00 | 7.53 | 1.42 | 0.188 | 0.079 | 2.70 |
| | 2.00 | 8.16 | 1.52 | 0.186 | 0.003 | 2.63 |

STD represents Standard deviation.

Table 2.2. The statistics of the wind velocity and the saltation activity

| N/Statistics | Average | STD | STD/average | Skewness | Kurtosis |
|--------------|---------|-------|-------------|----------|----------|
| I | 6.02 | 1.08 | 0.18 | 0.25 | 2.77 |
| | 10.51 | 14.94 | 1.42 | 2.84 | 14.71 |
| II | 6.02 | 1.08 | 0.18 | 0.30 | 2.96 |
| | 9.57 | 13.77 | 1.44 | 2.91 | 16.18 |
| III | 6.30 | 1.05 | 0.17 | 0.46 | 3.52 |
| | 15.73 | 22.01 | 1.40 | 3.25 | 17.34 |
| IV | 6.20 | 0.91 | 0.15 | 0.14 | 2.95 |
| | 16.82 | 19.86 | 1.18 | 2.79 | 16.60 |

I-IV is the group number. In each group, the first line represents wind velocity, and the second line is saltation activity.

near the Earth's surface through momentum exchange with erodible surfaces (see Fig. 2.15).

In order to define the time scale related to the sand transport process, the Mid-Smoothing Method is used. The value at time $k\Delta t$ is

$$X_s(k) = \frac{1}{2m_s + 1} \sum_{i=k-m_s}^{k+m_s} x(i), \quad k = m_s + 1, m_s + 2, \dots, N - m_s.$$

Here $\{x(t_0 + i\Delta t) = \{x(i)\}$ is experimental data series, $T_s = (2m_s + 1)\Delta t$ is the smooth period. Then the variance of the smoothed wind velocity (measured at 0.15 m) and the saltation activity (measured at 4 cm) are calculated for different time periods. The results show that the cross-correlation coefficient of the two variance series gets the largest value for 3-minute periods, which implies that the wind gusts in this time scale contribute the most to the sand erosion process. Similarly, Butterfield (1991) found that the responding time of the flow to the sand flux is 6–20 s, while Neumann et al. (2000) got a period of about 5–20 min through a power spectrum analysis method. The wind gusts found in our work or Neumann et al. (2000) are actually wind gusts. Zeng et al. (2007) revealed that the wind gusts of 3–5 min have some kind of coherent structure and our work shows that the wind gusts with coherent structure not only are related directly to the dust entrainment process in the region of 47–280 m, but they may also affect the movement of the Earth's surface sands.

2.6.2 Prediction Model I: Wind Gusts Vary with Time

We define T_g as the wind gusts period which represents the duration between two successive time points on which the wind velocity passes its mean value \bar{u} . Assume that the frequency approximates to its probability, i.e.,

$$f(T_g) = \frac{1}{N_g} \Delta N_g (T_g \leq T_e < T_g + \Delta T_g). \quad (2.57)$$

N_g is the total number of the periods, T_e is the wind gusts period calculated from the experimental data. Fig. 2.16 shows the variations of T_e in 30 min and they are computed from the wind velocity data at 2.0 m height, n_e is the series number of T_e . It is found that T_g follows an exponential distribution, expressed as

$$f(T_g) = \frac{1}{a} \exp\left(-\frac{T_g}{a}\right), \quad (2.58)$$

where the parameter a is about 5.0.

From Fig. 2.17 we can see that the wind variations show abrupt characteristics, making it seem to be the discontinuous square-wave function rather than a sine or cosine function. In shorter periods (5 min) the experimental data still shows small oscillations, which is called noise and can be represented by a Gaussian distribution with a standard deviation pre-specified.

Then suppose the wind velocity at the reference height has the following form:

$$u = \bar{u} + \langle u \rangle + u', \quad (2.59)$$

where \bar{u} is the mean velocity, $\langle u \rangle$, u' represent the turbulence fluctuations and the Gaussian noise respectively, where the turbulence fluctuations is simply expressed by a square wave function. The amplitude of the square wave is defined as Gm . We assume $Gm = \text{sign}(T_g)MT_g$, where $\text{sign}(T_g)$ is selected to make two successive period have an opposite sign, M is a parameter, which is calculated through introducing the ratio γ of the turbulence energy and the total energy and can be represented by the variance of the square wave function and the variance of the wind flow, T_g is denoted by a random number which obey the exponential distribution

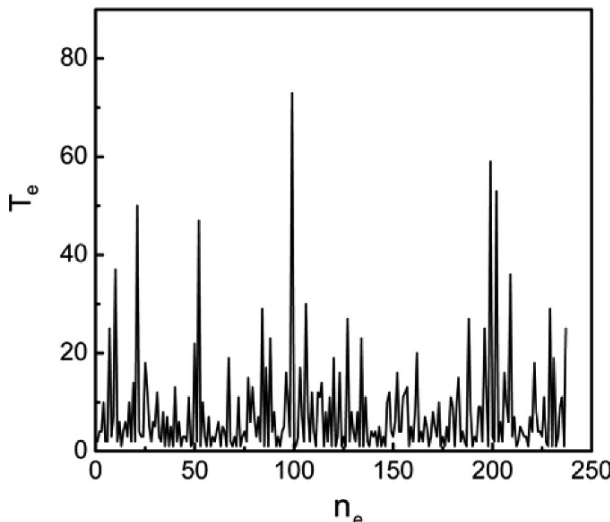


Fig. 2.16. Wind gusts period occurs in 30 minutes. T_e is the wind gusts period calculated from the experimental data, n_e is the series number of T_e . (the experimental data was measured by the author et al. on flat ground in Minqin, China, on November 2, 2007)

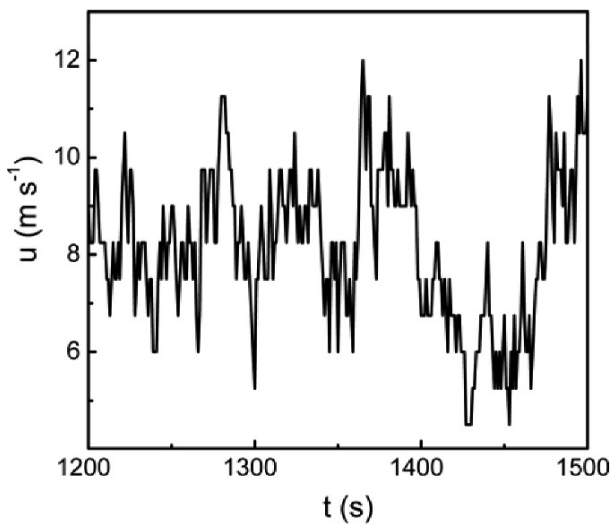


Fig. 2.17. Variations of wind velocity in 5 minutes (measured by the author et al. on flat ground in Minqin, China, on November 2, 2007)

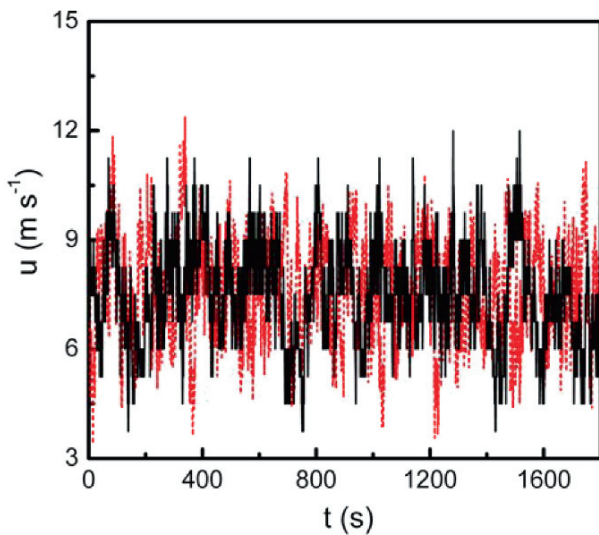


Fig. 2.18. Wind velocity predicted by Eq. 2.59 with $a=5.0$ and $\gamma \approx 0.8$ (red dot line) compared with the experimental data at 2.0 m (black solid line) measured by the author et al. on flat ground in Minqin, China on November 2, 2007

with a parameter of 5.0. The noise is represented by random numbers to follow a Gaussian distribution, the standard deviation is specified as $\sigma_T = \sqrt{\sigma_u^2(1-\gamma)}$. In the modeling, we first choose a γ and the initial value of M , then change M continuously until the sum of the variance of the square wave function and the variance of the Gaussian noise equals the total variance σ_u^2 , which is given as a model parameter.

Based on the average value and variance of experimental data measured at 2 m, the temporal variation of the wind velocity is simulated, in which $\gamma \approx 0.8$. It is found that the predicted velocity has a satisfactory agreement with experimental results (see Fig. 2.18).

2.6.3 Prediction Model II: Wind Gusts Vary with Height

We choose the wind velocity at 2.0 m as the reference wind velocity to generate the wind velocity beneath it. The difference between the velocity $u_h(h, t_i)$ at a height of h below 2 m and the reference wind velocity at time t_i is defined as u'' , then $u'' = u_r(h_r, t_i) - u_h(h, t_i)$, where h_r is the reference height while $u_r(h_r, t_i)$ is the corresponding wind velocity, then the mean of u'' is:

$$\bar{u}'' = \overline{u_r(h_r, t_i) - u_h(h, t_i)} = \overline{u_r(h_r, t_i)} - \overline{u_h(h, t_i)}. \quad (2.60)$$

Suppose the mean velocity obeys the logarithmic law, then through rewriting Eq. 2.60 we get:

$$\bar{u}'' = \frac{u_*}{k} \ln \frac{h_r}{z_0} - \frac{u_*}{k} \ln \frac{h}{z_0} = \frac{u_*}{k} \ln \frac{h_r}{h} = \frac{u_*}{k} \ln \frac{2.0}{h}. \quad (2.61)$$

So it is assumed that $\bar{u}'' = k_1 \ln(2.0/h) + k_2$, k_1, k_2 is to be determined based on experimental data, and the variance of u' is:

$$\sigma_{\Delta h}^2 = \overline{[(u_r - u_h) - (\bar{u}_r - \bar{u}_h)]^2} = \overline{(u'_r - u'_h)^2} = \overline{u'^2_r} + \overline{u'^2_h} - 2\overline{u'_r u'_h}.$$

Since $\overline{u'^2_r} = \sigma_r^2$, $\overline{u'^2_h} = \sigma_h^2$, if $\overline{u'_r u'_h} \approx \sigma_r \sigma_h$ is assumed, we get $\sigma_{\Delta h} = \sigma_r - \sigma_h$. According to Table 2.1, the turbulence does not change much with height, and we can suppose it keeps a constant near the surface, so:

$$I_h = I_r \quad \text{or} \quad \frac{\sigma_h}{\bar{u}_h} = \frac{\sigma_r}{\bar{u}_r}, \quad (2.62)$$

then $\sigma_{\Delta h} = \sigma_r - \sigma_h \propto \bar{u}_r - \bar{u}_h$, and we have $\sigma_{\Delta h} = k_3 \ln(2.0/h) + k_4$. k_3 and k_4 are also determined by the experimental data. On the basis of the wind ve-

lacity measured on the bare ground, we get: $k_1 = 2.37u_* + 0.07$, $k_2 = -0.3$, $k_3 = 0.06$, $k_4 = 0.56$.

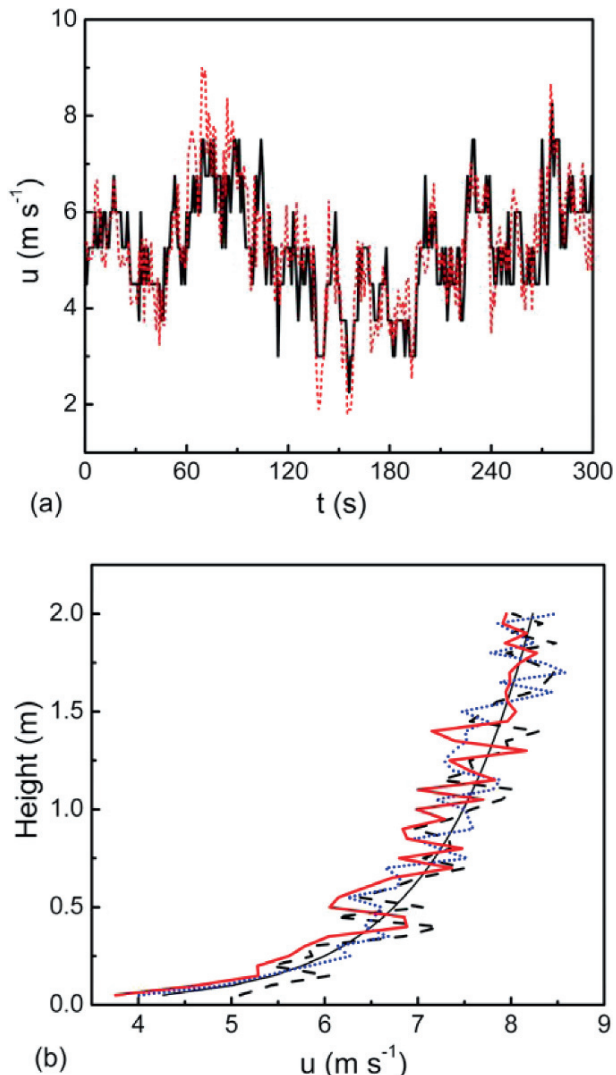


Fig. 2.19. (a) Comparison between results (----) predicted by the prediction model II (i.e., Eqs. 2.60 and 2.63) and experimental data (—) at 0.12 m which is the same as in Fig. 2.16, (b) Comparison between predicted wind profile (using model II, i.e., Eqs. 2.60 and 2.63, but change the height h continuously) and log-linear profile, in which the dash line (----), dot line (.....) and solid line represent the wind gusts at t_0 , $t_0 + \Delta t$, $t_0 + 2\Delta t$

In this context, we assume u'' obeys a Gaussian distribution

$$f(u'') = \frac{1}{\sqrt{2\pi}\sigma_{\Delta h}} \exp\left[-\frac{(u'' - \bar{u}'')^2}{\sigma_{\Delta h}^2}\right], \quad (2.63)$$

then we can calculate the wind gusts varying with height. Fig. 2.19a displays the comparison between the predicted and experimental wind velocity at 0.12 m. It can be seen that these two velocities agree very well. Then we give a prediction on the wind velocity varying with height in three successive seconds (Fig. 2.19b). From Fig. 2.19b it can be seen that the velocity distribution with height does not follow the logarithmic law and this deviation can attain $2\text{--}3 \text{ m}\cdot\text{s}^{-1}$. This proves that the consideration of wind gusts is essential.

Chapter 3 Sand Motion near the Sand Bed Surface

Under the direct action of aerodynamic forces, a portion of sand particles on the bed tend to roll and slide forward, which is called creeping, while some particles tend to lift off the sand bed with certain velocities, and then act as saltation or suspension. The creeping particles are likely to excite their neighboring particles to jerk up into the air, and the saltating ones, after falling back to the ground, are likely to rebound and eject several of their neighboring particles out of the bed. Such lift-off and splash processes taking place near the sand bed are a significant ingredient of wind-blown sand movement, they directly influence the trajectories of sand particles and the development of wind-blown sand flow, and they always serve as the initial conditions for theoretical prediction models of sand motion.

As we can imagine, the scale and dominating physical rules of a single particle's motion may be different in essence from those of wind-blown sand movement which involves a countless number of moving sand particles. In the view of a single particle's motion, too many variables are involved to simulate the wind-blown sand movement process, which makes it an absolutely formidable challenge to take the initial lift-off value of every sand particle into the equations of motion, even with a supercomputer. Therefore, when dealing with such multi-scale problems, we always need to draw lessons from the statistics. Similar to the roles the Avogadro and Boltzmann constants played in describing the properties of molecular motion and ideal gas respectively (Feynman 1963), it is necessary to introduce the probability density function (PDF) of lift-off velocities and the splash function as key statistical quantities to connect the two physical phenomena of different scales, i.e., the micro-scale motion of a single particle and the macro-scale behavior of the windblown sand movement process. The determination of the PDF of lift-off velocities and the splash function is always based on the analysis of the interaction between sand particles and the bed. Therefore, the content of this chapter is arranged as follows, Sect. 3.1 introduces the threshold wind velocity for sand entrainment; Sect. 3.2 presents the results of existing observations on particle-bed

collision processes and lift-off velocities of sand particles; Sects. 3.3 and 3.4 provide a theoretical model based on the stochastic particle-bed collisions to obtain the PDF of lift-off velocities and some numerical methods to obtain the splash function, respectively.

3.1 Threshold Wind Velocity for Sand Motion

3.1.1 Mechanism of the Entrainment of Sand Particles

The entrainment mechanism of sand particles is an important research subject in the study of wind-blown sand movement. From experiments, we can observe that it is a complex micro-process in which sand particles dislodging from the sand bed and move downstream under the wind force. When wind velocity reaches a certain level, a few protuberant particles begin to vibrate or swing backwards and forwards without leaving a stationary position under the influence of turbulence and pressure fluctuations. As wind velocity increases up to some threshold value, the amplitude and frequency of sand vibration, the frontal resistance F_D (i.e., the drag force) and the lifting force F_L acting on a sand particle increase accordingly to overcome the gravitational force F_g , which produces a large rotary moment, and hence results in some most susceptible sand particles rolling and sliding downwind. Because of the irregularity of a sand particles' shape, the diversity of sorting and packing, and variation in the acting forces, some rolling particles will collide with those protuberant ones resting on the bed or be impacted by other moving ones. In this way, they rapidly attain enough momentum to change the motion downwind into motion upward. After a transient moment of collision, such rapid change leads these particles to lift off the bed and become saltated in the airstream.

There have been several different arguments on the entrainment mechanism of sand motion. Based on wind tunnel observations, Bagnold (1941) regarded that the initial dislodgement occurs under the direct effects of wind forces when the wind velocity rises to some threshold value, which he called the fluid threshold. Afterwards Bagnold (1941) also suggested that the initial dislodgement may result from collision of saltating particles, and named the minimal wind velocity required to maintain the sand movement as the impact threshold velocity. However, Exner and Hampe (1953) concluded that the dislodgement of sand particles is a result of turbulent diffusion while Von Karman (1956) and Lyles and Krauss (1971) also found that the vertical fluctuation of turbulence plays a significant role in lifting sand particles from the bed. They argued that the turbulent shear

stress is always larger than the laminar shear stress, and the maximum fluctuation of airflow accounts for about 15% of the average value, so turbulence obviously performs a key activation role on the entrainment of sand particles. Nevertheless, there're still other different views on the effect of the turbulence. For example, Bagnold (1941) regarded that the effect of turbulence works only when the wind velocity is high enough, which therefore means he thought the turbulence is not the main reason for the entrainment of particles. Until now, there have been more than 8 different theoretical hypotheses concerning the mechanism of the entrainment of sand particles, which can be categorized into 2 groups, namely the contact force entrainment hypothesis and the non-contact force (aerodynamic force) hypothesis. The former includes the inclined flying hypothesis, the saltating impact hypothesis, and the vibration hypothesis; the latter includes the buoyancy force hypothesis, the aerodynamic drag hypothesis, the turbulence hypothesis, the negative pressure hypothesis and the vortex hypothesis. In summary, the complexity of the shape of sand particles and the configuration of sand packing make all of these coexisting hypotheses seem reasonable for the entrainment of sand particles.

3.1.2 Threshold Wind Velocity of Sand Motion

As far as the threshold wind velocity of sand motion is concerned, Bagnold (1941) showed that there are two thresholds for saltation: the fluid threshold, which is defined as the wind velocity at which particles start moving due to the action of wind only, and the impact threshold, which is defined as the wind velocity at which the combined action of wind forces and saltation impacts can just sustain sand movement, or alternatively, the wind velocity at which the energy received by saltating particles from the wind field can balance the energy losses when particles strike the bed. In general, the fluid threshold is of interest, and the impact threshold is 80% of the fluid threshold. Based on the balance between the frontal resistance F_D and the gravity F_g , we can get an expression for the threshold friction velocity u_{*t} in the following form (Bagnold 1941):

$$u_{*t} = A \sqrt{g D_s \frac{(\rho_s - \rho)}{\rho}} . \quad (3.1)$$

The threshold fluid velocity u_t at any height z can be obtained from the relationship between the friction velocity and wind velocity given by Eq. 2.30, that is,

$$u_t(z) = 5.75A \sqrt{gD_s \frac{(\rho_s - \rho)}{\rho}} \lg\left(\frac{z}{z_0}\right), \quad (3.2)$$

where, D_s is the particle's diameter, A is an empirical coefficient determined by experiment. For example, for 'uniform' sand, i.e., the diameters of sand particles lie within a certain range, it has been found that when $u^*r/v > 3.5$ (where u^*r/v is the Reynolds number, v is kinematic viscosity; r is the mean surface roughness which is of the order of the particle diameter). The critical Reynolds Number $u^*r/v = 3.5$ distinguishes the condition under which a surface may technically be considered either 'rough' or 'smooth'), the coefficient A in Eqs. 3.1 and 3.2 is nearly a constant, equal to 0.1 (Bagnold 1941) or, in the range 0.09–0.11 (Chepil 1945). Some other researchers argued that A is 0.12 (Zingg 1953) or some value within 0.17–0.20 (Lyles et al. 1971). For very small particles, when the critical Reynolds number u^*D/r is less than 3.5, especially when the particle size falls below 0.2 mm, the value of coefficient A begins to rise and the square root law no longer holds. For natural sand particles of varied size, the fluid threshold is determined by the predominant particle size. Fig. 3.1 presents the particle size distributions of the natural dune sand sampled from the Minqin desert region of Gansu province and the eastern edge of the Tengger Desert, China.

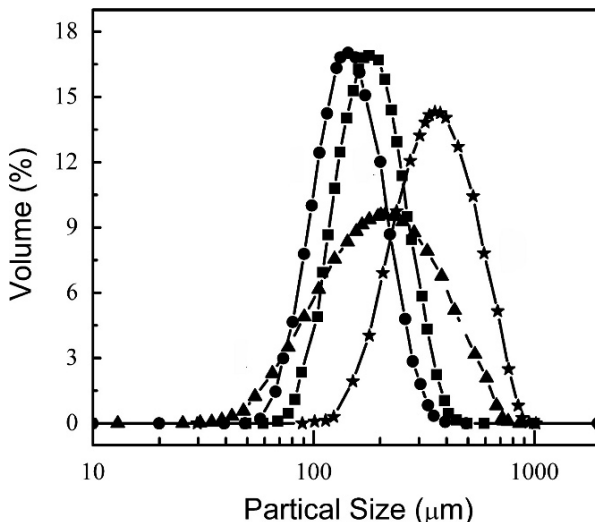


Fig. 3.1. Particle size distributions of dune sand sampled, —▲— and —★— sampled from Minqin; —●— and —■— sampled from the eastern edge of the Tengger Desert (measured by the author et al.).

From experiments conducted in a wind tunnel, we can obtain an intuitive understanding of the physical meaning of the fluid threshold and impact threshold. At the beginning stage, the flow blowing through a flat sand bed is pure wind without sand particles, and the minimum wind velocity at which sand particles begin to be dislodged is the so-called fluid threshold. As the wind velocity increases, the wind-blown sand flux begins to form. Then, if the wind velocity decreases to the fluid threshold, the wind-blown sand flux does not cease until it decreases to some value lower than the fluid threshold, which is called the impact threshold. Therefore, the impact threshold is the maximum wind velocity at which the wind-blown sand flux will cease. It can be seen that in a certain sense that these two threshold values play a similar role as the lower and upper critical Reynolds number play in the transition experiment of fluid dynamics.

3.1.3 Factors Affecting the Threshold Wind Velocity

Generally speaking, the fluid threshold velocity u_t is a piecewise function of particle diameter D_s . For ‘uniform’ sand, Bagnold (1941) suggested that if $D_s > 0.1$ mm, then $u_t \propto \sqrt{D_s}$, while some other experiments (Dong and Li 1998) argued that there exists a minimum threshold velocity when $D_s = 0.09$ mm. For $D_s > 0.09$ mm the motion of sand particles is dominated by inertial forces, thus u_t increases with D_s , while for $D_s < 0.1$ mm, it is dominated by cohesive force and u_t decreases with D_s . The threshold velocity of ‘mixed’ sand bed increases with the average sand diameter D_s , which is always lower than that of corresponding ‘uniform’ sand bed with the same sand diameter.

Surface conditions, such as vegetation and topography, also have an important effect on the threshold velocity through influencing the wind flow over the sand bed. Raupach et al. (1993) used drag partition theory to develop a formula for the effect of vegetation on the threshold velocity:

$$(u_{*t})_V = u_{*t} \sqrt{(1 - \sigma_V \lambda_V)(1 + \gamma_V \beta_V \lambda_V)} \quad (3.3)$$

where u_{*t} and $(u_{*t})_V$ are the threshold friction velocities for a bare-soil surface and a vegetated surface; λ_V is the roughness density or the frontal area index of the roughness; σ_V is the basal-to-frontal area ratio; γ_V is a parameter accounting for spatial non-uniformity in the surface stress, which equals 1 for uniform stress and decreases as non-uniformity increases; and $\beta_V = C_R / C_S$, where C_R is the drag coefficient for isolated roughness elements and C_S is that for the soil surface. Measurements results of the threshold friction velocity by Gillette and Stockton (1989) and Musick and

Gillette (1990) agree well with Eq. 3.3 when $\beta_V \approx 100$, $\gamma_V \approx 0.5$, and $\sigma_V \approx 1$. The effect of topography lies in the influence of surface slope which makes the threshold of sand particles resting on an upslope larger, and those on a downslope smaller than on a flat surface. Howard (1977) deduced a relation between the threshold velocity and the surface slope, that is,

$$(u_{*t})^2 = \frac{\rho_s}{\rho} BD_s g \left(\tan^2 \theta \sin \alpha - \sin^2 \chi \sin^2 \alpha^{1/2} - \cos \chi \sin \alpha \right), \quad (3.4)$$

where $B = 0.31$ and is a dimensionless constant; α is the angle of internal friction; θ is the surface slope angle; and χ is the angle between the wind direction and the normal line of the bed surface. This relation agrees well with the results of Hardisty and Whitehouse (1988) who conducted a field observation on sand dunes in the Sahara desert with a portable wind tunnel.

In addition, surface moisture is also an important variable in controlling the entrainment processes because of the cohesion produced by the tensile force between water molecules and sand particles. It was generally believed that the threshold velocities for sand particles with moisture content bear a linear relationship to the square root of surface moisture, and so adding the same quantity of moisture, the increment of the threshold velocities of sand particles with low moisture content is larger than that with high moisture content. However, some researches (Ravi and Odorico 2005; Ravi et al. 2006; Nickling and Ecclestone 1981; Nickling 1984) recently found that the threshold velocities for sand particles in arid areas do not always increase with moisture content. They explained that as the surface moisture exists in the form of hygroscopic water, the inter-particle cohesion of sand particles decreases rapidly with moisture content (Ravi et al. 2006). Since it is relatively difficult to measure the surface moisture, ambient air humidity is taken as a substitute (Ravi and Odorico 2005). Similarly, due to the cementation effect, salt content is also considered to have a major influence. Nickling and Ecclestone (1981) and Nickling (1984) have found through experiments that u_{*t} can be more than doubled with an increment of salt contents less than 1%, which is the reason for employing polymer binder and saline as a chemical sand solidification agent.

Besides these, some other factors, such as the shape of sand particles and electrostatic force also have significant influences on the threshold of sand motion (Kok and Renno 2008), but how these factors work is still not very clear. Therefore, some field observations or wind tunnel experiments were designed to determine the threshold velocity for specific region. For instance, Bagnold (1941) conducted field observations during the sand-

storm in the Libyan Desert and the results showed that the threshold value of u_{*t} for sand with an average diameter of 0.32 mm is about $0.23 \text{ m}\cdot\text{s}^{-1}$. Other empirical conclusions suggest that for dry bare-sand surfaces, sand particles will be uplifted when the wind velocity measured at 2 m height or recorded by metrological stations reaches about $4\text{--}5 \text{ m}\cdot\text{s}^{-1}$. Though a lot of pioneering work has been done on the entrainment of sand particles, there remain some unclear problems which are related to complex factors affecting the entrainment of sand particles. Therefore, these factors are still an important subject in the study of wind-blown sand movement until now.

3.2 Experimental Research on the Lift-off of Sand Particles

As we mentioned above, the velocities of sand particles lifting off the bed are significant initial conditions for predicting their trajectories in wind-blown sand movement. The most intuitive method for obtaining the lift-off velocities of sand particles is to observe the particle-bed collision process directly and capture the moment the sand leaves the bed. Such measurements can be divided into two types: laboratory experiments with ‘artificial’ sand and wind tunnel experiments with natural sand.

3.2.1 Experiments on Particle-Bed Collision with ‘Artificial’ Sand

Particle-bed collision processes have been studied since 1985 by direct observation on ‘artificial’ sand particles, such as steel spheres and spherical plastic beads. For example, Mitha et al. (1986) studied the direct collision of steel beads on a three-dimensional (3-D) packing of 60,000 steel beads. Both particles on the bed and the impacting particles were 4 mm steel spheres. The phenomenon was recorded through stroboscopic photography. Their results essentially confirmed the previous studies and supported Rumpel’s (1985) hypothesis about the amplification mechanism of the vertical speed at low angles. Francöis et al. (2000) conducted experiments to study the collision process of particles on a two-dimensional (2-D) granular bed with identical plastic beads. These experimental researches provide some meaningful results. For example, the incident bead does not affect the bottom of the bed when the height of the packing is of 6 layers or more; while the number of ejections is enhanced at low packing height. Moreover, the ejected particles come essentially from a local region surrounding the impact point of the collision; however, in some cases, parti-

cles can be ejected from a location which is far from the impact point. Furthermore, beads ejected from a point located in front of the impact position jump forwards whereas those ejected from a point behind the impact position move backwards. The ejected particles are much less energetic than the impact particle. The number of ejected particles almost linearly increases with the impact velocity. Also, 94% of high speed impact particles will rebound from the bed and the vertical component of rebound speed increases with impact angle, and so on. However, there are still some limitations for these ‘artificial’ particle experiments when their results are applied to explain natural wind-blown sand movement for the following reasons: (1) the material and surface curvature of particles do have a direct influence on the particle-bed collision process; (2) there might be scale effects in substituting the sand particles of smaller scale with particles of larger scale.

3.2.2 Measurements of the Linear Velocities of Lift-off Particles

The apparatus for a wind tunnel experiment on particle-bed collisions with natural sand is showed in Fig. 3.2. When wind blows over the sand bed, particle-bed collision processes and the trajectories of saltating sand particles can be captured by high-speed camera or stroboscope. The motion of sand particles in the saltation layer is usually identified at the height of 5 mm because of the dense concentration of sand particles below 5 mm. The lift-off velocity of a certain particle can be obtained through the following manner: firstly, arbitrarily select two points, like point 2 and point 3 in Fig. 3.3, along the trajectory, which are denoted by (x_2, z_2) and (x_3, z_3) , respectively; then record the time the particle takes traveling from point 2 to point 3; and finally take the average velocity \bar{V} as the lift-off velocity V . The components of V can be express as:

$$V_x = \frac{1}{\Delta t} (x_3 - x_2), \quad V_z = \frac{1}{\Delta t} (z_3 - z_2). \quad (3.5)$$

As we can see, the lift-off velocities of sand particles obtained in this manner are obviously not accurate enough. Therefore, the lift-off velocity can also be inversed by substituting the coordinates of point 2 and point 3 into the trajectory equations on the basis of a theoretical model of particle motions. It is notable that it’s difficult to obtain the analytical solution of trajectory function if all factors influencing the trajectory of sand particle are incorporated. However, on the other hand, oversimplification weakens the accuracy of lift-off velocity.

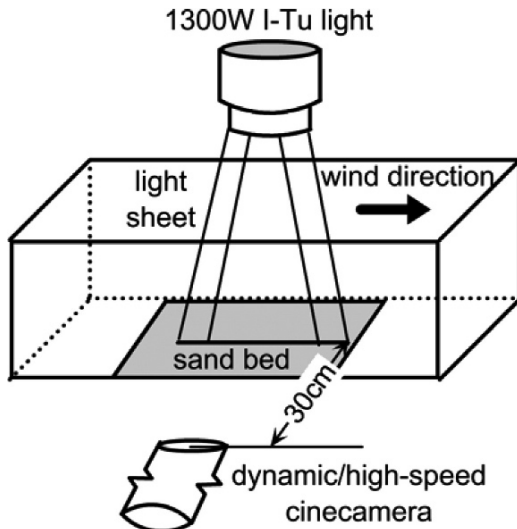


Fig. 3.2. Schematic diagrams of apparatus of wind tunnel experiment on particle-bed collision; 1300W I-Tu light is used to present a light sheet about 1 cm in thickness and dynamic/high-speed cinecamera is put outside of wind tunnel, 30 cm away from the wind tunnel

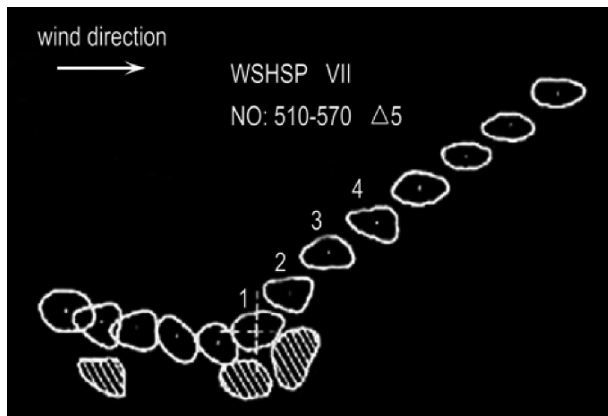


Fig. 3.3. Trajectory of a sand particle captured by high-speed camera and the number 1–4 denotes each position of a sand particle for 4 continuous photographs (from Xie et al. 2007)

Although high-speed cameras and stroboscopes are advantageous to capture continuous images of sand motions in time and space, it's difficult to differentiate the sand particles in a dense packing layer, which restricts

the height of measurement to 5 mm or higher above the sand bed (White and Schulz 1977; Zou et al. 2001). Moreover, judging experimental results by naked eyes restrains to some extent the number of sampling and the degree of accuracy. Recently, Phase Doppler Anemometry (PDA) and Phase Doppler Particle Analyzer (PDPA), in which the laser holographic technology is employed, are used to measure velocities of sand particles in the wind-blown sand flux. For example, Dong et al. (2002) used PDA to detect the saltation of size-sieved sand particles at different friction velocities in a wind tunnel, and presented the statistical results of the incident velocities, the lift-off velocities, the incident angles and the lift-off angles of the particles. Although it has the capability of analyzing a great deal of samples with the aid of computer, PDA technique is weak in determining the diameter of sand particles and in detecting the whole-field information. Besides, single-point PDA measurement fails to reflect the influence of varying measuring height resulting from the erosion or accumulation of sand bed in the wind-blown sand flux.

Based on the speckle technique, which has been applied to measure the strain-displacement of solids, the methods of Particle Image Velocimetry (PIV), and the Particle Tracking Velocimetry (PTV) algorithm (Dabiri and Ghairb 1991; Delnoij et al. 2000), can be used together to reveal the position, movement and diameter of sand particle in wind-blown sand flux. Compared with the PDA technique, PIV breaks through the space limitation of single-point measurement. It not only has the high accuracy and resolution of existing single-point measurement, but also the ability to obtain a fast and non-intrusive measurement and instantaneous image of entire flow fields. The measurement of the motion of sand particles in a wind-blown sand flux with a PIV system works like this: A dual laser is employed to provide a light sheet, an image capture device (i.e., a CCD Camera) is used to capture the flow field and sand particles passing through the light sheet. PIV images are gray level images. The position of sand particle is determined by image processing technique. The velocities of sand particles are obtained by measuring the distance each particle travels in a fixed time interval, a pair of pictures is captured by PIV to locate the particle and a cross-correlation algorithm is used to match the particles.

The procedures for acquiring the information of particle movement from these images are divided into three steps: the threshold segregation, locating particles and correlative particle matching. In the first step, as the gray level of irradiated particles is significantly larger than the dark background, they could be segregated from the background with certain thresholds of gray level. The pixels whose gray levels are larger than the threshold are assigned as 1, and those smaller than the threshold are assigned as

0. The gray level threshold is calibrated after a comparison of the calculated distribution of diameters and the distribution of the sand bed after the second step.

With the two-value image obtained in the first step, it is relatively easy to detect the edge of each particle area with an edge algorithm (Gonzalez and Woods 2003). Counting the number of pixels occupied by each particle and locating the center of each particle, we can calculate the diameters of sand particles by assuming that the shape of sand particle is a sphere and its cross-section is a circle.

In the last step, the cross-correlation algorithm is used to match correlative particles on a pair of PIV images captured within a certain time interval, thus we can get the displacement that the particle traveling in a certain interval of time, or its velocity vector. As there are particles in the first one of a pair of PIV images with large lateral velocity, they might not be captured in the second exposure, thus the cross-correlation algorithm could not match the image of the same particle in two frames, or matches the wrong pairs of particles. A threshold of correlative coefficient should be set to judge the matching of particles and eliminate pseudo-vectors. Finally, the position, speed and diameter of sand particles in a transient of wind-blown sand flow are obtained. Fig. 3.4 shows one of the results of image processing of PIV images of sand particle within 1.3 cm above the sand bed.

Through this method, we could obtain the distribution of lift-off velocities by referring to the sand particle near the sand bed with positive vertical velocity as the lift-off particle or by applying the trajectory equation to figure out the instantaneous lift-off velocity. The advantage of a PIV system make it possible to measure the diameter and the velocities

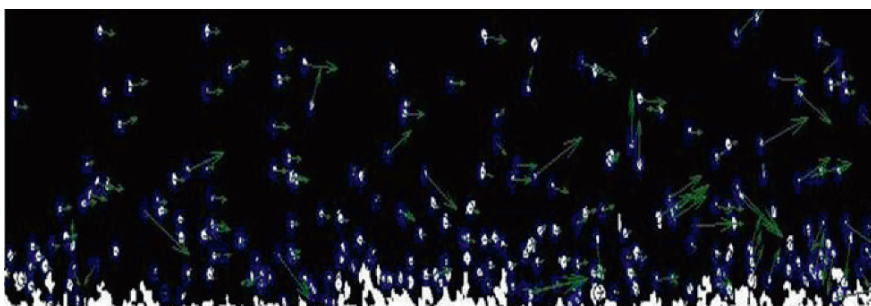


Fig. 3.4. The results of image processing of a pair of PIV images of sand particles within 1.3 cm above the sand bed, in which the hollow circles and arrows represent respectively the position and velocity vector of each sand particle. (photo by the author et al. in Multi-function wind tunnel of Lanzhou university)

of sand particles instantaneously, and therefore to study the affect of wind velocity and particle diameter on the entrainment of saltating sand particles. The preliminary result of wind tunnel experiment based on PIV show that, at certain wind velocities, the lift-off velocities of sand particles increase as their diameters decrease and the lift-off velocities of sand particles with a certain fixed diameter increase as the wind velocity increases.

Furthermore, wind tunnel experiments of particle-bed collision reveal that most sand particles lift-off along the wind direction, the rebound angle is roughly 40° – 60° and the rebound speed is roughly 50%–60% of pre-impact value, the ejection speed of splashed sand particles are of the order of 10% of the impact velocity, and the number of splashed sand particles is usually 2–10 (Willetts and Rice 1986; Rice et al. 1995). High speed impact sand particles may continuously rebound 19–20 times, but if the bed is perfectly rigid, the rebounding particle would most likely emerge from the collision at an angle of 30° – 50° (Anderson et al. 1991).

Directly measuring the transient lift-off velocities of sand particles is still an open problem at present. The sampling frequencies and resolutions of current instruments are restricted by the processing speeds and memory capacities of both the computer and the camera. Continuous whole field measurement of wind-blown sand flow is not possible yet. An ideal high-speed sampling method might trace the path of each sand particle in the whole field while measuring the diameter and speed of each particle so as to provide an accurate prediction of the lift-off velocity.

3.2.3 Measurement of the Angular Velocities of Saltating Particles

The angular velocity of a saltating particle is a key quantity to determine the Magnus force, which affect the trajectory of a sand particle and the profile of mass flux. It can be obtained by analysing the trajectory and counting the number of twist of the trajectory. The mean lift-off angular velocity was 200 – $1000\text{ rev}\cdot\text{s}^{-1}$ (Chepil and Woodruff 1963; Tanaka and Kakinuma 1960). Ewannouve (1972) regarded that the lift-off angular velocity was 100 – $600\text{ rev}\cdot\text{s}^{-1}$ for particles with diameters larger than 0.2 mm, 400 – $600\text{ rev}\cdot\text{s}^{-1}$ for particles with diameters of 0.15–0.2 mm. Rice et al. (1995) found that the lift-off angular velocity was 430 – $850\text{ rev}\cdot\text{s}^{-1}$ for particles with diameters of 0.425–0.6 mm and incident angular velocities of 300 – $670\text{ rev}\cdot\text{s}^{-1}$.

Recently, some new results have been obtained on saltating sand particles' angular velocities through laboratory measurement (Xie et al.

2007). The experiment was conducted in a blow-type, noncirculating wind tunnel. The sand particles employed in the experiment were natural quartz sand particles, which are usually not round and whose diameters range from 0.25 mm to 1.5 mm and the mean diameter is 1.0 mm. The sand particles were laid on the bed with a thickness of 5 cm in the tunnel. A 1300 W high color-temperature I-Tu lamp (LSY 220-1300) light source was mounted 30 cm above the sand bed. A high-speed (HEPING, 35 fs^{-1}) and a dynamic cinecamera (PENTAZET-ZL1-35) were set to take photos of saltating particles. Figs. 3.5a and 3.5b are two of the photos that were

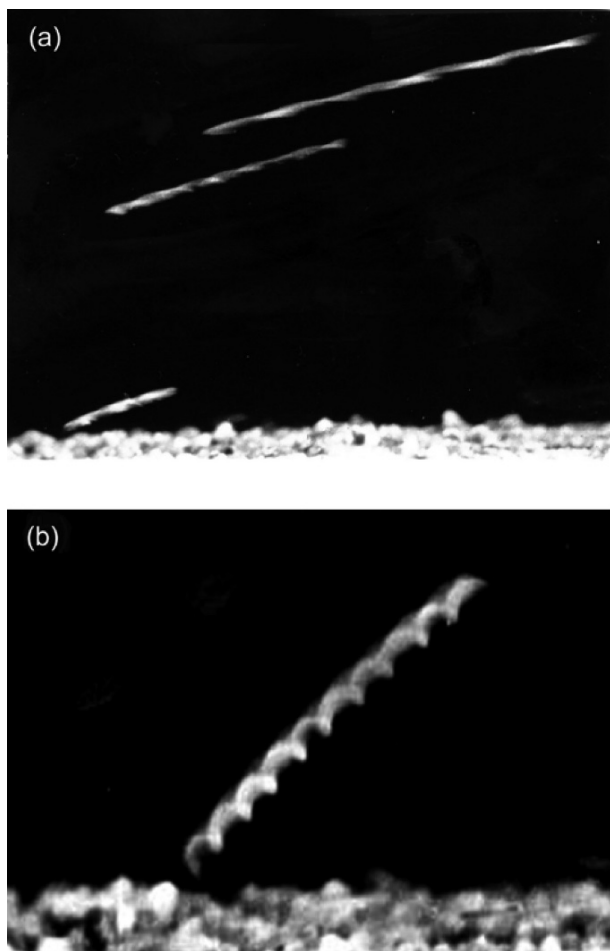


Fig. 3.5. Two basic spin patterns captured by dynamic cinecamera (a) in-plane spin, the rotation axis parallel with the linear velocity, and (b) out-plane spin, the rotation axis perpendicular to the linear velocity (from Xie et al. 2007)

taken by the dynamic cinecamera, in each of which a segment of trajectory of a saltating particle is captured. From the spiral shape of the trajectory in Fig. 3.5a, we can easily make out that the particle's spin axis is in the plane of the light sheet and verticle to the sand bed, and we name this spin pattern as an in-plane spin. The spin axis of the trajectory segment in Fig. 3.5b is vertical to the plane of the light sheet, which is named as out-plane spin. In general, the value and distribution of spin speed are different for the two kind of spin pattern, and in-plane spin is the major pattern.

Furthermore, from the photos captured by the dynamic cinecamera, we can easily recognize two kinds of in-plane spin, as shown in Fig. 3.6.

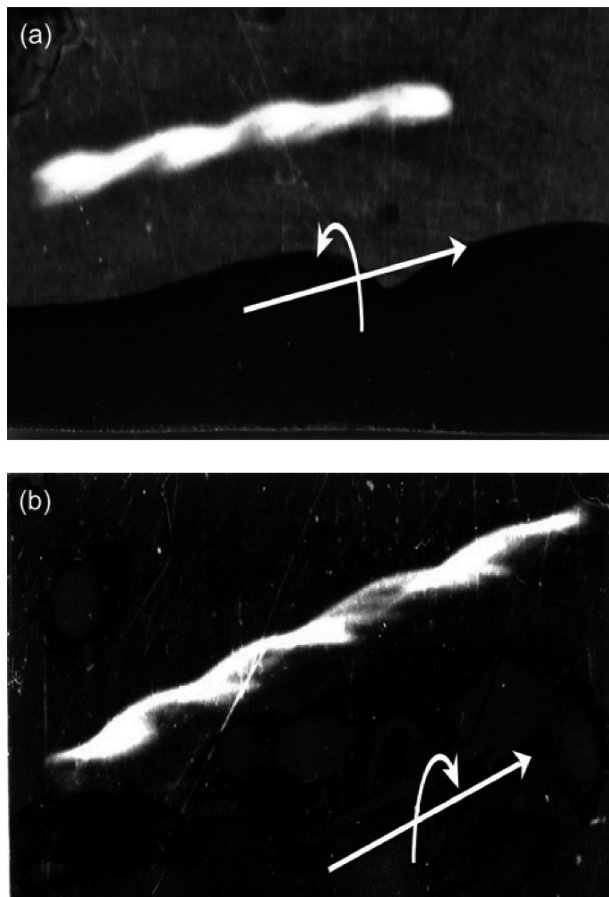
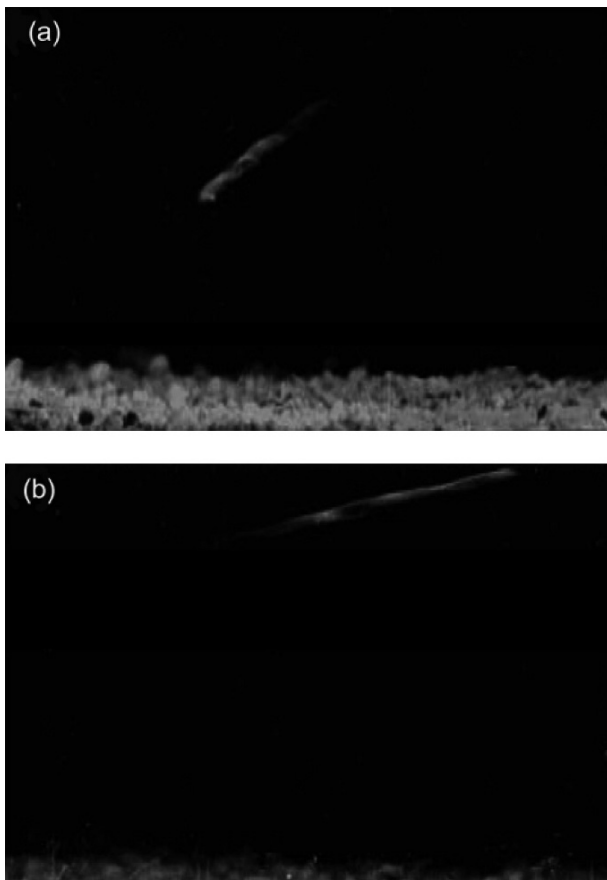


Fig. 3.6. Two patterns of in-plane spin. **(a)** left spin and **(b)** right spin, in which the straight arrows represent the translation directions of the sand particles and the curved arrows indicate the rotation directions (from Xie et al. 2007)

Table 3.1. Out-plane angular velocities at different stages of saltation trajectory

| Angular velocity [Rev·s ⁻¹] | Lift-off | Ascending flight | Descending flight | Impact |
|--|----------|------------------|-------------------|--------|
| Mean value | 344 | 348 | 254 | 167 |
| Maximum value | 896 | 1088 | 784 | 448 |
| Minimum value | 64 | 64 | 64 | 64 |

**Fig. 3.7.** Two unclear parts of saltation trajectories: **(a)** the tail is not clear and **(b)** the head is not clear, which maybe mean that the sand's trajectory is not in the light sheet (from Xie et al. 2007)

Keeping thumb pointing in the direction of movement, the direction of spin is left-handed in Fig. 3.6a and right-handed in Fig. 3.6b, which are left spin and right spin, respectively. The out-plane spin angular velocity ranges

from 0 to $1088 \text{ rev}\cdot\text{s}^{-1}$ and varies in its entire flight process, as shown in Table 3.1. It can be seen that sometimes the maximum value of out-plane rolling angular velocities may reach $1088 \text{ rev}\cdot\text{s}^{-1}$ and its minimum value as low as $64 \text{ rev}\cdot\text{s}^{-1}$, the angular velocity increases in the ascending flight of a sand particle and then decreases in its descending flight, and usually the impact angular velocity is lower than the lift-off angular velocity.

A very interesting result observed from the experimental photos is that some segments of trajectories are not clear, especially at the heads or the tails, as shown in Fig. 3.7. It is very possible that the segment is a part of a 3-D saltation trajectory. More studies are needed to verify whether the Magnus forces arising from spin make the sand particles' trajectories deviate from the 2-D plane.

3.3 Stochastic Model of Particle-Bed Collision

With the experimental method mentioned above, the lift-off velocities of sand particles and thus the probability density function of lift-off velocities can be obtained. However, there are some inherent limitations of the experimental measurement. For example, when the concentration of sand particles is very dense, the size of sand particles is too fine to be identified, or if the bed surface is very rough, the initial motion of the sand particles cannot be directly measured by experiment even with the most advanced equipment such as PIV or PDA. Besides, the accuracy of inverse calculation of the lift-off velocities through judging the position, motion or path of each particle in photographic images depends on the establishment and solution of the trajectory equations of sand motion. Therefore, modelling the particle-bed collision process from collision mechanics has intensified as an important tool to investigate the lift-off velocities of sand particles and to remedy the deficiency of experimental method. Here, we introduce a so-called stochastic particle-bed collision model which can further reflect the real particle-bed process compared with previous models.

3.3.1 Stochastic Model

For simplicity, we deal with the sand particles in the collision as two-dimensional (2-D) circular disks and an effective model of the real collision is given in Fig. 3.8 (Zheng et al. 2005, 2006). In order to describe this collision in Fig. 3.8, we take the representative particles *A* and *B* to indicate the descending particle and the creeping particle, respectively.

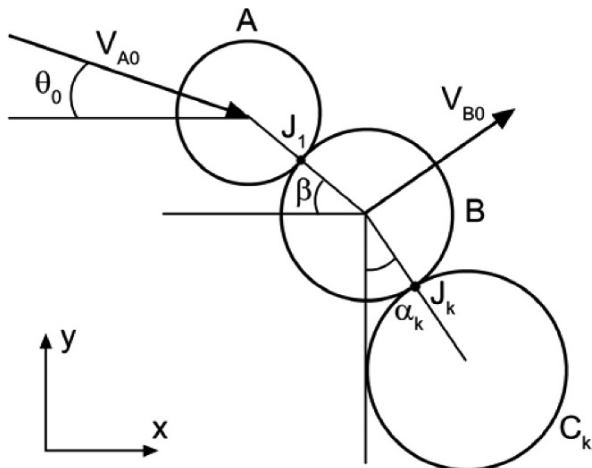


Fig. 3.8. Schematic drawing of the collision of descending particles with the sand bed at instant of the collision beginning. A and B are the descending particle and the creeping particle. V_{A0} and angle θ_0 are the incident velocity and incident angle. β is the impact angle and α_k is the contact angle. J_1 and J_k are the contact points between the incident sand and the creeping sand, and the creeping sand and sustain sand (from Zheng et al. 2005)

Assume that the particle A has an equivalent diameter of D_A , mass of m_A and descending velocity of magnitude V_{A0} and angle θ_0 from the horizontal, which collides with particle B . Particle B has an equivalent diameter of D_B , mass of m_B and velocity of V_{B0} . In contrast to previous particle-bed collision model (Werner 1988; Anderson and Haff 1991), we introduce an effective sand particle C_k , which has an equivalent diameter of D_k and mass of m_k , to reflect the resultant actions on the particle B by other k ($k = 1, 2, \dots$) sand particles on the sand bed. We denote the contact point between the particles A and B , and the particles B and C_k by J_1 and J_2 , respectively. In addition, we introduce two angle parameters called contact angle α_k and impact angle β to characterize the orientation of the lines connecting the centers of particles (see Fig. 3.8).

Another important difference between the stochastic particle-bed collision model and previous particle-bed collision model is to reflect the randomness of particle-bed collision processes, the diameter and mass of sand particle, the incident velocity V_{A0} , the creeping velocity V_{B0} , the incident angle θ_0 , the impact angle β as well as the contact angle α_k are all treated as random variables. In order to give the range of these random variables, it is necessary to analyze the probability distribution functions (PDFs) of these variables. According to the experimental observations of the particle-

bed collision process, the incident velocity V_{A0} , the creeping velocity V_{B0} and the impact angle β can be considered as independent variables. From observations using high speed cine-film, the sand particles on the sand bed are stationary or vibrate at a low speed of about $0\text{--}2.0 \text{ m}\cdot\text{s}^{-1}$ (Wu 1985) when the wind velocity approaches $18 \text{ m}\cdot\text{s}^{-1}$. Because the probabilities of sand particle moving downwind and upwind are equal, here a linear probability distribution function (PDF) is selected to approximate the PDF of creeping velocity, which is

$$f_{V_{B0}} = \begin{cases} -\frac{1}{4}V_{B0} + \frac{1}{2} & 0 \leq V_{B0} \leq 2.0 \\ \frac{1}{4}V_{B0} + \frac{1}{2} & -2.0 \leq V_{B0} \leq 0 \end{cases}. \quad (3.6)$$

From the experimental data measured by Dong et al. (2002), the probability density of the incident velocity approximately fits to the gamma density function

$$f_{V_{A0}} = \frac{1}{\Gamma(\lambda_1)} \lambda_2 (\lambda_2 V_{A0})^{\lambda_1-1} \exp(-\lambda_2 V_{A0}), \quad (3.7)$$

where $\lambda_1, \lambda_2 > 0$, $V_{A0} > 0$, and λ_1, λ_2 are the parameters determined by the mean value and the variance of experiment data (see Xie et al. 2005), $\Gamma(\cdot)$ is the gamma function. Based on the measurement results of Rumpel (1985), we assume $\theta_0 \leq \pi/2$, and the impact angle β is not greater than $(\theta_0 + \pi/2.0)$. In this case, the impact angle β lies in a range of $(\theta_0, \theta_0 + \pi/2.0)$. When $\theta_0 \leq \pi/2$, namely the collision happens in the lee side of particle B , we find that β lies in the range of $(\theta_0 - \pi/2.0, \theta_0)$ with similar reasoning. When the incident angle is given, the conditional PDF of the impact angle is expressed as

$$f_\beta(\beta | \theta_0) = \frac{2}{\pi}. \quad (3.8)$$

As far as the range of contact angle α_k is concerned, it is related to the pattern of sand particles in the sand bed, the incident velocity V_{A0} and the incident angle θ_0 . For simplicity, we suppose that the α_k be uniformly distributed in $(-\pi/2, \pi/2)$ although it is still worthy of further discussion. Then the probability distribution function of the contact angle is written as

$$f_{\alpha_k} = \frac{1}{\pi}. \quad (3.9)$$

After modeling the particle-bed collision process with the stochastic particle-bed collision model, we have to deal further with the collision between the particle A and B , so as to obtain the lift-off velocities of particles after collision. As we know, the collision problem has been widely studied in theoretical research and engineering application, however, the complexity of the collision process and the diversity of influencing factors make it still a significant field of mechanics (Nikolai et al. 2007; Belai et al. 2007). For the collision of two particles, several mechanical models have been put forward to simulate the collision process, which can be classified into the soft-particle approach and the hard-particle approach, depending on whether the deformation of the particle during the collision process is considered or not. Here, we briefly introduce the two approaches.

3.3.2 Soft-Particle Approach for Collision Process

The Discrete Element Method (DEM) was developed by Cundall and Stack (1979) and has been extended and applied in granular systems (Tsuji et al. 1993; Mikami et al. 1998). Werner and Haff (1988) introduced the DEM to simulate the particle-bed impacts in wind-blown sand flux. In the soft-particle approach, particle-particle interaction is usually modeled by using a spring, dash-pot and slider as shown in Fig. 3.9, in which the spring and dash-pot are employed to reflect the deformation and damping during contact, and slider is used to reflect the slip friction. If the diameter of one of the two particles is taken as infinity, then this model can be used to treat the collision between a particle and a wall. Here, we will only take the two-dimensional case to illustrate how to determine the lift-off velocities of sand particles after collisions in wind-blown sand flux by the soft-particle approach.

A rectangular coordinate system Oxz is established, with the x axis parallel to the wind flow direction and the z axis perpendicular to the bed surface and pointing upward. The neighboring particles in direct contact with particle B (x_B, z_B) during the collision process are j (x_j, z_j) ($j = 1, 2, \dots, N$). The forces acting on B include the gravitational force $\mathbf{F}_{gB} = m_B g$, the normal contact force \mathbf{F}_{pn}^{Bj} , the tangential friction force \mathbf{F}_{fi}^{Bj} , and the normal and tangential damping forces $\mathbf{F}_m^{Bj}, \mathbf{F}_{rt}^{Bj}$, which are respectively assumed to be proportional to both the normal and tangential displacements of particle j , and to the rate of change of the distance between centers of colliding particles. By resolving the above forces for the x and z axis, equations for the motion of particle B can be formulated as follow

$$\sum_j^N \left(\mathbf{F}_{pn}^{Bj} + \mathbf{F}_{ft}^{Bj} + \mathbf{F}_{rn}^{Bj} + \mathbf{F}_{rt}^{Bj} \right)_x = m_B \frac{d^2 x_B}{dt^2}, \quad (3.10)$$

$$\sum_j^N \left(\mathbf{F}_{pn}^{Bj} + \mathbf{F}_{ft}^{Bj} + \mathbf{F}_{rn}^{Bj} + \mathbf{F}_{rt}^{Bj} \right)_z - m_B g = m_B \frac{d^2 z_B}{dt^2}, \quad (3.11)$$

$$\sum_j^N \left[\mathbf{r}_{Bj} \times (\mathbf{F}_{ft}^{Bj} - \mathbf{F}_{rt}^{Bj}) \right] = I_B \frac{d\boldsymbol{\omega}_B}{dt}, \quad (3.12)$$

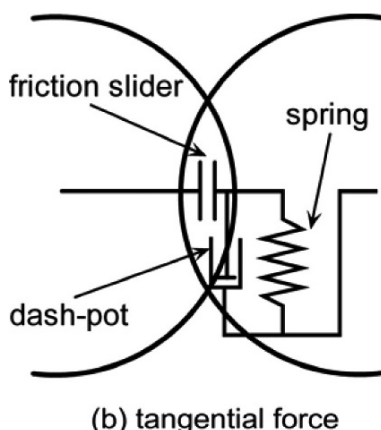
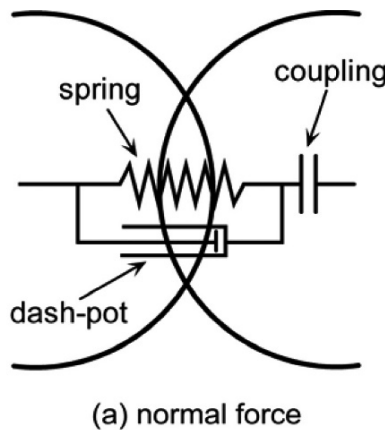


Fig. 3.9. Schematic view of the contact forces in the linear spring damping contact model, and (a) shows the normal force and (b) shows tangential force between two collision sand particle

The initial condition for particle B can be written as:

$$t = 0: x_B = x_{B0}, z_B = z_{B0}, \frac{dx_B}{dt} = V'_{B0x}, \frac{dz_B}{dt} = V'_{B0z}, \omega_B = 0. \quad (3.13)$$

Where I_B is the inertia moment of particle B about its center of mass, ω_B is the angular velocity, \mathbf{r}_{Bj} is a vector running from the centre of the particle B to the contact point of particle j , which can be derived from (x_B, z_B) and (x_j, z_j) , and $x_{B0}, z_{B0}, V'_{B0x}, V'_{B0z}$ are initial coordinates and velocity components of particle B . Through solving Eqs. 3.10–3.13, we can get the position (x_B, z_B) and the velocity components V_{Bx}, V_{Bz} of particle B after collision, and hence the lift-off velocity V_{B0x}, V_{B0z} of B .

3.3.3 Hard-Particle Approach for Collision Process

The hard-particle approach was first put forward by Alder and Wainwright (1957) to study the phase transition for hard-sphere systems, and was latter widely applied in granular dynamics, such as the simulation of a gas-solid two-phase flow in a two-dimensional (2-D) horizontal channel (Tsuiji et al. 1987), bubble and slug formation and segregation phenomena in gas-fluidized beds (Hoomans et al. 1996) and so on. In contrast to the soft-particle approach, in the hard-particle approach, particle-particle interaction is assumed to be a sequentially instantaneous two-body elastic collision without considering the deformation, overlap and collision forces of particles. Consequentially, according to the momentum conservation principle in the collision theory (Halliday et al. 1997; Chatterjee 1997), the linear and angular velocities of particles after collision can be deduced for given initial conditions.

Here, we still take the two-dimensional (2-D) case as an example. According to collision theory, a collision between two bodies can be split into two processes, compression and recovery. For particles A and B , the horizontal and vertical velocity components and the angular velocity of A and B in the compression and recovery process are respectively denoted by $V'_{Ax}, V'_{Az}, \omega'_A, V'_{Bx}, V'_{Bz}, \omega'_B, V_{Ax}, V_{Az}, \omega_A, V_{Bx}, V_{Bz}, \omega_B$. S'_n (S_n) and S'_τ (S_τ) stand for the impulse momentum of the interacting forces at the contact points during the compression (recovery) process, and subscripts τ and n represent the tangential and normal components of the impulse, respectively. S_1 (S'_1) and S_2 (S'_2) are the tangential and normal components of the impulse resulting from the action of the bed surface or effective particle C_k to particle B during compression (recovery) process. The impulse momentum and velocity components acting on particle A and B are shown in Fig. 3.10 (for simplicity, only the compression process is illustrated).

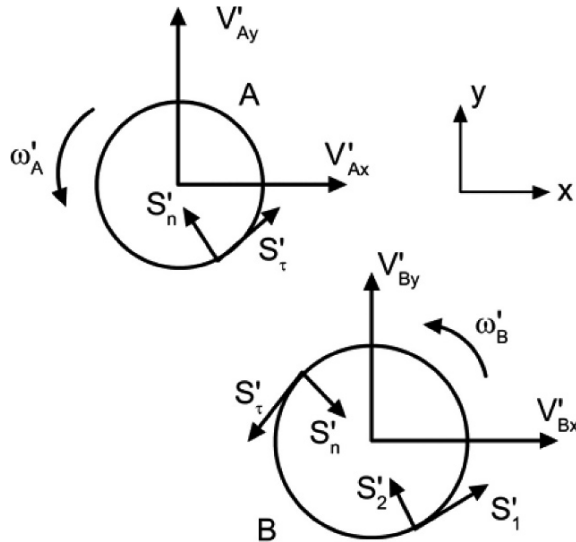


Fig. 3.10. Schematic drawing of the impulse momentum and velocity components of particle A and B ; V'_{Ax} , V'_{Ay} , ω'_A , V'_{Bx} , V'_{By} , ω'_B , S'_n and S'_τ stand for the linear velocity components, angular velocity components and impulse momentum of interact forces at contact points during compression reaching up its maximum

Therefore, the equations for the compression and recovery process of particles A and B are written as follows:

$$S'_\tau = m_A [V'_{Ax} \sin \beta + V'_{Ay} \cos \beta - V_{A0} \sin(\beta - \theta_0)], \quad (3.14a)$$

$$S'_n = m_A [V'_{Ay} \sin \beta - V'_{Ax} \cos \beta + V_{A0} \cos(\beta - \theta_0)], \quad (3.14b)$$

$$S'_\tau D_A = \frac{1}{4} m_A \omega'_A D_A^2, \quad (3.14c)$$

$$S'_1 \cos \alpha_k - S'_2 \sin \alpha_k + S'_n \cos \beta - S'_\tau \sin \beta = m_B (V'_{Bx} - V_{B0} \cos \alpha_k), \quad (3.15a)$$

$$S'_1 \sin \alpha_k + S'_2 \cos \alpha_k - S'_n \sin \beta - S'_\tau \cos \beta = m_B (V'_{By} - V_{B0} \sin \alpha_k), \quad (3.15b)$$

$$(S'_1 + S'_\tau) D_B = \frac{1}{4} m_B \omega'_B D_B^2, \quad (3.15c)$$

$$S_\tau = m_A \left[V_{Ax} \sin \beta + V_{Az} \cos \beta - V_{A0} \sin(\beta - \theta_0) \right], \quad (3.16a)$$

$$S_n = m_A \left[V_{Az} \sin \beta - V_{Ax} \cos \beta + V_{A0} \cos(\beta - \theta_0) \right], \quad (3.16b)$$

$$S_\tau D_A = \frac{1}{4} m_A \omega_A D_A^2, \quad (3.16c)$$

$$S_1 \cos \alpha_k - S_2 \sin \alpha_k + S_n \cos \beta - S_\tau \sin \beta = m_B (V_{Bx} - V_{B0} \cos \alpha_k), \quad (3.17a)$$

$$S_1 \sin \alpha_k + S_2 \cos \alpha_k - S_n \sin \beta - S_\tau \cos \beta = m_B (V_{Bz} - V_{B0} \sin \alpha_k), \quad (3.17b)$$

$$(S_1 + S_\tau) D_B = \frac{1}{4} m_B \omega_B D_B^2. \quad (3.17c)$$

Obviously, Eqs. 3.14–3.17, as a system of only 12 equations but containing 20 variables, is not closed. Therefore, some additional equations are required to solve them. Firstly, considering the joint conditions of contact points J_1 and J_2 , we get the following equations:

$$V'_{Ax} \cos \beta - V'_{Az} \sin \beta = V'_{Bx} \cos \beta - V'_{Bz} \sin \beta, \quad (3.18a)$$

$$\frac{1}{2} \omega'_A D_A + V'_{Ax} \sin \beta + V'_{Az} \cos \beta = -\frac{1}{2} \omega'_B D_B + V'_{Bx} \sin \beta + V'_{Bz} \cos \beta, \quad (3.18b)$$

$$V'_{Bz} \cos \alpha_k - V'_{Bx} \sin \alpha_k = 0, \quad (3.18c)$$

$$\omega'_B D_B / 2 + V'_{Bx} \cos \alpha_k + V'_{By} \sin \alpha_k = 0, \quad (3.18d)$$

Then, from collision theory, there is some loss of energy in the collision process, which is mainly dependent on the restitution coefficients that are related to the normal and tangential relative velocities between two contact bodies. Denoting the normal and tangential restitution coefficients by k_1 and k_2 , respectively and Applying the definition of restitution coefficient to the collision considered here, we have the following relations:

$$k_1 = \frac{V_{Az} \sin \beta - V_{Ax} \cos \beta - (V'_{Az} \sin \beta - V'_{Ax} \cos \beta)}{V'_{Az} \sin \beta - V'_{Ax} \cos \beta + V_{A0} \cos(\beta - \theta_0)}, \quad (3.19a)$$

$$k_2 = \frac{2(V_{Az} \cos \beta + V_{Ax} \sin \beta - V'_{Az} \cos \beta - V'_{Ax} \sin \beta) + D_A (\omega_A - \omega'_A)}{2(V'_{Az} \cos \beta + V'_{Ax} \sin \beta) - 2V_{A0} \sin(\beta - \theta_0) + \omega'_A D_A}, \quad (3.19b)$$

Afterwards, the linear and angular velocities of particles A and B can be deduced from Eqs. 3.14–3.19 for a given diameter and mass of particle A and B , e.g., incident velocity V_{A0} , creeping velocity V_{B0} , incident angle θ_0 , impact angle β , contact angle α_k and normal and tangential restitution coefficients k_1 and k_2 . It's notable that a significant advantage of these basic equations derived from the hard-particle approach is to incorporate the action of the bed surface to the particle being impacted, which essentially results from the character of the stochastic particle-bed collision model mentioned in Sect. 3.3.1.

3.3.4 Analytical Solution of Lift-off Velocity

Taking the assumption $k_1 = k_2 = k_{12}$ in the following discussion for simplicity (readers can refer to Francōis et al. (2000) and Namikas (2006) for more discussions on the restitution coefficient), the unknown variables of interest V_{Ax} , V_{Az} , V_{Bx} , V_{Bz} , ω_A and ω_B in Eqs. 3.14–3.19 proposed in Sect. 3.3.4 can be analytically solved in terms of the parameters α_k , β , V_{A0} , V_{B0} , θ_0 , D_A , D_B , and k_{12} . Here, we list the solutions of the ejected and rebound velocities of sand particles with the help of Matlab:

$$\begin{aligned} V_{Ax} = & \{(\cos \alpha_k + \sin \beta)[\sin(\beta - \theta_0) + \cos(\alpha_k + \theta_0) + 2\cos(\alpha_k + \beta)\cos(\beta - \theta_0)] \\ & 2D_A^3(1+k_{12})/D_B^3 - (1+k_{12})[1+\sin(\alpha_k + \beta)][\cos(\alpha_k + \theta_0) - \sin(\beta - \theta_0)]\sin \beta \\ & 4D_A^3/D_B^3 + 6(1+k_{12})\sin(\beta - \theta_0)\sin \beta\}V_{A0}/\{[1+\sin(\alpha_k + \beta)][2-\sin(\alpha_k + \beta)]\}, \quad (3.20) \\ & 4D_A^3/D_B^3 + 9\} - k_{12}V_{A0}\cos \theta_0 + 2[3\cos \alpha_k + \sin \beta - 2\sin \beta \sin(\alpha_k + \beta)]V_{B0} \\ & (1+k_{12})/\{[1+\sin(\alpha_k + \beta)][2-\sin(\alpha_k + \beta)]4D_A^3/D_B^3 + 9\} \end{aligned}$$

$$\begin{aligned} V_{Az} = & \{(\sin \alpha_k + \cos \beta)[\sin(\beta - \theta_0) + \cos(\alpha_k + \theta_0) + 2\cos(\alpha_k + \beta)\cos(\beta - \theta_0)] \\ & 2D_A^3(1+k_{12})/D_B^3 - (1+k_{12})[1+\sin(\alpha_k + \beta)][\cos(\alpha_k + \theta_0) - \sin(\beta - \theta_0)]\cos \beta \\ & 4D_A^3/D_B^3 + 6(1+k_{12})\sin(\beta - \theta_0)\cos \beta\}V_{A0}/\{[1+\sin(\alpha_k + \beta)][2-\sin(\alpha_k + \beta)]\}, \quad (3.21) \\ & 4D_B^3/D_B^3 + 9\} + k_{12}V_{A0}\sin \theta_0 + (1+k_{12})[3\sin \alpha_k + \cos \beta - 2\cos \beta \sin(\alpha_k + \beta)] \\ & 2V_{B0}/\{[1+\sin(\alpha_k + \beta)][2-\sin(\alpha_k + \beta)]4D_A^3/D_B^3 + 9\} \end{aligned}$$

$$\begin{aligned} V_{Bx} = & \cos \alpha_k [\sin(\beta - \theta_0) + \cos(\alpha_k + \theta_0) + 2 \cos(\alpha_k + \beta) \cos(\beta - \theta_0)] \\ & 2D_B^3(1+k_{12})V_{A0}/\{9D_B^3+4D_A^3[1+\sin(\alpha_k+\beta)][2-\sin(\alpha_k+\beta)]\}+ \\ & 6(1+k_{12})V_{B0}\cos\alpha_k/\{9+4D_A^3[1+\sin(\alpha_k+\beta)][2-\sin(\alpha_k+\beta)]/D_B^3\}, \\ & -k_{12}V_{B0}\cos\alpha_k \end{aligned} \quad (3.22)$$

$$\begin{aligned} V_{Bz} = & \sin \alpha_k [\sin(\beta - \theta_0) + \cos(\alpha_k + \theta_0) + 2 \cos(\alpha_k + \beta) \cos(\beta - \theta_0)] \\ & 2D_A^3(1+k_{12})V_{A0}/\{9D_B^3+4D_A^3[1+\sin(\alpha_k+\beta)][2-\sin(\alpha_k+\beta)]\}+ \\ & 6(1+k_{12})V_{B0}\sin\alpha_k/\{9+4D_A^3[1+\sin(\alpha_k+\beta)][2-\sin(\alpha_k+\beta)]/D_B^3\}, \\ & -k_{12}V_{B0}\sin\alpha_k \end{aligned} \quad (3.23)$$

$$\begin{aligned} \omega_A = & 4D_A^2\{[1+\sin(\alpha_k+\beta)][\cos(\alpha_k+\theta_0)-\sin(\beta-\theta_0)]-3\sin(\beta-\theta_0)\} \\ & 2(1+k_{12})V_{A0}/\{9D_B^3+4D_A^3[1+\sin(\alpha_k+\beta)][2-\sin(\alpha_k+\beta)]\} \\ & +8(1+k_{12})[1+\sin(\alpha_k+\beta)]V_{B0}/\{9D_A+4D_A^4[1+\sin(\alpha_k+\beta)] \\ & [2-\sin(\alpha_k+\beta)]/D_B^3\} \end{aligned} \quad (3.24)$$

$$\begin{aligned} \omega_B = & -[\sin(\beta - \theta_0) + \cos(\alpha_k + \theta_0) + 2 \cos(\alpha_k + \beta) \cos(\beta - \theta_0)] \\ & 4(1+k_{12})V_{A0}/\{9D_B+4D_A^3[1+\sin(\alpha_k+\beta)][2-\sin(\alpha_k+\beta)]\} \\ & /D_B^2\}-12(1+k_{12})V_{B0}/\{9D_B+4D_A^3[1+\sin(\alpha_k+\beta)] \\ & [2-\sin(\alpha_k+\beta)]/D_B^2\} \end{aligned} \quad (3.25)$$

If the direction of wind flow and incident velocity lie in different planes, it is necessary to establish a three-dimensional (3-D) stochastic particle-bed collision model to describe the lateral component of lift-off velocities. Through solving the equations of a 3-D model, Zheng et al. (2008) deduced not only horizontal and vertical components of lift-off velocities, with the angular velocity rotating around the x axis (named rolling angular velocity), but also the lateral velocity, the lateral angular velocity rotating around the y axis and the upward angular velocity rotating around the z axis. Their results show that the resultant of lateral and rolling angular velocities, namely the left/right angular velocities are typically in the region of 200–300 rev·s⁻¹ and the maximum value can reach up to about 1000 rev·s⁻¹, which agree well with the experimental results (Xie et al. 2007). Compared with the results of the 2-D model, it can be found that all components of both the rebound and the ejected velocities obtained by the 3-D model except the horizontal rebound velocity are lower than the corresponding ones from the 2-D model, and the differences increase with impact velocity. When the impact velocity is higher than 1.5 m·s⁻¹, the lateral

velocity is comparable with the vertical one and the lateral and upward angular velocities reach up to several revolutions per second and thus all of them cannot be ignored. Therefore, it is necessary to employ a 3-D particle-bed collision model to calculate the lift-off velocities in wind-blown sand flux.

3.4 Probability Distribution of Lift-off Velocities

The statistical distribution of velocities at which sand particles of different diameters leave the bed surface, is called the probability distribution of lift-off velocities. It describes the range of saltating particles' lift-off velocities and the probability of a sand particle rising from the bed surface with a certain velocity in wind-blown sand movement. In the theoretical prediction of wind-blown sand flux, the form of splash function and distribution of particles' lift-off velocities serve as an initial condition and significant quantities connecting the behavior of a single particle and that of wind-blown sand flux, so they have become key issues in the subject of wind-blown sand movement, especially after the International Conference on Aeolian Research hold in Aarhus, Denmark, 1986.

Common statistical methods include the orthogonal array method, the sampling test method, the histogram method, and the histogram method is the most widely applied method. Here, the equal distance histogram method is employed to calculate the probability distribution of lift-off velocities. First, all experiment data are collected as a sample space, and the region of velocities is equally divided into several subregions, then by calculating the number of velocities in each subregion, we can get the probability distribution of lift-off velocities. For example, experiments by Xie et al. (2007) show that the left/right spin angular velocities of sand particles range from 0 to $850 \text{ rev}\cdot\text{s}^{-1}$, so the region $(0 \text{ rev}\cdot\text{s}^{-1}, 850 \text{ rev}\cdot\text{s}^{-1})$ is divided into 8 subregions with equal interval $100 \text{ rev}\cdot\text{s}^{-1}$. By calculating the number of angular velocities in each subregion, we can get the probability distribution of left/right angular velocities shown in Fig. 3.11. Since the distributions of left and right angular velocities have the same form, we only give the distribution of left angular velocity. From Fig. 3.11, we can find that the distributions of both the left and right spin angular velocities are single-peaked and skewed, and most of the angular velocities are distributed in the region $(150 \text{ rev}\cdot\text{s}^{-1}, 250 \text{ rev}\cdot\text{s}^{-1})$.

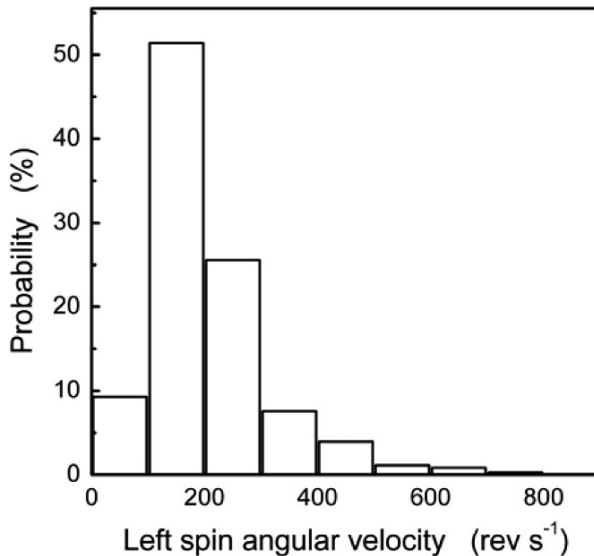


Fig. 3.11. Probability distribution of left angular velocities, analyzed by the equal distance histogram method on the basis of 1335 clear segments of saltation trajectories (from Xie et al. 2007)

Through the normalization method, that is, dividing the probability of each subregion by its interval, we can get the probability density distributions (PDFs) of lift-off velocities or angular velocities. With the aid of the theory of hypothesis testing (DeGroot and Schervish 2002), the corresponding PDFs can be determined.

For example, based on a wind tunnel experiment with Phase Doppler Anemometry (PDA), Xie et al. (2005) obtained the probability density function of lift-off velocities through a χ^2 -test. They found it follows a Gamma function (Table 3.2). More existing probability density functions of lift-off velocity and its vertical component are listed in Table 3.2 and illustrated in Fig. 3.12, respectively. It can be found that there exist large discrepancies among the existing PDFs of lift-off velocities both in quality and quantity, which may result from the limitations of the experimental measurement.

Here, with the aid of the probability theory of multi-random variables (Bickel and Doksum 1977), we present a theoretical prediction of the PDF of lift-off velocities based on the analytical solutions of rebound and ejected velocities given in Eqs. 3.20–3.25. For simplicity, only the two-dimensional ‘uniform’ case is illustrated.

Table 3.2. Several forms of existing PDFs of lift-off velocities

| Authors (in publishing date) | Probability density function of lift-off velocities | Remark |
|---------------------------------|---|--|
| Anderson and Hallet (1986) | $f(V) = \frac{1}{0.63u_*} \exp\left(-\frac{V}{0.63u_*}\right)$ | u_* represents the friction wind velocity |
| Nalpanis et al. (1993) | $f(V) = \frac{(3V)^3 \exp\left(-\frac{3V}{0.96u_*}\right)}{2(0.96u_*)^4}$ | μ_V, σ_V^2 represent the mean and variance of lift-off velocities respectively |
| Zhu et al. (2001) | $f(V) = \frac{\exp\left(-\frac{V^2}{2A}\right)}{\sqrt{2\pi C}}$ | A, C is parameters |
| Zou et al. (2001) | $f(V) = a + \frac{b}{1 + 4 \frac{(H-c)^2}{d^2(2^{1/e}-1)^e}}$ | H is the height from sand surface; a, b, c, d, e are parameters varying with the height |
| Xie et al. (2005) | $f(V) = \frac{\lambda_1^{\lambda_2} V^{(\lambda_2-1)} \exp(-\lambda_1 V)}{\Gamma(\lambda_2)}$ | λ_1, λ_2 are parameters determined by the mean value and the variance of experiment data |

Let X_1, X_2, \dots, X_n be real random variables, $Y = Y(X_1, X_2, \dots, X_n)$ be a real function, and $Z = [Y, X_2, \dots, X_n]^T$ is a real transform from n-dimensional realspace \Re^n to \Re^n . If Z satisfies the following conditions: (a) all first order partial differentials of Z are continuous in $\mathcal{B} \subseteq \Re^n$; (b) the transform between Z and X is a one-to-one mapping in $\mathcal{B} \subseteq \Re^n$ and (c) the Jacobian determinant $J_Z(\mathbf{X})$ is always not zero, then we can write the PDF $f_Y(Y)$ of random variable Y as follow:

$$f_Y(Y) = \int \cdots \int f_Z(Z) dX_2 dX_3 \cdots dX_n = \int \cdots \int f_X(\mathbf{X}) \left| \frac{1}{J_Z(\mathbf{X})} \right| d\mathbf{X}, \quad (3.26)$$

in which $\mathbf{X} = [X_1, X_2, \dots, X_n]^T$ and $\int_Z |f(\mathbf{X})| d\mathbf{X} < \infty$. Denoting $Y = V$ (V is taken as any component of lift-off velocity), $X_1 = V_A$, $X_2 = \alpha_k$, $X_3 = \beta$, $X_4 = \theta_0$ and $X_5 = V_B$ and employing the probability density distribution

given by Eqs. 3.6–3.9, the probability density of lift-off velocities can be derived from Eq. 3.26, that is:

$$f_{V_{Ax}} = \iiint \frac{f_{V_{A0}} f_{\theta_0} f_{V_{B0}} \left| 9 + \frac{4D_A^3}{D_B^3} [1 + \sin(\alpha_k + \beta)] [2 - \sin(\alpha_k + \beta)] \right|}{(1+k_{12})\pi^2 |3\cos\alpha_k + \sin\beta - 2\sin\beta\sin(\alpha_k + \beta)|} d\theta_0 d\beta d\alpha_k dV_{A0}, \quad (3.27)$$

$$f_{V_{Az}} = \iiint \frac{f_{V_{A0}} f_{\theta_0} f_{V_{B0}} \left| 9 + \frac{4D_A^3}{D_B^3} [1 + \sin(\alpha_k + \beta)] [2 - \sin(\alpha_k + \beta)] \right|}{(1+k_{12})\pi^2 |3\sin\alpha_k + \cos\beta - 2\cos\beta\sin(\alpha_k + \beta)|} d\theta_0 d\beta d\alpha_k dV_{A0}, \quad (3.28)$$

$$f_{V_{Bx}} = \iiint \frac{2f_{V_{A0}} f_{\theta_0} f_{V_{B0}} \left| 9 + \frac{4D_A^3}{D_B^3} [1 + \sin(\alpha_k + \beta)] [2 - \sin(\alpha_k + \beta)] \right|}{\pi^2 \left| 6 - 3k_{12} - \frac{4k_{12}D_A^3}{D_B^3} [1 + \sin(\alpha_k + \beta)] [2 - \sin(\alpha_k + \beta)] \right| |\cos\alpha_k|} d\theta_0 d\beta d\alpha_k dV_{A0}, \quad (3.29)$$

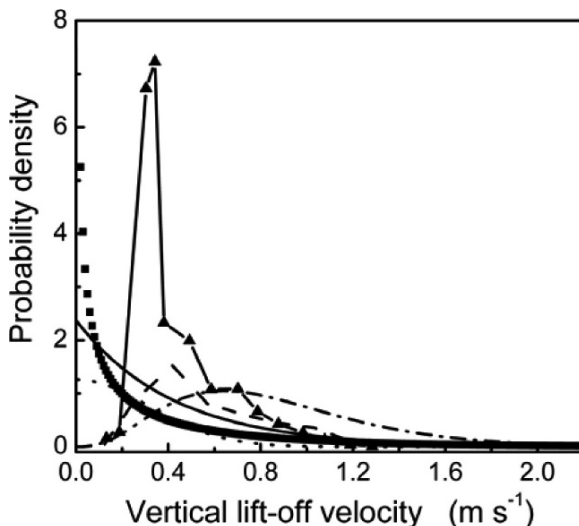


Fig. 3.12. Probability density function (PDF) of vertical lift-off velocities with shear wind velocity $u_* = 0.68 \text{ m}\cdot\text{s}^{-1}$. —— the measured results presented by Nalpanis et al. (1993), —▲— the measured results presented by Zou et al. (2001), ■ the theoretical results presented by Xie et al. (2005), the theoretical results presented by Zhu et al. (2001), ——— the exponent curve fitted by Anderson and Hallet (1986), -·-·- the Gamma curve fitted by Anderson and Hallet (1986)

$$f_{V_B} = \iiint \frac{2 f_{V_{A0}} f_{\theta_0} f_{V_{B0}} \left| 9 + \frac{4D_A^3}{D_B^3} [1 + \sin(\alpha_k + \beta)] [2 - \sin(\alpha_k + \beta)] \right|}{\pi^2 \left| 6 - 3k_{12} - \frac{4k_{12} D_A^3}{D_B^3} [1 + \sin(\alpha_k + \beta)] [2 - \sin(\alpha_k + \beta)] \right| \sin \alpha_k} d\theta_0 d\beta d\alpha_k dV_{A0}, \quad (3.30)$$

$$f_{\omega_4} = \iiint \frac{D_A f_{V_{A0}} f_{\theta_0} f_{V_{B0}} \left| 9 + \frac{4D_A^3}{D_B^3} [1 + \sin(\alpha_k + \beta)] [2 - \sin(\alpha_k + \beta)] \right|}{4(1 + k_{12}) [1 + \sin(\alpha_k + \beta)]} d\beta d\theta_0 d\alpha_k dV_{A0}, \quad (3.31)$$

$$f_{\omega_B} = \iiint \frac{D_B f_{V_{A0}} f_{\theta_0} f_{V_{B0}} \left| 9 + \frac{4D_A^3}{D_B^3} [1 + \sin(\alpha_k + \beta)] [2 - \sin(\alpha_k + \beta)] \right|}{6(1 + k_{12})} d\beta d\theta_0 d\alpha_k dV_{A0}. \quad (3.32)$$

It is notable that from Eqs. 3.20–3.23, we can deduce the expression of creeping velocity V_{B0} and its corresponding components in terms of incident velocity V_{A0} , the incident angle θ_0 , the impact angle β , and the contact angle α_k . Therefore, the expressions 3.27–3.32 do not integrate with V_{B0} .

Besides, using a numerical integration method, such as the Gaussian integration of 4 nodes, the rebound and ejected velocities for a given diameter of sand particle and wind velocity can be obtained. Taking the velocities with positive vertical component as sample space, we can get the corresponding probability density function (PDF). Fig. 3.13 gives the probability density distribution of horizontal and vertical lift-off velocities, and Fig. 3.14 gives the probability density distribution of angular velocities when the wind velocity is $8 \text{ m}\cdot\text{s}^{-1}$ and the diameter of sand particle is 0.35 mm.

It can be seen that the horizontal lift-off velocities follow a unimodal distribution, the vertical lift-off velocities follow a negative exponential distribution and the angular velocities follow an asymmetrical unimodal distribution. In addition, the range of rebound velocities is wider than that of ejected velocities, rebound angular velocities follow a Gumble distribution and ejected angular velocities follow a Gaussian distribution. Furthermore, wind velocity and the diameter of the sand particle affect the distributions of lift-off and angular velocities but do not change their type.

In practice, the lift-off sand particles include rebound and ejected ones, and the measured PDFs of lift-off velocities are of total lift-off particles including both rebound and ejected ones and are, however, difficult to identify by present experiments in a wind-blown sand flux. In order to get them from the theoretical predictions of these cases, we use the notations N_r , N_e and N_s represent the numbers of rebound, ejected and total lift-off

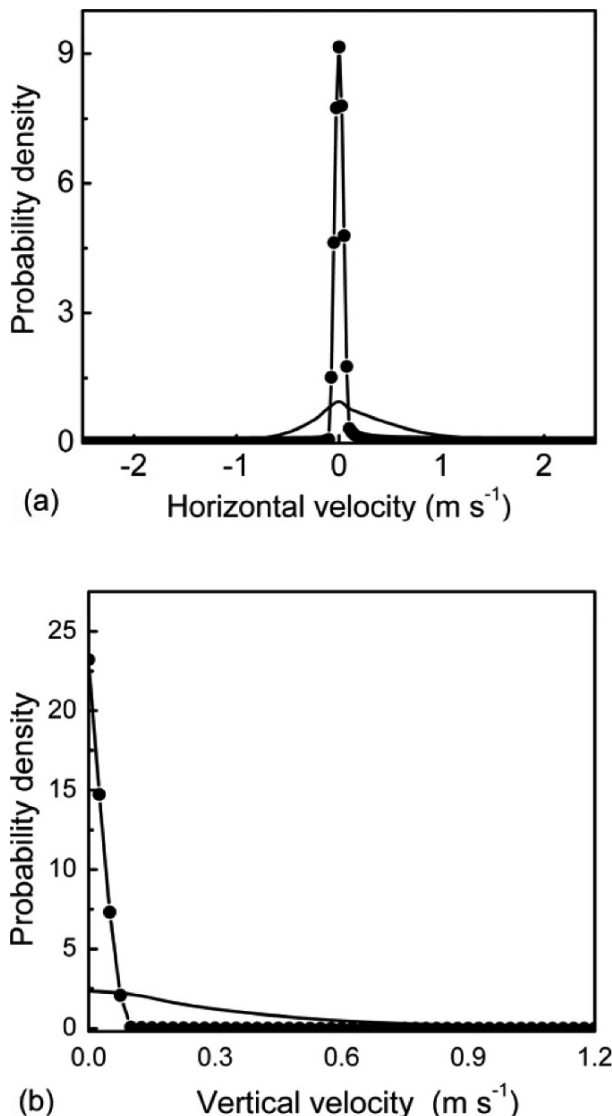


Fig. 3.13. The probability density distribution of (a) horizontal velocity and (b) vertical velocity of rebound and ejected sand particles when the wind velocity is $8 \text{ m}\cdot\text{s}^{-1}$ and the diameter of sand particle is 0.35 mm ; — the rebound components, —●— the ejected components (Zheng et al. 2005)

sand particles per unit area per unit time, respectively. They satisfy $N_s = N_r + N_e$. Denote $a_r = N_r / N_s$ and $a_e = N_e / N_s$, it is obviously that a_r and a_e stand for the fractions of rebound and ejected sand particles respec-

tively, and $a_r + a_e = 1$. Then we can write the PDF of lift-off velocities of total lift-off sand particles as follows:

$$f(V) = \lim_{\Delta V \rightarrow 0} \frac{N_r \int_V^{V+\Delta V} f^{(r)}(V) dV + N_e \int_V^{V+\Delta V} f^{(e)}(V) dV}{N_s \Delta V}, \quad (3.33)$$

$$= a_r f^{(r)}(V) + a_e f^{(e)}(V)$$

where ΔV is the interval of velocity subregion, and the recommended values for a_r and a_e are listed in Table 3.3 for different wind velocities and diameters of sand particle. A comparison between predictions made by the stochastic particle-bed collision model and experimental data on the PDF of vertical component is shown in Fig. 3.15. It can be seen that the results of the stochastic particle-bed collision model agree with the experimental data made by Dong et al. (2002), and are better than the results given by the other functions listed in Table 3.2, which verifies the reliability of the stochastic particle-bed collision model to some extent.

In addition, some researchers attempted to investigate the PDF of lift-off velocities through combining the traditional experimental measurements with theoretical predictions of sand flux and wind velocity profile (Huang et al. 2006). They first gave an initial PDF with several undetermined

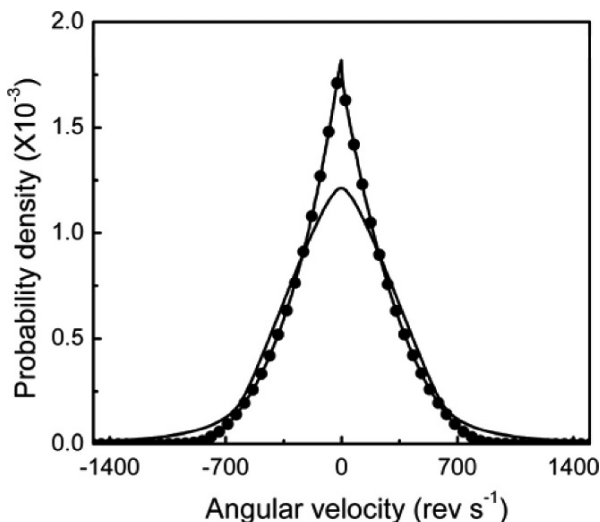


Fig. 3.14. The probability density distribution of rebound and ejected angular velocity when the wind velocity is $8 \text{ m}\cdot\text{s}^{-1}$ and the diameter of sand particle is 0.35 mm ; — the rebound components, —●— the ejected components (Zheng et al. 2006)

parameters, and numerically calculated the sand transport rate using the model of wind-blown sand movement (see Chap. 5), and then by adjusting the values of the pending parameters made all numerical results could be close to the experimental results, finally an optimization PDF could be obtained using an optimization method, such as the penalty function method. They obtained an exponential density function for vertical lift-off velocities of sand particles with respect to shear velocity.

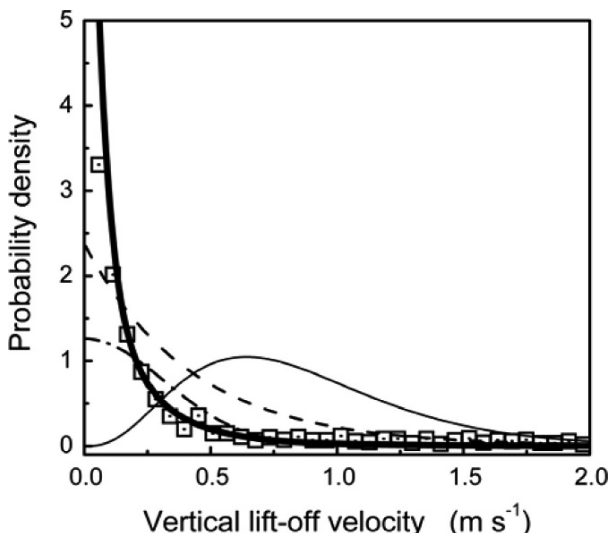


Fig. 3.15. Comparison of predictions and experimental data of the PDF of vertical component with $a_r = 0.87$ and $a_e = 0.13$. \square experimental results (Dong et al. 2002), — theoretical results (Zheng et al 2005), — Gamma function, - - exponent function and (Anderson and Hallet 1986) - · - Gauss function (Zhu et al. 2001)

Table 3.3. The values of a_r and a_e for different wind velocities and diameters of sand particles

| Wind velocity [$m \cdot s^{-1}$] | Diameter [mm] | a_r | a_e | Wind velocity [$m \cdot s^{-1}$] | Diameter [mm] | a_r | a_e |
|---------------------------------------|------------------|-------|-------|---------------------------------------|------------------|-------|-------|
| 8.0 | 0.25 | 0.93 | 0.07 | 12.0 | 0.35 | 0.94 | 0.06 |
| 10.0 | 0.25 | 0.93 | 0.07 | 14.0 | 0.35 | 0.945 | 0.055 |
| 12.0 | 0.25 | 0.94 | 0.06 | 8.0 | 0.45 | 0.84 | 0.16 |
| 14.0 | 0.25 | 0.955 | 0.045 | 10.0 | 0.45 | 0.96 | 0.04 |
| 8.0 | 0.35 | 0.87 | 0.13 | 12.0 | 0.45 | 0.94 | 0.06 |
| 10.0 | 0.35 | 0.9 | 0.1 | 14.0 | 0.45 | 0.92 | 0.08 |

The probability density functions of lift-off velocities discussed and presented in this section are all for steady wind fields. If the wind field is fluctuating, we can extend the above results by adjusting the friction wind velocities in Table 3.3 to instantaneous fluctuating values.

3.5 Splash Function

The splash function is an expression of the particle-bed collision process, which describes the mean number of sand particles (including rebound and ejected ones) rising from the bed surface subsequent to a single impact of a sand particle for a given velocity and particle diameter. It directly reflects the characteristics of momentum, energy and mass exchange between the incident particle and the bed surface and serves as a bridge crossing the microscopic behavior of a single particle to the macroscopic wind-blown sand movement. Existing splash functions have two basic types. One is to present the mean number of sand particles jumping from the bed per impact for a given impact velocity V_{im} and impact diameter D_{im} , namely the integral-type splash function $\bar{N}_{ej}(V_{im}, D_{im})$, the other is to give out the rebound probability $N_r(V_j, V_{im}, D_{im})$ and the number of ejected particles $N_e(V_j, V_{im}, D_{im})$ leaving the bed in velocity bin V_j with a given V_{im} and D_{im} , namely the discrete-type splash function. As we introduced in Sect. 3.2, a general description of the collision process and the splash function can be obtained on the basis of direct observation. However, because of the dense concentration within the layer under 0.5 cm height, only those distinguishable and slow-moving particles can be identified. Therefore, the observation results cannot draw a comprehensive understanding of the particle-bed collision process. In order to remedy these limitations, some researchers attempt to simulate the whole particle-bed collision process with the aid of computer simulation, which can accurately monitor the motion of every sand particle, and hence reflect the character of particle-bed collision in quality and reveal the splash function and the PDF of lift-off velocities in quantity. Here, we briefly introduce the results of splash functions through the DEM simulation for ‘uniform’ sands and ‘mixed’ sands.

3.5.1 Splash Function for ‘Uniform’ Sands

Werner and Haff (1988) made two-dimensional simulations for ordered packing of beads using a discrete element method. The particle-bed collisions were simulated by propelling a single particle into a bed of 384 circular particles with diameter of 1 cm. The interaction forces between parti-

cles have been modeled as follows. The normal force is described as a stiff damped oscillator and the shear force as well, except that it is limited by the usual friction force. In particular, he was able to extract a law for the normal restitution coefficient for the impacting bead e_z , which is independent from the impacting speed. He also found that the ejected particles acquired roughly 1–20% of the incident velocity, and established an integral-type splash function as a function of the incident angle θ_{im} and incident speed V_{im} :

$$\bar{N}_{ej}(\theta_{im}, V_{im}) = 3.36(0.572V_{im} - 0.915)\sin \theta_{im} \quad (3.34)$$

where \bar{N}_{ej} is the mean number of ejected particles.

Anderson and Haff (1988) performed two-dimension simulations of single-grain impacts into a granular bed with 87 identical slightly inelastic, 1 mm-diameter grains to evaluate the splash process quantitatively. Interactions between grains were characterized by a coefficient of restitution, an inter-grain friction coefficient, and an elastic modulus. The simulations were performed by dropping 8 particles with random initial velocities into a box with periodic boundaries, whose width was chosen such that the resulting bed was about ten grains deep. Three such granular beds with different packing configurations were used and each of them was impacted 20 times to develop the splash statistics for each impact angle and speed. The results showed that the mean rebound speed is approximately 50% to 60% of the impact velocity, and the mean rebound angle is 30° to 40° from the horizontal. The mean speed of the ejected particles appears to saturate at 9%–10% of the speed of the impacting grain, and the mean ejection angle tends to oriented downwind at 60° to 70° from the horizontal, the mean number of grains ejected increases roughly linearly with impact velocity. Later, Anderson and Haff (1991) conducted simulations of 20 impacts into a bed of 500 identical spheres using more typical aeolian sand sizes: $D_s = 0.23$ mm and $D_s = 0.32$ mm. The impact angles and speeds were chosen to cover the ranges typical of aeolian saltation impacts in air (angles 8°–15°; speeds 0.25–8 m·s⁻¹) with the number of impacts as 20 for each case. Their results suggest that for the chosen grain parameters, the mean rebound speed, ejected speed and the mean number of ejected particles all increase with the impact velocity. The rebound speed is approximately 50%–60% of the impact velocity, the mean rebound angle is 35°–45° from the horizontal; and the mean ejected speed is roughly 9%–10% of the impact velocity. Based on their simulations, they present a discrete-type splash function:

$$N_r(V_j) = N_{r0} \exp\left(-\frac{V_j - bV_{im}}{cV_{im}^2}\right) dV \quad (3.35)$$

$$N_e(V_j) = N_{e0} \exp\left(-\frac{V_j}{hV_{im}^k}\right) dV \quad (3.36)$$

where $N_{r0} = 0.95$, $N_{e0} = (1.75 V_{im})^{1.0}$, $b = 0.56$, $c = 0.2$, $h = 0.25$ and $k = 0.3$. In each case $dV = 0.1 \text{ m}\cdot\text{s}^{-1}$ which is the width of the ejection velocity bin. $N_r(V_j)$ and $N_e(V_j)$ represent the number of rebound and ejected grains leaving the bed in the j -th ejection velocity bin, labelled V_j , subsequent to a single impact of velocity V_{im} . Distribution of rebound and ejected particles can be fitted by a Gaussian distribution and exponential function respectively. Further, Haff and Anderson (1993) employed the soft-particle approach to simulate the particle-bed collisions in wind-blown sand flux. In their simulation, an initial bed containing 500 grains was prepared, with approximately 33% of the particles of diameter 0.0328 cm and 67% of diameter 0.0231 cm. In particular, a ‘particle cooling’ technique was used to speed up the bed generation process, that is, firstly the grains were given random velocities and allowed to fall under the influence of gravity, which made the granular system initially have a significant kinetic energy due to the grains’ motion, later, it will be artificially converted into a state in which all particle velocities are set equal to zero so as to set up a convenient bed as economically as possible. Besides, they investigated the dependence of the splash pattern on variations of particle properties, such as the spring constant and the coefficient of restitution. These results contributed a lot to the further application of the DEM in granular systems and sediment transport systems.

Based on the work of Haff and Anderson (1993), Xie (2005) performed similar simulations to investigate the influence of sand particle diameter on the splash process characteristic. 12 impacts were run for sand particles with diameters ranging from 0.1 mm to 0.5 mm, and the results showed that except for the impact velocity V_{im} the diameter of sand particles also has a significant influence on the splash function (Fig. 3.16). Since in ‘uniform’ sand case, the impact particle and the particles on the bed have the same diameter, we denote the diameter of sand particle as D_{bed} for simplicity. Then the integral-type splash function given in Xie (2005)’s doctoral dissertation can be expressed as:

$$\bar{N}_{ej} = C_1 + C_2 V_{im}, \quad (3.37)$$

where $C_1 = -99.708D_{bed}^2 + 81.391D_{bed} - 15.146$, $C_2 = 110.665\exp(-D_{bed}/0.047) + 1.555$.

Since the impact velocity V_{im} is believed to be a random variable, the mean number of ejected sand particles \bar{N}_{ej} is also supposed to be a random variable. Denoting the distribution of \bar{N}_{ej} by $F_{Ne}(n_e)$, it can be written as

$$F_{N_e}(n_e) = P(N_e < n_e), \quad (3.38)$$

where $P(N_e < n_e)$ represents the probability of the case that the mean number of ejected particles is less than n_e . Substituting Eq. 3.38 into Eq. 3.37, we get

$$F_{N_e} = P(C_1 + C_2 V_{im} < n_e) = P\left(V_{im} < \frac{n_e - C_1}{C_2}\right) = F_{V_{im}}\left(\frac{n_e - C_1}{C_2}\right). \quad (3.39)$$

Therefore, for a given probability distribution of impact velocities, such as the one given by Dong et al. (2002), the probability density of the number of lift-off sand particles can be expressed as:

$$f_{N_e} = f_{V_{im}}\left(\frac{n_e - C_1}{C_2}\right). \quad (3.40)$$

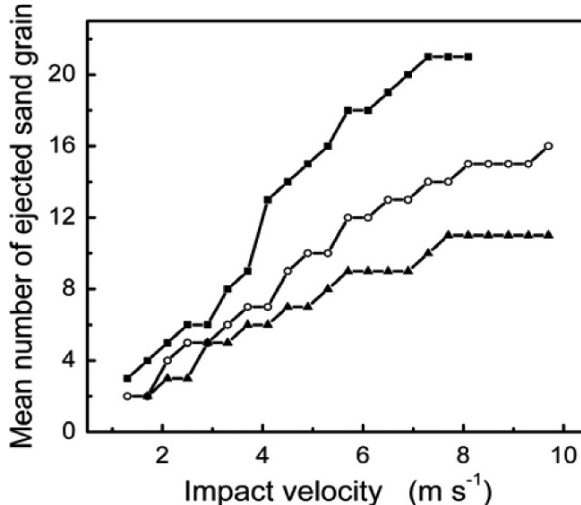


Fig. 3.16. The mean number of ejected particles versus impact velocity for several particle diameters; —■— for particle diameter 0.23 mm, —○— for particle diameter 0.34 mm and —▲— for particle diameter 0.46 mm (Xie 2005)

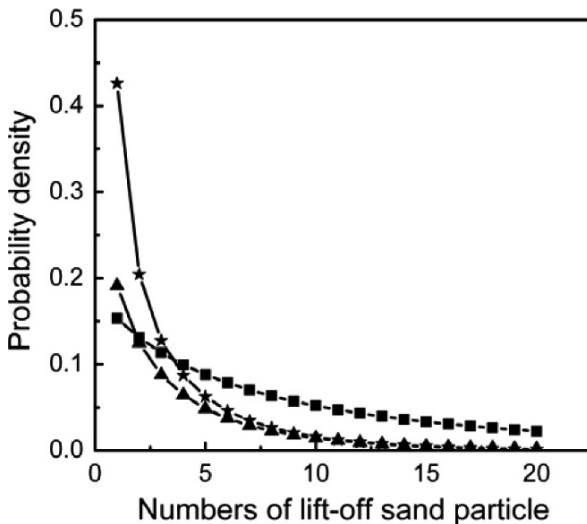


Fig. 3.17. The effect of particle diameter on the probability density of the number of lift-off sand particles with wind velocity $7.0 \text{ m}\cdot\text{s}^{-1}$; —■— for particle diameter 0.15 mm, —▲— for particle diameter 0.20 mm and —★— for particle diameter 0.25 mm (Xie 2005)

Since parameters C_1 and C_2 are functions of sand diameter D_{bed} and impact velocity V_{im} is related to wind velocity, the probability density of the number of lift-off sand particles, the so-called number density, is supposed to be a function of wind velocity and sand diameter.

Fig. 3.17 illustrates the number density of lift-off sand particles for diameter 0.15 mm, 0.2 mm and 0.25 mm, respectively. It can be seen that for a given wind velocity the probability density curve becomes steeper when the particle diameter is larger, in other words, larger sand particles are less susceptible to being ejected under the impact of sand particles of the same size. From a comparison of the probability densities of the sand particles with a diameter of 0.25 mm under wind velocity $8.0 \text{ m}\cdot\text{s}^{-1}$, $12.0 \text{ m}\cdot\text{s}^{-1}$ and $15.0 \text{ m}\cdot\text{s}^{-1}$, we can conclude that the effect of wind velocity is negligible.

3.5.2 Splash Function for ‘Mixed’ Sands

Although the effect of the particle diameter on the splash process has been mentioned in the studies mentioned above, most of these investigations are limited to ‘uniform’ sand case, which cannot give a realistic description of natural particle-bed collision. In order to acquire an understanding of grain collisions in wind-blown sand movement, it is necessary to simulate the

stochastic collisions on a sand bed composed of ‘mixed’ sand particles. The simulation procedures can be taken as follows:

Step 1: Generation of a ‘mixed’ sand bed. In order to simulate natural sand particle-bed collision, one of important steps for us is to generate a ‘mixed’ sand bed with randomly distributed particle size of the same diameter distribution as that obtained in field measurements. A periodic rectangular box is taken to be of length L_b and height H_b , the sizes of the N particles in the bed are chosen to fit the distribution of natural sand; and the bottom of the box is covered by an array of large particles which are assumed to be immobile during the simulation. The particles fall down to the bed with random positions $X_i(x_i, z_i)$ and velocities $V_i(V_{x_i}, V_{z_i})$ ($i = 1, 2, \dots, N_b$). Due to the inelasticity of grain collisions, the total kinetic energy of the granular system decreases with time and the system finally develops into a ‘natural’ bed with particles of varying sizes.

Step 2: Contact detection. After the selection of impact velocity V_{im} , impact diameter D_{im} , and impact points on the bed, we need to deal with the particle-particle interaction between neighboring particles. Over the course of each particle-bed collision event, a series of ‘chain reaction’ are initiated by the impact particle. That is, any two particles may in principle eventually come into contact, even though initially they may be far apart. Therefore, an additional computational issue is the detection of contacts between neighboring grains.

Step 3: Calculating the motion of each particle. From the contact detection in Step 2, we can establish a ‘neighbor list’ for each particle in the system, and sequentially obtain the velocity and position of each particle by solving the equations of motion based on the soft-particle or hard-particle approach presented in Sects. 3.3.2 and 3.3.3.

Step 4: Collecting the rebound and ejected particles. Repeat the calculations from step 2 to step 3 until the incident particle rebound from the bed surface, and then collect the lift-off velocity V_e of ejected particles.

After performing simulations for each combination of sand diameter and impact velocity, we can find some possible regions of variables, denoted by $V_{ej} \in [0, V_{ej}^{\max}]$. Dividing the region into k^* subregions and calculating the number of rebound and ejected particles in each subregion, we can get the discrete-type splash function

$$N_{rD}(V_j) = 0.85 \exp\left[-\frac{(V_j - \mu_{rD})^2}{2\sigma_{rD}^2}\right], \quad N_{eD}(V_j) = A \exp(-BV_j). \quad (3.41)$$

For discrimination, subscript D is used to represent the mean diameter of the sand bed particles; N_{rD} and N_{eD} represent the probability of rebound

and ejected particles; A , B , μ_{rD} , σ_{rD} are fitting parameters. For the width of velocity subregion taken as $0.1 \text{ m}\cdot\text{s}^{-1}$, they can be written as follows, respectively,

$$A = 0.02V_{im}(V_{im} + 150D_{im} - 15) + D_{im}(8.3D_{im} - 4),$$

$$B = 0.02D_{im}(D_{im} + V_m - 37.5) - 0.15V_{im}(V_{im} - 5.87) + 1.44,$$

$$\sigma_{rD} = V_{im}(0.04V_{im} - 0.7D_{im} + 0.14) + 0.4D_{im} - 0.1,$$

$$\mu_{rD} = 9D_{im} + 0.65V_{im} - 0.16.$$

It is worth noting that Eq. 3.41 is a statistical result based on simulations of a sand bed with 4000 particles of varied size, in which 10 groups of representative diameters: 0.09 mm, 0.12 mm, 0.14 mm, 0.16 mm, 0.18 mm, 0.19 mm, 0.2 mm, 0.21 mm, 0.28 mm and 0.45 mm are selected to construct the ‘natural’ bed, with corresponding volume percentage being 0.095%, 0.13%, 12.58%, 31.54%, 27.69%, 15.83%, 7.47%, 3.22%, 1.33% and 0.11%, respectively. The resulting sandy bed is of 4.5 cm length, 0.45 cm height. The mean particle diameter of the whole bed and the surface layer are 0.203 mm and 0.22 mm respectively.

Comparing the discrete-type splash function given by Anderson and Haff (1991) and Eq. 3.41 (see Fig. 3.18), we can find for the same impact velocity V_{im} , if the impact diameter D_{im} is equal to the mean diameter D , both the ejection speed and the ejection number in the ‘mixed’ sand case are a little larger than those in ‘uniform’ sand case; if the impact diameter D_{im} is larger than the mean diameter D , the discrepancy becomes much higher. It is because in ‘mixed’ sand case, the small sand particles near the impact position are easier to be ejected when the impact velocity reaches a certain value. While in the ‘uniform’ sand case, the sand particles near the impact position have the same diameter as the impact particle, which makes them less easily to be ejected.

Summing over all possible ejection speed subregions, we get the integral-type splash function for ‘mixed’ sands:

$$\bar{N}_{ej} = V_{im}(0.08V_{im} + 7.1D_{im} - 1.2) + D_{im}(33.3D_{im} - 16.1). \quad (3.42)$$

Comparison between the results of Eq. 3.42 and other integral-type splash functions are shown in Fig. 3.19, in which the results calculated by Eqs. 3.36 and 3.37 are proposed by Anderson and Haff (1991) and Xie et al. (2005) for a ‘uniform’ sand bed respectively. Zhou et al. (2006) presented

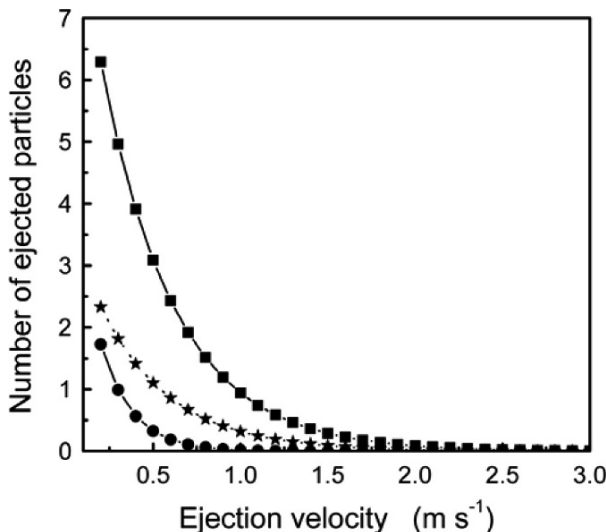


Fig. 3.18. Comparison between the results of discrete-type splash functions; —●— the results calculated by Eq. 3.36 for ‘uniform’ sand case ($D_{im}=0.32 \text{ mm}$), —★— the results given by Eq. 3.41 for ‘mixed’ sand case ($D_{im}=0.32 \text{ mm}$), —■— the results given by Eq. 3.41 for ‘mixed’ sand case ($D_{im}=0.5 \text{ mm}$)

an integral-type splash function for ‘mixed’ sands through their simulations on a ‘mixed’ sand bed with mean diameter 300 μm . Their results can be written as follow:

$$\bar{N}_{ej} = 17.96 + 18.05 \ln \left(0.37 + \frac{1}{6} D_{im}^3 \pi \rho_s V_{im} \right). \quad (3.43)$$

From Fig. 3.18, we can find that either for ‘uniform’ sand case or ‘mixed’ sand case, the mean ejection number increases with the impact velocity. Quantitatively speaking, the results of the ‘mixed’ sand case get close to the results of the ‘uniform’ sand case for an impact diameter of 300 μm which is the same as the diameter of the ‘uniform’ sand bed when impact velocity is lower than 5 m s^{-1} , after that, results given by Eq. 3.42 are a little higher while those given by Eq. 3.43 are a little lower than the results of the ‘uniform’ sand case. This mainly arises from the fact that particles larger than 300 μm on the sand bed employed in Zhou et al. (2006) form a considerable percentage of the number ejected which are less easily ejected compared with the ‘uniform’ sand case. Besides, from the comparison between the results of two ‘mixed’ cases, we can also find that the mean ejection number subsequent to the impact of sand particles of

500 μm is larger than that of 300 μm (which is equal to the mean particle diameter of the sand bed). Specifically, the results calculated by 3.41 are lower than those calculated by 3.42 for $V_{im} < 8 \text{ m}\cdot\text{s}^{-1}$, while the latter are higher than the former for $V_{im} > 8 \text{ m}\cdot\text{s}^{-1}$. This is also a result of different size distribution of the sand bed employed in the numerical simulation.

It is notable that by applying the above method, we can also obtain information about the lift-off velocities of sand particles. For example, Zhou et al. (2006) concluded that for a given diameter and impact velocity, the mean ejection velocity follows the relation,

$$\bar{V}_e = 0.43 + 0.077 \ln \left(0.029 + \frac{1}{6} D_{im}^3 \pi \rho_p V_{im} \right). \quad (3.44)$$

Taking all of the sand particles lifting from the sand bed in the simulations as a sample space the probability distribution of lift-off velocities for

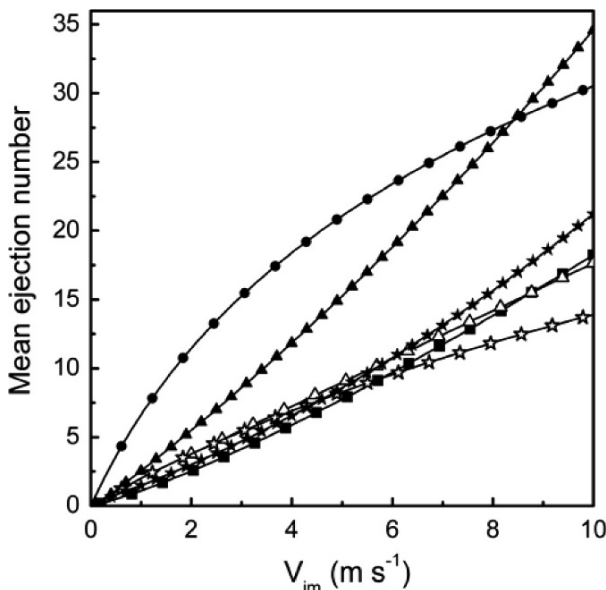


Fig. 3.19. Comparison of the results of existing integral-type splash functions for ‘uniform’ sand case and ‘mixed’ sand case; —■— the results calculated by Eq. 3.36 for ‘uniform’ sand case ($D_{bed} = 0.32 \text{ mm}$), —△— the results calculated by Eq. 3.37 for ‘mixed’ sand case ($D_{bed} = 0.3 \text{ mm}$), —★— the results calculated by Eq. 3.43 for ‘mixed’ sand case ($D_{im} = 0.3 \text{ mm}$) —●— the results calculated by Eq. 3.43 for ‘mixed’ sand case ($D_{im} = 0.5 \text{ mm}$), —★— the results calculated by Eq. 3.42 for ‘mixed’ sand case ($D_{im} = 0.3 \text{ mm}$), —▲— the results calculated by Eq. 3.42 for ‘mixed’ sand case ($D_{im} = 0.5 \text{ mm}$)

a given shear velocity can be obtained. Fitting all sets of the numerical results of particle-bed collision with the least squares method, the PDF of vertical, downwind and upwind horizontal and resultant velocities follow an exponential function as follow,

$$f(V, u_*) = A \exp\left[-A(|V| - V_{cr})\right], \quad (3.45)$$

where V represents vertical, downwind and upwind horizontal or resultant velocities; V_{cr} is the threshold starting velocity of a sand particle, which is proved to be a constant approximately for any shear wind velocity; $A (> 0)$ is a function of shear wind velocity u_* and it represents the probability of a sand particle launching with low velocity. Results fitted by the least squares method are shown below:

$$A_V = 8.66359 + \frac{0.72975}{0.33586\sqrt{0.5\pi}} \exp\left[-2\left(\frac{u_* - 0.6672}{0.33586}\right)^2\right], (V_{cr})_V = 0.0324 \quad (3.46a)$$

$$A_{V_y} = 2.66168 + \frac{0.19333}{0.18352\sqrt{0.5\pi}} \exp\left[-2\left(\frac{u_* - 1.03772}{0.18352}\right)^2\right], (V_{cr})_{V_y} = 0.2237 \quad (3.46b)$$

$$A_{V_{x-}} = 18.5185, \quad (V_{cr})_{V_{x-}} = -0.0895 \quad (3.46c)$$

$$A_{V_{x+}} = 2.31227 + \frac{0.14236}{0.23775\sqrt{0.5\pi}} \exp\left[-2\left(\frac{u_* - 1.01733}{0.23775}\right)^2\right], (V_{cr})_{V_{x+}} = 0.5236 \quad (3.46d)$$

where V , V_y , V_{x-} and V_{x+} are resultant, vertical, upwind horizontal and downwind horizontal lift-off velocities of sand particles, respectively. Substituting Eq.3.44 into Eq. 3.43 we get the PDFs of resultant, horizontal and vertical lift-off velocities in a ‘mixed’ wind-blown sand flux, where the sand particle diameters follow log-normal distribution shown as in Fig. 3.1. The PDF for angular velocities of sand particles can be formulated in the same way as:

$$f(\omega, u_*) = \frac{0.8727}{(205.8 + 2.2u_*)\sqrt{0.5\pi}} \exp\left[-2\left(\frac{\omega + 0.4693}{205.8 + 2.2u_*}\right)^2\right] \quad (3.47)$$

Chapter 4 Wind-Blown Sand Electrification

Many researchers were aware of that sand particles can charge up and they demonstrated that the electric field in sand (dust) storm is much stronger than the one of fair weather (Rudge 1913, 1914; Kunkel 1950; Latham 1964; Kamra 1969; Stow 1969). The charged sand particles and wind-blown sand electrification may affect wind-blown sand flow, which attract more attentions recently. In fact, sand charging and wind-blown sand electric field have significant effects upon the entrainment of sand particles, transportation and deposition, whereas, sand particles acquire substantial charges during their entrainments and collisions which conversely affect the wind-blown sand electric field. Besides, particles in an electric field are known to self-assemble into complex patterns (Sapozhnikov 2003). Clouds of charged dust regularly produce devastating explosions in particle and coal plants (Palmer 1973), and a calamitous blast can be occurred by a lot of charged particles. In exploring outer space, charged grit attaches itself to spacesuits and works its way into suit joints, causing them to leak air and so cut exploration time. Therefore, the studies on wind-blown sand electrification are expected to clarify these problems, to explore the mechanism of sand particles charged, and further to predict the effect of wind-blown sand electrification on the formation and evolution of the landforms on Mars. Back to Earth, the study of wind-blown sand electrification is meaningful to reveal how sand particles be entrained, transport and deposit in wind-blown sand flux, and to explore other planets successfully.

However, it is difficult to reveal how a sand particle becomes charge and what is the property of the electrical charges, especially in quantity. In addition, due to the limitations of the experiment instruments and methods, there are few studies on the experimental measure of wind-blown sand electric field and sand particles' charges.

The content of this chapter is arranged as follows, Sect. 4.1 reviews the existing studies on the phenomenon and mechanism of sand particles charging are introduced; Sects. 4.2 and 4.3 introduce the measurement results and theoretical prediction of wind-blown sand electric field, and finally Sect. 4.4 discusses the effect of wind-blown sand electrification on the entrainment of sand particles and propagation of electromagnetic wave in quantity. The effect of wind-blown sand electrification on the wind-

blown sand transportation and the theoretical prediction of dust devil will be discussed in next chapter.

4.1 Charged Sand Particles and their Charging Mechanisms

4.1.1 Observations and Measurements

Although electrical charges on sand particles have long been studied, researchers just argue how sand particles charge and their polarity. Rudge (1913) is one of the earliest researchers who studied sand charging, and he disrupted sand by means of an air jet and found that the large sand particles acquired positive charges and the air contained (or probably very small particles of sand suspended in the air) negative charges; Shaw (1929) blew sand through a sandpaper sheath at room temperature and found that the sandpaper became positively charged and the blown sand negatively charged. The charging was of the same sign but greater in magnitude when the temperature of the air was increased to 58 °C. Gill (1948) poured sand though a metal funnel and observed that smaller sand particles acquired positive charges and the larger ones acquired negative charges. By poured sand though a silica funnel, Peterson (1949) found that the sand acquired a negative charge. Since 1950s, many researchers begin to pay their attentions to a single sand particle's charge. Kunkel (1950) produced a puff of sand and measured the charge carried by individual particles. He found that although most particles were charged, the electrification was symmetrical, i.e., for each size range the total charge carried by the positively charged particles was equal to that carried by the negatively charged particles. From then on, many studies confirmed that sand particles can be electrified and the sign of the charge carried by a sand particle is relative to its size. For example, for quartz sand, Greeley and Leach's experimental (Greeley and Leach 1978) results showed that particles larger than 60 μm in diameter acquired negative charges, and particles smaller than 60 μm acquired positive charges, however, the critical diameter for the sign of charge is somewhat variable.

Since both sand and silt are tiny, it is quite difficult to measure the magnitude of charge carried by a single sand particle. Instead, many researchers measured the average charges of saltating sand particles such as the average charge-to-mass ratio. Using a sand trap to collect the sand particles, the average charge-to-mass ratio can be obtained by measuring the total charges and mass in the trap. For example, at Seminoe Reservoir (30 m

northeast of Rawlins, Wyoming), Schmidt et al. (1998) used Faraday-cage drift trap at 5 cm height and measured an average charge-to-mass ratio $60 \mu\text{C}\cdot\text{kg}^{-1}$ and $150 \mu\text{m}$ average sieve diameter of collected in the trap.

Although we have got some results from the researches on wind-blown sand electrification, as mentioned above, it is far away from exploring this field. In fact, there are many factors which may affect the average charge-to-mass ratio of saltating sand particles, such as the sand diameter and wind velocity. In order to clarify the effect of these factors, we conducted electrification experiments in the field environmental wind tunnel of the Institute of Cold and Arid Regions Environmental Engineering of the Chinese Academy of Sciences. A D-Q3 digital amperemeter is used to measure the electric charges of sand particles by connecting the moustache of the amperemeter onto the surface of steel of the sand collector. In addition, the mass of collected sands in the collector chamber is weighted so as to determine the average charge-to-mass ratio, or the average charge per kilogram of sand, by dividing the measured charge with the measured mass. Experimental sands were sampled from the Tengger Desert, and the sand diameter ranges mainly in $40\text{--}600 \mu\text{m}$ whose distribution is shown in Fig. 4.1. Through sifting the ‘mixed’ sand with sieves of different aperture size, we got some ‘uniform’ sand samples to which the diameter distributes in a narrow band. Here, three ‘uniform’ sand samples with diameters of $0\text{--}75 \mu\text{m}$, $100\text{--}150 \mu\text{m}$ and $500\text{--}1000 \mu\text{m}$ were employed. After starting wind tunnel, the charge-to-mass ratios are measured when the wind-blown

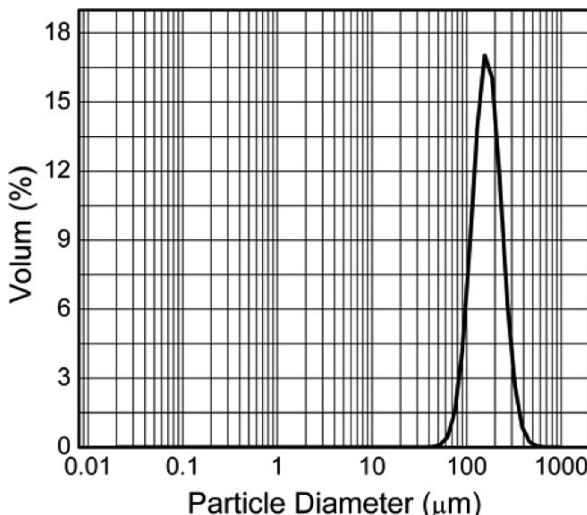


Fig. 4.1. Diameter distribution of sand particles used in wind tunnel experiments, which were sampled from the Tengger Desert (by the author et al.)

Table 4.1. Average charge-to-mass ratio for the ‘uniform’ sand measured under different wind velocities

| Partical diameter [μm] | Wind velocity [m s^{-1}] | Charge-to-mass [$\mu\text{C kg}^{-1}$] |
|-------------------------------------|-------------------------------------|--|
| 0–75 | 7 | -124.5 |
| 0–75 | 15 | -40.2 |
| 100–250 | 7 | -64.2 |
| 100–250 | 15 | -3.6 |
| 500–1000 | 10 | 0.95 |
| 500–1000 | 15 | 0.13 |

Table 4.2. Average charge-to-mass ratio for the ‘mixed’ sand under different wind velocities

| Wind velocity [m s^{-1}] | Charge-to-mass [$\mu\text{C kg}^{-1}$] |
|-------------------------------------|--|
| 7 | -23.4 |
| 10 | -19.3 |
| 15 | -15.9 |
| 20 | -9.8 |

Table 4.3. Variation of average charge-to-mass ratio for the ‘mixed’ sand with height under different wind velocities

| Height [cm] | Wind velocity [m s^{-1}] | Charge-to-mass [$\mu\text{C kg}^{-1}$] |
|-------------|-------------------------------------|--|
| 2–6 | 10 | -24.5 |
| 2–6 | 20 | -13.8 |
| 6–10 | 10 | -125.0 |
| 6–10 | 20 | -31.9 |
| 26–30 | 10 | -330.0 |
| 26–30 | 20 | -198.0 |
| 50–54 | 10 | -1120.7 |
| 50–54 | 20 | -890.2 |

sand flux is steady. For the three ‘uniform’ sand samples, the experiment is repeated to measure the average charge-to-mass ratio at different heights under different axial wind velocities. Tables 4.1 list some measured results of the average charge-to-mass for the three ‘uniform’ sand samples under three different axial wind velocities of $7 \text{ m}\cdot\text{s}^{-1}$, $10 \text{ m}\cdot\text{s}^{-1}$, and $15 \text{ m}\cdot\text{s}^{-1}$.

From Tables 4.1–4.3, it can be found that sand particles saltate at the height of 0.02–0.54 m with each axial wind velocity; the sign of electric charge generated on the sands is mainly dependent upon the diameter of the sand particles, that is, when the diameter of the ‘uniform’ sand is less

than or equal to 250 μm , the charge is negative, whereas the sign is positive when the diameter is greater than or equal to 500 μm . In addition, results listed in Table 4.1 and Table 4.2 indicate that the magnitude of the charge-to-mass ratio for both the ‘uniform’ sand and the ‘mixed’ sand decreases with the axial wind velocity increasing, and increases with height for the ‘mixed’ sand. For the ‘mixed’ sand, a positive charge-to-mass ratio is measured when the axial wind velocity increases up to 20 $\text{m}\cdot\text{s}^{-1}$ as shown in Table 4.2, which is similar to the results given by Schmidt et al. (1998) as pointed out in the introduction.

4.1.2 Charging Mechanisms of Sand Particles

When the wind-blown sand electrification is confirmed by field or laboratory observations, people begin to pay an attention to the mechanisms of sand particles charged. Confined by the experiment instruments and measurement methods, up to now, it is still difficult to make quantitative measurements of sands charging procedure and there have no idea on measurements of magnitudes of charges acquired by a single sand particle. So the charging mechanism for sand particles is just a speculation. Latham is one of researchers who early tried to explain the charging procedure of sand particles. Earlier, Workan and Reynold (1948) investigated the mechanism of the thunder to observe that the ice acquires negative charges and the water droplet acquires positive charges after the water drip colliding with the ice. Their studies was based on the phenomenon of the snowstorm electrification, that is, smaller snow particles carry positive charges and larger snow particles carry negative charges. Similar to the mechanism of the thunder, Latham thought the asymmetric collision between large and small sand particles results in sand particles acquiring charges, and because of their smaller area of contact the small particles would become hotter than the larger ones. The temperature difference between the contact particles impels the charges’ transfer, so the contact particles are charged. This explanation is so-called the temperature-gradient theory by Latham and Mason (1961). Later, Latham (1964) found that charge transfer drastically resulting from thermoelectricity when snow particles become coarser and the collision velocity is higher, which provided some experimental evidences for the temperature-gradient theory. However, we can not confirm the temperature-gradient theory directly because it is hard to measure the temperature difference and the magnitude of charge carried by particles with different diameters at the moment of collision. Even now, we can not learn more whether the temperature difference resulting from the collision between small sand particles can impels the charge transfer.

Besides Latham's work, there are many speculations and explanations to infer how the sand particles charged. Kanagy and Mann (1994) reviewed the seven mechanisms which have been recognized as potentially contributing to electrical charges on sand particles, that is: (1) Polarization by Earth's atmospheric electric field: Some researchers think that sand particles in atmospheric electric field, as a kind of dielectric material, will be polarized and the excess charges will be repulsed to the two sides of sand particles. Through collision among sand particles and breaking into small fragments, the particles are not neutral any more; (2) Triboelectric charging: that is to say two neutral sand particles will be charged by rubbing them. Ling et al. (1984) thinks that the electric field in sand (dust) storm is induced by sand particles, and those sand particles moves in anomalous trajectories and rub each another, maybe produce the charges, which is the triboelectrical phenomena; (3) Contact electrification: contact electrification generally involves two dissimilar materials which have come into contact and then are separated; (4) Cleavage/fractoelectrification: charges also may develop on sand particles as a result of cleavage or fracture; (5) Bombardment charging (photons; charging particles): sand particles will be charged due to solar wind bombardment or photoelectron ejection from sunlit surface; (6) Pyroelectric charging: when the crystal is heated is known as pyroelectricity, the charges will occur at the ends of a crystal; (7) Piezoelectric and electret effect charging: the crystal acquires charges when pressure is applied. The speculations (1), (5) and (7) indicate that sand particles can acquire charges even though they do not move, but through wind tunnel experimental results, it can be found that the magnitude of charges and the electric field are obviously variable when wind-blown sand transportation is stronger. So there is a relationship between the wind-blown sand electrification and sand transport. The speculations (1) and (5)–(7) maybe give a mechanism for sand particles charging, they are not the definitive one. Those speculations can not narrate why larger sand particles acquire the positive charges and the smaller ones acquire the negative charges when all those particles are acted upon the same actions such as polarization, pulverization, bombardment by solar ray, heating and piezoelectric charging. For the speculation (3), difference among the materials of sand particles at same place is hardly remarkable, so the probability for sand particles charging is little due to materials' difference, and further the speculation (4) is not appropriate. The speculation (2) agrees with the Latham's theory to some extent, if we deem the rubbing in speculation (2) as a result of collisions between particles with different diameters.

4.2 Measurements of Wind-Blown Sand Electric Field

4.2.1 Atmospheric Electric Field

The excess charges carried by atmosphere are the combination of several ions with opposite polarity. Observations indicate that there is downward electric field in the lower fair weather, which means that earth surface acquires the negative charges. In fact, atmosphere is a kind of weak electric material, and average density of current is $3 \times 10^{-12} \text{ A}\cdot\text{m}^{-2}$ in fair weather. The density of surface charges delivered to the earth surface is about $-10^{-9} \text{ C}\cdot\text{m}^{-2}$, and the total charge is about $-5 \times 10^5 \text{ C}$. For the simplicity, we usually let the electric field E_a of fair weather be negative. The direction and the magnitude of E_a around the world are almost equal everywhere, but E_a fluctuates slightly from time (place) to time (place). Usually, the electric field of fair weather is $120 \text{ V}\cdot\text{m}^{-1}$, and it is $130 \text{ V}\cdot\text{m}^{-1}$ above sea level.

The electric field of fair weather decreases with height increasing, and reaches up to its maximum at ground level. From Gaussian theorem, the relationship of atmospheric electric field E_{a0} at ground level with the density of surface charges $\delta_e (\text{C}\cdot\text{m}^{-2})$ can be deduced, which is $E_{a0} = -4\pi\delta_e$. At the height 10 km, the atmospheric electric field is about 3% of E_{a0} . Due to the influence of buildings and the fluctuation of topography, the atmospheric electric field has a horizontal component, however, the effect of the building and topography on the atmospheric electric field can be ignored when one measures atmospheric electric field at a place 5 times higher than hill and building, and 3 times higher than slim building such as telegraphy pole (Fei et al. 2003).

Atmospheric electric field is related to the local atmosphere variation, because the local atmosphere variation can result in electric properties' variation of atmosphere such as the conductance and body charges, which determines the atmospheric electric field. At some terrestrial observation stations, two peaks of atmospheric electric field can be found that maximum values appear at 7:00–10:00 and 19:00–21:00 in local time while minimum values appear at 4:00–6:00 and 12:00–16:00. It can be found that the variations of atmospheric electric field are significant in the regions where the maximum electric field appears. For example the electric field increases from $70 \text{ V}\cdot\text{m}^{-1}$ to about $600 \text{ V}\cdot\text{m}^{-1}$ within 1 hour.

Furthermore, the atmospheric electric field is also related to the atmosphere pollutant. When the pollution is heavy, air conductance decreases and the atmospheric electric field increases rapidly. In ocean area, the arctic and Antarctic area, and some sparsely populated inland areas, the atmospheric electric field regularly varies in every day, and that is to say,

atmospheric electric field reaches up to its maximum at 18:00–19:00 and minimum at 4:00. Turbulence due to iron transport by air and thunderstorm also affects the atmospheric electric field. When the global thunderstorm is strongest, the atmospheric electric field reaches up to its maximum.

4.2.2 Field Observation of Wind-Blown Sand Electric Field

Rudge (1913) measured the atmospheric electric field in South African by electrometer, during an ordinary fine weather day, a dusty day and a very dusty day. He found that sand (dust) storm could increase the electric field and strong sand (dust) storm could completely modify the direction of electric field, which verified the observation by Michie Smith in India. In addition, Rudge found the electric field can reach up to $10 \text{ kV}\cdot\text{m}^{-1}$ (let downward be positive, henceforth). From then on, many researchers investigated the wind-blown sand electric field, and they found the electric field is fluctuant and is related to wind velocity, temperature, relative humidity and observation site (Kamra 1972; Qu 2003). Kamra (1972) measured the atmospheric electric field and wind-blown sand electric field at many places near a desert of the southwestern states. He found that wind velocity, especially the turbulent component of wind velocity, has a great effect on the wind-blown sand electric field. Such puffs and whirls of dust caused by wind gusts often produce stronger electrical perturbation which last for

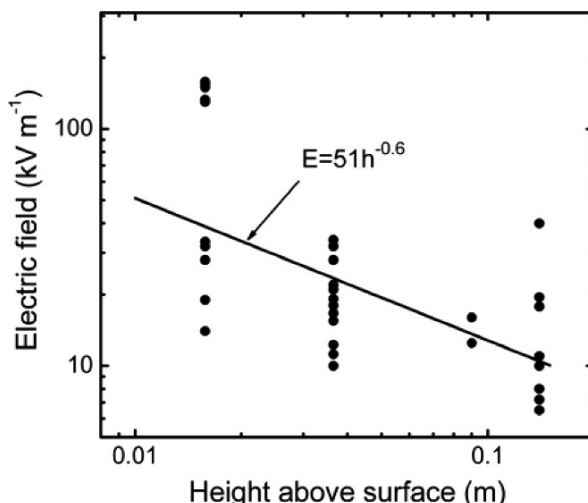


Fig. 4.2. Measurements of wind-blown sand electric field and its fit curve, where the average wind velocity is $7.0 \text{ m}\cdot\text{s}^{-1}$ at 1.5 m height (from Schmidt et al. 1998)

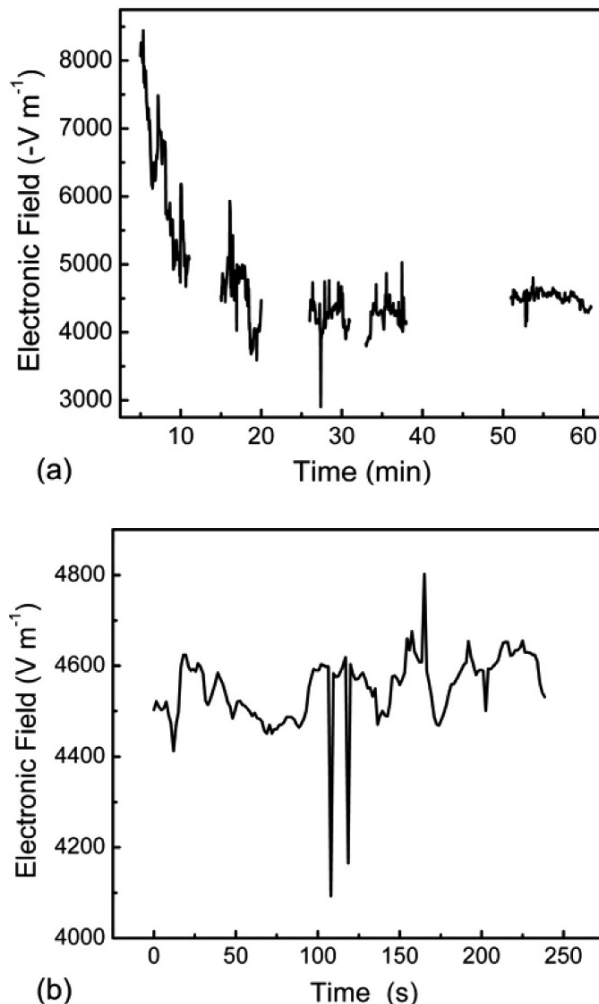


Fig. 4.3. Profile of electric field measured on the top of a building in Lanzhou University, at the height about 60 m, (a) record time is 16:05–16:54 and (b) record time is 16:50–16:54 (by the author et al.)

a few minutes, and their frequency depends on the gustiness of wind. Schmidt et al. (1998) measured the wind-blown sand electric field above a sand dune, and he found that the electric field decreased rapidly with the height above the sand dune surface, became zero at about 20 cm and approached to the fair-weather field above 2 m. The electric field measurements for the region 1.73–20 cm are shown as Fig. 4.2. From the Fig. 4.2, it can be found that electric field exponentially decreases with and increasing

of height and we fitted a power-law profile below 15cm under a condition that the average wind velocity is $7.0 \text{ m}\cdot\text{s}^{-1}$ at 1.5 m height.

In a sand (dust) storm, the electric field becomes stronger near the building in the center of city. In March 9th, 2003, we measured the electric field

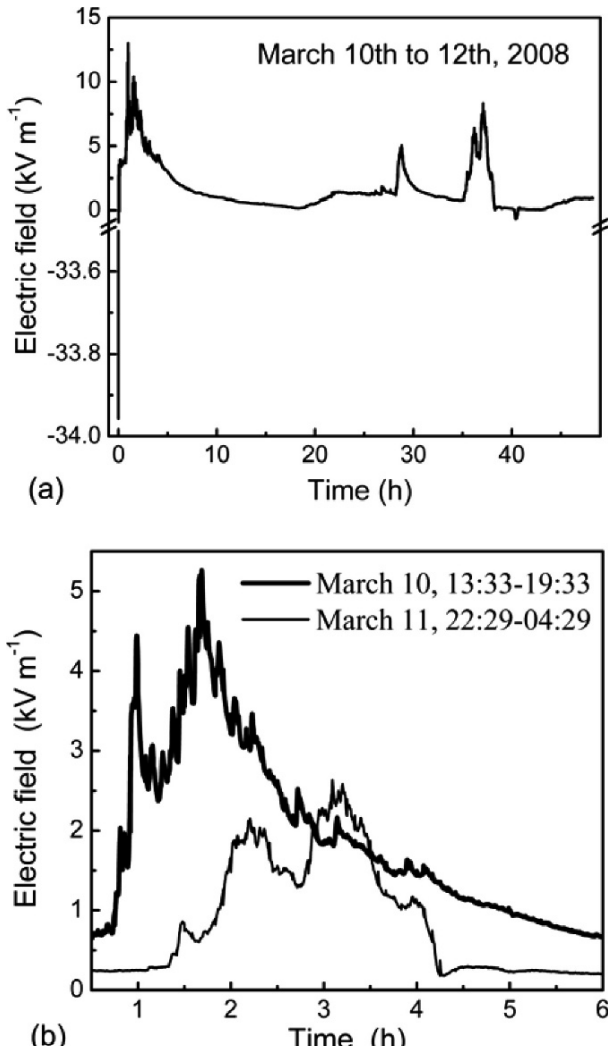


Fig. 4.4. Profile of electric field near a sand dune measured in the Badain Jaran Desert during March 10th to 12th, 2008 with sampling frequency 1 Hz; (a) the electric filed during the whole record time; (b) the wind-blown sand electric field during two dusty weather conditions, which are the amplificatory images of results in the circles of (a) (by the author et al.).

at the top of a building in Lanzhou University which is in the center of Lanzhou city. The electrical field is measured at a height of 60 m when a sand (dust) storm happened and the visibility was 800 m. The wind-blown sand electric could reach up to $8 \text{ kV}\cdot\text{m}^{-1}$, and it was about $4.5 \text{ kV}\cdot\text{m}^{-1}$ even the sand (dust) storm becomes weak (see Fig. 4.3a). From Fig. 4.3b, it can also be found that the electric field is very unstable.

Wind-blown sand electric field is related to the temperature and humidity. We measure the electric field and its variation with temperature and humidity near a sand dune in the Badain Jaran Desert during March 10th to 12th, 2008. Fig. 4.4 shows the measurement results of electric field from March 9th to 12th, 2008, with the sampling frequency is 1 Hz. Fortunately, during our measurement, we experienced two sand storms, so we measured the electric field of two dusty weather. One sand (dust) storm happened in the afternoon of March 10th, 2008 with low wind velocity, about $10 \text{ m}\cdot\text{s}^{-1}$, and the other sand (dust) storm happened in deep night of March 11th, 2008 with the stronger wind $17.0 \text{ m}\cdot\text{s}^{-1}$. Sand particles can be blown away from earth surface about 30 cm during the first storm and almost dry sand particles were blown away during the second one. The electric fields during the two sand (dust) storms are shown in the Fig. 4.4a and we marked them in red circle lines for well distinguishing. It is noteworthy that temperature in the afternoon of March 10th, 2008 is lower than the one at night of March 11th, 2008, with a difference about 12°C , and humidity of the former is higher than the one of latter, about 60% difference. The electric field of former is weaker than the latter. In order to distinguish them, we plot the electric field serials in Fig. 4.4b during two dusty weather conditions, which indicate that the temperature and humidity have an effect on the wind-blown sand electric field. In addition, our measurement shows that the electric field periodically varies with the same period as the one of temperature and humidity.

4.2.3 Wind Tunnel Measurement of Wind-Blown Sand Electric Field

It is first time that the author et al. investigated the electric field in wind tunnel (Zheng et al. 1998; 2000), and measured the electric field of the ‘uniform’ wind-blown sand flux and the ‘mixed’ wind-blown sand flux shown as Fig. 4.5. It can be found that the wind-blown sand electric field (named by E_z), perpendicularly to the earth surface, is opposite to the electric field of fair weather. Fig. 4.5a, the wind-blown sand electric field decreases with the height increasing, where the electric field holds its absolute value. For the ‘uniform’ wind-blown sand flux, the electric field

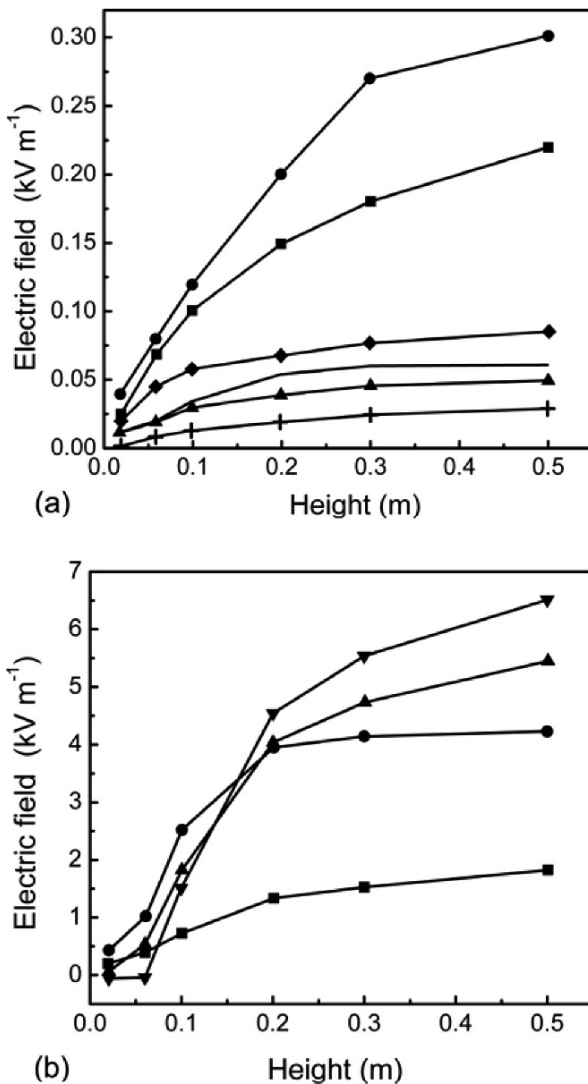


Fig. 4.5. Wind-blown sand electric field versus height **(a)** for the ‘uniform’ wind-blown sand flux, and **(b)** for the ‘mixed’ wind-blown sand flux; There are six results for ‘uniform’ wind-blown sand flux, —■— the results for the wind velocity $u_{ax} = 7 \text{ m}\cdot\text{s}^{-1}$ and $D_s = 0\text{--}75 \mu\text{m}$, —●— the results for the wind velocity $u_{ax} = 15 \text{ m}\cdot\text{s}^{-1}$ and $D_s = 0\text{--}75 \mu\text{m}$, —▲— the results for $u_{ax} = 7 \text{ m}\cdot\text{s}^{-1}$ and $D_s = 100\text{--}250 \mu\text{m}$, —◆— the results for $u_{ax} = 15 \text{ m}\cdot\text{s}^{-1}$ and $D_s = 100\text{--}250 \mu\text{m}$; —+— the results for $u_{ax} = 10 \text{ m}\cdot\text{s}^{-1}$ and $D_s = 500\text{--}1000 \mu\text{m}$, ——— the results for $u_{ax} = 20 \text{ m}\cdot\text{s}^{-1}$ and $D_s = 500\text{--}1000 \mu\text{m}$; There are four results for the ‘mixed’ wind-blown sand flux, and —■—, —●—, —▲— and —▼— are results for the wind velocity $7 \text{ m}\cdot\text{s}^{-1}$, $10 \text{ m}\cdot\text{s}^{-1}$, $15 \text{ m}\cdot\text{s}^{-1}$ and $20 \text{ m}\cdot\text{s}^{-1}$, respectively (from Zheng et al. 2000)

increases with the particles diameter increasing and also increases with wind velocity increasing (see Fig. 4.5a). The variation of electric field with wind velocity is complex for the mixed wind-blown sand flux, especially near the earth surface (see Fig. 4.5b). Comparison of electric field of

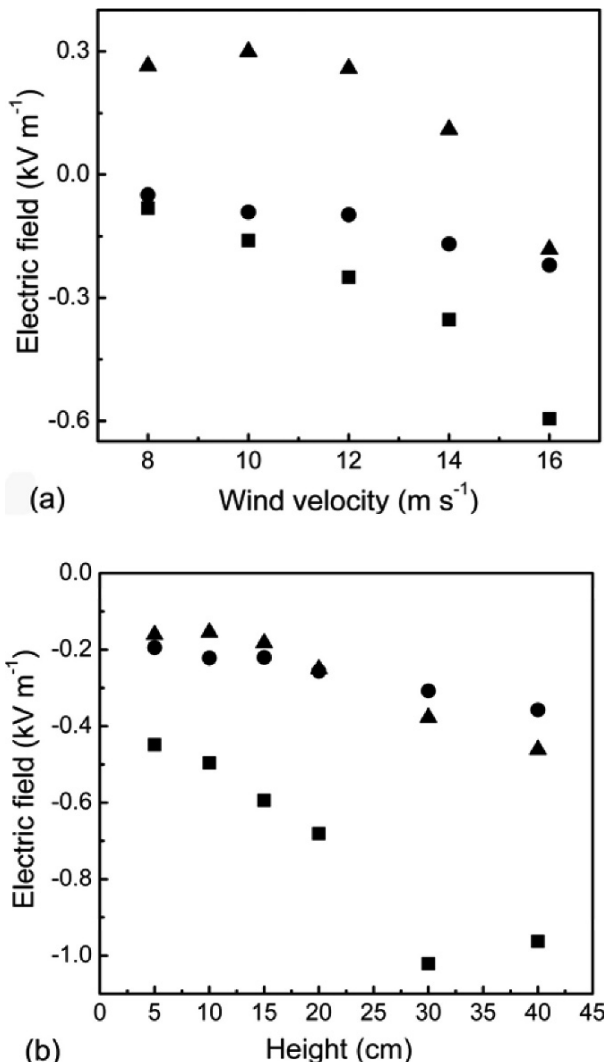


Fig. 4.6. The electric field vary with (a) wind velocity and (b) height; ■ horizontal electric field E_x ; ● lateral electric field E_y ; ▲ vertical electric field E_z (measured by the author et al in the Multi-function environmental wind tunnel of Lanzhou University)

mixed wind-blown sand flux with one of ‘uniform’ wind-blown sand flux, it can be found that the former is much higher than the latter, and at the wind velocity $20 \text{ m}\cdot\text{s}^{-1}$, the maximum of the former is 20 times of the latter.

It is known that the electric field is a vector, but there are few works reported on its other components (E_x and E_y). Here, we let E_x be parallel to the axes of wind tunnel and opposite to the wind direction, and E_y be perpendicular to the both E_x and E_z . Though E_x and E_y are far lower than the wind-blown sand field E_z (see Fig. 4.6), they can reach up to $0.2 \text{ kV}\cdot\text{m}^{-1}$ in the ‘mixed’ wind-blown sand flux, which is higher than the fair weather electric field. From Fig. 4.6, it can be found that E_x and E_y decrease with height or wind velocity increasing. Fig. 4.7 shows that both $|E_x/E_z|$ and $|E_y/E_z|$ rapidly increase with the increase of wind velocity for wind velocity lower than $14.0 \text{ m}\cdot\text{s}^{-1}$. For wind velocities higher than $14.0 \text{ m}\cdot\text{s}^{-1}$, $|E_x/E_z| > 0.8$ and $|E_y/E_z| > 0.85$. At any height, there is a critical wind velocity, and when wind velocity is higher than the critical value, $|E_x/E_z|$ and $|E_y/E_z|$ are larger than 1, which indicate that E_x and E_y are stronger than E_z . In addition, E_x is larger than E_y under a certain wind velocities and heights. Of course, we need to verify if the wind tunnel results can simulate the one of field, it is maybe necessary to consider the effect of wind tunnel’s scale on the wind-blown sand electric field.

In order to describe the relationship between E_x and E_z , the E_y and E_z , we fit $|E_x/E_z|$ and $|E_y/E_z|$ as an exponent-law profile and a linear-law profile, respectively. At the same time, they are functions of wind velocity and height as follows,

$$|E_x/E_z| = a_x \exp\left(\frac{u_{ax}}{b_x}\right) + c_x, \quad (4.1)$$

$$|E_y/E_z| = a_y u_{ax} + b_y, \quad (4.2)$$

where u_{ax} is the axial wind velocity in the wind tunnel and its dimension is $\text{m}\cdot\text{s}^{-1}$.

$$\begin{aligned} a_x &= -0.0283 + 0.0092h - 3.665 \times 10^{-4} h^2, \\ b_x &= 1.6044 + 0.2769h - 0.0106h^2, \\ c_x &= 0.2936 - 0.0604h + 0.0028h^2, \\ a_y &= -0.4189 - 0.1422h + 0.0065h^2, \\ b_y &= 0.0151 + 0.0302h - 0.0015h^2. \end{aligned} \quad (4.3)$$

and h is the height above the sand bed with dimension cm.

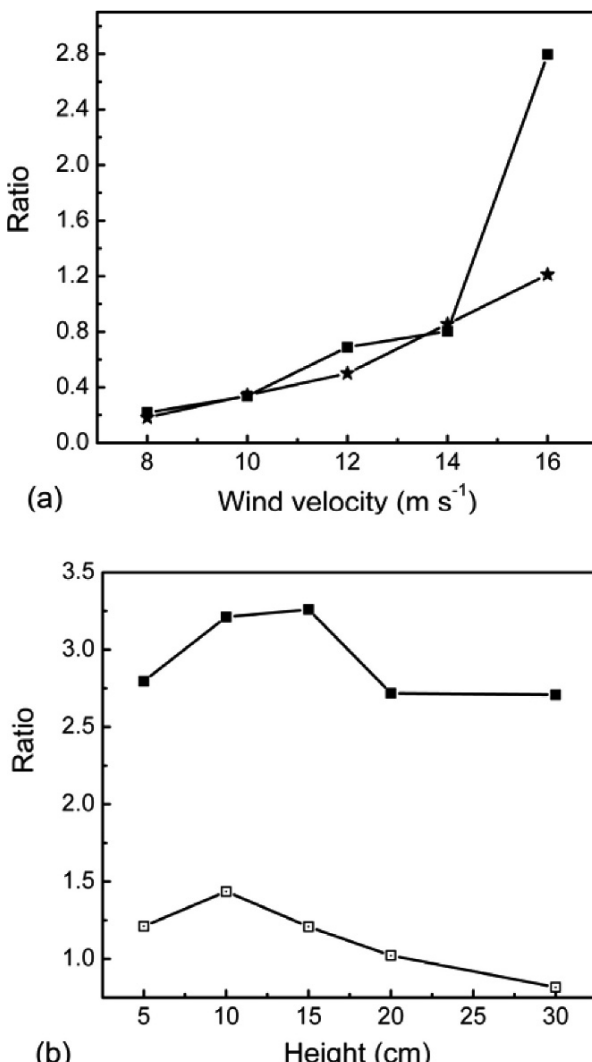


Fig. 4.7. Ratio of horizontal electric field to vertical electric field $|E_x/E_z|$ (—■—) and ratio of lateral electric field to vertical electric field $|E_y/E_z|$ (—□—), vary with (a) wind velocity and (b) height (measured by the author et al. in the Multi-function environmental wind tunnel of Lanzhou University)

4.3 Theoretical Calculation of Wind-Blown Sand Electric Field

Zheng et al. (2004) derived a formula to calculate the wind-blown sand electric field. Shown in Fig. 4.8, let the surface of sand bed as xOy -plane, and the x coincides with the wind direction and z is perpendicular to the xOy -plane. Assuming that the sand bed is infinite, we need only consider the effects of the charged particles enclosed within the rectangular with sides $2a \times 2b$, and centered at the projection of the point P to be observed in the xOy -plane.

Without loss of generality, we located coordinate system in such a way that the point P lies on the z axis with coordinate $P(0, 0, z)$. Then the horizontal component of the electric force at the point P produced by a charged particle located at (x', y', z') is equal in magnitude and opposite in direction to that produced by one at $(x', -y', -z')$, and they will cancel each other out. Therefore the electric field has only a vertical component, and that is the vertical component of wind-blown sand electric field, namely E_z .

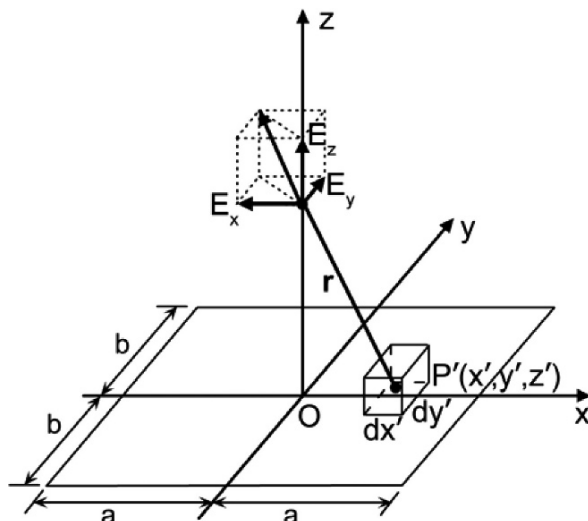


Fig. 4.8. Schematic of electric field, including horizontal component E_x , lateral component E_y and vertical component E_z , produced by a point charge at the point $P'(x', y', z')$ (from Zheng et al. 2004)

4.3.1 Electric Field Due to Sand Particles Moving in Air

When wind-blown sand flux is at steady state, the distribution of the sand particles ejected from the sand bed and accelerated by the wind just reproduces itself after impacting the bed, which means the numbers of ejected and impacting sand particles are approximately equal to each other. Thus the number density of the particles N (i.e., the number of moving particles per unit volume) in the windblown sand flux may be assumed to vary only with the height over the sand bed, i.e., $N = N(z)$. Then, the distribution of electric charges of saltating or suspending sand particles could be described by the volume charge density $\rho_q(z)$, which is given by

$$\rho_q(z) = \frac{1}{6} \pi \rho_s D_s^3(z) N(z) C_q(z). \quad (4.4)$$

Where $D_s(z)$ and $C_q(z)$ are the particle diameter and the charge-to-mass ratio respectively. ρ_s is the particle density. It is noteworthy to point that usually $D_s(z)$ and $C_q(z)$ are not constants in real wind-blown sand flux, but for simplicity, here we let $D_s(z) = D_s$ and $C_q(z) = C_q$.

Consider a differential volume $dx'dy'dz'$ in the wind-blown sand flux as shown in Fig. 4.8. It contains a distribution of electric charges characterized by a volume charge $\rho_q(z')dx'dy'dz'$. According to Coulomb's law (Frankle, 1986), the differential electric field dE_{sz} at a point $P(0, 0, z)$ due to a differential amount of charge $\rho_q(z')dx'dy'dz'$ contained in the volume $dx'dy'dz'$ is given by

$$dE_{sz} = \frac{\rho_q(z')dx'dy'dz'}{4\pi\epsilon_0 r^3} \mathbf{r} = \frac{\rho_s C_q D_s^3 N(z')dx'dy'dz'}{24\epsilon_0 r^3} \mathbf{r}. \quad (4.5)$$

Where $\epsilon_0 (= 8.85 \times 10^{-12} \text{ C}^2\text{N}^{-1}\text{m}^{-2})$ is the electrical permittivity of air and \mathbf{r} is the vector from the point P' to point P with magnitude $r = \sqrt{x'^2 + y'^2 + z'^2}$. By applying the principle of linear superposition, the total electric field can be obtained by integrating the fields produced by all the charges making up the charge distribution. Thus

$$E_{sz} = \frac{\rho_s C_q D_s^3}{6\epsilon_0} \int_{z_0}^{\infty} \text{sign}(z-z') N(z') \arcsin \frac{ab}{\sqrt{[a^2 + (z'-z)^2][b^2 + (z'-z)^2]}} dz'. \quad (4.6)$$

Where z_0 is the aerodynamic roughness related to the surface property. When $z = z'$, $\text{sign}(z-z') = 0$, and when $z > z'$ and $z < z'$, $\text{sign}(z-z') = 1$ and $\text{sign}(z-z') = -1$, respectively. It is seen from Eq. 4.6 that the electric field intensity depends mainly on the number density of the charged particles in

the wind-blown sand flux. Generally, the number density $N(z)$ changes not only with the height, but also with the movement of sand particles. Let $N_1(z)$ and $N_2(z)$ respectively represent the number densities for saltating and suspending sand particles, then the electric field produced by saltating particles, E_{sz}^1 , and that produced by suspending ones, E_{sz}^2 , can be obtained.

Based on the assumption that all saltating and suspending sand particles carry negative charges, from Eq. 4.6, we can find that the electric field at height z produced by saltating sand particles or suspending sand particles lower than height z is downward and increases with height increasing, whether z lies in the saltation layer, the suspending layer or the layer above of the suspending layer. The electric field at height z produced by saltating sand particles or suspending sand particles higher than height z is upward and decreases with height increasing. So the direction of the electric field produced by saltating and suspending sand particles is opposite to the electric field of fair weather and it is upward. This electric field decreases with height increasing, and there exists a height z' and $E_{sz'}^1 = 0$ or $E_{sz'}^2 = 0$. The electric field is opposite to the atmospheric electric field, when $z > z'$, the electric field is inverted with a same direction as the one of fair weather electric field, and it increased with height increasing. When electric field reaches up its extremum and it will decrease with height increasing. $E_{sz} \rightarrow 0$ when $z \rightarrow \infty$. We can also find that both the electric field E_{sz} produced by saltating sand particles and the electric field E_{sz}^2 produced by suspending sand particles make the wind-blown sand electric field stronger or weaker, but their strengths are not equal due to the difference of volume number of saltating sand particles from the one of suspending sand particles.

4.3.2 Electric Field Due to Sand Particles in Sand Bed

Assuming the charge's distribution across a surface, which is characterized by the surface charge density σ_q , the total charges of the particles on the surface and those in the air should be zero according to the law of conservation of electric charge (Frankle 1986). Thus

$$\int_{-a}^a \int_{-b}^b \sigma_q dx' dy' + \int_{-a}^a \int_{-b}^b \int_{z_0}^{\infty} \rho_{q1}(z') dx' dy' dz' + \int_{-a}^a \int_{-b}^b \int_{z_0}^{\infty} \rho_{q2}(z') dx' dy' dz' = 0. \quad (4.7)$$

Where $\rho_{q1}(z)$ and $\rho_{q2}(z)$ are the volume charge densities of saltating and suspending sand particles respectively. We can get

$$\sigma_q = -\frac{1}{6} \pi \rho_s C_q D_s^3 \left[\int_{z_0}^{\infty} N_1(z') dz' + \int_{z_0}^{\infty} N_2(z') dz' \right]. \quad (4.8)$$

The electric field produced by sand particles in sand bed can be written:

$$E_{cz} = -\frac{\rho_s C_q D_s^3}{6\epsilon_0} \left[\int_{z_0}^{\infty} N_1(z') dz' + \int_{z_0}^{\infty} N_2(z') dz' \right] \arcsin \left(\frac{a}{\sqrt{a^2 + z^2}} \frac{b}{\sqrt{b^2 + z^2}} \right). \quad (4.9)$$

It is obvious that charges carried by sand particles in sand bed are positive when we let saltating and suspending sand particles acquire negative charges. So the electric field produced by sand particles in sand bed is downward and decreases with height increasing, that is to say if $z \rightarrow \infty$, $E_{cz} = 0$.

4.3.3 Total Electric Field Due to Charged Sand Particles in Wind-Blown Sand Flux

Considering the electric field of fair weather, the real electric field produced by charged sand particles is $E_z = E_a + E_{sz}^1 + E_{sz}^2 + E_{cz}$. Here we take $E_a = -0.1 \text{ kV}\cdot\text{m}^{-1}$ and sign ‘-’ is opposite to z . As we know, the volumetric concentration of the suspending sand particles is only about $10^{-8}\text{--}10^{-6}$ (Anderson and Hallet 1986), which is much less than the transport rate generated by saltating particles approximating 75% in the wind-blown sand flux (Bagnold 1941). That is $N_2(z) \ll N_1(z)$. Therefore the electric field produced by suspending sand particles is usually neglected.

The complete profiles of the electric field produced by charged particles in wind-blown sand flux at different wind velocities are respectively plotted in Fig. 4.9a for the height $z \leq 0.02 \text{ m}$ and in Fig. 4.9b for $z \geq 0.02 \text{ m}$, where the friction wind velocities are $0.3 \text{ m}\cdot\text{s}^{-1}$, $0.5 \text{ m}\cdot\text{s}^{-1}$ and $0.78 \text{ m}\cdot\text{s}^{-1}$, respectively. It could be seen in Fig. 4.9 that the variations of the electric field does not always monotonically increase or decrease with the height. In fact, the profile of the electric field is composed of three layers. In the first layer near the bed, the electric field can reach several hundred kilovolts per meter in magnitude directed upward, and decreases quickly to zero with height increasing. In the second layer, i.e., after the field becomes zero, the direction of the electric field changes from upward to downward, which is the same as that of the fair weather’s electric field, and the magnitude of the electric field intensity increases from zero to an order of several kilovolts per meter within 10–20 cm. The third layer is the upper one in which the direction of the electric field is also the same as that of the fair weather field and the magnitude of the field decreases as the height reaches until it is equal to that of the fair weather field. This finding coincides well with the phenomena described by Schmidt et al. (1998).

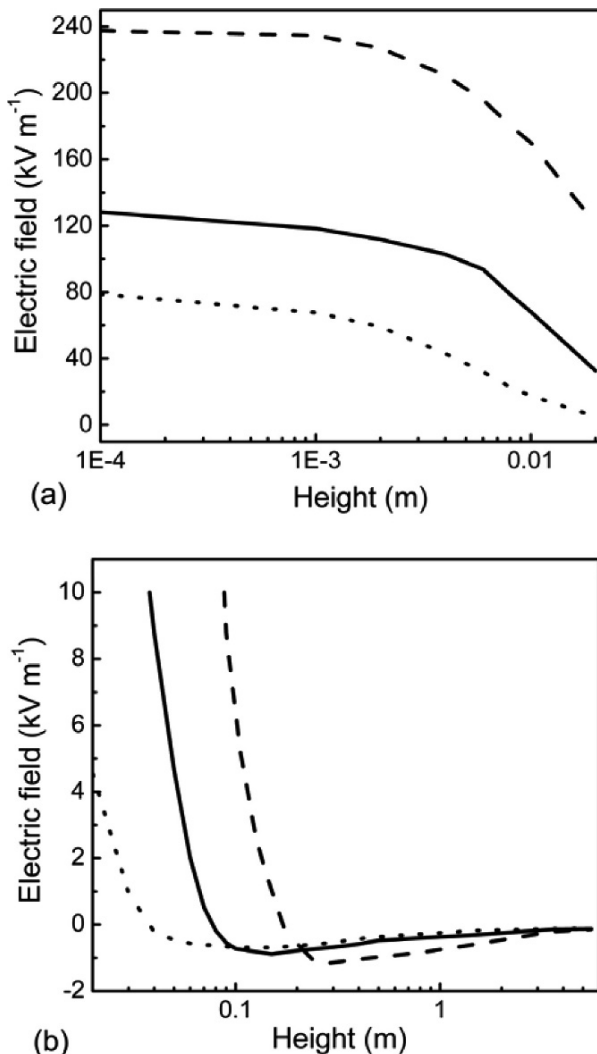


Fig. 4.9. Profile of electric field produced by all charged sand particles in wind-blown sand flux ($D_s = 0.25 \text{ mm}$, $C_q = -60 \mu\text{C}\cdot\text{kg}^{-1}$); (a) for $0.0001 \text{ m} \leq z \leq 0.02 \text{ m}$; (b) for $z \geq 0.02 \text{ m}$; — for $u_* = 0.78 \text{ m}\cdot\text{s}^{-1}$, ——— for $u_* = 0.50 \text{ m}\cdot\text{s}^{-1}$ and - - - for $u_* = 0.30 \text{ m}\cdot\text{s}^{-1}$ (from Zheng et al. 2004)

Ignoring E_{sz}^2 and E_{cz} , we can get the electric field produced by only saltating sand particles (see Fig. 4.10). From Fig. 4.10, the profile of electric field produced by charged saltating sand particles also display a structure of three layers, and the variation of the electric field in each layer is same as the one of the electric field produced by all charged sand particles. In

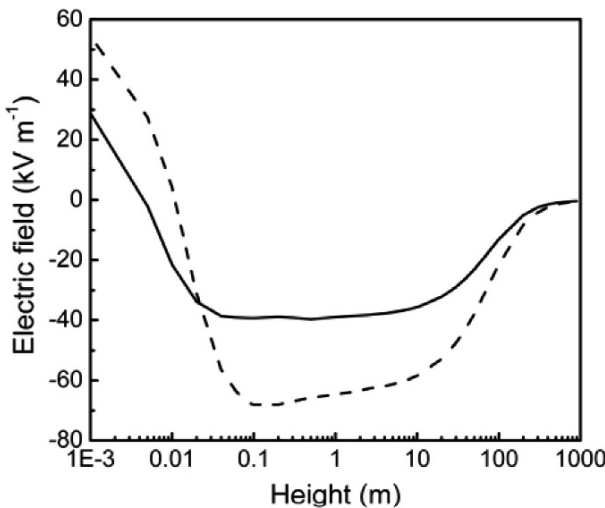


Fig. 4.10. Profile of the electric field produced by charged saltating sand particles in wind-blown sand flux with different charge-to-mass ($C_q = -60 \mu\text{C}\cdot\text{kg}^{-1}$, $D_s = 0.25 \text{ mm}$), — the results for $u^* = 0.30 \text{ m}\cdot\text{s}^{-1}$; - - - the results for $u^* = 0.50 \text{ m}\cdot\text{s}^{-1}$ (modified from Zheng et al. 2004)

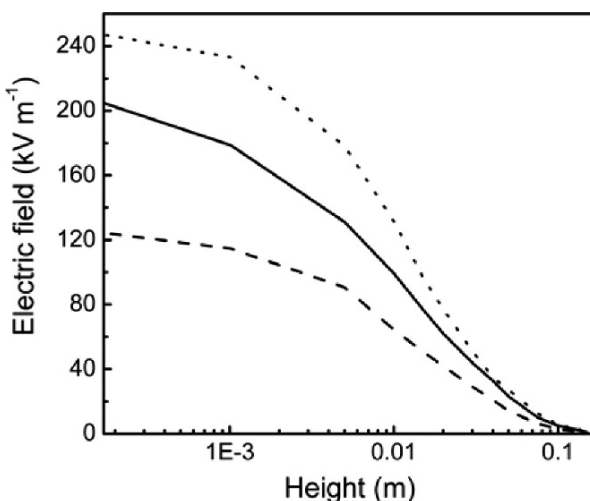


Fig. 4.11. Profile of the electric field produced by all charged sand particles in wind-blown sand flux with different charge-to-mass ($u^* = 0.69 \text{ m}\cdot\text{s}^{-1}$, $D_s = 0.25 \text{ mm}$), - - - for $C_q = -90 \mu\text{C}\cdot\text{kg}^{-1}$; — for $C_q = -60 \mu\text{C}\cdot\text{kg}^{-1}$ and - - - for $C_q = -30 \mu\text{C}\cdot\text{kg}^{-1}$ (modified from Zheng et al. 2004)

addition, we find that electric field indeed increases within a height, which agrees with the measurement results by Zheng, et al. (2003), and the electric field produced by only saltating sand particles also is affected by the particle diameter and wind velocity.

From Eqs. 4.7 and 4.9, it is obviously that the charges carried by sand particles have an effect on the wind-blown sand electric field, and Fig. 4.11 shows the wind electric field varies with height when friction wind velocity is $0.7\text{m}\cdot\text{s}^{-1}$ and the charge-to-mass is $-90\ \mu\text{C}\cdot\text{kg}^{-1}$, $-60\ \mu\text{C}\cdot\text{kg}^{-1}$ and $-30\ \mu\text{C}\cdot\text{kg}^{-1}$ respectively. Near the earth surface ($z < 5\text{ cm}$), the charge-to-mass has a significant effect on the electric field, and the larger of charge-to-mass, the stronger of electric field at the same height. With height increasing, the charge-to-mass has a little effect on the field, and the wind-blown sand electric field approaches to the fair weather's electric field.

Friction wind velocity also has an effect on the wind-blown sand electric field. Shown as Fig. 4.9b, before the wind-blown sand electric field approaches to the fair weather's electric field, the wind-blown sand electric field increases with the friction wind velocity increasing.

It is noteworthy to point that the mass flux is also affected by the wind-blown sand electric field, which will be discussed in next chapter. Recently, some work is conducted to simulate the wind-blown sand electric field following the idea mentioned above, Zheng et al. (2004) and Kok et al. (2006, 2008) take the charges transfer during particle-bed collision and sand particles start acted by wind-blown sand electric field into account. But Kok et al. (2006, 2008) didn't display the simulation results of the wind-blown sand electric field.

4.4 Effects of Charged Sand Particles

4.4.1 Effects on the Entrainment of Sand Particles'

Earth's surface is generally a good conductor because soil particles are usually covered by a thin, conducting film of water (Kanagy and Mann 1994). Therefore, the atmospheric electric field or external electric field can induce charges at the surface (Wahlin 1986). It is the first time that Yue et al. (2003) conducted a study on the threshold wind velocity of an irregular sand particle subjected to electrostatic force, and they also considered the effect of the eccentric distance, eccentric angle and particle diameter. They find that wind-blown sand electric field indeed has an effect on the threshold wind velocity. Especially for a relative high field, it greatly decreases the threshold wind velocity of sand particles.

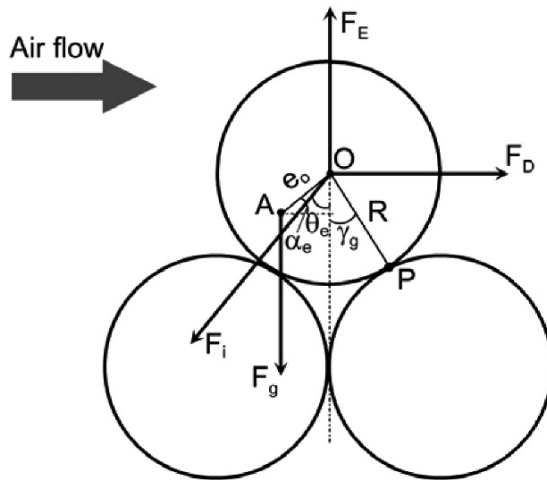


Fig. 4.12. A Schematic illustration of a packed form of sand particles in sand bed, and e_o , α_e and γ_g are the eccentricity, eccentricity-angle and the angle between inter-particle force and gravity, respectively; Point A and O are the center of mass and center of geometry of the sand particle. Point P is the start point of the sand particle. F_i , F_D , F_E and F_g are the inter-particle force, drag force, electrostatic force and gravity

Kok and Renno (2006) analyzed the sand lift acting upon the gravitation, inter-particle force and electric force, considering sand particles charged under the external electric field. With the aid of experiments, Kok and Renno deduced (2008) the threshold electric field necessary to lift a particle under the windless condition. It can be found the critical electric field strength firstly decreases and then increases with sand particle diameter increasing. When the electric field exceeds $150 \text{ kV}\cdot\text{m}^{-1}$, a sand particle can be directly uplifted from surface. They also confirmed that the wind-blown sand electric field can reduce the threshold friction velocity by providing an additional upward force.

In addition, a sand particle in sand bed is always packed by other sand particles (see Fig. 4.12), so its entrainment is confined by its neighboring sand particles. Considering the gravity, inter-particle force, drag force and electrostatic force, we can deduce the threshold friction velocity for a sand particle as

$$u_{st}^2 = \frac{1}{A_1 \rho} \cos \gamma_g \left[\frac{g \pi D_s}{6} (\rho_s - \rho) \left(\sin \gamma_g + \frac{e_o}{R} \cos \alpha_e \right) + \frac{A_2}{D_s} \sin(\theta_e + \gamma_g) - \frac{1.37 \pi \epsilon_0 E_z^2}{C_s} \sin \gamma_g \right]. \quad (4.10)$$

Where E_z is the total field. C_s is a scaling constant introduced to account for the non-sphericity of solid particles ($C_s = 0.4761$), A_1 and A_2 are

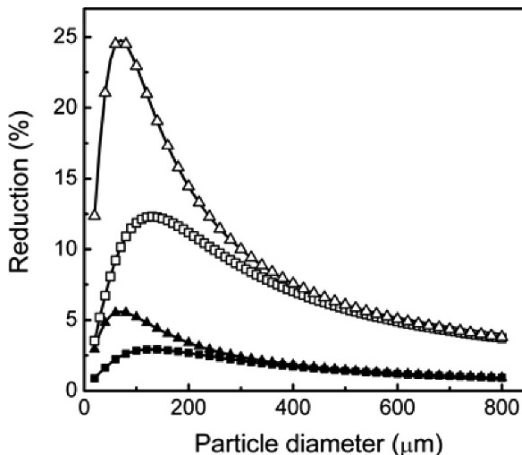


Fig. 4.13. Reduction of the threshold friction velocity as a function of particle diameter, wind-blown sand electric field and packed form; —■— the results under the electric field $50 \text{ kV}\cdot\text{m}^{-1}$ for $\gamma_g = 2^\circ$, $\theta_e = 1^\circ$; —▲— the results under the electric field $50 \text{ kV}\cdot\text{m}^{-1}$ for $\gamma_g = 85^\circ$, $\theta_e = 70^\circ$; —□— the results under the electric field $100 \text{ k}\cdot\text{Vm}^{-1}$ for $\gamma_g = 2^\circ$, $\theta_e = 1^\circ$; —△— the results under the electric field $100 \text{ k}\cdot\text{Vm}^{-1}$ for $\gamma_g = 85^\circ$, $\theta_e = 70^\circ$ (by the author et al.)

dimensionless empirical coefficients associated with the aerodynamic drag and inter-particle force, and they are 4 and $1.5 \times 10^{-4} \text{ kg}\cdot\text{s}^{-2}$, respectively. e_o and α_e are the eccentricity and eccentricity-angle (see Fig. 4.12). θ_e and γ_g are angles between inter-particle force and gravity, and line of OP to gravity. From Eq. 4.10, it can be found that the threshold friction velocity decreases under the wind electric field, and it also can be found that the percent reduction of the threshold friction velocity are effected by the particle diameter, the wind-blown sand electric field and the packed form. Given a packed form, the percent reduction varies with the particle diameter shown as Fig.4.13, and the threshold friction velocity can fall 25% when the wind-blown sand electric field is about $100 \text{ kV}\cdot\text{m}^{-1}$.

4.4.2 Effects on Electromagnetic Wave Propagation

The attenuation of microwaves in sand (dust) storm is directly observed by Al-Hafid et al. (1979a, 1979b, 1980) and Chen (1991). They found that the sand (dust) storm not only has an effect on the attenuation of electromagnetic wave propagation, for example, the microwaves of 10 GHz weakened at a velocity 10–15 dB per tens of minutes, in a sand (dust) storm occurring in Nasiriya-Daraji, but also, to some bad extent, the microwaves

can be completely weakened within several hours. The attenuation of electromagnetic waves is relative to the sand particles radius, and for the electromagnetic waves of 10 GHz, the attenuation reaches up to maximum when the wave length is comparative to the particle radius.

Based on the scattering theory of millimeter microwaves and Rayleigh approximation, Ryde (1941) is the earliest researcher who calculated the scatter of microwaves propagating in a sand (dust) storm. Haddad et al. (1983) measured the permittivity and diameter distribution of sand particles collected from a sand (dust) storm happened in Iraq, and then they calculated the attenuation of microwaves of 9.4 GHz propagating in a sand (dust) storm by the relationship of optical visibility and dust concentration presented by Chu (1974), which is $0.001 \text{ dB}\cdot\text{m}^{-1}$ for the sand particles with mass density $6\times 10^{-5} \text{ g}\cdot\text{cm}^{-3}$. In order to verify the calculation results, Haddad measured an attenuation of $0.0034 \text{ dB}\cdot\text{m}^{-1}$ under the same condition as one in calculation, and it is as much as 34 times larger than the calculated value, which shows that the effect of a sand (dust) storm on electromagnetic wave propagation is notable.

Zhou et al. (2005) presented a new model to investigate the effect of charges carried by sand particles on attenuation of electromagnetic waves. For simplicity, they took a sand particle as a sphere with the permittivity ε_s and the volume V_s , and the electrical charges uniformly distribute in the shape of a spherical cap as shown in Fig. 4.14. In real sand (dust) storms,

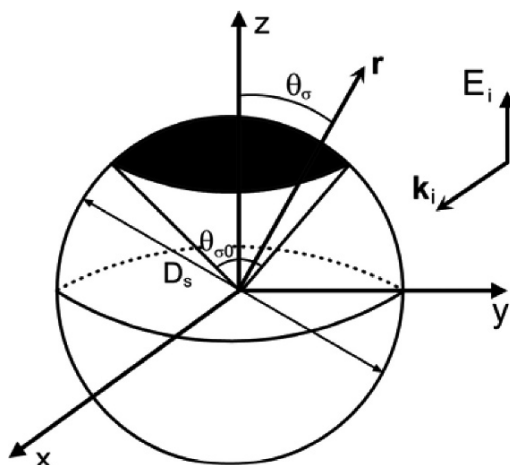


Fig. 4.14. Schematic drawing of a sand particle with the electric charges distributed on a spherical cap (marked by the black domain) with angle $\theta_{\sigma 0}$ and density of surface charge σ_q , and \mathbf{k}_i and \mathbf{E}_i are incident direction of the incident electromagnetic wave and incident E-field direction, respectively

the radius of a sand particle is far smaller than the wavelength of centimeter microwaves or millimeter microwaves, so we can use the Rayleigh approximation to solve the inner electric field of the particles.

Eq. 4.7 gives an analytical formula of the scattering attenuation (denoted by A) when a microwave with wave number k propagates in a sand (dust) storm which has a visibility V_b and average sand particle with a partial distribution of electric charges σ_q and $\theta_{\sigma 0}$, and derivation of formula is reported by Zhou et al. (2005) for details.

$$A = \frac{20}{V_b} k^4 D_s^4 \left| \frac{\varepsilon_s - \varepsilon_0}{\varepsilon_s + 2\varepsilon_0} \right|^2 + \frac{90}{V_b} D_s k \varepsilon_r'' \left| \frac{\varepsilon_0}{\varepsilon_s + 2\varepsilon_0} \right|^2 + \frac{7.5}{9} k^4 D_s^6 C_q^2 \frac{\rho_s^2 (\varepsilon_s - \varepsilon_0)^2 \sin^2 \theta_{\sigma 0}}{\varepsilon_0^4 E_i^2 (1 - \cos \theta_0)^2 V_b}. \quad (4.11)$$

Where ε_r'' is the relative permittivity of sand particles to air. E_i is the electric field of incident electromagnetic wave.

Characteristic curves of the attenuation coefficient varying with angle $\theta_{\sigma 0}$ of electric charge distribution for different densities of surface charge σ_q shown as Fig. 4.15, in order to compare them with the measured results by Haddad et al. (1983). Here the same parameters as ones in the real sand (dust) storm are used, such as frequency 9.4 GHz, radius of sand 40 μm , permittivity of sand $2.634 + 0.734i$, visibility 10 m and the intensity of incident electric field $50 \text{ V}\cdot\text{m}^{-1}$. The measured value of attenuation coefficient in this experiment is $0.034 \text{ dB}\cdot\text{m}^{-1}$ (Haddad 1983), which is plotted

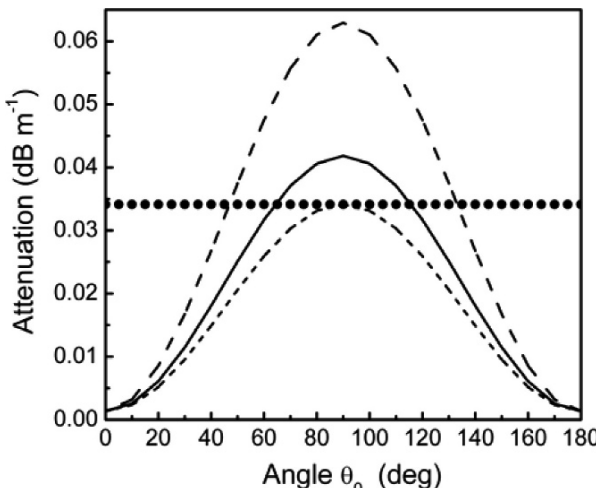


Fig. 4.15. Characteristic curves of the attenuation coefficient varying with angle $\theta_{\sigma 0}$ of electric charge distribution for different densities of surface charge σ_q ; --- for $\sigma_q = 2.7 \mu\text{C}\cdot\text{m}^{-2}$, — for $\sigma_q = 3.0 \mu\text{C}\cdot\text{m}^{-2}$ and - - - for $\sigma_q = 3.7 \mu\text{C}\cdot\text{m}^{-2}$. Measured value, ● attenuation coefficient $A = 0.034 \text{ dB}\cdot\text{m}^{-1}$ (from Zhou et al. 2005)

by a straight line parallel to the horizontal axis in Fig. 4.2. When the sand particles are not charged, the attenuations are $0.001 \text{ dB}\cdot\text{m}^{-1}$, which is equal to the one calculated by Haddadt (1983). From Fig. 4.15, it can be found that the attenuation coefficient varies with the increase of $\theta_{\sigma 0}$ in a sinusoidal curve, given the charge-to-mass ratios. When $\theta_{\sigma 0}=0$ and $\theta_{\sigma 0}=\pi$, the attenuation coefficient is minimum, and $\theta_{\sigma 0}=\pi/2$, the attenuation coefficient reaches up to its maximum value. That is to say that the charges carried by sand particles have a significant effect on the attenuation of electromagnetic waves. When $\sigma_s = 2.7 \mu\text{C}\cdot\text{m}^{-2}$ and $\sigma_s = 3 \mu\text{C}\cdot\text{m}^{-2}$, the attenuation coefficients are equal to the measured one, accordingly $\theta_{\sigma 0} = 63^\circ$ and $\theta_{\sigma 0} = 117^\circ$. It also indicates that the sand particles are partly charged. And an important conclusion can be induced that sand particles are charged partly.

Though we can solve the problem mentioned above by Mie theory (Bohren and Huffman 1983) when the size of dust particles is not smaller than the wavelength of electromagnetic waves, it is necessary to consider the effect of sand particles' velocity and multiple-scattering among sand particles on the attenuation of electromagnetic waves. So it requires a further study.

Chapter 5 Wind-Blown Sand Flux and its Prediction

Wind-blown sand transport in the near surface layer is the key form as well as the most concentrated and popular content of wind-blown sand physics. It is also an important process in the formation of aeolian landforms. In the early stage of wind-blown sand physics, scientists studied the sand transport mechanisms through field measurements and wind tunnel experiments. They studied the movement of a single particle in wind-blown sand flow, explored its lift-off mechanisms, defined different motion patterns of a single particle through theoretical analysis. These works established the base of wind erosion research. In order to further reveal the regularities of wind-blown sand flux and to satisfy the need of the development of space science (it seems that sand (dust) storms and dust devils happen more frequently on other planets, for example on Mars, than on Earth), people began to study the macroscopic structure of wind-blown sand flow in 1970s.

It is very important to predict theoretically the whole behavior of wind-blown sand transport, because it is difficult to get its initiating and developing mechanisms on other planets and sometimes even on Earth through measurements, for example, the revealing of the stratification phenomenon in the mass flux (see Sect. 5.4). In the meantime, the research on prediction of the whole structure of wind-blown sand flux will continuously promote the development of computational fluid dynamics, will improve the accuracy of prediction mode of sand (dust) storm and promote the realization of theoretical prediction on the initiating and developing processes of sand (dust) storm, and will make the engineering design of sand prevention and control more rational. But it is a stepwise process of developing and improving to realize the accuracy prediction of the evolution process of wind-blown sand movement, for the research which involves multi-scale, coupling of multi-field, turbulence and other common scientific problems. In this chapter, Sect. 5.1 introduces the expressions of the forces exerted on a saltating sand particle; Sect. 5.2 provides the theoretical predicting methods and results on sand saltation cloud under both of steady state and unsteady wind fields, with emphasis on the effects of sand electrification and Magnus force on wind-blown sand movement; Sect. 5.3 proposes an ex-

precision of sand transport rate fitted by data of wind tunnel experiment and introduces a methodology to effectively improve precision for fitting experimental data for the sand flux; Finally, Sect. 5.4 presents the theoretical models, methods and quantitative results for predicting the evolution process of sand saltation cloud and simulating the development of dust devil.

5.1 Forces on Saltating Sand Particles

Force analysis is the base of describing the motions of objects or mediums. And it is also true for sand particles moving in air flow. We will analyze forces on the moving particles in the wind flow and then deduce the inverse force by particles on the wind field \mathbf{F}_x .

For simplicity, a spherical particle with diameter D_s and density ρ_s is assumed to travel in a two-dimension wind field with density ρ and velocity u as shown in Fig. 5.1, where x is in the mean wind direction and z is in the vertical direction. Forces acting on the particle include aerodynamic drag \mathbf{F}_D , the gravity force \mathbf{F}_g , aerodynamic lift \mathbf{F}_L , the Magnus force \mathbf{F}_M , the electric force \mathbf{F}_E , the Saffman force \mathbf{F}_s and Basset force \mathbf{F}_B .

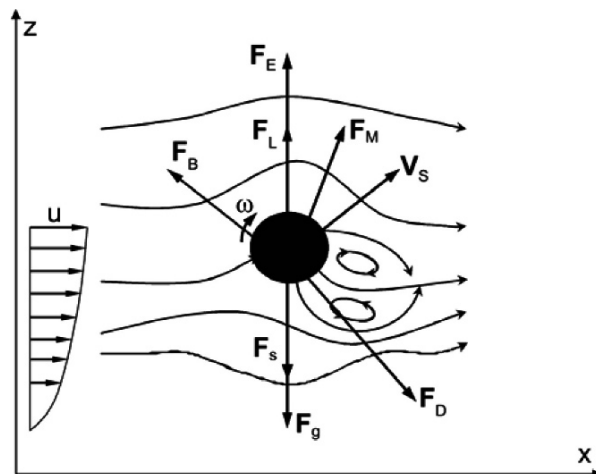


Fig. 5.1. An schematic illustration of forces acting on a particle, including aerodynamic drag \mathbf{F}_D , the gravity force \mathbf{F}_g , aerodynamic lift \mathbf{F}_L , the Magnus force due to particle rotation \mathbf{F}_M , and the electric force \mathbf{F}_E due to the movement of the charged particle in the electric field produced by charged particles, the Saffman force \mathbf{F}_s and Basset force \mathbf{F}_B , u is the wind velocity, \mathbf{V}_s is velocity of sand particle, ω is angular velocity of sand particle

The particle-to-air density ratio is about 2000 for the density of quartz particle is about $\rho_s = 2.65 \text{ g}\cdot\text{cm}^{-3}$ while the air density is approximately $1.2\text{kg}\cdot\text{cm}^{-3}$. Hence, the buoyancy upon an airborne soil particle is negligible though it should be subtracted in the calculation of gravity force, and the gravity force \mathbf{F}_g can be given by

$$\mathbf{F}_g = \frac{1}{6}\pi D_s^3 \rho_s \mathbf{g}. \quad (5.1)$$

If a particle moves in air flow, a force in the opposite direction of the relative velocity between the particle and air is exerted by the fluid on the particle. This force is known as the drag that arises from the pressure differences between the frontal region and the wake region of the particle and from the transfer of momentum from the fluid to the particle through molecular motion, namely the viscous effect. The force \mathbf{F}_D exerted by the flow on the particle is equal to the integral of total stress (or momentum flux) over the surface of the particle and it can be expressed as

$$\mathbf{F}_D = \frac{1}{8}\pi C_D \rho D_s^2 |\mathbf{u} - \mathbf{V}_s| (\mathbf{u} - \mathbf{V}_s). \quad (5.2)$$

Where the aerodynamic drag coefficient C_D is a function of the particle Reynolds number $Re = |\mathbf{u} - \mathbf{V}_s| D_s / \nu$ which can be expressed as the following experiential formula in the range of (1,100), see Morsi and Alexander (1972).

$$C_D = \frac{24}{Re} \left(1 + 0.15 Re^{0.687} \right) \quad (5.3)$$

Through the Bernoulli equation for a steady-state inviscid and barotropic flow in which the total head (sum of velocity head, pressure head and gravity head) remains constant along a given streamline, we know that for a spherical particle placed in a shear flow, pressure in the faster-flow region over the upper surface of the particle is smaller than that in the slower-flow region over the lower surface. The aerodynamic lift increases with shear stress, which results in a normal pressure gradient to the shear in the direction of decreasing velocity. In similar way to aerodynamic drag, the aerodynamic lift can be approximately given by

$$\mathbf{F}_L = \frac{1}{8}\pi C_L \rho D_s^2 \left[(\mathbf{u}^{top})^2 - (\mathbf{u}^{bot})^2 \right] \quad (5.4)$$

where \mathbf{u}^{top} and \mathbf{u}^{bot} are velocities of the flow over the upper and the lower surface of particle respectively, C_L is the aerodynamic lift coefficient, it is

usually assumed to be proportional to the aerodynamic drag coefficient, for example $C_L = 0.85C_D$. For spherical particle, \mathbf{F}_L is important only in strong shear flow. For a non-spherical particle, however, \mathbf{F}_L can be significant even in uniform flows.

A particle transporting in fluid often rotates, especially after impacting with other particles or with the surface. As discussed in Chap. 3, rotation of particles with angular velocity ω from hundreds to thousands circle per second may take place in the processes of both lifting off from sand surface and moving in the air, as a result the particle will be affected by a so called Magnus force whose direction perpendicular to both the direction of rotation and the direction of motion (Tritton 1988). Based on the motion equation and a series of assumptions, the principal vector F_{Mz} and principal moment M_{Mz} of Magnus force \mathbf{F}_M and moment M in oxz plane can be derived (Rubinow and Keller 1961; White and Schulz 1977) as follow.

$$\mathbf{F}_{Mz} = \frac{1}{8}\pi D_s^3 \rho |\mathbf{V}_s - \mathbf{u}| \left(\omega - \frac{1}{2} \frac{\partial u}{\partial z} \right), \quad M_{Mz} = \pi \mu D_s^3 \left(\omega - \frac{1}{2} \frac{\partial u}{\partial z} \right), \quad (5.5)$$

where μ is the viscosity of air, usually is taken as $1.8 \times 10^{-5} \text{ kg}\cdot\text{m}^{-1}\text{s}^{-1}$.

From the physics of electrostatic theory we know that the electrostatic force \mathbf{F}_E exerted on a particle moving in an electric field $\mathbf{E}_s = (E_x, E_y, E_z)$ with charge q^c is equal to $\mathbf{F}_E = \mathbf{E}_s q^c$ as described by Coulomb's law. If only the component of \mathbf{E}_s along z direction is considered, we can see from Chap. 4 that the total electric field is composed of atmospheric electric field E_a , the electric fields $E'_{sz}(z)$ and $E''_{sz}(z)$ produced by the saltation and suspension sand particles respectively, and electric field $E_{cz}(z)$ produced by creep sand particles. Given the specific charge C_q of a particle, which is defined as the charge per unit mass and can be obtained through experiment, the electrostatic force F_{Ez} along z direction exerted on the spherical particle with charge $q^c = 3C_q\pi\rho_s D_s^3 g/32$ is:

$$F_{Ez} = \frac{3}{32} C_q \pi \rho_s D_s^3 g [E_a + E'_{sz}(z) + E''_{sz}(z) + E_{cz}(z)], \quad (5.6)$$

where the atmospheric electric field is assumed to be $E_a = -120 \text{ V}\cdot\text{m}^{-1}$, $E'_{sz}(z)$, $E''_{sz}(z)$ and $E_{cz}(z)$ are calculated by Eqs.4.6 and 4.9 respectively. It is noticeable that the electric field caused by wind-blown sand is related to particle concentration at different heights, since electrostatic force directly affects the acceleration of sand particles and further their trajectories and distribution, so electrostatic force and wind-blown sand flow are coupled.

A spherical particle moves through a viscous liquid with a transverse velocity gradient will experience a transverse force which is perpendicular to

the flow direction even if the particle does not rotate (Saffman 1965). The force is called Saffman force and can be written as (Saffman 1965):

$$\mathbf{F}_s = 1.615 D_s^2 (\mathbf{u} - \mathbf{V}_s) \sqrt{\rho \mu \nabla \times \mathbf{u}}, \quad (5.7)$$

where ∇ is gradient operator. Saffman force is caused by viscosity in nature, so it is different from the lift force \mathbf{F}_L caused by the velocity difference between two adjacent flow layers.

Further, when the inertia of the fluid boundary layer around a particle's surface is considered, the particle which is moving in viscous fluid will bear a force called Basset force, which is associated with the movement history of the particle and is caused by the unsteadiness of the fluid boundary layer over it. Basset force can be expressed by (Odar and Hamilton 1964):

$$\mathbf{F}_B = \frac{3}{2} D_s^2 \sqrt{\rho \pi \mu} \int_0^t \frac{1}{\sqrt{t-\tau}} \frac{d(\mathbf{u} - \mathbf{V}_s)}{d\tau} d\tau, \quad (5.8)$$

It is notable that the direction of Basset force can not be determined for the reason that it is calculated through integrating the relative acceleration between the particle and viscous fluid. The research of Vojir and Michalides (1994) reveals that if the ratio of the density of fluid and of particle is less than 0.002 then the Basset force can be neglected. So in the case of sand particle moving in air flow, the Basset force is usually neglected.

According to the Newton's third Law, the forces which are put on a particle by the wind flow when it is moving in air have corresponding forces which equal to the above forces in quantity but have opposite directions, and these certain forces will be put on the fluid. Taking the component along x direction (air flow direction) as an example, we try to explain the calculation of the force of sand particles on the air. Defining the derivative (\dot{x}, \dot{z}) and (\ddot{x}, \ddot{z}) as the velocity and the acceleration of particle with mass m_s at point (x, z) respectively. If the particle number flux from surface bed $N_s(t)$ (the number of ejected particles per unit area per unit time) and the lift-off velocity probability density at vertical direction $f(V, t)$ at t are both given, then the particle number within the zone $[z - dz, z]$ at t will be $N_s(t)(1/|\dot{z}_\uparrow| + 1/|\dot{z}_\downarrow|)dz$ (Ungar and Haff 1987), where \dot{z} is the mean vertical velocity of particle in $[z - dz, z]$, the subscripts ' \uparrow ' and ' \downarrow ' respectively represent those quantities corresponding to ascending and descending particles. The force per unit volume on the wind at the height z by all sand particles is given as

$$F_x(z, t) = m_s \int_{V_{\min}}^{V_{\max}} N_s(t) f(V, t) \left[\frac{\dot{x}_\uparrow}{|\dot{z}_\uparrow|} + \frac{\dot{x}_\downarrow}{|\dot{z}_\downarrow|} \right] dV \quad (5.9)$$

where $m_s = \rho_s \pi D_s^3 / 6$ is the mass of a sand particle, $f(\dot{z}_0, t)$ can be obtained from chap. 3, and $N_s(t)$ consists of $N_a = N_0(\tau_a - \tau_c)$ which is called the aerodynamic entrainment rate and $\bar{N}_r = \int_{V_{im-\min}}^{V_{im-\max}} N(V_{im}) \int_{V_r \min}^{V_r \max} f_{V_r}(V_{im}) dV_r dV_{im}$, $\bar{N}_e = \int_{V_{im-\min}}^{V_{im-\max}} N(V_{im}) \int_{V_e \min}^{V_e \max} f_{V_e}(V_{im}) dV_e dV_{im}$, the latter two parts are respectively called the rebound entrainment rate and the ejection entrainment rate which are caused by the rebounding and ejecting process when a particle impact sand bed, in which $N(V_{im})$ is the number of particles impacting the sand bed with velocity V_{im} per unit area per unit time, $f_{V_r}(V_{im})$ and $f_{V_e}(V_{im})$ are numbers of rebounding and ejecting sand particles with the velocities of V_r and V_e respectively after a single particle impacts the sand bed with a velocity of V_{im} , and $V_{r\min}$ and $V_{r\max}$ are the possible minimum and maximum rebounding speeds respectively while $V_{e\min}$ and $V_{e\max}$ are the minimum and maximum ejecting speeds respectively, the boundary value ' $V_{im-\max}$ ' and ' $V_{im-\min}$ ' are the maximal and minimal velocities of sand particles which impact sand-bed. For the aerodynamic entrainment rate part, N_0 is a constant, for example $N_0 = 10^5 \text{ N}^{-1} \text{ s}^{-1}$, τ_a is instantaneous fluid shear stress near the bed, τ_c is the critical fluid shear stress, which can be obtained by experiment. It is remarkable that $F_x(z)$ is connected to the lift-off velocity and movement of sand particles. Through a coupling process between wind profile and $F_x(z)$ then finally the wind-blown sand flow can reach equilibrium. If results of Anderson and Haff (1991) are accepted (see Eqs. 3.34 and 3.35), then $N_s(t)$ is given as

$$\begin{aligned} N_s(t) &= N_a + \bar{N}_e + \bar{N}_r \\ &= N_0(\tau_a - \tau_c) + 0.95 \int_{V_{\min}}^{V_{\max}} \int_{V_{im-\min}}^{V_{im-\max}} \exp \left[-\frac{(V - 0.56V_{im})}{(0.2V_{im})^2} \right] dV dV_{im} . \quad (5.10) \\ &\quad + 1.75 \int_{V_{\min}}^{V_{\max}} \int_{V_{im-\min}}^{V_{im-\max}} V_{im} \exp \left[-\frac{V}{0.25V_{im}^{0.3}} \right] dV dV_{im} \end{aligned}$$

Where V presents lift-off speed of particle rebounding or ejecting from the bed. $V_{\min} = \sqrt{2gD_s}$ and $V_{\max} = 5u_*$ are the minimum and maximum lift-off speeds of sand particles respectively. It is the coupling effect that finally makes wind-blown sand flow reaches the equilibrium. From Eq. 5.10, $N_s(t)$ the number of particles lifting off the bed with different speeds V and an-

gles θ can be gained, and through statistical method the probability density of initial lift-off speed function of sand particles $f(V, t)$ can also be obtained. It is remarkable that $F_x(z, t)$ is connected to the lift-off velocity and movement of sand particles, whereas the lift-off velocity and movement of sand particles are affected by wind. It is the coupling effect that finally makes the wind-blown sand flow reaches the equilibrium (Ungar and Haff 1987).

5.2 Sand Saltation

5.2.1 The Effect of Wind-Blown Sand Electric Field on Sand Saltation

Based on the analysis of forces above and Newton's second law, the dynamical equation of a particle can be expressed as

$$m_s \mathbf{a}_s = \mathbf{F}_g + \mathbf{F}_D + \mathbf{F}_L + \mathbf{F}_M + \mathbf{F}_E + \mathbf{F}_S + \mathbf{F}_B, \quad (5.11a)$$

$$I_s \dot{\omega} = M_z, \quad (5.11b)$$

where \mathbf{a}_s is the acceleration of sand particle and its components in oxz are \ddot{x} and \ddot{z} , respectively. I_s denotes the processional moment. Assuming that the sands are similar to spheres, the processional moment can be expressed by $I_s = D_s^2 m_s / 10$. $\dot{\omega}$ is the angular acceleration of sand particles. M_z is the moment of force by air flow. If only gravity force \mathbf{F}_g , the aerodynamic drag \mathbf{F}_D , the Magnus force \mathbf{F}_M and the electric force \mathbf{F}_E are considered on spherical sand particles, the dynamical equations with the initial and boundary conditions of a single sand saltating in oxz plane can be expressed as

$$\begin{aligned} m_s \ddot{x} &= F_{sx} = (\mathbf{F}_D + \mathbf{F}_M)_x + E_x q^c \\ &= -\frac{1}{8} \rho \pi D_s^2 \left[\frac{24\nu}{D_s \sqrt{(u-\dot{x})^2 + \dot{z}^2}} + \frac{6}{1 + \sqrt{\frac{D_s}{\nu} \sqrt{(u-\dot{x})^2 + \dot{z}^2}}} + 0.4 \right], \quad (5.12a) \\ &\times (u-\dot{x}) \sqrt{(u-\dot{x})^2 + \dot{z}^2} + \frac{1}{8} \pi \rho D_s^3 \dot{z} \left(\omega - \frac{1}{2} \frac{\partial \dot{x}}{\partial z} \right) + E_x q^c \end{aligned}$$

$$\begin{aligned}
m_s \ddot{z} &= F_{sz} = \mathbf{F}_g + (\mathbf{F}_D + \mathbf{F}_M)_z + E_z q^c \\
&= -\frac{1}{8} \rho \pi D_s^2 \left[\frac{24\nu}{D_s \sqrt{(u-\dot{x})^2 + \dot{z}^2}} + \frac{6}{1 + \sqrt{\frac{D_s}{\nu} \sqrt{(u-\dot{x})^2 + \dot{z}^2}}} + 0.4 \right], \quad (5.12b) \\
&\times \dot{z} \sqrt{(u-\dot{x})^2 + \dot{z}^2} - m_s g + \frac{1}{8} \pi \rho D_s^3 (u-\dot{x}) \left(\omega - \frac{1}{2} \frac{\partial \dot{x}}{\partial z} \right) + E_z q^c
\end{aligned}$$

$$m_s \dot{\omega} = 10 \pi \mu D_s \left(\omega - \frac{1}{2} \frac{\partial \dot{x}}{\partial z} \right), \quad (5.12c)$$

$$t = 0 : \quad x = 0, z = 0, \dot{x} = 0, \dot{z} = V, \omega = \omega_0. \quad (5.12d)$$

where F_{sx} and F_{sz} are the components of the forces acting on a saltating particle., E_x and E_z are horizontal and vertical components of electric field. V and ω_0 are given initial linear and angular velocities respectively. As a sand particle moving in air flow, which is considered to in a steady state and keep a fixed horizontal direction, the wind profile in Eq. 5.12 can be taken as logarithmic for the reason that the effect on air flow caused by a single sand particle is neglected. Through solving Eq. 5.12 we can get the saltation trajectory and characteristics of a single particle moving in steady atmospheric boundary flow.

Here, we assume that a particle bears only gravity force \mathbf{F}_g , aerodynamic drag force \mathbf{F}_D and Magnus force F_{Mz} , and it has a diameter of 0.25 mm and a density of $2650 \text{ kg}\cdot\text{m}^{-3}$, and its lift-off velocity $V = 0.45 \text{ m}\cdot\text{s}^{-1}$. Following White and Schulz (1977), we select three kinds of ejection angular velocities: $\omega_0 = 275, 600, 900 \text{ rev}\cdot\text{s}^{-1}$. Fig. 5.2 presents the trajectories of a particle with four different angular velocities. From Fig. 5.2 we can see that the length and height of sand saltation trajectory are respectively 58 mm and 8.9 mm for $\omega_0 = 0$, whereas the length and height of the sand saltation trajectory are 80 mm and 10 mm for $\omega_0 = 275 \text{ rev}\cdot\text{s}^{-1}$, which increase 36% and 20% compared to the former values respectively. When $\omega_0 = 600 \text{ rev}\cdot\text{s}^{-1}$, the length and height of the saltation trajectory are 118 mm and 12.5 mm, which increase 104% and 40% compared to the corresponding values for $\omega_0 = 0$ respectively. Therefore Magnus force has obvious effect on saltation trajectories, and this effect on the saltation trajectory increases with the initial angular velocity.

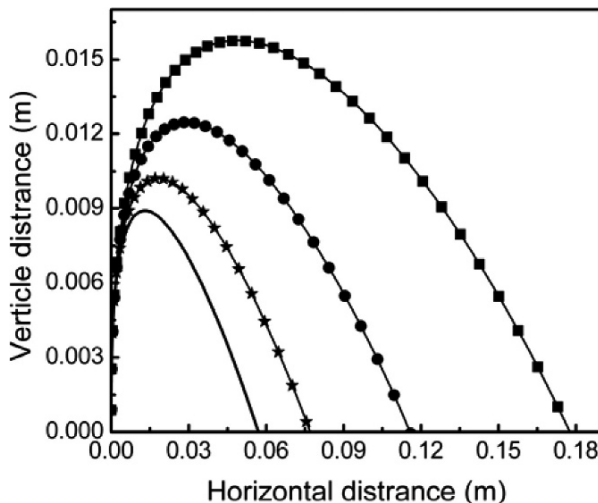


Fig. 5.2. The trajectories of a particle with four ejection angular velocities, with sand diameter 0.25 mm, mass density $2.65 \text{ g}\cdot\text{cm}^{-3}$ and ejection velocity $0.45 \text{ m}\cdot\text{s}^{-1}$; — the simulated for the initial angular velocities $\omega_0 = 0 \text{ rev}\cdot\text{s}^{-1}$, —★— the simulated for the initial angular velocities $\omega_0 = 275 \text{ rev}\cdot\text{s}^{-1}$, —●— the simulated for the initial angular velocities $\omega_0 = 600 \text{ rev}\cdot\text{s}^{-1}$, —■— the simulated for the initial angular velocities $\omega_0 = 900 \text{ rev}\cdot\text{s}^{-1}$, respectively (by author et al.)

Another noticeable question is whether the effect of electrostatic force on sand saltation cloud is important. Zheng et al. (2003) proposed a theoretical model with consideration of coupling among sand particles, wind field and electric field to reveal the effect of electrostatic force on sand saltation, an obvious effect was observed when electrostatic force was considered into their model. But just as Shinbrot and Herrmann (2008) pointed out in their article published in the Journal of Nature that: ‘despite experimental data demonstrating that particles readily acquire substantial charges, with few notable exceptions (Zheng et al. 2003), surprisingly little fundamental analysis has been done on how charge affects granular flow’. In order to investigate this problem further, we promote a model in the following. For simplicity, we only take the average saltation trajectory in stable atmospheric boundary as an example. Besides the motion equation and initial boundary condition given in Eq. 5.12, we need to consider the reacting force of sand particles on wind field $u(z)$ in sand saltation cloud. Therefore it needs to substitute Eq. 5.9, which calculates the reacting force of sand particles on wind, into Eq. 2.32. That is:

$$\int_{V_{\min}}^{V_{\max}} N_s m_s f(V) \left(\frac{\ddot{x}_\uparrow}{|\dot{z}_\uparrow|} + \frac{\ddot{x}_\downarrow}{|\dot{z}_\downarrow|} \right) dV + \frac{d}{dz} \left[\rho k^2 z^2 \left(\frac{du}{dz} \right)^2 \right] = 0 \quad (5.13a)$$

Accordingly the boundary conditions can be taken as:

$$z = z_0 : u = 0 \quad (5.13b)$$

$$z \rightarrow \infty : kz \frac{du}{dz} = u_* \quad (5.13c)$$

Here $z_0 = D_s / 30$ presents the roughness of flat bed. u_* is the friction velocity of air flow. It should be noticed that there exist internal relations and interactions among the particle number flux N_s , wind velocity u and initial speeds of sand particles V and ω_0 , which is different from the calculations of a single sand particle. Therefore it needs to determine the number flux and initial speeds V and ω_0 of sand particles by splash function and probability density function of lift-off velocities of sand particles, which are depicted in Chap. 3.

The practical calculations are as follows: input u_* , ν , κ , D_s , m_s , ρ , ρ_s , C_q and components of the electric field E_x , E_z . To be conveniently compared with the results of Schmidt et al. (1998), C_q , E_x and E_z are given initially although they are actually related to the intensity of wind-blown sand flux. At first assume du/dz in Eq. 5.13c to be a positive constant $(c)_1 > 0$ to be adjusted and choose the values of lift-off velocity (V)₁ of sand particles (for simplicity the rotation of particles is not taken into consideration) and the number flux of particles entrained directly by the aerodynamic force of air flow N_a , which is taken as the initial value of the particle number flux N_s . Then calculate the initial wind profile $u_1(z)$ under given friction velocity of u_* through solving Eq. 5.13. Based on initial wind profile $u_1(z)$ the saltation trajectory can be obtained through solving Eq. 5.12, denote the results by $x_1(t)$ and $z_1(t)$. Then calculate the new wind profile $u_2(z)$ through solving Eq. 5.13a and boundary conditions Eqs. 5.13b and 5.13c. If the condition $|u_{i+1}(z) - u_i(z)|_{\max} < \bar{\varepsilon}_1$, in which $\bar{\varepsilon}_1$ is a pre-precision, is not satisfied, replace wind profile $u_1(z)$ by $u_2(z)$ and calculate a new sand's saltation trajectory and wind profile. Repeat the above steps until the condition $|u_{i+1}(z) - u_i(z)|_{\max} < \bar{\varepsilon}_1$, is satisfied. Based on the calculated impact velocity V_{im} of sand particles, the probability density function of lift-off velocities of sand particles (Anderson and Hallet 1986), which are depicted in Sects. 3.4 and 3.5 can be confirmed. In this way, the new lift-off velocity of sand particles and particle number flux are calculated, which are denoted as (V)₂ and (N_s)₂ respectively. At these new conditions, repeatedly calculate the

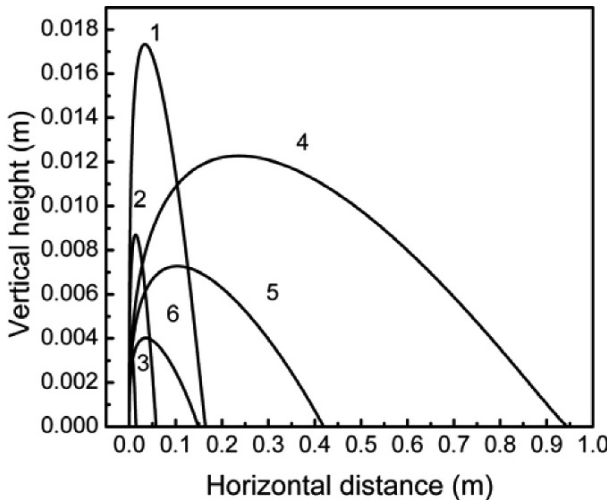


Fig. 5.3. The average trajectories of sand motion in saltation cloud in a stable atmospheric boundary, with $u_* = 0.4 \text{ m}\cdot\text{s}^{-1}$, $E_x = E_y = 0$, $E_z = 51000(0.01y)^{-0.6} \text{ V}\cdot\text{m}^{-1}$. Curves 1, 2, 3 are results when the coupling effect of sand particles and wind is taken into account, curves 4, 5, 6 results when are the coupling effect of sand particles and wind is not taken into account, and Curves 1, 2, 3, and 4, 5, 6 represent the average trajectories of particles with average specific charges $C_q = 60, 0, -60 \mu\text{C}\cdot\text{kg}^{-1}$, respectively (Zheng et al. 2003)

wind profile until iterative calculated lift-off velocity of sand particles and particle number flux satisfy the pre-precisions. Then iterate the assuming constant (c)₁ until the pre-precision is satisfied. Finally the sand saltation regularities, which include wind profile and the motion of sand particles can be obtained. Another simpler way to calculate the sand saltation regularities is to choose the simplest splash function proposed by Ungar and Haff (1987), just as what Zheng et al. (2003) have done.

Fig. 5.3 shows a comparison among the simulated average trajectories of sand motion in saltation cloud in a stable atmospheric boundary when the effect of the electric force on wind flow is and is not taken into account in the simulation model, and the sand possesses different electric charges. Similar to the result in Schmidt et al. (1998) which did not consider the effect of drag force on wind flow, the parameters of average specific charge and electric field are taken as same as those in Schmidt et al. (1998), i.e., $C_q = 60, 0, -60 \mu\text{C}\cdot\text{kg}^{-1}$, $E_x = 0$, $E_z = 51000(0.01z)^{-0.6} \text{ V}\cdot\text{m}^{-1}$. The other parameters, such as particle density, air density and lift-off speed of sand particles are also the same as those in Schmidt et al. (1998). According to Fig. 5.3 one can find that the average trajectory of sand motion in the saltation

tion layer is strongly dependent upon the electric charge. For example, when electric charge of the moving sand is not considered in the simulation, i.e., $C_q = 0$, the horizontal distance and height of the sand motion are respectively 58.0 mm and 8.2 mm when the effect is considered for the case $u_* = 0.4 \text{ m}\cdot\text{s}^{-1}$ that discussed by Ungar and Haff (1987), while they are respectively when the effect of sand particles on wind flow is not taken into account. Compared to the values when the effect is considered, the horizontal distance of the sand motion increases 620% and height of the sand motion deceases 11%. Therefore, the effect of sand particles on wind flow cannot be neglected in the study of wind-blown sand movement. There is a notable effect of electric charge on the average trajectory of sand motion in saltation layer as shown in Fig. 5.3 after the mutual interaction between the sand movement and the wind flow is considered in the simulation, and this is similar to the result in Schmidt et al. (1998). In this case, we get the horizontal distance of 58.0 mm and the height of 8.2 mm when $C_q = 0$. However, the corresponding values of 160.0 mm and 17 mm for $C_q = 60 \mu\text{C}\cdot\text{kg}^{-1}$ which increase 170% and 95% compared to $C_q = 0$, and 15.0 mm and 4.0 mm for $C_q = -60 \mu\text{C}\cdot\text{kg}^{-1}$ which decrease 75% and 46% compared to $C_q = 0$ are obtained. These results show that electrostatic and the mutual interaction between the sand movement and the wind flow have obvious effects on average trajectory of saltating particles even in stable atmospheric boundary.

5.2.2 The Effects of Particle's Mid-Air Collisions on Sand Saltation Trajectories

More and more researchers believe that the particle concentration in the near-surface layer, which is hard to observe and measure directly, is so high that mid-air collisions are almost inevitable and it may has important effects on sand movement (Shao, 2000; Sørensen, 1991). Because of the complexity and randomness of the sand particle trajectories in air, many researchers had not taken the influence of saltating particles' mid-air collisions into account when they study wind-blown sand flux just for simplicity.

Huang et al. (2008) developed a simulation model to calculate the probability of mid-air collisions in an aeolian saltation cloud. They assume the collision probability of saltating particle is $p(A_i)$ when the particle passes from the trajectory point (x_i, z_i) to (x_{i+1}, z_{i+1}) , here A_i ($i = 1, 2, \dots, n$) are stochastic events that mid-air collisions occur in the section from point (x_i, z_i)

to (x_{i+1}, z_{i+1}) of trajectory, and are related to the particle concentration $c(z_i \pm \dot{z}t) \cdot p(A_i)$ can be expressed by:

$$p(A_i) = 1 - \exp(\mp a \int_{z_i}^{z_{i+1}} c(\zeta) d\zeta) \quad (5.14)$$

where $a = \pi D_s^2 / \sin \theta$, θ is the angle of sand velocity to the horizontal, the symbols '+' and '-' respectively represent sand particle in the ascending stage and descending stage. Apparently if the u_* is larger, the corresponding particle number flux N_s will increase, thus the collision probability $p(A_i)$ will increase too. Meanwhile, the collision probability in the descending stage is greater than that in the ascending stage for a given lift-off velocity and free-stream wind velocity. The collision probability in the descending stage is greater due to the fact that the descending trajectory is longer than the ascending trajectory because of the saltating particle's acceleration by wind. The longer trajectory provides the saltating particle with a greater chance to collide with other particles (Huang et al. 2008).

Based on the hard ball model recounted in Chap. 3, the velocities of sand particles after their mid-air collisions are calculated. The calculated velocity is taken as the initial velocity at the collision point (x_i, z_i) . Then

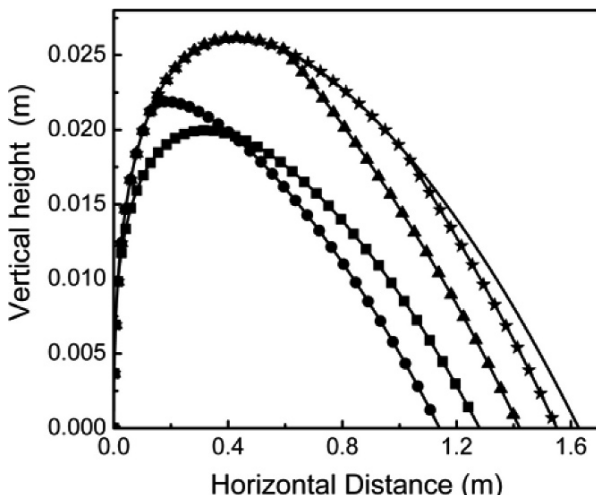


Fig. 5.4. Sand saltation trajectories with and without mid-air collisions when $u_* = 0.8 \text{ m}\cdot\text{s}^{-1}$, $D_s = 0.17 \text{ mm}$ and, $V = 1.2 \text{ m}\cdot\text{s}^{-1}$; — trajectory without collisions, and the ‘line + symbol’ represent results with collisions at different height: —■— collision at the ascending stage at height 1.0 mm, —●— collision at the ascending stage at height 2.17 mm, —▲— collision at the descending stage at height 2.54 mm, —★— collision at the descending stage at height 1.84 mm (Huang et al. 2008)

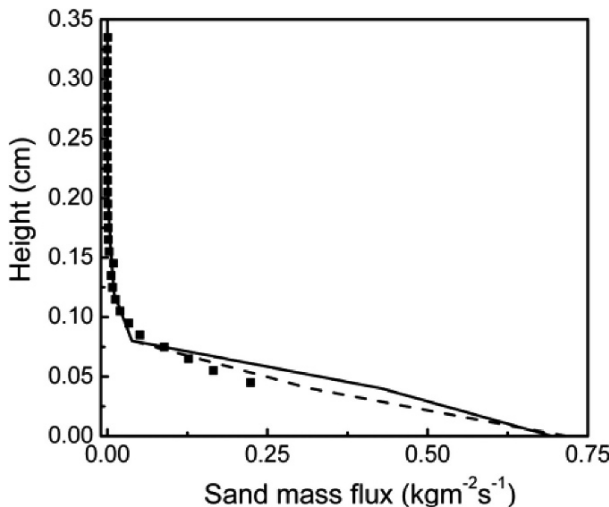


Fig. 5.5. The difference between the mass flux with and without consideration of mid-air collisions when the axial wind velocity $u_{ax} = 10 \text{ m}\cdot\text{s}^{-1}$, $D_s = 0.228 \text{ mm}$, — the simulation results without collisions, - - - the simulation results with collisions, ■ the experimental results (Huang et al. 2008)

the trajectories of sand particles after their mid-air collisions are calculated by Eq. 5.12. In the whole calculating process the coupling effect between sand particles and wind field are not considered. Fig. 5.4 shows the comparison of the sand saltation trajectories with and without mid-air collisions for $u_* = 0.84 \text{ m}\cdot\text{s}^{-1}$, particle diameter $D_s = 0.17 \text{ mm}$ and lift-off velocity of particle $V = 1.2 \text{ m}\cdot\text{s}^{-1}$. From Fig. 5.4, it can be seen that mid-air collisions also has obvious influence on sand saltation trajectory. For example, the length and height are 1.62559 m and 0.0261 m respectively without collisions, while the corresponding results are 1.27912 m and 0.0199 m respectively when the sand particle collides at the height $z = 1.0 \text{ mm}$ in ascending stage. Compared to the results without collisions, the length and the height are 21.3% shorter and 23.7% lower respectively. Meanwhile, the colliding point and particle diameter also influence sand saltation trajectory. For example, the length and height of a saltating particle are 1.13946 m and 0.0219 m respectively when the sand collides at the height $z = 2.17 \text{ mm}$ in ascending stage, are 30.0% shorter and 16.3% lower than the results without collisions, while they are 13.9% shorter and 9.8% higher than the results when the particle collides at the height $z = 1.0 \text{ mm}$. In the same way, mid-air collisions also have obvious influence on the mass flux. The research of Huang et al. (2008) shows the mass flux

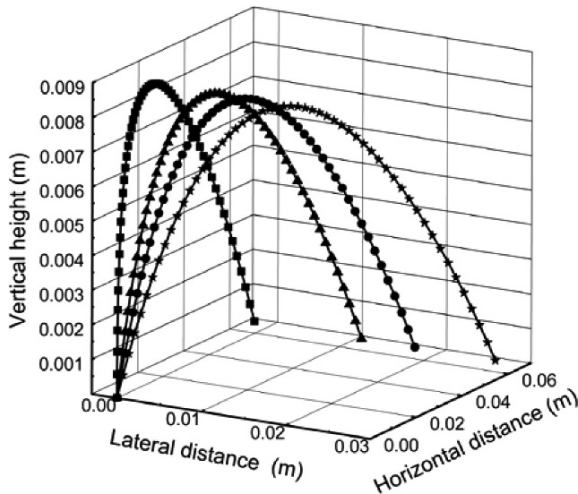


Fig. 5.6. The three-dimensional sand trajectory with different lateral velocities when $u_* = 0.192 \text{ m}\cdot\text{s}^{-1}$, $D_s = 0.25 \text{ mm}$, horizontal initial velocity is $0 \text{ m}\cdot\text{s}^{-1}$, vertical initial velocity is $0.45 \text{ m}\cdot\text{s}^{-1}$; —■— lateral initial velocities $V_y = 0.0 \text{ m}\cdot\text{s}^{-1}$, —▲— lateral initial velocities $V_y = 0.2 \text{ m}\cdot\text{s}^{-1}$, —●— lateral initial velocities $V_y = 0.3 \text{ m}\cdot\text{s}^{-1}$, —★— lateral initial velocities $V_y = 0.45 \text{ m}\cdot\text{s}^{-1}$ (by the author et al.)

including mid-air collisions is different from that without consideration of collisions, the difference between the mass flux with and without consideration of mid-air collisions increases with wind velocity and is much closer to the corresponding values of experiments (see Fig. 5.5).

Here it needs to be emphasized that when we simplify the three-dimensional sand-wind flow to two-dimensional issue, it actually implies that we transform the spherical sand particle into an equivalent disk, i.e., the sphere and the disk have the same mass. When we discuss the ejection of sand particle, we neglect the other three component of the lift-off velocity of sand particles in fact, namely the lateral velocity which is vertical plane oxz , rolling angular velocity, and upward angular velocity. The research (Zheng et al. 2008) suggests that it is worth considering these three velocities if the incident velocity is larger enough. And the lateral velocity which is perpendicular to oxz plane will induce sand trajectory to deviate the oxz plane (see Fig. 5.6).

5.2.3 Saltation Trajectory and Saltation Activity in a Fluctuating Wind Field

It is well known that the near surface atmospheric flow is turbulent, and it is natural for the particles moving in it will be influenced by turbulent fluctuations to a certain extent, just as described in Chap. 2. Here, however, only the effect of vertical fluctuations (though the wind fluctuations is actually three-dimensional) is taken into account because it is one of the crucial factors that influence the transport mode of sand particles.

For the homogeneous steady flow, the Langevin equation, namely, the ‘first order’ Lagrangian stochastic (LS) model (Wilson and Sawford 1996) is generally adopted to model the movement of one flow parcel along the z direction, in order to modeling the vertical fluctuations experienced by a sand particle, Anderson (1987) modified the ordinary Langevin equation to the following form

$$dw(t) = -\frac{1}{T_L^*} w(t) dt + \sigma_w \zeta_w \sqrt{\frac{2}{T_L^*}} . \quad (5.15)$$

where $T_L^* = \tau_L [1 + A_1(|\mathbf{u} - \mathbf{u}_s|/\sigma_w)^{2/3} (\tau_L/\Delta t)^{1/3}]$ is the integration time scale of the vertical velocity fluctuations along the sand particle trajectory and it is a modified form of $\tau_L = a_1 z / u_*$, which is the integration time scale of a single moving air parcel; Δt is the time step; ζ_w is a random number drawn from a normal distribution $N(0, \Delta t)$; $\sigma_w = a_2 u_*$ is the vertical velocity standard deviation of flow parcel and $A_1 = 0.5$, $a_1 = 0.4$, $a_2 = 1.3$ (Anderson 1987). If gravity force and aerodynamic drag \mathbf{F}_D is remained in the equation of motion, with the velocity component of particle and wind to be marked as (\dot{x}, \dot{z}) and (u, w) respectively, and the differential equation of motion and initial conditions are given as:

$$\ddot{x} = \frac{K}{\alpha} (u - \dot{x}), \quad \ddot{z} = -g + \frac{K}{\alpha} (w - \dot{z}), \quad (5.16a)$$

$$t = 0 : \quad \dot{x} = 0, \quad \dot{z} = V . \quad (5.16b)$$

Where $\alpha = D_s^2 \rho_s / 18 \nu \rho$ denotes the response time for particle that ideally obeys Stokes law (Csanady 1963), K is a constant introduced when Eq. 5.3 is approximated to be expressed as $C_D = 24K/\text{Re}$. While the logarithmic profile of wind velocity (Eq. 2.35) along the wind direction is adopted, particle trajectories can be obtained by solving Eqs. 5.15 and 5.16 jointly. One hundred realizations of trajectories of particles with different lift-off velocity, diameter and friction velocity u_* when $z_0 = 0.0201 u_*^2 / 2g$ (Owen

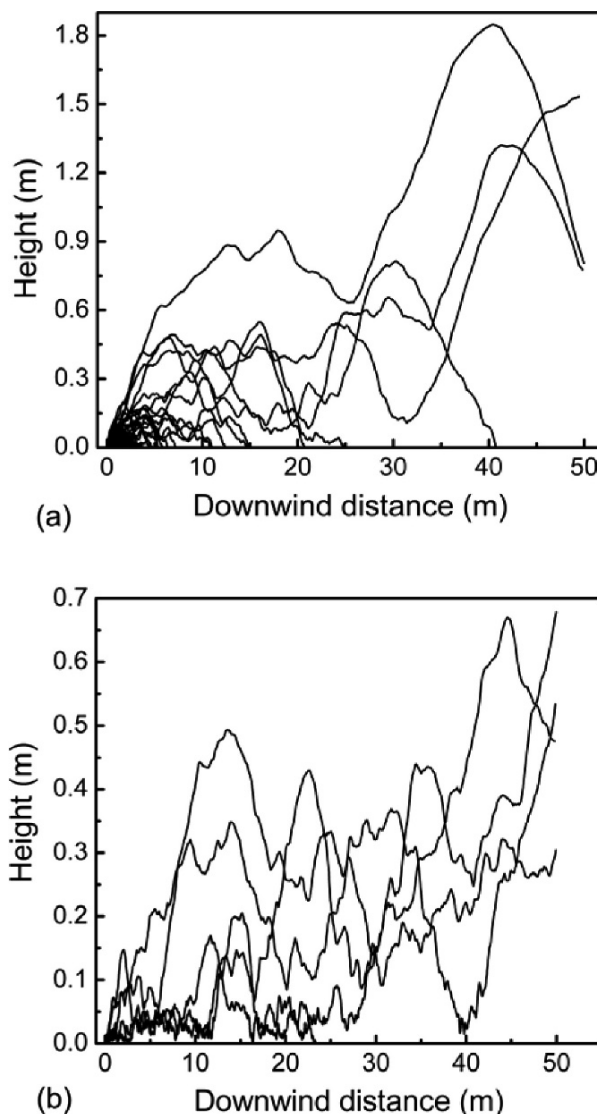


Fig. 5.7. One hundred particle trajectories of different lift-off velocity in a logarithmic wind ($z_0 = 0.201u_*^2/2g$), arising from turbulence with turbulent intensities $\sigma_w = 1.3u_*$. Significant differences in trajectories include the hop length and hop height even with identical initial conditions in each figure; **(a)** $D_s=0.04 \text{ mm}$, $u_*=0.5 \text{ m}\cdot\text{s}^{-1}$, $V=1.0 \text{ m}\cdot\text{s}^{-1}$; **(b)** $D_s=0.04 \text{ mm}$, $u_*=0.5 \text{ m}\cdot\text{s}^{-1}$, $V=2.0 \text{ m}\cdot\text{s}^{-1}$

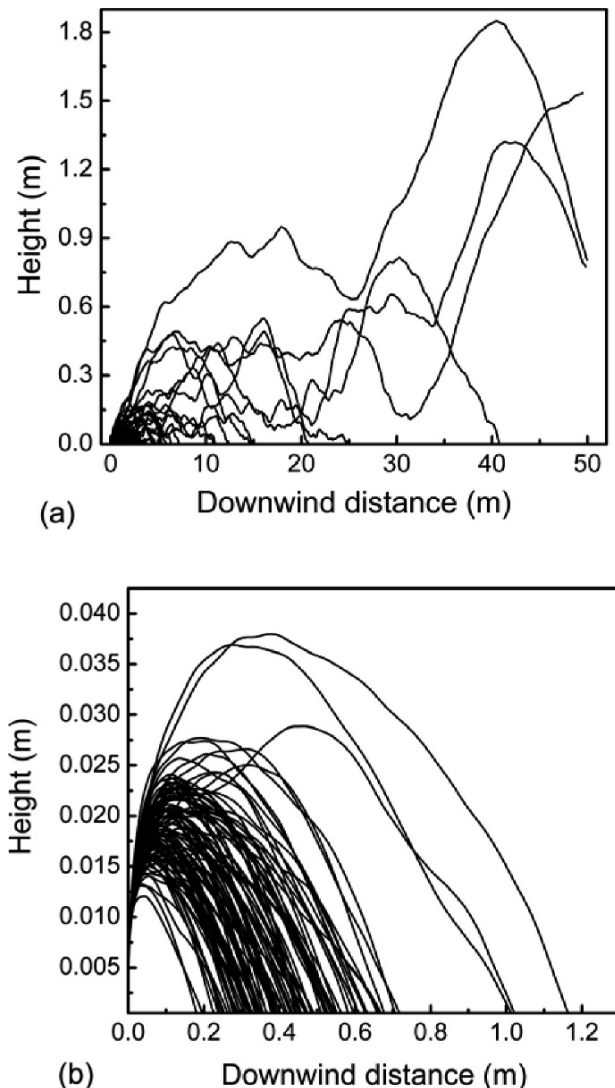


Fig. 5.8. One hundred particle trajectories of different particle diameter in a logarithmic wind ($z_0 = 0.201u_*^2/2g$), arising from turbulence with turbulent intensities $\sigma_w = 1.3u_*$. Significant differences in trajectories include the hop length and hop height even with identical initial conditions in each figure as shown in Fig. 5.7 (a) $D_s = 0.04 \text{ mm}$, $u_* = 0.8 \text{ m}\cdot\text{s}^{-1}$, $V = 1.0 \text{ m}\cdot\text{s}^{-1}$, (b) $D_s = 0.1 \text{ mm}$, $u_* = 0.5 \text{ m}\cdot\text{s}^{-1}$, $V = 1.0 \text{ m}\cdot\text{s}^{-1}$

1964) are shown in Fig. 5.7, from which we can conclude that they are fluctuant and do differ from those presented in Fig. 5.2 because of turbulence. Significant differences in trajectories include the hop length and hop height even with identical initial conditions (such as particle diameter and lift-off velocity).

In order to describe particle saltation more objectively, gusty wind, instead of logarithmic wind profile (Eq. 2.30) could be used in the above analysis. That is, according to the prediction model of gusty wind proposed in Sects. 2.6.1 and 2.6.2, wind velocity of any height $z < 2$ m at time t_i will be expressed as:

$$u(z, t_i) = u_r(z_r, t_i) - u'' = \bar{u} + \langle u \rangle + u' - u'' = \bar{u} + MT_g \text{sign}(T_g) + \sigma_t \zeta_t - u'' \quad (5.17)$$

where u'' obey Eq. 2.63, definitions of the parameters are identical to those in Chap. 2. It is noticeable that the horizontal wind is expressed in an Eulerian frame, while the vertical wind fluctuations is treated as Lagrangian turbulence with smaller fluctuation magnitude and shorter time scale.

Considering a sand sample which obeys log-normal distribution with its mean diameter is 0.316 mm, the calculating procedures are taken as follows: (1) At each 1 s time interval, the measured wind velocity at a reference height $z_r = 2$ m is substituted to Eq. 2.60 to generate wind velocity of

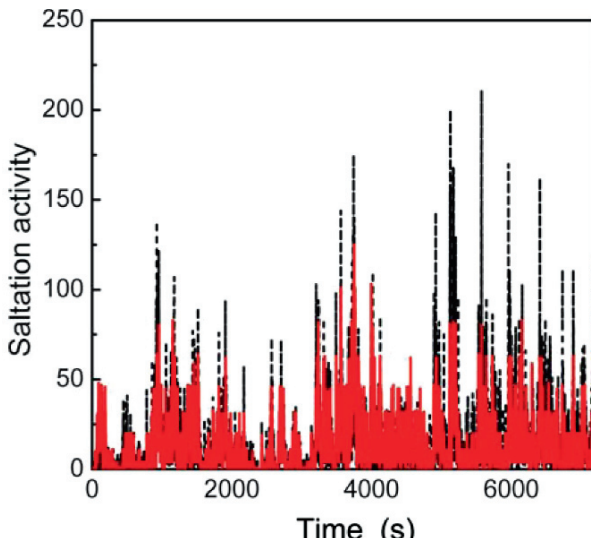


Fig. 5.9. Comparison between the measured (black dot line) and simulated saltation activity (red solid line) in the gusty wind. The total count and the intermittency agree well though they are not synchronous completely (by the author et al.)

any height below 2 m; (2) Recent studies on instantaneous sand transport indicated that the horizontal wind velocity component is of much more important than shear stress for saltation transport (Sterk et al. 1998; Leenders et al. 2005). Following the $N_s \sim (u_*^2 - u_t^2)$ relationship for fluid threshold (Anderson and Haff 1991; Shao 2000) and the suggestion given by Sterk et al. (1998) the aerodynamic drag will be proportion to u^2 instead of the square of the shear stress, and the sand number ejected from unit area of the surface bed per second N_s should be written as $N_s = \zeta(u^2 - u_t^2)$, where ζ is an experimental constant, u is measured wind velocity at 2 m height and $u_t = 7.05 \text{ m}\cdot\text{s}^{-1}$ is the threshold mean wind velocity in the measured period, see Stout (2004, 2007) for its calculation; (3) Particle sizes are classified into 21 classes between 0.04 mm and 0.46 mm (0.02 mm size interval). The lift-off velocity distribution is chosen to be exponential (see Table 3.2), calculation will continue till the particle re-encounter the bed or the flying time is larger than 1 s. Finally, the number of particle flying higher than the 4 cm and lower than 5.3 cm are counted and multiplied by the diameter of the SENSIT (2.5 cm) to get the simulated saltation activity and then compared with experimental data as shown in Fig. 2.15.

Fig. 5.9 indicates that the characteristics of random and intermittency of simulated saltation activity is compared well and has the identical tendency, though not completely synchronous, with the measured result by SENSIT.

5.2.4 The Criterion of Saltation and Suspension

The criterion of saltation and suspension is another parameter being concerned. Present criterions can be divided into several groups. The first group uses the particle diameter as a basis (Bagnold 1941), which is very simple. The second is the ratio of the particle settling velocity w_{st} to flow vertical diffusion velocity $w (= ku_*)$, i.e., $\alpha_d (= w_{st}/w)$ which gives a reasonable dimensionless parameter including the shear stress u_* . However, there still remains the question of reference value choosing e.g., $\alpha_d = 0.12$ in Gillette et al. (1972), $\alpha_d = 0.5$ in Shao (2000), $\alpha_d = 1.0$ in Scott (1995) besides the neglect of lift-off velocity which is proved to be crucial according to Fig. 5.7. The third one was suggested by Anderson (1987) who proposed a ‘saltation parameter’ $P_s (= \alpha/\tau_h, \tau_h = 2V/g$, here $\theta = 0$), is the hop time of particle with vertical lift-off velocity V_{in} the absence of nongravitational forces as the criterion. The influence of the lift-off velocity upon sand movement is taken into account, but it is neglected in the parameter P_s .

To find a more reasonable criterion, we redefine the ‘saltation parameter’ P_s of Anderson (1987) as $P_{sal} = \alpha/(\tau_L K)$ and express the vertical velocity standard deviation of sand particle σ_w^s as below following Edson and Fairall (1994)

$$\sigma_w^s = \frac{\sigma_w}{\sqrt{1 + \frac{\alpha}{K\tau_L}}} = \frac{1.3u_*}{\sqrt{1 + P_{sal}}}. \quad (5.18)$$

Then, for a given friction velocity, σ_w^s is only related to the parameter P_{sal} . Because $\tau_L = 0.4z/u_*$ increases with z which relates to the velocity V , if z is substituted by the σ_w^s largest hop height $z_{max} (= V^2/2g)$ of a particle ejected with velocity V in the absence of nongravitational forces, the ‘saltation parameter’ $P_{sal} = \alpha/(\tau_L K)$ may be written as $P_{sal} = \alpha u_* g / 0.2V^2 K$. Curves of σ_w^s as a function of P_{sal} for two different friction velocities are shown in Fig. 5.10. It is shown that σ_w^s decreases with P_{sal} . All curves decrease rapidly with σ_w^s when $P_{sal} < f_1$ and almost keeps a constant when $P_{sal} > f_2$ for a given wind velocity (where f_1 and f_2 are both arbitrary values), which

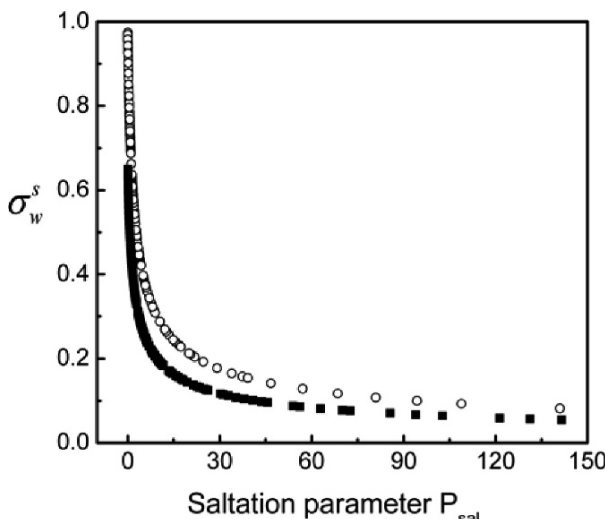


Fig. 5.10. Vertical velocity standard deviation of sand as a function of ‘saltation parameter’ under two different wind velocities, \circ for $u_* = 0.75 \text{ m}\cdot\text{s}^{-1}$ and \blacksquare for $u_* = 0.5 \text{ m}\cdot\text{s}^{-1}$, respectively. The rapid decrease indicates that particle will experience a smooth saltation because the less effect of turbulence with large P_{sal} , i.e., large diameter, small wind and lift-off velocity

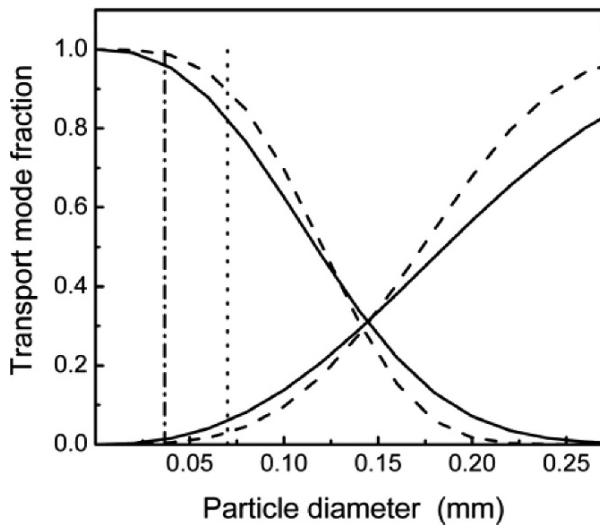


Fig. 5.11. The relationship between transport mode fraction and particle diameter in wind condition, characterized by $u_*=0.5 \text{ m}\cdot\text{s}^{-1}$ (—), together with some other criterions given by Anderson (1987) (---), by Shao (2000) (····) and diameter criterion $D_s = 0.07 \text{ mm}$ (-·-·-), respectively

encourages us to define $P_{sal(1)}=f_1$ and $P_{sal(2)}=f_2$ as the critical values for sand particle entrainment into suspension and saltation. From Fig 5.10, the chosen cutoffs are $f_1 = 2$ and $f_2 = 20$ respectively for $u_*=0.5 \text{ m}\cdot\text{s}^{-1}$. Then, the critical ejection velocities of suspension and saltation are defined as

$$V_{(1,2)} = \sqrt{\frac{D_s^2 \rho_s g u_*}{3.6 \rho v K P_{sal(1,2)}}} \quad (5.19)$$

The subscripts (1, 2), similar to f_1, f_2 , correspond to suspension and saltation. Finally, it is possible to estimate the corresponding fraction of each particle size class expected to travel in each mode for a given wind

$$\text{Suspension: } F_{sus} = \frac{\int_{V_{(2)}}^{\infty} f(V) dV}{\int_0^{\infty} f(V) dV} = \int_{V_{(2)}}^{\infty} f(V) dV, \quad (5.20a)$$

$$\text{Saltation: } F_{sal} = \frac{\int_0^{V_{(t)}} f(V) dV}{\int_0^{\infty} f(V) dV} = \int_0^{V_{(t)}} f(V) dV. \quad (5.20b)$$

Here, using the lift-off velocity distribution of Anderson and Hallet (1986) and assume $K \approx 1$ (see Table 3.2), we get the results as plotted in Fig. 5.11 which illustrates that applying the new criterion the suspension fractions are different from that depending on particle size or particle terminal velocity. Even if the diameter is above a certain ‘critical’ size and influenced by identical initial conditions, the particle could still become a saltation particle or a suspension one. So the transport mode fraction must relate to the lift-off velocity and the friction velocity for a given diameter.

5.3 Experiments and Observations on Sand Transport Rate

Qualitative results of sand transport rate of wind-blown sand flux obtained through field observation and wind tunnel experiment reveal that 90% of sand particles are transported in the region of 0–31 cm from surface (Chepil 1945; Sharp 1964; Butterfield 1991), and the mass flux per unit area and unit time decreases with the increase of height in terms of negative exponential function. But because the efficiency of the sand collector is not good enough for the measurement of sand transport, especially near-surface that current results are not consistent with each others. For example, Kawamura (1951) and Zingg (1953) hold that the mass flux per unit area and unit time near surface are deviated from the exponential function. Therefore, many scholars try to use new equipment and method, such as the stroboscope photography and particle image velocimetry (PIV), to measure the intensity of wind-blown sand flux near surface (Wang et al. 2006; Dong et al. 2006).

The intensity of wind-blown sand flux is measured by the transported rate of sand, which is the quantity of sand particle conveyed through per unit width (or area) and per unit time by wind. It is critical to reveal the law of the wind-blown sand movement and for the design of sand prevention and control engineering. Before any theoretical estimation of macroscopic mass flux is made, one usually needs to obtain an experiential formula fitted from the data of the mass flux per unit area and unit time by field observations and wind-tunnel experiments. For example, as early as

1936, O'Brien and Rindlaub (1936) had made an observation, and subsequently Bagnold (1941) theoretically proposed that the sand transport rate Q is proportional to the third power of the friction wind velocity u_* . On the basis of Bagnold (1941), Kawamura (1951) introduced the threshold friction velocity u_{*t} to the expression of sand transport rate as a characteristic parameter of sand particles. The work of Bagnold (1941) and Kawamura (1951) are widely accepted by many scholars, such as Owen (1964), Lettau and Lettau (1978), White (1979), Sørensen (1991). Nevertheless, Ungar and Haff (1987) and Pomeroy and Gray (1990) supposed that the transport rate Q is proportional to the one or two power of the friction velocity u_* .

Usually, there are empirical parameters that need to be defined in empirical formula and be obtained from the measurement of experiments. As it is different among the experimental results themselves and among the processing methods, the empirical parameters in different models vary greatly which makes the expressions including these parameters have large diversity, although these empirical parameters are all chosen in similar way. Thus the consistency of the estimated results by these models and observed data are different, and the difference between estimated results and observed data could be as much as 3 times (Shao 2000). Here we introduce a method to fit the formula of the mass flux per unit area and unit time, and further sand transport rate from the experimental data.

To get the sand transport rate Q , the mass flux per unit area and unit time $q(z)$ along height should be obtained firstly. Traditionally, the processing of the measured data is conducted by an artificial extension of the experimental results of the sand collector, i.e., drawing the experimental data for mass flux per unit area and unit time measured in a sand collector on graph paper to find an empirical curve, then extending the curve to the domain outside the height region of the sand collector, and finally calculating the area surrounded by the curve and the axes of the graph by means of numerical arithmetic. The area is then considered as a measurement of the rate of the wind-blown sand transport per unit width and unit time (Zhou et al. 2002). Obviously, this approach is depended on the rationality of the extrapolation and the accuracy of the computation of the area, and that is the main obstacle to improve the accuracy of the sand transport rate, especially when the data of the experiments is limited in practice. Therefore it is important to improve the fitting processes with deficient experimental data. Zhou et al. (2002) puts forward a processing method which possesses higher accuracy of the fitting of experiment data. Consider the fact that the mass flux per unit area and unit time along the height has the characteristic of negative exponential function, the following exponential equation is used as an assumption to fit the experimental data:

$$q(z) = C + A \exp\left(-\frac{z - z_r}{B}\right), \quad (5.21)$$

where z_r is offset of z , C is the offset of $q(z)$, A is the amplitude, B is the constant of attenuation. The values of these constants can be obtained from fitting experiment data by the least square method (LSM). The main idea of the LSM is as follow, firstly choose the fitting function and express it as $y = y(x, a_1, a_2, \dots, a_m)$, here a_k ($k = 1, 2, \dots, m$) are pending parameters. Then set σ_i as the standard deviation of i point (x_i, y_i) ($i = 1, 2, \dots, m$), and build the function $\chi^2 = \sum_{i=1}^n [y_i - y(x_i, a_1, a_2, \dots, a_m)]^2 / \sigma_i^2$ with observed data (x_i, y_i) ($i = 1, 2, \dots, n$). We can get parameters a_k through finding the proper parameter a_k with which the value of χ^2 is minimum. In other words, the parameters a_k can be obtained through solving the nonlinear algebraic equation

$$\frac{\partial \chi^2}{\partial a_k} = 0 \quad k = 1, 2, \dots, m \quad (5.22)$$

The commercial software Origin can realize the LSM. Zhou et al.(2002) set the z_r as an appropriate fixed value in Origin as minimum value of the variable z ; the bias C is set to be close to the asymptotic value of the function $q(z)$ when z is large enough. Usually z_r is taken as the position of the central height of the lowest opening of the sand collector (in this section $z_r = 4.5$ cm). There is evident that, when z becomes large enough, $q(z)$ will approach zero when suspension is neglected. Thus, we set $C = 0$. Then we can get the values of the coefficients A and B in Eq. 5.21 by the LSM with the measured q_i of each height of sand collector z_i at each axial wind velocity. The values of the coefficients A and B actually change with the axial wind velocity u_{ax} , that is, $A = A(u_{ax})$ and $B = B(u_{ax})$.

It is a key step to find suitable fitting equations of $A = A(u_{ax})$ and $B = B(u_{ax})$ for developing an explicit form of the empirical equation of the mass flux per unit area and unit time, and, further, that of the sand transport rate varying with axial wind velocity or friction velocity, as seen later. When $C = 0$ in Eq. 5.21, we know that the coefficient A implies how intense the mass flux is and u_{cr} is used to denote the threshold of the axial wind velocity of wind tunnel that makes the sand move. In order to display the fact that the sand movement occurs only when the axial wind velocity is above the threshold value, according to the relationship between axial

wind velocity and A showed by experimental data, a satisfactory test function was found to be

$$A = A(u_{ax}) = a_1 u_{ax}^2 (u_{ax} - u_{cr})^{a_2}, \quad (5.23a)$$

$$B = B(u_{ax}) = b_1 + b_2 u_{ax} + b_3 u_{ax}^2. \quad (5.23b)$$

Here, the fitting coefficients a_1, a_2, b_1, b_2, b_3 and u_{cr} are dependent on the sand sample employed and can be obtained by fitting experimental data. Substituting the obtained Eqs. 5.23a and 5.23b into Eq. 5.21, we get an explicit form of the empirical equation $q(z)$ varying with axial wind velocity u_{ax} and height z . That is

$$q(z) = A(u_{ax}) \exp\left[-\frac{100z - 4.5}{B(u_{ax})}\right]. \quad (5.24)$$

Here, the unit of height z is meters. It is found that the results of the empirical fitting formula by Zhou et al (2002) are in good agreement with the measured data.

In most equations of wind-blown sand transport, the expressions are formulated in terms of the friction velocity u_* . The wind-blown sand experiments were conducted in the field environmental wind tunnel of the Institute of Cold and Arid Region Environmental Engineering of the Chinese Academy of Science. For this wind tunnel, following formula is introduced by Zhou et al. (2002). u_{ax} is expressed as $u_{ax} = d_1 u_* + d_2$ in which the constants d_1 and d_2 are obtained by $d_1 = 11.49557$, $d_2 = 4.32337$. The threshold friction velocity u_{*t} is calculated by Bagnold's formula (Bagnold 1941): $u_{*t} = C_* \sqrt{(\rho_s - \rho) g D_s / \rho}$. Here, C_* is the empirical constant. Substitution of axial wind velocity in wind tunnel u_{ax} and friction velocity u_* and the threshold friction velocity of Bagnold's into Eq. 5.23, as the $A = A(u_{ax})$ and $B = B(u_{ax})$ are replaced with $\tilde{A} = \tilde{A}(u_*)$ and $\tilde{B} = \tilde{B}(u_*)$. Consider the efficiency e of the sand collector, it leads to an explicit form of the empirical expression with respect to the variables of friction velocity and its threshold for the mass flux per unit area and unit time varying with height and friction velocity, i.e.,

$$q(z) = \tilde{A}(u_*) \exp\left(-\frac{100z - 4.5}{\tilde{B}(u_*)}\right). \quad (5.25)$$

Integrating Eq. 5.25 with respect to the variable of height z , we can obtain a formula for the sand transport rate caused by saltation (denote it by Q_s) can be obtained. Near surface sand transportation is usually composed of saltation and creep movement, and the total sand transport rate should

be the sum of both. Bagnold (1941) found from wind tunnel experiments that the contribution of sand creep motion to the sand transport rate Q_c is about 25% of the total transport. Chepil (1945, 1946) recognized the ratio to be about 15.7% for sands with diameters of 0.15–0.25 mm, and about 24.9% for sands with diameters of 0.25–0.87 mm. Horikawa and Shen (1960) obtained a ratio of 20%, which is not changed with wind velocity. Here, the ratio is chosen as 20%. Thus the total sand transport rate may be written as

$$Q = 1.25 \int_0^{\infty} q(z) dz = \frac{1.25}{100e} \tilde{A}(u_*) \tilde{B}(u_*) \exp \frac{4.5}{\tilde{B}(u_*)}. \quad (5.26)$$

The results of sand transport rate provided by Eq. 5.26 are compared to the results predicted by the widely accepted Bagnold's formula (1941) and Kawamura's equation (1951). Fig. 5.12 illustrates a comparison among the predictions when natural mixed sand is employed, the constant C_* in Bagnold's formula (1941) is set as 1.8, $D_s = 0.228$ mm. The constant in Kawamura's equation (1951) is set to be 1.0 (Horikawa and Shen 1960). From fig. 5.12, it is found that the predictions of the Kawamura equation in the range of friction velocity of $u_{*t} \leq u_* \leq 0.35 \text{ m}\cdot\text{s}^{-1}$ and those of the

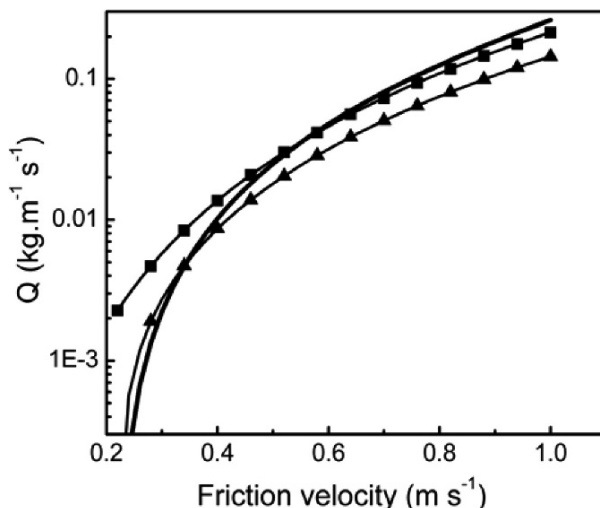


Fig. 5.12. Comparison among the predictions of sand transport rate, as for the naturally mixed sands employed. The sand transport rate given by Eq. 5.26 (—) are close to results predicted by Kawamura equation (—▲—) and that by Bagnold formula (—■—) in their effective range, $u_{*t} \leq u_* \leq 0.35 \text{ m}\cdot\text{s}^{-1}$ and $u_* \geq 0.47 \text{ m}\cdot\text{s}^{-1}$, respectively

Bagnold formula when $u_* \geq 0.47 \text{ m}\cdot\text{s}^{-1}$ are close to the measurement results given by the empirical Eq. 5.26. In addition, the results from Eq. 5.26 transit smoothly from the prediction of the Kawamura equation to that of the Bagnold formula in the region of $0.35 < u_* < 0.47 \text{ m}\cdot\text{s}^{-1}$ as the friction velocity increases, while the estimation of Kawamura's equations and Bagnold's equation are very different. Therefore the famous Kawamura's and Bagnold's sand transport rate equation per unit width are effective in the range of $u_{*t} < u_* < 0.35 \text{ m}\cdot\text{s}^{-1}$ and $u_* > 0.47 \text{ m}\cdot\text{s}^{-1}$ respectively (Wu 2003; Horikawa and Shen 1960).

It should be pointed out that no matter how the saltation activity or the sand transport rate is measured, the wind tunnel experiments and field observations are performed under steady air flow or collected with a time step more than one hour. Although scientists gradually have realized that the turbulence of near-surface atmosphere boundary layer has significant effect on the movement of wind-blown sand (Zeng et al. 2007; Ni et al. 2003), and started to make some real-time synchronous measurements of the field blown mass flux (as in Sect. 2.6.1), there is still much work need to be done. Especially, ‘there exist very few sets of reliable simultaneous measurements of the characteristics of the wind and the sand transport rate that can be used to constrain or validate the mathematical models (Anderson 1991)’. Moreover, ‘Mathematical models which quantify the conceptual model of wind-blown sand transport are still far from the point at which reliable predictions of sand transport rate can be made’. To build and verify an efficient model for predicting the sand transport rate, the experimental observation of wind-blown sand movement need to be strengthened.

5.4 Theoretical Simulations on the Evolution of Wind-Blown Sand Flux

The evolution of saltation process of wind-blown sand particles can be divided into four sub-processes, i.e., aerodynamic entrainment, particle motion driven by wind, particle-bed collisions and momentum coupling with the wind. Within saltation process, the horizontal and vertical flow will be coupled with the saltation sand flow and electric field, finally the sand flow will attain a equilibrium. Although many investigators (Anderson and Haff 1988, 1991; Werner 1990; McEwan and Willetts 1991, 1993; Nalpanis et al. 1993; McEwan et al. 1999; Shao and Li 1999) tried to simulate the evolution of sand flow, most of them employed steady flow field and ignored the effect of electrostatic force and thermal effect on the evolution

of wind-blown sand flux. This section will treat in detail the evolution of wind-blown sand flux considering both the effect of electrostatic force and buoyancy force.

Due to the effect of buoyancy force, the flow field here includes not only the x-axial velocity component $u(z, t)$ as described in Sect. 5.2, but also has the vertical velocity component $w(z, t)$. Now the basic equations of wind field include the continuity equation (Eq. 2.1), momentum conservation equation (Eq. 2.17) and energy equation (Eq. 2.18) of thermal effect. Here we introduce the expression $\mu = \beta T^{1.5}/(T + S)$, where β, S are constants, and substitute it for μ in all equations. Meanwhile, bring state Eq. 2.19 into Eq. 2.18, and bring the body force (see Eq. 5.9) per unit volume caused by particle motion into Eq. 2.18, and the vertical component of the body force can be obtained merely by replacing \ddot{x}_\uparrow and \ddot{x}_\downarrow with \ddot{z}_\uparrow and \ddot{z}_\downarrow in Eq. 5.9, respectively. Then, the basic equations describing wind field can be expressed as:

$$\frac{\partial \rho}{\partial t} + w \frac{\partial \rho}{\partial z} + \rho \frac{\partial w}{\partial z} = 0, \quad (5.27a)$$

$$\frac{\partial u}{\partial t} + w \frac{\partial u}{\partial z} = \frac{\beta T^{1.5}}{\rho(T+S)} \frac{\partial^2 u}{\partial z^2} + m_s \int_{V_{\min}}^{V_{\max}} N_s(t) f(V, t) \left(\frac{\ddot{x}_\uparrow}{|\dot{z}_\uparrow|} + \frac{\ddot{x}_\downarrow}{|\dot{z}_\downarrow|} \right) dV, \quad (5.27b)$$

$$\frac{\partial w}{\partial t} + w \frac{\partial w}{\partial z} = -g - \frac{R}{\rho} \frac{\partial(\rho T)}{\partial z} + \frac{\beta T^{1.5}}{\rho(T+S)} \frac{\partial^2 w}{\partial z^2} + m_s \int_{V_{\min}}^{V_{\max}} N_s(t) f(V, t) \left(\frac{\ddot{z}_\uparrow}{|\dot{z}_\uparrow|} + \frac{\ddot{z}_\downarrow}{|\dot{z}_\downarrow|} \right) dV, \quad (5.27c)$$

$$\frac{\partial T}{\partial t} + w \frac{\partial T}{\partial z} = -\frac{g}{c_p} + k_T \left(\frac{\partial^2 T}{\partial z^2} \right). \quad (5.27d)$$

The corresponding initial and boundary conditions are respectively given as:

$$t = 0 : w = 0, T = T_0, \rho = \rho_0, u(z) = \frac{u_*}{k} \ln \left(\frac{z}{z_0} \right), \quad (5.28a)$$

$$z = z_0 = \frac{D_s}{30} : u = 0, w = 0, T = T_a, \frac{\partial T}{\partial z} = \eta_0, \quad (5.28b)$$

$$z \rightarrow \infty : kz \frac{du}{dz} = \sqrt{\frac{\tau}{\rho}}. \quad (5.28c)$$

Where T_0 and ρ_0 are respectively the initial temperature and density of the air flow; $\eta_2=0.0065 \text{ K}\cdot\text{m}^{-1}$ is the variation rate of initial temperature of air flow with height;

$$\tau(z,t) = \rho k^2 z^2 \left| \frac{\partial u}{\partial z} + \frac{\partial w}{\partial z} \right| \left(\frac{\partial u}{\partial z} + \frac{\partial w}{\partial z} \right)$$

is the short-term mean shear stress at the bed; T_a is the temperature of the air flow at height $z = D_s/30$ in which D_s is the diameter of sand particle, T_a is related to the sand-bed temperature T_s , which can be ascertained by calculating the following energy equilibrium equation of the bed (Jacquemin and Noilhan 1990):

$$\rho_s C_s \sqrt{\frac{K_s}{2\omega}} \frac{\partial T_s}{\partial t} = R_s - R_L + \rho L \xi_* \psi_* + \rho C_p \xi_* \vartheta_* - \rho_s C_s K_s \sqrt{\frac{\omega_e}{2K_s}} (T_s - \bar{T}_s), \quad (5.29)$$

in which $\rho L \xi_* \psi_*$ is turbulent latent heat flux, $\rho C_p \xi_* \vartheta_*$ is turbulent heat flux, ω_e is earth rotation speed, \bar{T}_s is the average temperature on the surface of the Earth, C_s and K_s are heat ratio capacity and heat conduction constant of sand particles respectively; R_s and R_L are short wave radiation and long wave radiation of earth surface, and can be written respectively as:

$$R_s = \begin{cases} S_0 (1 - m_a A_a) (1 - A_s) \cos \theta_z & \cos \theta_z > 0 \\ 0 & \cos \theta_z \leq 0 \end{cases}, \quad (5.30)$$

$$\text{and } R_L = \varepsilon_e \sigma_a T_s^4 - \varepsilon_a \sigma_a T_a^4. \quad (5.31)$$

Where $S_0 = 1353 \text{ W}\cdot\text{m}^{-2}$ is the solar constant; $A_a = 0.28 / (1 + 6.43 \cos \theta_z)$ is the atmospheric reflectivity; $A_s = 0.2$ presents the surface reflectivity; $m_a = 5$ is the atmospheric humidity; $\sigma_a = 5.67 \times 10^{-8} \text{ W}\cdot\text{m}^{-2}\text{K}^{-4}$ is the Stefan-Boltzsman constant; $\varepsilon_a = 1.24(e_a / T_a)^{1/7}$ denotes the atmospheric radiation coefficient; e_a is the vapor pressure (hPa), ε_e is the surface radiation coefficient, θ_z is solar zenith angle, and $\cos \theta_z = \sin \varphi_e \sin \zeta + \cos \varphi_e \cos \zeta \cosh h$, where φ_e is the geographic latitude, ζ is the solar declination, $h = 15^\circ(12 - t_h)$ is the solar altitude, t_h is the local time.

As discussed in Sect. 5.2, the movement of a sand particle lift-off the sand-bed will obey Eq. 5.12. In this simulation, the Magnus effect is neglected, the electric field in sand flow is determined by Eq. 4.3 and the initial conditions are:

$$t = 0 : x = 0, z = 0, \dot{x} = V \cos \theta, \dot{z} = V \sin \theta \quad (5.32)$$

where θ is the angle between the initial lift-off speed of the particle and the x -direction.

The definite problem of evolution process of sand flow with consideration of electrostatic force and thermal effect is composed by Eqs. 5.12, 5.27 and boundary condition (Eq. 5.28). To determine the duration time for the evolution process of the saltating population, regard $t_0 = 0$ as the starting point of $t_j = t_0 + j \times \Delta t$ ($t_0 = 0, j = 1, 2, \dots$), in which the time step $\Delta t = \sqrt{2D_s/g}$ is determined by the shortest trajectory time. Moreover, the Eqs. 5.12 and 5.27 at a given time can be solved by an iterative method similar to the method mentioned in Sect. 5.2.1. But it needs to add temperature transmission Eq. 5.27c to determine the vertical wind velocity to consider the effect of sand concentration on wind-blown sand electric field. Substituting Eqs. 4.4 and 4.6 into the right side of Eq. 5.6, the wind-blown sand electric field is given by:

$$E(z) = -0.1 + \frac{\rho_s c D_s^3}{6\epsilon_0} \left(\int_{z_0}^z - \int_z^\infty \right) N_1(z') \cdot \arcsin \frac{ab}{\sqrt{[a^2 + (z' - z)^2][b^2 + (z' - z)^2]}} dz' \\ - \frac{\rho_s c D_s^3}{6\epsilon_0} \arcsin \frac{ab}{\sqrt{(a^2 + z^2)(b^2 + z^2)}} dz' \int_{z_0}^\infty N_1(z') dz'. \quad (5.33)$$

In order to distinguish sand particles bearing different lift-off speeds, the ejecting particles are classified into n groups and each one has a different lift-off velocity, any single group can be represented with a number k , $k = 1, 2, \dots, n$. Then we can get the components of impacting velocities $[V_{im}(k)]_{t_j}$ at time t_j after completing one step calculation at the end of t_j , and furthermore, can get the ejected particle flux $[N_s(k)]_{t_{j+1}}$ and the lift-off velocity probability density $f[V(k)]_{t_{j+1}}$ at next moment t_{j+1} by Eq. 5.10. Then continue with the next t_{j+1} moment calculation, repeat the above procedures until the following expressions $|u(z, t_j) - u(z, t_{j+1})|_{\max} < \delta_1$ and $|w(z, t_j) - w(z, t_{j+1})|_{\max} < \delta_2$ are satisfied, which means saltating population of wind-blown particles reaches an equilibrium. With this method, we can obtain the duration time of wind-blown sand flow, the wind profile $u(z, t)$ and $w(z, t)$, the mass flux per unit area and unit time $q(z, t)$ and the sand transport rate of particles $Q(z, t)$ at different time in the evolution process. Applying the above method, we can simulate the evolution of wind-blown sand flow with uniform particle size and take the thermal effect and electrostatic force into account (Yue and Zheng 2006). As a result, the evolution of wind-blown sand flow and the mass flux per unit area and unit time

are shown in Figs. 5.2 and 5.14 (curve 2), respectively, and curve 3 is the experimental data (Shao and Raupach, 1992). In this simulation the particle size $D_s = 0.25$ mm, the particle mass $m_s = 2.168 \times 10^{-8}$ kg, the charge quantity of a single particle $q^c = +1.3 \times 10^{-12}$ C (the charge-mass rate $C_q = +60 \mu\text{C}\cdot\text{kg}^{-1}$, Schmidt et al. 1998), the inflow friction velocity of air flow $u_* = 0.5 \text{ m}\cdot\text{s}^{-1}$, the earth surface temperature $T_s = 318$ K and the ejected particle flux $N_a = N_0(\tau_a - \tau_c)$ (Anderson and Haff 1991). From Fig. 5.12, it can be seen that all calculated curves show the same tendency with experiment result, which means the sand transport rate of particles exponentially increases at the beginning of the evolution process of wind-blown sand flow and then gradually slows down until it finally reaches the steady state. In other words, these mathematical models, no matter whether they take into consideration of thermal effect and electrostatic force or not, can capture the main characteristic of the self-regulating saltation process of saltation and the feedback mechanism as well. But there exist obvious distinctions in quantity when involving different factors. For example, when neglecting thermal effect and electrostatic force (Anderson and Haff 1991) the results (shown as curve 4) of the sand transport rate in Fig. 5.13 and the mass flux in Fig. 5.14 have large deviations compared to the experimental

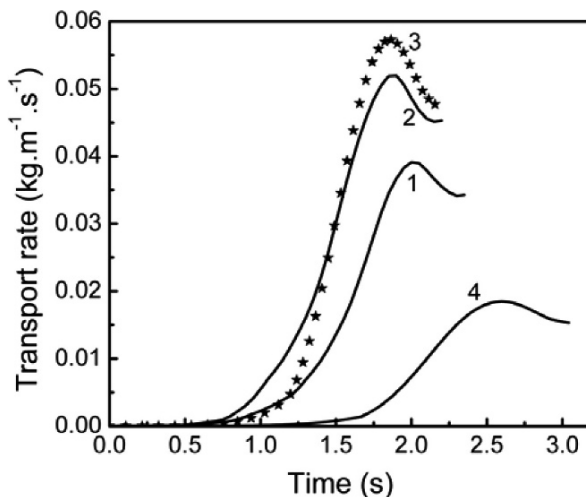


Fig. 5.13. Comparison of simulated sand transport rate with the experimental data when $u_* = 0.5 \text{ m}\cdot\text{s}^{-1}$, $D_s = 0.25$ mm, $m_s = 2.168 \times 10^{-8}$ kg, $q^c = +1.3 \times 10^{-12}$ C and $T_s = 318$ K; line 1: the results when electrostatic force is taken into account, line 2: the results when both electrostatic force and thermal diffusion are taken into account, ★: the measured results of Shao and Raupach (1992), line 4: the results of Anderson and Haff's model (1991)

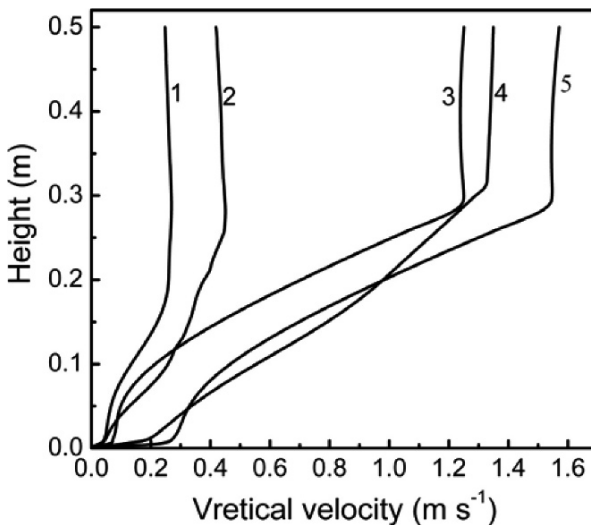


Fig. 5.14. Comparison of simulated mass-flux profiles at a steady state with the experimental data when $u_* = 0.5 \text{ m}\cdot\text{s}^{-1}$, $D_s = 0.25 \text{ mm}$, $m_s = 2.168 \times 10^{-8} \text{ kg}$, $q^c = +1.3 \times 10^{-12} \text{ C}$ and $T_s = 318 \text{ K}$; line 1: the results when electrostatic force is taken into account, line 2: the results when both electrostatic force and thermal diffusion are taken into account, line 3: the measured results of Shao and Raupach (1992), line 4: the results of Anderson and Haff's model (1991)

data, in which the duration time is longer, the steady value are much smaller, and the decay rate of the mass flux with height is much faster than the corresponding results of measurement. Although there still exist differences, the results including the electrostatic force (shown as curve 1) in Figs. 5.13 and 5.14 are more accordant with the experimental data than the former results, especially that the relative error of duration time is only 3% compared to the experimental data, while the relative error of the duration time calculated by Anderson and Haff (1991) in curve 4 is 26%. So the effect of electrostatic force on the evolution of the wind-blown sand flow is obvious. Meanwhile, the results, with both the electrostatic force and thermal effect, are considered to be much closer to the experimental data. For example, the sand transport rate at steady state is $Q = 0.045 \text{ kg}\cdot\text{m}^{-1}\cdot\text{s}^{-1}$ (curve 2), which is merely 5.26% lower than the experimental ones. The duration time (i.e., the time for the entire system to reach a steady state) is 2.2 seconds, only 1.85% longer than the experimental ones. At 10 cm height the mass flux is $0.35 \text{ kg}\cdot\text{m}^{-2}\cdot\text{s}^{-1}$, which is 2.63% lower comparing to the experimental result. Figs. 5.13 and 5.14 also suggest that the results of sand transport rate and the mass flux with and without in-

volving the thermal effect have obvious difference (TD is ‘with consideration of thermal effect’ and NTD is ‘without with consideration of thermal effect’). This is because the vertical wind velocity, caused by surface thermal effect, is about $1 \text{ m}\cdot\text{s}^{-1}$, which makes the sand particle lift off from surface more easily and makes its moving time becomes longer. In a word, the thermal effect, which can not only decrease the duration time but also increase the transport mass, is a remarkable and important factor in aeolian research.

The Figs. 5.15 and 5.16 show the vertical component of wind field during the evolution process of wind-blown sand flux in the condition of different initial surface temperatures $T_s = 298 \text{ K}, 308 \text{ K}, 318 \text{ K}, 328 \text{ K}, 338 \text{ K}$. From Fig. 5.15, it can be seen that the vertical wind velocities are varied greatly at different initial surface temperatures. The vertical wind velocities at higher surface temperature are much bigger than those at lower surface temperatures. For example, the vertical wind velocity $1.547 \text{ m}\cdot\text{s}^{-1}$ at 30 cm height with initial surface temperature 338 K , is much bigger than the vertical wind velocity $0.2683 \text{ m}\cdot\text{s}^{-1}$ with initial surface temperature 298 K . The vertical wind velocity increases first with height near the bed, and reaches its maximum at about 30 cm height, and then decreases slowly. From Fig. 5.16, it can be seen that the duration time decreases, the maximal value of sand transport rate and the mass flux at steady state increase with surface temperature. For example, the duration time is 1.8 s, the sand transport rate is $0.26 \text{ kg}\cdot\text{m}^{-2}\cdot\text{s}^{-1}$ when surface temperature is 338 K corresponding to the duration time 2.4 s, the sand transport rate $0.207 \text{ kg}\cdot\text{m}^{-2}\cdot\text{s}^{-1}$ at the normal temperature 298 K , it can be found that the duration time decreases 25%, the sand transport rate increases 25.6%. Although from above analysis we know that the thermal effect caused by the earth’s surface temperature has obvious influence on the evolution process of sand flow, it is difficult to induce a sand storm merely by thermal effect.

Figs. 5.17 and 5.18 show the variation of electric field with time during the evolution of mass flux, which correspond to the results in Fig. 5.13, and the horizontal wind velocity profiles at different moments. From Fig. 5.17, it can be seen that the variation regularity of electric field with height is similar to the developing law of sand transport rate, which first increases to the maximum, then decreases a little to a steady state. The reason is that the electric field intensity is closely related to the sand concentration (see Eq. 5.29). Meanwhile, due to the effect of thermal effect on the vertical wind velocity the electric field intensity with the thermal effect is usually larger than the electric field intensity without it. For example, the electric field intensity at 1cm height on steady state condition is $207.86 \text{ kV}\cdot\text{m}^{-1}$, which is $44.41 \text{ kV}\cdot\text{m}^{-1}$ higher than the value $163.45 \text{ kV}\cdot\text{m}^{-1}$ without

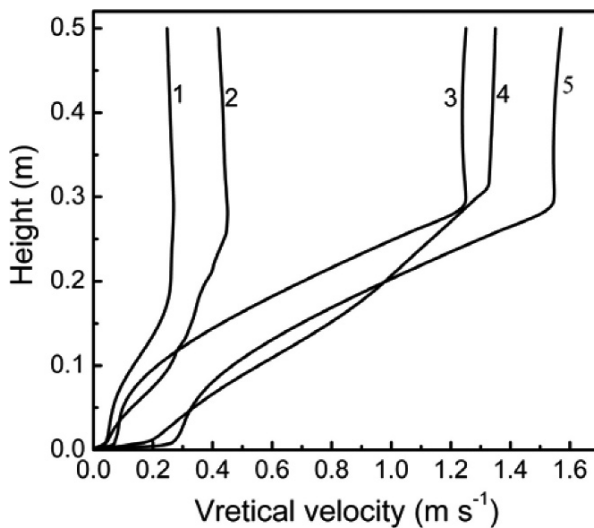


Fig. 5.15. The variations of vertical speed along the height under different surface temperatures with $u_* = 0.5 \text{ m}\cdot\text{s}^{-1}$, $D_s = 0.25 \text{ mm}$, $m_s = 2.168 \times 10^{-8} \text{ kg}$, $q^c = 1.3 \times 10^{-12} \text{ C}$. lines 1, 2, 3, 4 and 5 represent the results when surface temperature $T_s = 298 \text{ K}$, 308 K , 318 K , 328 K , 338 K , respectively

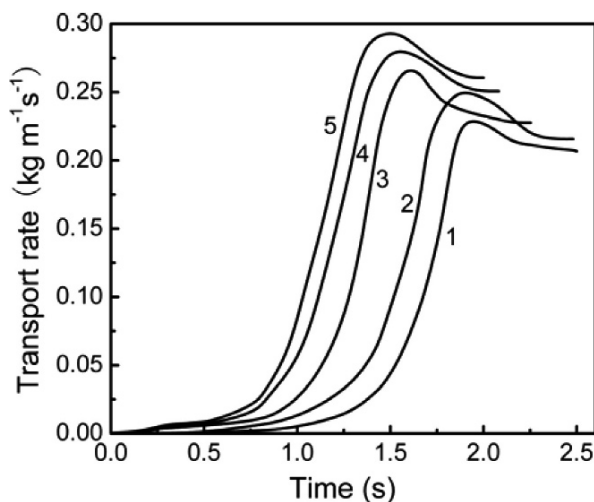


Fig. 5.16. The sand transport rate under different surface temperatures with $u_* = 0.5 \text{ m}\cdot\text{s}^{-1}$, $D_s = 0.25 \text{ mm}$, $m_s = 2.168 \times 10^{-8} \text{ kg}$, $q^c = +1.3 \times 10^{-12} \text{ C}$. The lines 1, 2, 3, 4, 5 represent the results when surface temperature $T_s = 298 \text{ K}$, 308 K , 318 K , 328 K , 338 K , respectively (Yue and Zheng 2006)

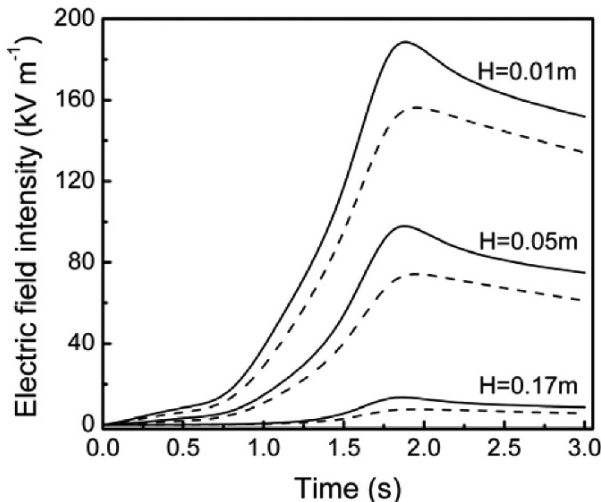


Fig. 5.17. The variation regularity of electric field with height when $u_* = 0.5 \text{ m}\cdot\text{s}^{-1}$, $D_s = 0.25 \text{ mm}$, $m_s = 2.168 \times 10^{-8} \text{ kg}$, $q^c = +1.3 \times 10^{-12} \text{ C}$. ‘Solid line’ is the electric field when the effect of thermal diffusion is taken into consideration, ‘dashed line’ is the electric field when the effect of thermal diffusion is not taken into consideration (Yue and Zheng 2006)

considering the thermal effect. Fig. 5.17 also suggests that there is a rapid attenuation of the electric field intensity with height. The value $16 \text{ kV}\cdot\text{m}^{-1}$ of electric field at steady state at 17 cm height is, for example, only 7.7% of the electric field at 1 cm height. This is also because the sand concentration rapidly decreases with height. In addition, Fig. 5.18 shows that the horizontal wind velocity in saltation layer obviously deviates from logarithmic distribution due to the reaction force of sand particles, which is different from the pure wind field where the horizontal wind velocity obeys the logarithmic distribution with height. Because of the retardance of sand particles, the velocities over surface are all smaller than their initial values, and the thermal effect makes this variation more obvious.

Using the theoretical analysis method depicted in this chapter, we find that the distribution of mass flux with height $q(z, t)$ presents obvious stratification pattern (Zheng et al. 2004). According to the saltation activity, the mass flux can be stratified into three layers: the first layer is near the surface, where the mass flux increases linearly with height, which is called a linear increment layer, the second layer is the saturation layer, where the mass flux tends to saturation and reaches to a maximum value with the increment of height, and correspondingly the height, at which the mass flux attains the peak value, is named as the saturation height; when the height

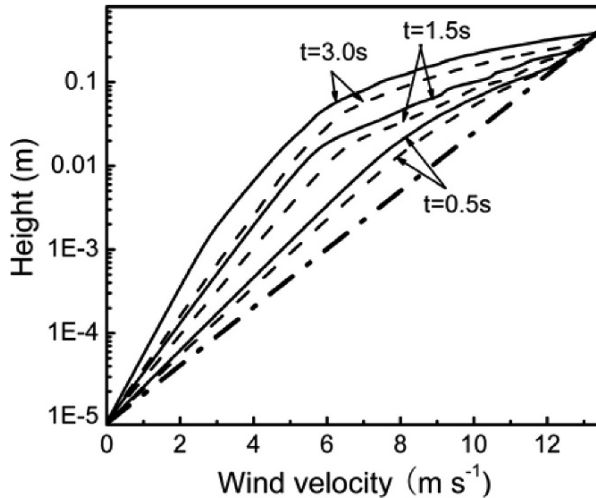


Fig. 5.18. The horizontal wind profile at different moments when $u^*=0.5 \text{ m}\cdot\text{s}^{-1}$, $D_s=0.25\text{mm}$, $m_s=2.168\times 10^{-8}\text{kg}$, $q^c=+1.3\times 10^{-12} \text{ C}$; — the electric field when the effect of thermal diffusion is taken into consideration, - - - the electric field when the effect of thermal diffusion is not taken into consideration, and - - - - is the initial profile (Yue and Zheng 2006)

is higher than the saturation layer, the mass flux decreases continuously as the negative exponent attenuation of e , this layer is called a monotonic decrement layer, the third layer which presents the monotone descending law of the wind-blown sand flow structure just as the characteristics of wind-blown sand flow structure described in common literature. In despite of the limitation of experiment to get the refined measurement of mass flux, it is not difficult to understand the stratification pattern according to the definition of mass flux, namely mass flux equals the product of particle horizontal speed and its number density. This is because, generally speaking, the number density of sand attains its maximum immediately above the surface, while the horizontal velocity of sand is at the lowest value. With increment of the height, the horizontal velocity increases rapidly, while the number density decreases. So, there must exists a height (saturation height) at which the mass flux, i.e., the product of the horizontal velocity and the number density, reaches a peak value. Below this saturation height, the mass flux increases rapidly with increasing height, but it declines above the saturation height. The analysis on the stratification pattern of mass flux density can probably help us to understand why the erosion of

wind-blown sand flux to plants and other objects occurs at the certain height above surface but not the surface.

Here, it needs to emphasize that the researches in this chapter did not consider the asymmetry of the nature wind field along the wind direction. Actually, because of some reasons, such as the difference of surface quality, the randomness of lift-off profile of sand particles and the turbulence characteristics of wind field, there exist asymmetry of sand movement, sand flow concentration, and mass flux along the wind direction. For example, Butterfield (1991) measured the relationship of the instantaneous mass flux and the instantaneous wind through wind tunnel experiments designed by himself. The results suggest that there exists large fluctuation of the instantaneous mass flux and thus he concluded that the spatial distribution of mass flux is asymmetric. Therefore it is not suitable to represent the sand transport rates of all points along wind direction with the sand transport rate at a fixed spot. Some scholars have noticed the turbulence characteristics of air flow. For example, Shao and Li (1999) adopt the Large Eddy Simulation and $K-\varepsilon$ model for sub-grid turbulent stress term in solving the N-S equation. They calculated the evolution of the wind-blown sand flux, gained the saturation length. Xing and Guo (2004) also applied $K-\varepsilon$ turbulent model to simulate air flow in their wind-blown sand flux model. But these models are far from realizing the revelation of the effect of fluctuations of air flow along wind direction on the sand transport process. We bring forward a simulation method to reveal the change of mass flux along wind direction and the effect of turbulence on sand movement, where the fluid phase is described by average spatial hydrodynamics equation and the resistance of sand particles to wind field is considered. In this simulation model, we adopt the Large Eddy Simulation at the turbulent stress part, and use the DEM method to describe the sand phase. Then the splashing function is applied to obtain the motion characteristics of the whole wind blown sand movement system. The results show that the sand transport rate along the wind direction is heterogeneous, which reproduce the experimental results of Butterfield (1991). Meanwhile, the intensity of turbulence of air flow is obviously enhanced by saltating particles. Through analyzing the sand transport rate, it is found that the variation relations of mass flux and wind in the same time period are opposite. That is the wind friction velocity decreases as sand transport rate increases and vice versa.

5.5 Dust Devil

Different from wind-blown sand flux, where dust particles mainly move along wind direction, the dust particles whirlily rise under the action of air flow field. Its shape looks like a reverse cone and is similar to that of cyclone, see the Fig. 5.19. They are common meteorological phenomena in desert areas on the Earth as well as Mars (NASA). Early studies of dust devils are field measurements (Ives 1947; Sinclair 1964, 1965, 1973; Carroll and Ryan 1970; Hess and Spillane 1990), and some meteorological characteristics of dust devils were obtained from these observations, for example, the temperature 1–2 m above surface increases from 4 K to 8 K and pressure in the center of dust devil decreases 2.5 hPa to 4.5 hPa after dust devil happens, the velocities in both tangential and vertical directions are usually $15 \text{ m}\cdot\text{s}^{-1}$. Most researchers believe that the mechanism of dust devil involves: strong daytime heating of the local surface generates intense turbulence and convective plumes, air converging into these plumes tends to conserve any initial angular momentum. If the plume and initial angular momentum are sufficiently intense, a spinning vortex develops.



Fig. 5.19. Dust devil, taken in Michigan June 10th, 2005, it looks like a reverse cone and similar to that of cyclone, 30 meters wide and about a kilometer high, with winds of $40 \text{ km}\cdot\text{hr}^{-1}$ (from NASA)

The spinning air picks up sand particles to form the visible dust devils (Sinclair 1965, 1976; Hallet 1968; Kaimal and Businger 1970; Carroll and Ryan 1970; Cortese and Balachandar 1993; Shapiro and Kogan 1994). Levy (2003) also pointed out that high temperature at local surface heated by solar radiation and other factors may result in dust devil. In dust devils, particles in contact with each other and some of them are known to generate electric charge via frictional or triboelectric processes (Mills 1977). These charged particle will generate electric field in dust devil (Renno et al. 2004; Freier 1960; Farrell et al. 2003, 2004). Renno et al. (2004) measured that electric field could reach $10 \text{ kV}\cdot\text{m}^{-1}$ in a large dust devil. The strong electric field in dust devils may be a possible nuisance or hazard to future human explorers and equipments on the surface of planets (Farrell et al. 2004), and therefore more and more scientists pay their attention on the study of electric field in dust devils.

Because it is difficult to get detailed information of the electric field in dust devils through measurement, the simulation becomes an effective way to study the electric field (Renno et al. 1998; Kurgansky 2005). Kanak et al.(2000) and Fiedler and Kanak (2001) found that there were vertical vortices, which was called dust devils in their simulation of the convective boundary layer by the method of Large Eddy Simulation. Gu et al.(2003, 2006) simulated dust devils through enacting a constant thermal flux and the initial conditions of spherical temperature gradient, which can form hot-plumes. In this section we introduce a model based on the surface energy-balance equation and atmospheric movement equations, and Coulomb's law, to simulate the whole process of dust devil development and the electric field in dust devil. This model can directly get the simulating results of dust devil and electric field in it and abandons the artificial conditions of Gu et al. (2003, 2006). The result shows that the inhomogeneity of local earth surface temperature is an important factor for the formation of dust devil.

To achieve the basic equation describing the dust devil, the atmospheric Eqs. 2.19, 2.22, 2.24 and 2.25 are applied here. Based on K -theory, (Yamamoto et al 1968), assume $\tau_{\phi x} = -\rho\bar{\phi}u' = K_H\rho\partial\phi/\partial x$, $\tau_{\phi y} = -\rho\bar{\phi}v' = 0$ and $\tau_{\phi z} = -\rho\bar{\phi}w' = K_m\rho\partial\phi/\partial z$, where ϕ represents the three components u , v , w of wind velocity. Apply Reynolds Average method to energy equation (Eq. 2.22), and substitute potential temperature $\theta \approx T_d + \text{const}$ for temperature T_d , where the *const* is the temperature at reference height. Then assume the thermal flux $H_{\theta x} = \rho\bar{\theta}u' = -K_H\rho\partial\theta/\partial x$, $H_{\theta y} = \rho\bar{\theta}v' = 0$, and $H_{\theta z} = \rho\bar{\theta}w' = -K_\theta\rho c_p\partial\theta/\partial z$, where K_m , K_H and K_θ are thermal diffusion parameters. Then we have the following momentum and energy conservative equations (Stull 1988):

$$\frac{\partial u}{\partial t} + u \frac{\partial u}{\partial x} + v \frac{\partial u}{\partial y} + w \frac{\partial u}{\partial z} = -\frac{1}{\rho} \frac{\partial p}{\partial x} + \frac{\partial}{\partial z} \left(K_m \frac{\partial u}{\partial z} \right) + K_H \frac{\partial^2 u}{\partial x^2}, \quad (5.34a)$$

$$\frac{\partial v}{\partial t} + u \frac{\partial v}{\partial x} + v \frac{\partial v}{\partial y} + w \frac{\partial v}{\partial z} = -\frac{1}{\rho} \frac{\partial p}{\partial y} + \frac{\partial}{\partial z} \left(K_m \frac{\partial v}{\partial z} \right) + K_H \frac{\partial^2 v}{\partial x^2}, \quad (5.34b)$$

$$\frac{\partial w}{\partial t} + u \frac{\partial w}{\partial x} + v \frac{\partial w}{\partial y} + w \frac{\partial w}{\partial z} = -\frac{1}{\rho} \frac{\partial p}{\partial z} + \frac{\partial}{\partial z} \left(K_m \frac{\partial w}{\partial z} \right) + K_H \frac{\partial^2 w}{\partial x^2}, \quad (5.34c)$$

$$\frac{\partial \theta}{\partial t} + u \frac{\partial \theta}{\partial x} + v \frac{\partial \theta}{\partial y} + w \frac{\partial \theta}{\partial z} = \frac{\partial}{\partial z} \left(K_\theta \frac{\partial \theta}{\partial z} \right) + K_H \frac{\partial^2 \theta}{\partial x^2}. \quad (5.34d)$$

Here we omit the superscript ‘-’ on variables for simplicity. The above equations and the mass conservative equation (Eq. 2.1), the state equation (Eq. 2.19) and the surface energy-balance equation (Eq. 5.29) compose the basic equations of dust devils. The computation domain is shown in Fig. 5.20, and the initial and boundary conditions are as follows:

$$z=0: u=v=w=0, T_S = \begin{cases} T_{s0} & r < r_0 \\ T_{s0} - \eta_1 r & r_0 \leq r \leq R_0 \end{cases}, \quad (5.35a)$$

$$z=H: \frac{\partial u}{\partial z} = \frac{\partial v}{\partial z} = 0, \quad T = T_a - \eta_2 H, \quad p = p_0 \left(1 - \frac{\eta_2}{T_a} H \right)^{\frac{g}{\eta_2 R}}, \quad (5.35b)$$

$$r=R_0: u=v=w=0, \quad \frac{\partial u}{\partial z} = \frac{\partial v}{\partial z} = 0, \quad T = T_a - \eta_1 z, \quad p = p_0 \left(1 - \frac{\eta_2}{T_a} H \right)^{\frac{g}{\eta_2 R}}, \quad (5.35c)$$

$$t=0: \quad T = T_a - \eta_1 z, \quad \theta = T \left(\frac{p_0}{p} \right)^{-\frac{R}{c_p}}, \quad p = p_0 \left(1 - \frac{\eta_2}{T_a} H \right)^{\frac{g}{\eta_2 R}},$$

$$\frac{\partial p}{\partial x} = \frac{\partial p}{\partial y} = 0, \quad \frac{\partial p}{\partial z} = -\rho g, \quad (5.35d)$$

$$u = \begin{cases} 0 & 0 < z < H \\ u_0 \sin \alpha & z = H \end{cases}, \quad v = \begin{cases} 0 & 0 < z < H \\ u_0 \cos \alpha & z = H \end{cases}, \quad w = 0.$$

where T_{s0} is the earth surface temperature for the area $r \leq r_0$, and for the other area $r_0 < r \leq R_0$, it obeys the damping law with the rate η_1 along radial direction. r_0, R_0, H are the radius of the center part and outer part and the height of computation domain respectively, as shown in Fig. 5.20. The pressure p_0 at the bottom is 1013 hPa, $c_p = 1.005 \text{ K}\cdot\text{J}\cdot\text{kg}^{-1}$ is the value of specific heat at constant pressure, the gas constant $R = 8.3145 \text{ J}\cdot\text{mol}^{-1}\cdot\text{K}^{-1}$, $\alpha \in [0, 2\pi]$ is the angle between the line from center point to valuating point and x -direction in $z=H$ surface, $u_0=0.4 \text{ m}\cdot\text{s}^{-1}$ is the initial tangential velocity. The maximal tangential velocity is about $15 \text{ m}\cdot\text{s}^{-1}$ in dust devil, so the initial tangential velocity is common in nature, and Gu et al. (2006) take it as $0.5 \text{ m}\cdot\text{s}^{-1}$.

Through calculation and comparison, it is found that the drag force \mathbf{F}_D acting on the sand particles is much greater than other forces, such as gravitation and so on (Gu et al. 2006). So only the drag force is considered in Eq. 5.12. Assuming that the sand source is rich, the sand particles are randomly selected from three groups whose diameter are 0.15 mm, 0.2 mm and 0.25 mm with a ratio of 1:1:1. When solving the atmospheric equation, the grid type is taken as uniform cube. For simplicity, the grids of ground surface are the same as that of space over the surface. When wind velocity

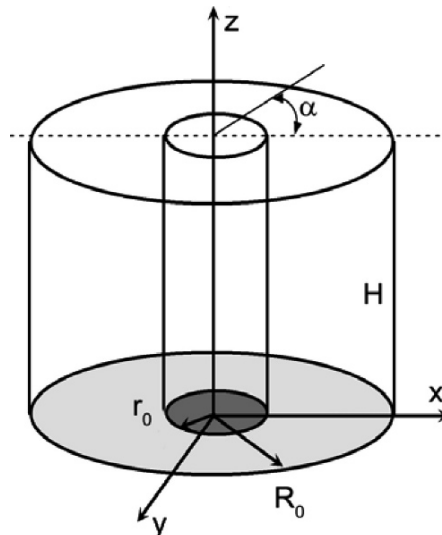


Fig. 5.20. The illustration of the dust devil simulation domain; r_0, R_0, H are the radii of the center part and outer part and the height of computation domain, respectively

exceeds the threshold velocity sand particle will lift off from bed. The lift-off velocity \bar{V} of a sand particle is randomly taken from the domain of $[\sqrt{2gD_s}, 5u_*]$, $n = (\bar{V}/\pi D_s^3)\Delta t$ is the number of lifting particles in each time step, D_s is the mean diameter of sand particles.

In modeling, as sand particles impact with the surface and as particle-particle collisions happen, they will be positively or negatively charged and these charged sand particles will generate electric field. Assuming the charge quantity of a particle is q_i^c , according to Coulomb's law (Stratton 1941), the electric field at a given point $P(x, y, z)$ in dust devil can be expressed (see Fig. 4.9):

$$\mathbf{E} = k \sum_{i=1}^{N_d} \frac{q_i^c}{\mathbf{r}_i^2} \quad (5.36)$$

Where $k = 1/4\pi\epsilon_0$, $\epsilon_0 = 8.854 \times 10^{-12} \text{ F}\cdot\text{m}^{-1}$ is spatial dielectric constant (Stratton 1941), \mathbf{r} is vector distance between the charged sand particle and the point $P(x, y, z)$, N_d represents the particle number in dust devil, it is obtained by computation.

The wind velocity field can be obtained by solving the Eq. 5.3, then based on the velocity components u, v, w to calculate sand particles trajectories. Let $T_{s0} = 318 \text{ K}$, and the damping rate $\eta_1 = 0.2$ according to our measurement, we can get the isothermal distribution in the evolution of dust devil. Simulated results are shown in Fig. 5.21a, it can be seen that hemispheric isothermal distribution is forming at the beginning of the simulation and isotherms deliver upward step by step. Then isotherms break down at a height, and the high temperature delivers further upwards. In this process the zone of high temperature extends gradually, and the isotherms change from fastigium shape to dome shape (see Fig. 5.21b). Meanwhile, intense turbulence and convective plumes are generated, air Fig. 5.22 presents the simulated results of the whole flow field at the time about 200 seconds from the beginning of our simulation. It can be seen from Fig. 5.22 that a whirly wind field is formed in the calculating region. In the center and outside region of dust devil the wind velocity is small, but at the interior region between the center and outside region of dust devil the wind velocity is much greater and can reach a maximum value of $30 \text{ m}\cdot\text{s}^{-1}$.

The simulated results also show that more and more sand particles with different diameters are picked up into rotational wind field until the number of particles in air attaining a dynamic balance. It needs about 90 s from the moment when a sand particle is ejected from the bed to a fully developed dust devil. It can be seen from Fig. 5.23 that smallest sand particles

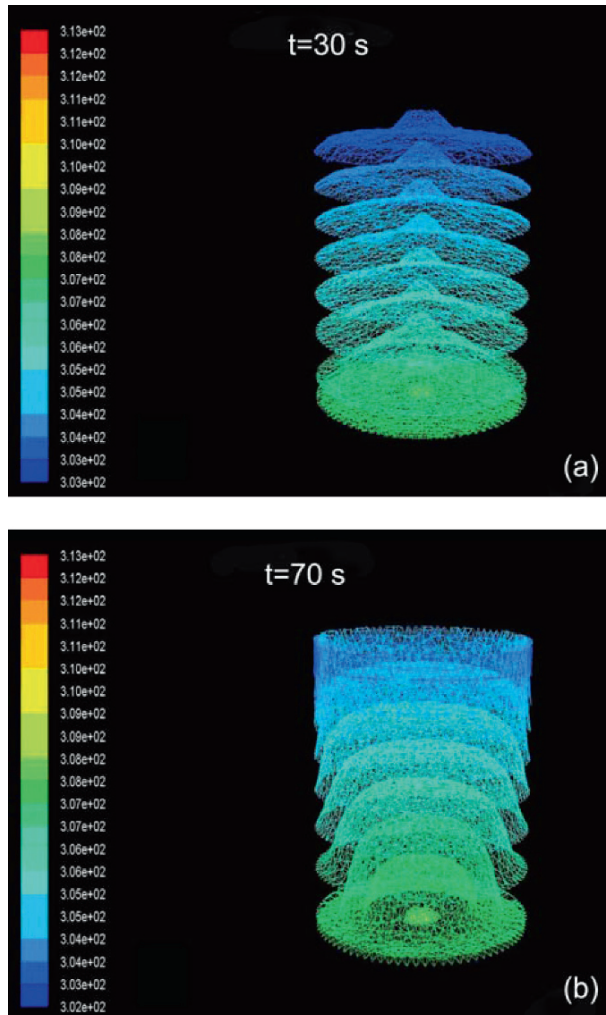


Fig. 5.21. The isothermal distribution in the evolution of dust devil through the large eddy simulation (a) is the isothermal distribution at the moment 30 s when hemispheric isothermal distribution is formed. (b) is the isothermal distribution at the moment 70 s when the isotherms change from fastigium shape to dome shape; The temperature varies 302 K to 313 K. ($H=400$ m, $r_0=4$ m, $R_0=50$ m, $T_{s0}=318$ K, $\eta_1=0.2$, $u_0=0.4$ m·s⁻¹) converging into these plumes tends to conserve initial angular momentum and a spinning vortex develops. It indicates that the generation of plumes is caused by the inhomogeneity of surface temperature, which is common in desert region. Therefore, we can conclude that the inhomogeneity is the essential reason and necessary condition for the formation of dust devils.

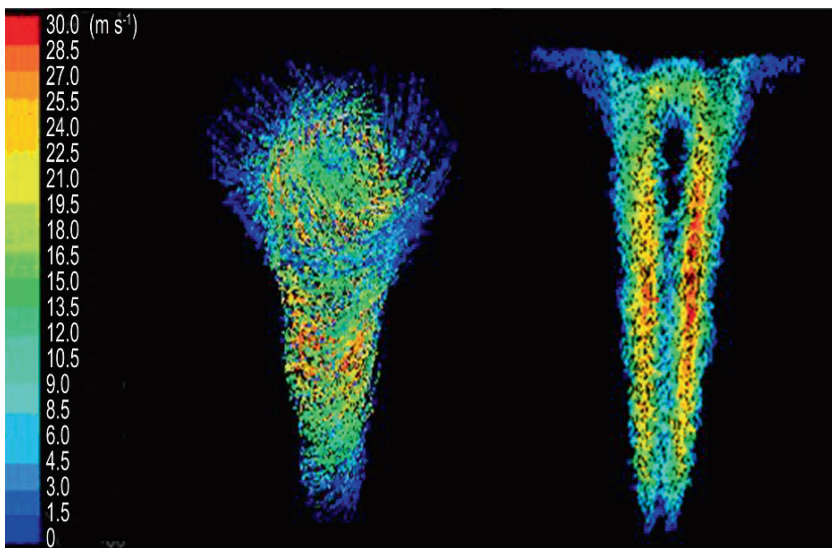


Fig. 5.22. Wind velocity vector graph of dust devil (right graph is section plane), at interior region between the center and outside region of dust devil the wind velocity is much greater and can reach a maximum value of $30 \text{ m}\cdot\text{s}^{-1}$ (Let $H = 400 \text{ m}$, $r_0 = 4 \text{ m}$, $R_0 = 50 \text{ m}$, $T_{s0} = 318 \text{ K}$, $\eta_1 = 0.2$, $u_0 = 0.4 \text{ m}\cdot\text{s}^{-1}$. The numerical method is the large eddy simulation)

(red dots, $D_s = 0.15 \text{ mm}$) usually move higher and the sand particles with biggest diameter (blue dots, $D_s = 0.25 \text{ mm}$) move lower, and the sand particles with $D_s = 0.20 \text{ mm}$ (green dots) move between smallest sand particles and biggest sand particles. This indicates that when sand particles with different diameters move in dust devil, stratification will occur: small sand particles are usually above big sand particles. This phenomenon is contrary to ripple stratification (see Chap. 6) in aeolian landforms.

If the specific charges of sand particles are given, for example, the specific charges of sand particles with diameters 0.15 mm, 0.2 mm and 0.25 mm are taken as -120 , -60 and $57 \mu\text{C}\cdot\text{kg}^{-1}$ respectively, we can calculate the electric field by Eq. 5.35 after account for the sand particles number at different heights and times. Fig. 5.24 presents the calculated results of electric field distributions of 20 m height along radial direction for four different moments. From Fig. 5.24 it can be seen that at the beginning of the evolution of dust devil the electric field strengthens with time, especially in the central range (0, 6 m) of dust devil the electric field is bigger and the amplitude is significant. But when electric field of dust devil trends to stabilization or dynamic balance, the electric field changes little as the

number of particles in dust devil almost does not increase. This is characterized by the fact that the curves of electric fields at 80 s and 90 s are almost superposed. So we may conclude that it takes about 90 s for dust devil to attain to stabilization. The electric fields at different heights are described in Fig. 5.25 in a stable dust devil. From Fig. 5.25 it can be seen

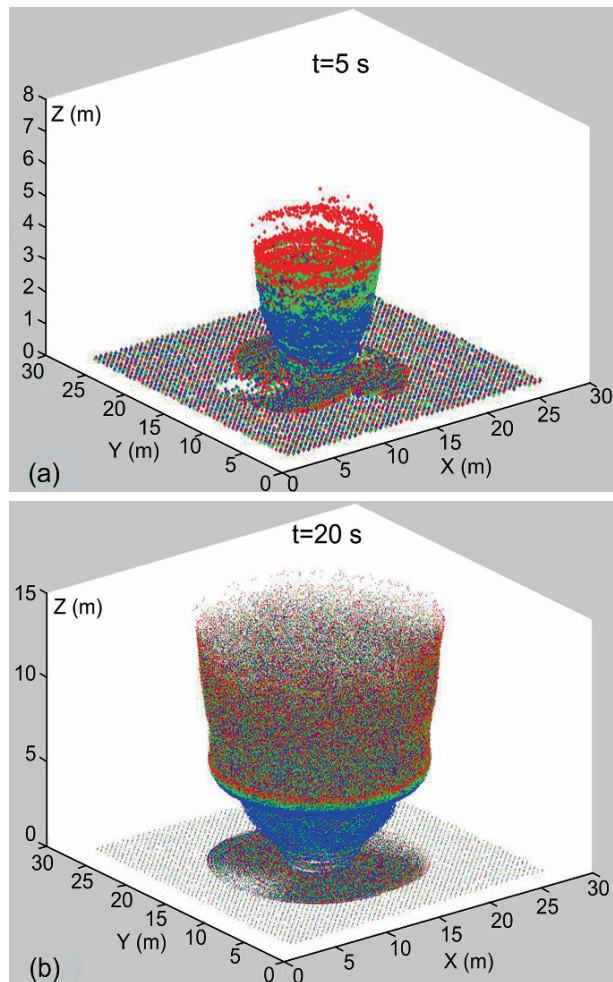


Fig. 5.23. The processes of dust devil, smallest sand particles (red dots, $D_s = 0.15$ mm) usually move higher and sand particles with biggest diameter (blue dots, $D_s = 0.25$ mm) move lower, and sand particles with $D_s = 0.20$ mm (green dots) move between smallest sand particles and biggest sand particles

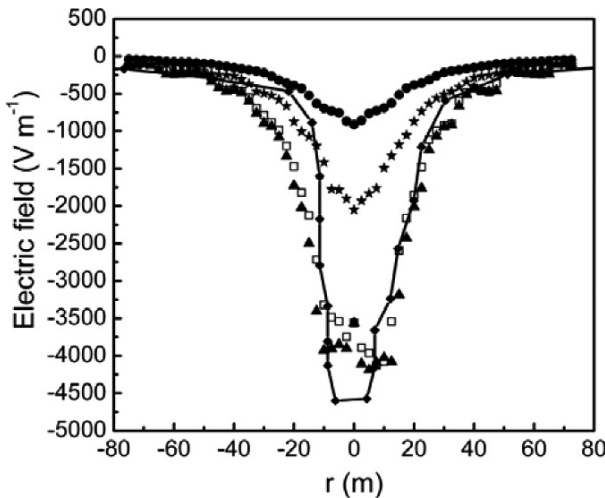


Fig. 5.24. Electric field distributions at the height of 20 m along radial direction for four different moments. The specific charges of sand particles with diameters 0.15 mm, 0.2 mm and 0.25 mm are taken as -120 , -60 and $57 \mu\text{C}\cdot\text{kg}^{-1}$, respectively; ● the simulated electric field at 20 s, ★ the simulated electric field at 40 s, □ the simulated electric field at 80 s, ▲ the simulated electric field at 90 s, —◆— the electric field measured by Farrell et al.

that the electric field at different heights reach maximums at the center of dust devil and decrease rapidly along radial. The electric field increases with height below 20 m, but at 30 m height the value is much less than that at 20 m, which may be related to sand concentration distribution. The maximum electric field in a stable dust devil is in the center of it and at a height of 20 m above surface and its value is about $4.128 \text{ kV}\cdot\text{m}^{-1}$. Fig. 5.24 and Fig. 5.25 reproduce the results of measurements by Farrell et al. (2004). Compared with the observations, we can find that simulated results in this book, such as the maximum point or the distribution of electric field along radius direction, are accordant with the observations. For example at 20m height the calculated electric field is $4.128 \text{ kV}\cdot\text{m}^{-1}$, which is only 10.2% smaller than $4.599 \text{ kV}\cdot\text{m}^{-1}$ of the measurement. Therefore it can be confirmed that the simulation results of dust devil are reliable to some extent.

It is noteworthy that the electric field results stand on the assumption that the specific charges of sand particles with diameters 0.15 mm, 0.2mm and 0.25 mm are -120 , -60 and $57 \mu\text{C}\cdot\text{kg}^{-1}$ respectively. If we change the

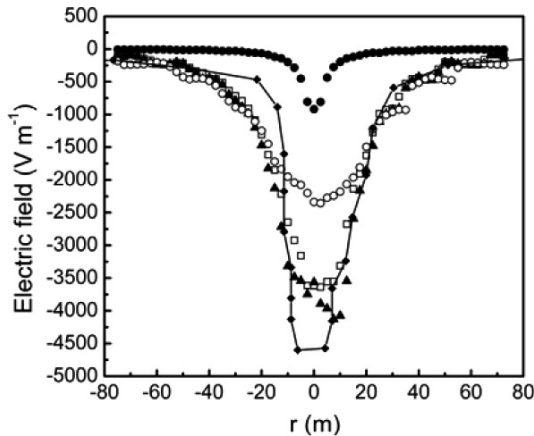


Fig. 5.25. The Electric fields along the radial direction for four different heights in a stable dust devil, all electric fields at the four heights reach maximums at the center of dust devil and decrease rapidly along radial. the specific charges of sand particles with diameters 0.15 mm, 0.2 mm and 0.25 mm are taken as -120 , -60 and $57 \mu\text{C}\cdot\text{kg}^{-1}$ respectively. ● the simulated electric field at 1m in height, ○ the simulated electric field at 10m in height, □ the simulated electric field at 20 m in height, ▲ the simulated electric field at 30 m in height, —◆— the electric field measured by Farrell et al

specific charges, the results should vary accordingly. However, from recent progress of wind-blown sand research, it can conclude that it is difficult to obtain the exact specific charges of sand particles with different sizes, because the specific charge of sand particles are not only affected by particle size, but also related to wind velocity and other factors. So the key issue of the wind-blown sand electrification study is how to correctly determine the specific charges. Besides direct measurements, it may be an effective way to reverse the specific charge from the measured value of electric field by the model and methods introduced in this chapter.

Chapter 6 Aeolian Geomorphology and its Simulation—Aeolian Sand Ripples

In desolate deserts, sand particles are arranged by wind into various geomorphologic patterns, like aeolian sand ripples and aeolian sand dunes, according to certain rules. Aeolian landforms exist not only on Earth (see Fig. 6.1) but also on other planets, such as Mars (see Fig. 6.2). Strikingly, the corresponding patterns on different planets and the different patterns on a same planet have a similarity. Therefore, it is meaningful to reveal the dominating mechanism governing the formation, evolution and distribution of aeolian landforms, which is beneficial to the understanding of wind erosion, transportation and deposition of sand (dust) materials. In addition, it is also helpful to the theoretical guidance for the designs of sand-fixing facilities and sand-controlling projects in deserts, for example, the roads and railways passing through deserts are required to avoid the moving route of sand dunes.

Aeolian geomorphology system is a typical complex dynamical system, which presents a complex hierarchical structure. The scales of ripples, dunes and draas are 10^{-2} – 10^{-1} m, 10^{-1} – 10^2 m and 10^2 – 10^3 m respectively. Ripples, as the smallest member of the hierarchy, are frequently observed on sand bed surface and dune surface. Although neither ripples can grow into dunes nor can dunes grow into draas and their formation mechanisms are not the same, all of these three landforms' patterns have an obvious similarity (see Figs. 6.1 and 6.2). Surprisingly, such erratic and orderly patterns are derived from disorderly moving of sand particles, whose scale is micrometer in magnitude. Besides, there are many interesting phenomena; for example, the self-reparation of ripples on a smoothed surface under wind action, and the critical collapsing or 'avalanche' during sand accumulation. These together make the aeolian geomorphology system be a characteristic example and natural laboratory for non-linear science. More and more scientists in mathematics, physics, mechanics, and other fields have been paying attention to this subject. Till now, aeolian desert geomorphology system has been an important subject of granular material research. The rich spatial-temporal dynamical behaviors involved in the aeolian geomorphology system make it also be a typical example in pattern

dynamics. Moreover, macro-scale phenomena of aeolian geomorphology system in deserts can give an image comparison explanation to microscopic structures of crystal and many other materials. For example, sand pile models have long been used to study superconductor (Gennes 1966). The formation mechanism of large compound sand dunes will help deepen understanding the process of biological evolution from simplicity to complexity, etc. Altogether, the understanding, recognition and description of aeolian geomorphology system, which mainly include multi-level, trans-scale, self-organization, self-reparation, critical and non-linear properties

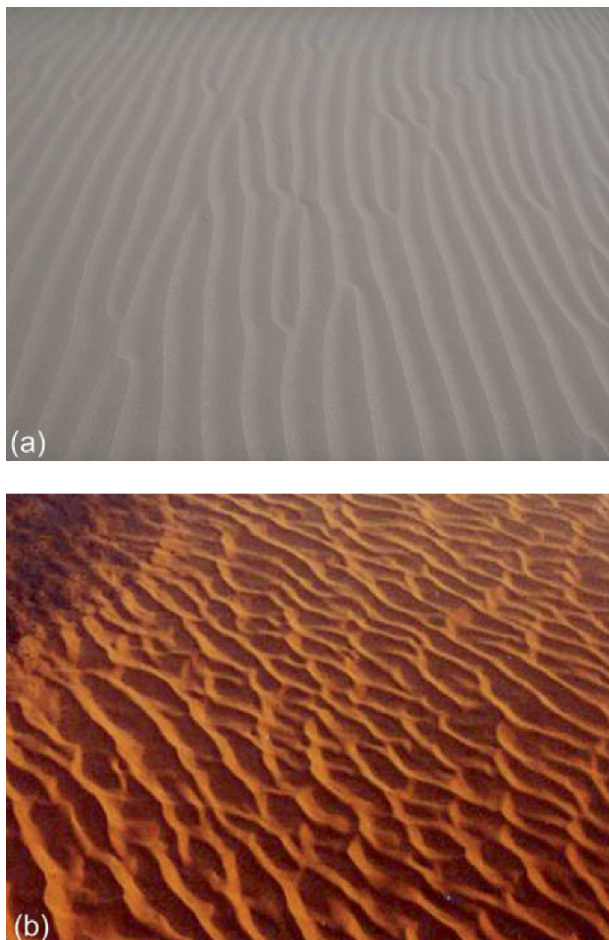


Fig. 6.1. Aeolian landforms on Earth, (a) aeolian sand ripples in the Badain Jaran Desert (photo by the author et al.) and (b) aeolian sand dunes in the Tengger Desert, China (photo by YQ Ling)

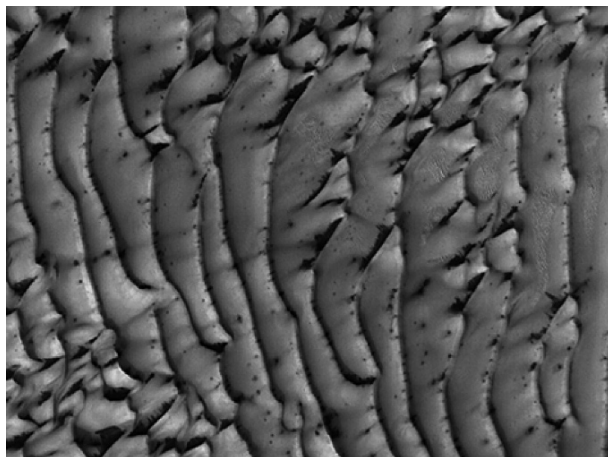


Fig. 6.2. Frost covered sand dunes in the Martian North polar region acquired by Mars Orbiter Camera on 29 August 2005 (Courtesy NASA/JPL-Caltech)

of complex systems, and the development process from disorder to order (Shinbrot and Muzzio 2001) have been fundamental issues in numerous scientific forefronts. It has universality and extreme significance in science (Werner 1999).

This chapter will mainly launch the discussion on aeolian sand ripples. In Sect. 6.1, some field observations and wind tunnel experiments on basic features of aeolian sand ripples and their formation mechanism are introduced. Sects. 6.2 and 6.3 provide two main methods used for simulating the formation and evolution of aeolian sand ripples, namely, the continuous sand ripples model and discrete sand ripples models. Sect. 6.4 devotes to the description of the discrete particle tracing method, a new numerical method proposed by the author et al. to simulate aeolian sand ripples. The results of this method agree with the real formation and development process of aeolian sand ripples not only in quality (in pattern) but also in spatial and temporal scale.

6.1 Observations of Aeolian Sand Ripples

6.1.1 The Basic Characteristics of Aeolian Sand Ripples

Aeolian sand ripples refer to the slight fluctuation on loose sand surface under wind action, which is usually accompanied by the Y-junctions or



Fig. 6.3. The cross-section profile of a aeolian sand ripple captured in wind tunnel, the axial wind velocity is $12 \text{ m}\cdot\text{s}^{-1}$, the sand is natural dune sand sampled from the Badain Jaran Desert, China, and the size distribution of sand particles is shown in Fig 4.1 (photo by the author et al. in the multi-function wind tunnel of Lanzhou University)

bifurcations (Fig. 6.1a). The spacing between neighboring crests is approximately uniform, namely the wavelength. Field observations and wind tunnel experiments show that aeolian sand ripples have the following properties.

Asymmetric Shape: The profile of an aeolian sand ripple is obviously asymmetry. From wind tunnel experiments (Here, the sand used in experiment is natural dune sand sampled from the Badain Jaran Desert, China), it can be found that when wind velocity varies from $7 \text{ m}\cdot\text{s}^{-1}$ to $20 \text{ m}\cdot\text{s}^{-1}$, the saturated ripple is asymmetric (see Fig. 6.3), with a convex windward (stoss) slope having a angle of $8^\circ\text{--}15^\circ$ and a concave leeward slope. For the leeward slope, the angle in the peak is about 30° which is close to the repose angle of sand, whereas the slope angle at the bottom is a little smaller, which is about 20° . The wavelength λ of a ripple is typically between $7.5\text{--}15 \text{ cm}$, and amplitude H is between $0.5\text{--}1.0 \text{ cm}$. The ripple index $RI = \lambda / H$ and symmetry index $RSI = i / s$ are usually used to depict the undulation shape characteristic, where i and s are the projected length of windward slope and leeward slope respectively. Our field observations in the Badain Jaran Desert showed that the ripple index lies in a range of $9 \leq RI \leq 22$ and has a linear relationship with the wind velocity. The average index is about 15, which is a little smaller than the ripple index of 18 in the Mojave Desert Kelso Dunes of the United States (Sharp 1963). That may be caused by the difference of wind velocity and size distribution of sand particles.

Wind Velocity Relativity: The results of both wind tunnel experiments and field observations show that the wavelength of an aeolian sand ripple increases with wind velocity. In the developmental stage of an aeolian sand ripple, its amplitude slowly increases with the wind velocity, but

when wind velocity exceeds a certain threshold, which is about $14 \text{ m}\cdot\text{s}^{-1}$ (the axis wind velocity in wind tunnel), its wavelength decreases with wind velocity and the ripple starts dying out. Similarly, the ripple index increases with the wind velocity. However, the symmetry index has little change with variations of wind velocity (Ling et al. 1998). Generally speaking, under the blowing of high-velocity wind, ripples become straight, ripple index reaches as high as 50–60, and the threshold wind velocity for the disappearance of aeolian sand ripples is about 3–4 times to the threshold wind velocity for the startup of sand particles. In addition, our field observations conducted in the Badain Jaran Desert of China showed that: the ripples in the windward and the leeward slope of dune arms have slightly different disposition. Generally, the ripple index in the windward slope is greater than that in the leeward slope. In the windward slope of a dune, the direction of ripple's crest is normal to the main wind direction and the scales of ripples increase with the height of bed surface. While in the leeward slope of a dune, the direction of ripple's crest is parallel to the main direction extending from the dune crest to the foot of the leeward and their wavelengths and amplitudes first increase and then

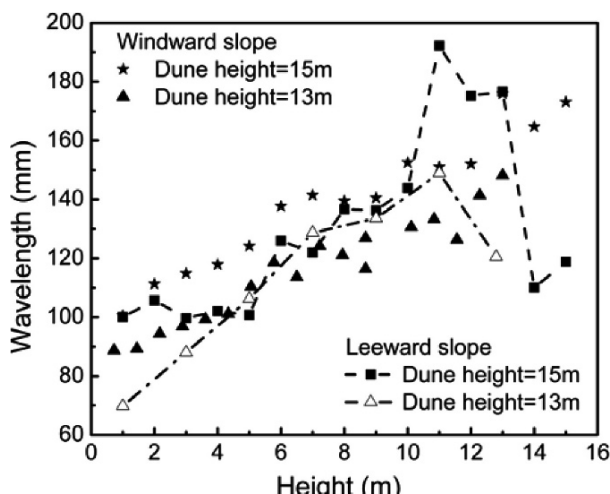


Fig. 6.4. The variations of saturated ripple's wavelength with the surface height; the measurements are conducted at windward and leeward slopes respectively on two sand dunes in the Badain Jaran Desert (by the author et al.); ★ the results measured on the windward slope of a 15 m-high dune, ▲ the results measured on the windward slope of a 13m-high dune, —■— the results measured on the leeward slope of a 15 m-high dune, —△— the results measured on the leeward slope of a 13m-high dune

decrease with the height of bed surface (see Fig. 6.4). For the Y-junctions, the wavelength of upwind junction is less than that of downwind, and their difference first decreases and then increases with the friction wind velocity (see Fig. 6.5).

Particle Diameter Dependence: Both of the wavelengths and the amplitudes of ripples are proportional to the sand diameter. For example, Stone and Summers (1972) suggested that $L = 63.8D_s^{-0.75}$; here, D_s (mm) is the average sand diameter in the crest of ripples. Usually, aeolian sand ripples present a stratigraphic structure, that is, the coarsest material collects at the crest, and the finest in the trough. This characteristic distinguishes without exception the ripples from the dunes, wherein the reverse is invariably the case (Bagnold 1941). Besides, sand gradation is also a key factor influencing the height and shape of the ripple. For ‘uniform’ sands, the height of an aeolian sand ripple is relatively low, and the ripple index generally follows $RI < 30$ (Bagnold 1941). However, the ripple with broad size range and poor size separation has a ripple index reaching as low as 15, even about 10. This is because the coarse sand particles are more difficult to be transported under the wind action, and thus gather at the crest of ripple.

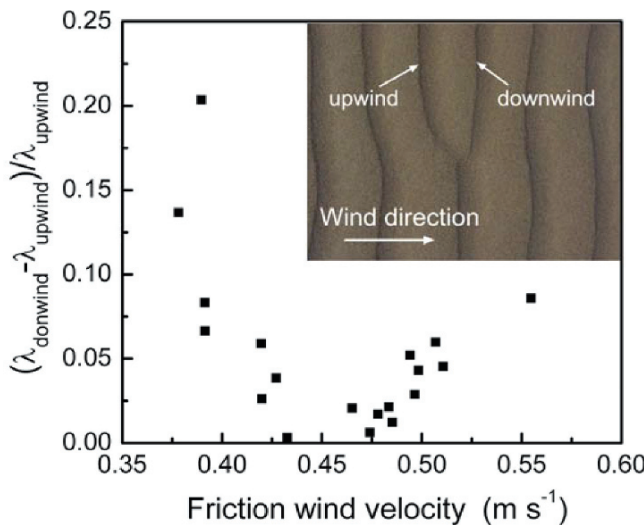


Fig. 6.5. The difference between the downwind wavelength ($\lambda_{\text{downwind}}$) and the upwind wavelength (λ_{upwind}) of Y-junctions for different friction wind velocities. ■ – measured data in the Badain Jaran Desert, the embedded picture is a photo of a Y-junction in the field (by the author et al.)

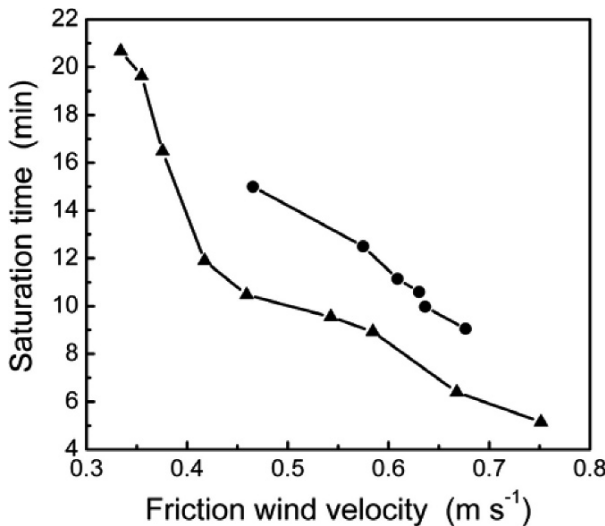


Fig. 6.6. The relation between the saturation time of aeolian sand ripples and friction wind velocity; —●— measured results in the Badain Jaran Desert; —▲— measured results in the multi-function environmental wind tunnel of Lanzhou University (by the author et al.)

Development Stage: Wind tunnel experiments (Andreotti et al. 2006) and our field observations showed that the formation of aeolian sand ripples can be divided into three stages: Initially, the flat sand bed deforms and tiny structures appear, then the tiny structures start merging so that the pattern exhibits coarsening, and finally the pattern tends to be saturated. After saturation, the ripples maintain their forms and sizes to move along the wind direction with velocities proportional to the friction wind velocity. Our experiments also find that the duration of ripples developing from initial unsaturation to saturation decreases with the increase of the friction wind velocity (see Fig. 6.6), and the saturation time in the field is longer than wind tunnel which probably results from the intermittency of natural wind. Besides, aeolian sand ripples are capable of self-reparation (Sharp 1963), that is, when destroyed, the ripples will reappear under wind action, and these ripples will connect with other neighboring ripples gradually, and ultimately eliminate the traces of breakage.

6.1.2 The Formation Mechanism of Aeolian Sand Ripples

There have been many hypotheses proposed to explain the formation mechanism of aeolian sand ripples, including the separation hypothesis, the

wave hypothesis and the impact hypothesis. The separation hypothesis (Энаменский 1960) considered the formation of aeolian sand ripples as a result of the separation of moving sand particles of different size, which led the coarse sand particles accumulating on the crest and fine sand on the trough. The wave hypothesis (Cooke et al. 1993) suggested that ripples are formed by the regular small-scale vortex structure near the bed surface generated by the unstable airflow in the atmospheric boundary layer. Another interpretation of wave hypothesis (Kennedy 1969) deemed the Helmholtz's wave as a main reason of aeolian sand ripples' formation. The Helmholtz's wave appears at the interface between two different density flows - sand particle flow and air flow. Now more generally accepted hypothesis is the impact hypothesis proposed by Bagnold (1941). The impact hypothesis thinks that the formation of aeolian sand ripples is mainly due to the collision between saltating sand particles and bed surface. In other words, due to the existence of a number of tiny unevennesses of sand surface, the intensity of bombardment on windward slope is higher than that on leeward slope, which results in the original hollow getting bigger. And since the bombardment is more intense on the windward slope than it is on the level surface downwind, the particles that have been excavated from the hollow will accumulate at the junction of windward slope and downwind surface, because they are not being removed downwind as quickly as they are coming. As the accumulation at the junction rises, it forms a second lee slope, and here the particle movement is again feeble. This in turn causes the surface at the foot of the second lee slope to be depleted of particles, because they are being removed faster than they can now move down the second leeward slope by a more intense bombardment. Therefore, a second hollow is formed, and so on. From the above, it appears that a flat sand surface must be unstable, because any occasional deformation tends to become accentuated by the local sand-removing action of the saltation.

It is a difficult task to investigate the validity of the above hypotheses from the perspective of field observations and wind tunnel experiments, because the temporal and spatial scale involved in the formation and evolution of aeolian sand ripples are too small, the reliability of direct observation to a large extent depends on the resolution and accuracy of observation methods and equipments. Therefore, theoretical modeling and computer simulation may serve as important supplements to reveal the process, the mechanism and the laws of the formation and development of aeolian sand ripples.

6.2 Continuous Models for Aeolian Sand Ripples

In continuous models, the bed elevation $z(x, t)$ is treated as an undetermined function of the horizontal coordinate x paralleling to the wind direction and time t . Through solving the differential equations based on corresponding initial and boundary conditions, we can determine the bed elevation and its rate of change. Here, we briefly introduce two types of continuous model: the Anderson's continuous model (1987) which is based on saltating movement of sand particles, and the granular surface flow model based on hydrodynamics.

6.2.1 The Anderson's Continuous Model

A high-energy impact characteristically gives rise to several low-energy ejection particles which leap once near the surface with a distance smaller than saltation length but longer than creeping length. This movement of sand particles is so-called reptation. Anderson (1987) deemed that the instability of bed surface is mainly caused by the reptating sand, but not the saltating sand. Therefore, the rate of change of bed elevation is a function of the divergence of reptating sand flux. We denote the mass of sand particle by m_s , the reptation length by l_{rep} , the number of reptating particles per unit area per unit time by N_{ej} which is related to the number of saltating particles N_s arriving at a flat horizontal bed per unit area per unit time and the number of particles n_0 ejected per impact, the incident angle of the impacting particles by θ and the angle the bed makes with the horizontal by α , then N_{ej} can be written as:

$$N_{ej} = N_0 n_0 \left(1 + \frac{\tan \theta}{\tan \alpha} \right) \cos \theta. \quad (6.1)$$

In this way, the flux of reptating particles $Q_{rep}(x)$ at x can be expressed as

$$Q_{rep}(x) = m_s \int_{x-l_{rep}}^x N_{ej}(x') dx' = m_s \int_{x-l_{rep}}^x N_s(x') n_0(x') \left(1 + \frac{\tan \alpha}{\tan \theta} \right) \cos \alpha dx'. \quad (6.2)$$

When the wind-blown sand flow achieves steady-state, the flux of reptating particles should be subject to the forms of mass conservation equations. Taking into account the bed slope $\tan \alpha = \partial z / \partial x$, accordingly, partial differential equations for the rate of change of bed elevation are:

$$\frac{\partial z}{\partial t} = \frac{m_s n_0 N_s}{\rho_b} \left(1 + \frac{\partial z}{\partial x} \cot \theta \right) \left[1 + \left(\frac{\partial z}{\partial x} \right)^2 \right]^{-\frac{1}{2}} \quad x \in [x - l_{rep}, x] \quad (6.3a)$$

$$t = 0 : \quad z_{ini} = z_0 e^{ikx} \quad (6.3b)$$

Here, $\rho_b = (1-\eta)\rho_s$ is the bulk density of the sediment in the bed, ρ_s is the particle density, and η is the porosity of the bed. A translating sinusoidal perturbation z_{ini} on a flat granular bed is assumed, in which z_0 is the initial amplitude of the bedform (half of the height from the trough to the crest of form), k is the wave number of ripples, i is the imaginary unit and the sand flux passing through arbitrary cross-section per unit time is the total particles ejected from $x - l_{rep}$ to x , therefore, the value of integral upper limit and lower limit of bed elevation are $x - l_{rep}$ and x respectively.

According to the Anderson's continuous model (1987), we can obtain the laws of the translation velocity c_i and the growth rate c_r of ripple amplitude changing with the ratio between wavelength λ and the reptation length l_{rep} (see Fig. 6.7). From Fig. 6.7, it can be found that both the translation velocity and the growth rate first increase and then decrease with λ/l_{rep} for (I) uniform reptation length, (II) exponential distribution of reptation lengths and (III) Gamma distribution of reptation lengths, that is, with the increase of ripple wavelength, the growth rate of ripple amplitude changes quickly and then slowly reaching its maximum value at the peak point. However, the peak point of the growth rate of ripple amplitude is different. For case (I), the peak points locate at $\lambda/l_{rep} = 4/(2n-1)$, ($n = 1, 2, \dots$); For (II) and (III), they have only one location, that is $\lambda/\bar{l}_{rep} \approx 6$. In addition, for case (I) and (II), the translation velocity decreases with the wavelength, but for case (III), with wavelength increasing, the translation velocity firstly increases and then decreases, reaching its maximum at $\lambda/\bar{l}_{rep} \approx 2$.

Although Anderson's continuous model (1987) has considered the erosion process on bed surface through connecting the change of bed surface with erosion rate, but it did not consider the deposition process of wind-blown sand flow, which is significant to the formation of aeolian sand ripples. In addition, since the motion of sand particles in this model are considered as 'uniform reptation', namely the diameter of saltating sand D_s , the impact angle θ , the reptation length l_{rep} , the number of saltating particles N_s arriving at a flat horizontal bed per unit time per unit area, and the number of ejected particles per impact n_0 are all taken identically, so the simulated aeolian sand ripples are symmetric, and do not have the same

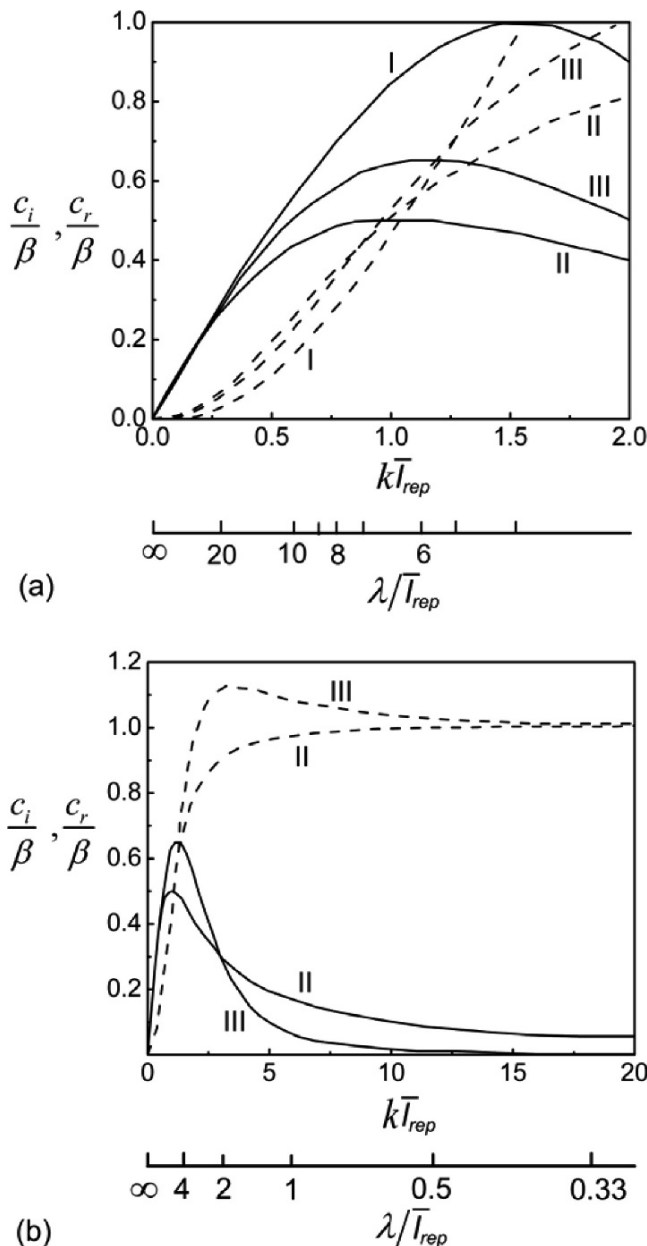


Fig. 6.7. The variations of the growth rate c_r and the translation velocity c_i with reptation length l_{rep} for (I) uniform reptation length, (II) exponential distribution of reptation lengths and (III) Gamma distribution of reptation lengths where $\lambda = 2\pi/k$, $\beta = (mn_0N_0\cot\alpha)/\rho$ (redrawn from Anderson 1987).

characteristic of leeward slope as actual situation. Though the translation velocity c_i and the growth rate c_r of ripple amplitude changing with the ratio between the wavelength and the reptation length were discussed in this model, but the fact that the wavelength of aeolian sand ripples are varying during the formation of aeolian sand ripples was neglected.

6.2.2 The Granular Surface Flow Model

In recent years, the granular surface flow model which is inspired from the viewpoint of phase transition in the hydrodynamic theory has been developed to study the aeolian sand ripples. It was originally employed to investigate the subaqueous ripple (Cornish and Jeffreys 1934), and then was adapted to study the formation of aeolian sand ripples by Bouchaud and his coworkers (Bouchaud et al. 1994). This model is a kind of continuous description where dynamics of the two pertinent particle layers, that is the surface flowing layer and the static layer, are considered separately. The former (including reptation layer and saltation layer) is characterized as a flow phase with the average velocity \bar{V}_f and moving particles density $N_u(x, t)$, while the latter is considered as a solid phase with the height $z(x, t)$. So the formation process of aeolian sand ripples can be regard as a phase transition process caused by mass exchange between the surface flowing layer and the static layer. Assume that the rate of change of bed elevation in solid phase is $\partial z(x, t)/\partial t = \Gamma$, due to the reason that the height of solid phase is a result of the deposition rate Γ_{dep} and the ejection rate Γ_{ej} , which follows: $\Gamma = \Gamma_{dep} - \Gamma_{ej}$, the rate of change of thickness of the surface flowing layer can be expressed as:

$$\frac{\partial N_u}{\partial t} = \bar{V}_f \frac{\partial N_u}{\partial x} - \Gamma(x, t) \quad (6.4)$$

Many analytical models of aeolian sand ripples have been derived based on different descriptions of Γ_{ej} and Γ_{dep} . For example, Prigozhin (1999) deemed that: the ejection rate Γ_{ej} is related to the impact of saltating sand, while the deposition rate Γ_{dep} is related to the accumulation of reptating sand particles which are determined by bed slope and the number of sand particles in the surface flowing layer. According to the way of sand motion, the deposition rate is assumed to be proportional to the number R of reptating particles, that is $\Gamma_{dep} = N_u/t_{dep}$, where, where t_{dep} represents the typical time during which the reptating particles are moving before being incorporated to the sand bed. Through introducing the erosion rate c_1 of flat bed surface determined by the intensity of saltating sand, and the recip-

reciprocal of reptating time c_2 respectively, we can consider the influence of the impact angle θ of saltating sand, bed slope α and repose angle α_r to the exchange rate between the moving particles and the particles at rest, which can be expressed as:

$$\frac{\partial z}{\partial t} = \Gamma_{dep} - \Gamma_{ej} = c_2 N_u \left(\frac{1 - |\nabla z|^2}{\tan^2 \alpha_r} \right) - \frac{c_1}{\sin \theta} \sin(\theta + \alpha) \quad (6.5)$$

Combining Eqs. 6.5 and 6.3b, it establishes a fixed solution problem of the height $z(x, t)$. Different from the Anderson's continuous model (1987) (Eq. 6.3), Prigozhin (1999) takes into account the rolling and avalanching movement of particles under the influence of the gravity in leeward, the shadowing effect of leeward slope (see Fig. 6.8) and the influence of deposition rate Γ_{dep} to the variation of bed surface. It successfully reproduced the asymmetrical ripple pattern, and forecasted the variation of scale during the evolution process and the typical ripple interaction (see Fig. 6.9). However, it still exists deficiency, that is, the slope angle, scale and development process of simulated ripples by Prigozhin (1991) are inconsistent with the actual states. For example, the wavelengths of natural aeolian sand ripples are generally 7–15 cm, but the simulated results showed that the wavelength can reach up to 33 cm which is bigger than the scale of actual sand ripples. This is mainly because Prigozhin's model (1999) neglected the influence of bed surface curvature to the ejection rate Γ_{ej} and deposition rate Γ_{dep} . In addition, the erosion rate c_1 and the reciprocal of reptating time c_2 are artificially set as constants in this model. However, in fact, it should be related with wind velocity, surface configuration and sand diameter at the eroded position.

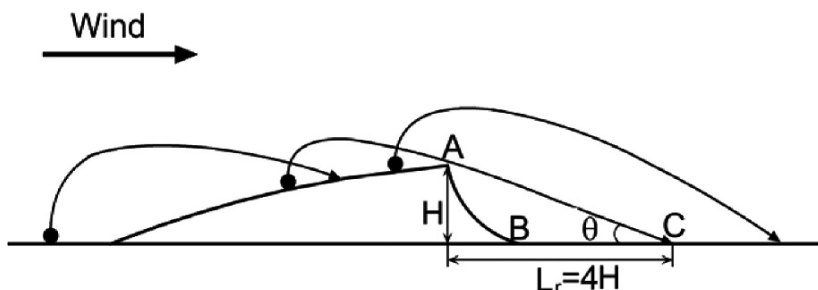


Fig. 6.8. The schematic illustration of the shadowing effect of leeward slope. • represents the saltating sand; θ is impact angle of saltating sand. Due to the shadowing effect of leeward slope, the area ABC is protected from the impact of saltating sand particles, which is so-called the protection zone, H is the height of the aeolian sand ripple, L_r is the length of the protection zone

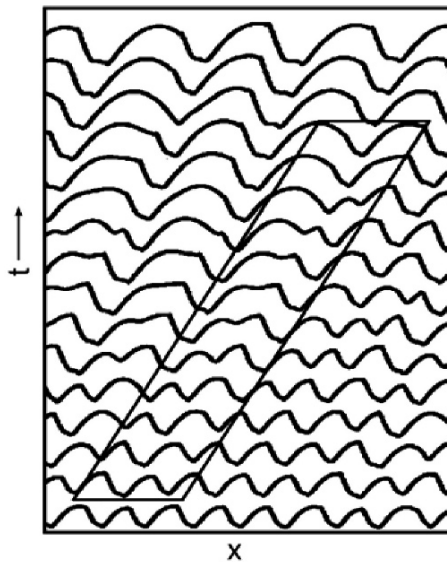


Fig. 6.9. The evolution of aeolian sand ripples predicted by Prigozhin's model (from Prigozhin 1999)

As an improvement of Prigozhin's model (Prigozhin 1999), Valance and Rioual (1999) deemed the ejection rate Γ_{ej} as a result of the impact of saltating particles and the direct entrainment of wind force, that is, $\Gamma_{ej} = \Gamma_{ej}^{imp} + \Gamma_{ej}^{wind}$. This model adopted the expression of the number of ejected particles per unit time per unit area from the surface given by Anderson (1987), and took into account the influence of the bed curvature: $k = (\partial^2 z / \partial x^2) / [1 + (\partial z / \partial x)^2]^{3/2}$ (Csahók et al. 2000). The ejection rate in this model therefore can be written as:

$$\Gamma_{ej} = D_s^3 n_0 N_s \left(1 - c_s \frac{\frac{\partial^2 z}{\partial x^2}}{\left[1 + \left(\frac{\partial z}{\partial x} \right)^2 \right]^{\frac{3}{2}}} \right) \left(1 + \frac{\partial z}{\partial x} \cot \theta \right) \left[1 + \left(\frac{\partial z}{\partial x} \right)^2 \right]^{\frac{1}{2}} - \beta_2 \frac{\partial^2 z}{\partial x^2} \quad (6.6)$$

where, β_2 represents the relation between the ejection rate and the bed curvature which can be determined by experiment, and c_s is a constant. The deposition rate Γ_{dep} is assumed to be affected by the bed curvature and slope, that is:

$$\Gamma_{dep} = N_u \gamma_0 \left(1 \pm \gamma_1 \frac{\partial z}{\partial x} + \gamma_2 \frac{\partial^2 z}{\partial x^2} \right) \quad (6.7)$$

where γ_0 corresponds to the reciprocal of typical lifetime of a reptating particle on a flat surface; γ_1 describes the influence of stoss slope gradient, if the wind drag is negligible near the surface, the deposition process will be enhanced on the stoss slope (positive in front of γ_1). But if the wind drag near the bed surface is significant to be considered, the deposition process will be weakened on the stoss slope (negative sign in front of γ_1); γ_2 describes the curvature effect, namely, the bigger the slope curvature and the neighboring slope gradient, the shorter the reptating time, and the bigger the deposition probability will be (Hoyle and Mehta 1999).

Substituting the ejection rate Γ_{ej} (i.e. Eq. 6.6) and deposition rate Γ_{dep} (i.e. Eq. 6.7) into $\partial z(x, t)/\partial t = \Gamma_{ej} + \Gamma_{dep}$, it comes into being a fixed solution problem of height $z(x, t)$ for the initial condition (i.e. Eq. 6.3b), which is known as the Valance and Rioual's model (1999).. It can predict the development process and the merger behavior of small ripples. Since the influences of the bed curvature to the deposition rate Γ_{dep} and ejection rate Γ_{ej} are involved during the evolution of aeolian sand ripples, the resulting windward and leeward slope are close to the actual ripples. However, it occurs only when the reptation length l_{rep} is large enough. For the case l_{rep} is small, the windward slope and leeward slope angles do not match, such as the slope angles of windward and leeward will be bigger than the actual values, and there does not exist a saturated status too. It's probably because that the model does not consider the influence of wind velocity, particle diameter and the bed topography to the number of saltating particles hitting a flat surface per unit time and unit surface N_s , the number of ejected particles per impact n_0 and the typical time of reptating particles in air γ_0^{-1} . Besides, some parameters such as β_2 , γ_1 and γ_2 must be given in the application of Valance and Rioual's model (1999). to the simulation of aeolian sand ripples, which also makes it difficult to predict the formation and evolution of natural aeolian sand ripples in quantity.

In summary, in the continuous model, an artificially initial bed such as a sinusoid curve is needed, and it can not reflect the influence of wind velocity, diameter and bed topography to the main physical quantities of wind-blown sand movement, such as the reptation length l_{rep} , the number of saltating particles N_s impacting on a flat surface per unit time and unit surface, the number of ejected particles per impact n_0 and the typical time of reptating particles in air γ_0^{-1} , as well as some parameters such as β_2 , γ_1 and γ_2 which are difficult to be determined. Therefore, these models can to some extent reproduce asymmetrical ripples and their growth processes

and interactions. However, the scales of simulated ripples with this class of models do not agree very well with the actual ripples, and the saturation characteristic can not be predicted. These problems cause their simulation results can not connect with wind velocity and diameter of sand particle. Moreover, because of avoiding the discrete character of sand motion, the simulation results can not predict the size segregation of aeolian sand ripples.

6.3 Discrete Models for Aeolian Sand Ripples

In this section, we will introduce briefly three typical discrete models to simulate aeolian sand ripples, they are the Anderson-Bunas model (Anderson and Bunas 1993) based on Cellular Automata method, the Landry-Werner model (Landry and Werner 1994) based on discrete element method and the Nishimori-Ouchi model (Nishimori and Ouchi 1993) based on Coupled mapping lattice method respectively. In the next section, we will present another discrete model proposed by the author et al. recently, that is, the discrete particle tracing method (Zheng et al. 2008) which reflects the entire formation process and the main features of aeolian sand ripples more objectively.

Anderson (1987) addressed that, during the formation of aeolian sand ripples, the ‘surface particles’ move mainly in the form of reptation, including the ejection, transportation and deposition of reptating sand. The difference among the Anderson-Bunas model (1993), the Landry-Werner model (1994) and the Nishimori-Ouchi model (1993) lies in the treatment of these three key processes; in other words, the artificial rules governing the three processes are distinct.

6.3.1 Cellular Automata Model (Anderson-Bunas Discrete Model)

Cellular automata model is a class of spatially (bed length) and temporally discrete mathematical model characterized by local interaction and synchronous dynamical evolution. The state variables of interest (such as: bed height) at any position in any time can be determined through the state variables of the current and other positions in the previous time. Taking Anderson-Bonas discrete model (Anderson and Bunas 1993) they investigated the formation and evolution of aeolian sand ripples with a two-particle-size cellular automation, the simulation procedures are simplified as follows:

Step 1: Bed surface establishment: Since the Cellular automata model is based on the discrete of the space and the state variables, the model divides the sand bed into a certain number of units along horizontal and vertical direction. For example, the bed was initially 1,250 particles wide and 100 particles deep (Anderson and Bunias 1993) where the lengths and heights of units are both taken as the maximum sand diameter, such as 0.32 mm, that means each cell includes only one sand particle. In the model, the particle size is randomly assigned, with a fine (0.23 mm)/coarse (0.32 mm) ratio of 2:1.

Step 2: Determining the impact velocity of saltating sand and the ejection velocity of reptating sand. After establishing the bed, it requires to select the velocity of impact sand particle on any position of bed surface, and determine the number and velocities of sand particles ejected from impacted position according to certain rules. For example, in Anderson-Bunas discrete model, saltating particles are fired at the bed one by one, the particles that strike the bed have an identical size distribution; impact angle θ and impact velocity V_{im} are randomly selected from a Gaussian distribution with mean value 11° , variance 2° and an exponential distribution $f(V_{im}) = (1/u_*)\exp(-V_{im}/u_*)$, respectively. The mean number of ejecta N_{ej} and the ejection speed V_e can be determined by the soft sphere collision model (in Sect. 3.3.2 and Fig. 6.10). It is worth mentioning that in this model the time of a single impact of sand particle is considered as a computation step, and when the number of computation step is equal to the number of units in the bed surface, then one operation step completes. This kind of stipulation was also introduced into the discrete element method which will be introduced in the following.

Step 3: Stipulating the transportation and deposition of reptating sand. For a given wind velocity, the N_{ej} ejected sand particles, with the ejected velocities V_e are compelled to transportation l_r along wind direction and then deposit. In this model, the transportation distance l_r was calculated by trajectory equation of saltating sand, that is, the saltating length along flat bed surface when wind velocity and diameter is given.

Step 4: Stipulating the number of operation steps. If the current number of operation steps is less than the stipulated number (for example in Anderson and Bunias (1993), the operation steps were 5 million, 10 million and 20 million respectively), then return to the step 2 and carry on the next operation step computation, and the new resulting bed surface is used as the initial bed surface for the next operation step, until the number of operation steps is equal to the stipulated number.

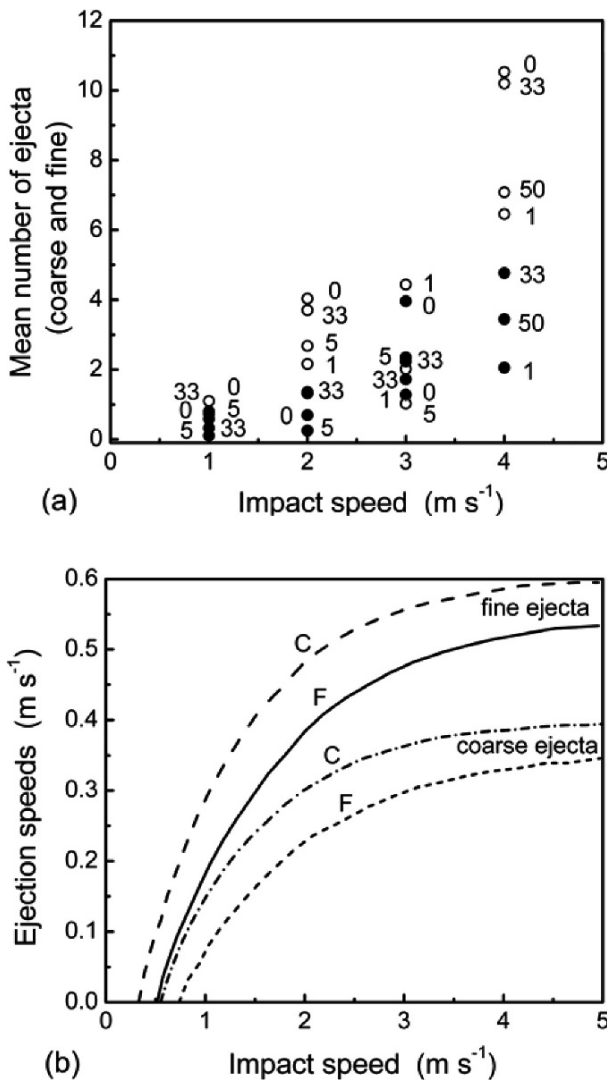


Fig. 6.10. Number of ejected particles and ejection speed per impact as a function of impact speed (a) ○ coarse impactor; ● fine impactor (b) C and F respectively correspond to the coarse and fine impactor (redrawn from Anderson and Bunas 1993)

The pattern of ripples reproduced by Anderson-Bunas model (1993) is shown in Fig. 6.11. From Fig. 6.11 we can find that the ripples are asymmetric which display convex stoss slopes and concave lee slopes as natural ripples do. Besides, the ripples display strong segregation of particles, that is coarse particles are on the ripple crests, and fine particles are on the

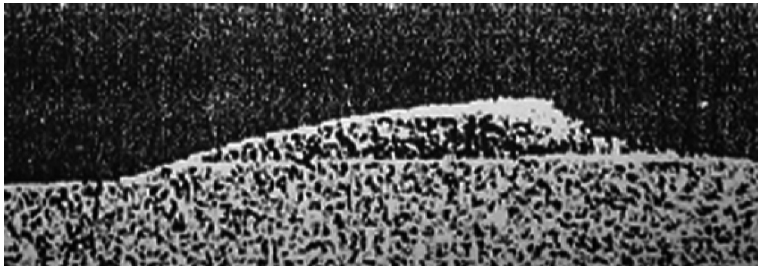


Fig. 6.11. The simulated aeolian sand ripple's shape by cellular automata model (from Anderson and Bunias 1993)

trough of the ripple. However, In Anderson-Bunas model (1993), after each collision the ejected sands lift off from the same position with the same ejected speed, which is contradictory with the actual particle-bed collision process. Moreover, the variation of local topography, such as the salient of bed surface during the formation of aeolian sand ripples can prevent the sand particles to travel l_r , which therefore should be treated specifically. In addition, when the reptating sand particles return back to the bed after hopping, the energy is not zero, so they will be rolling a certain distance along sand bed (namely, surface creep); such process has not been considered in this model. More important thing is that although the operation step in this model was called ‘time step’ (Baas and Nield 2007), in fact, it only represents the completion of one cycle operation. Such kind of ‘time step’ is very difficult to correspond with actual time, which thus limits the model to reflect the real time scale of the formation and evolution of aeolian sand ripples, especially to reproduce and describe the saturation process of aeolian sand ripples.

6.3.2 Discrete Element Model (Landry-Werner Model)

The Landry-Werner Model (1994) is a kind of three-dimensional Discrete Element Model (DEM) for aeolian sand ripples, where the ejection, transportation and deposition of bed surface sand are parameterized. In the following part, we will take the Landry-Werner model (1994) as an example to introduce its main simulation steps.

Step 1: Generating the bed surface. The establishment of Landry-Werner model (1994) is based on the tracking of the sand motion in system. The bed particles are taken to be a single size (0.25 mm) and are constrained to lie on a hexagonally close packed lattice (Fig. 6.12). The size of bed surface is about 25×21 cm, and the bed is initially assumed as a mot-

tled appearance and is characterized by roughly coherent, organized sand piles approximately 2–3 of particle diameters in height.

Step 2: Regulating the transportation distance of reptating sand. Chosing a sand particle from bed surface randomly and making the sand move a distance of l_r along the wind direction. The transportation distance l_r can be determined as follows: first, calculating the average ejected speed base on the soft sphere collision model (in Sect. 3.3.2) on different slope, then determining the saltating distance along the flat bed surface according to the

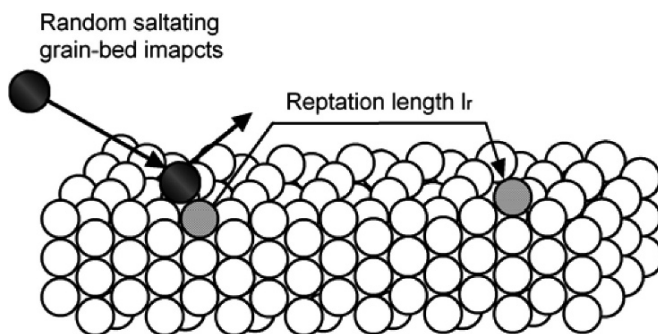


Fig. 6.12. The package of sand particles (redrawn from Landry and Werner 1994)

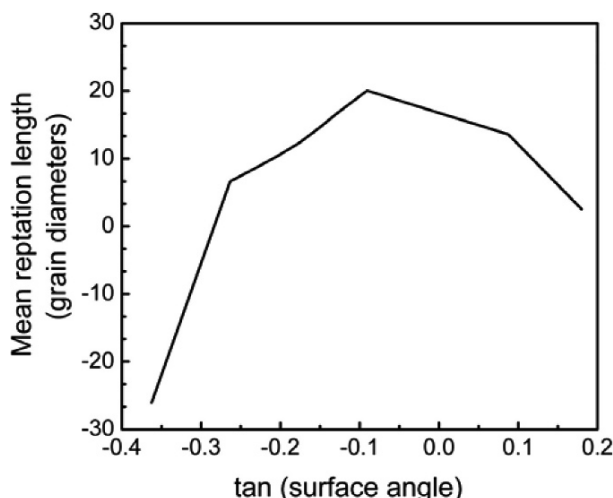


Fig. 6.13. The influence of surface gradient to trajectory length of reptation sand (from Landry and Werner 1994)

trajectory equation of saltating sand (in Sect. 5.), so as to determine the transport distance of sand in different gradient cases (see Fig. 6.13) ('gradient' algorithm).

Step 3: Regulating the transportation and deposition of reptating sand. The reptating particle is transported a specified number of particle diameters l_r downwind irrespective of the variations of surface gradient during its

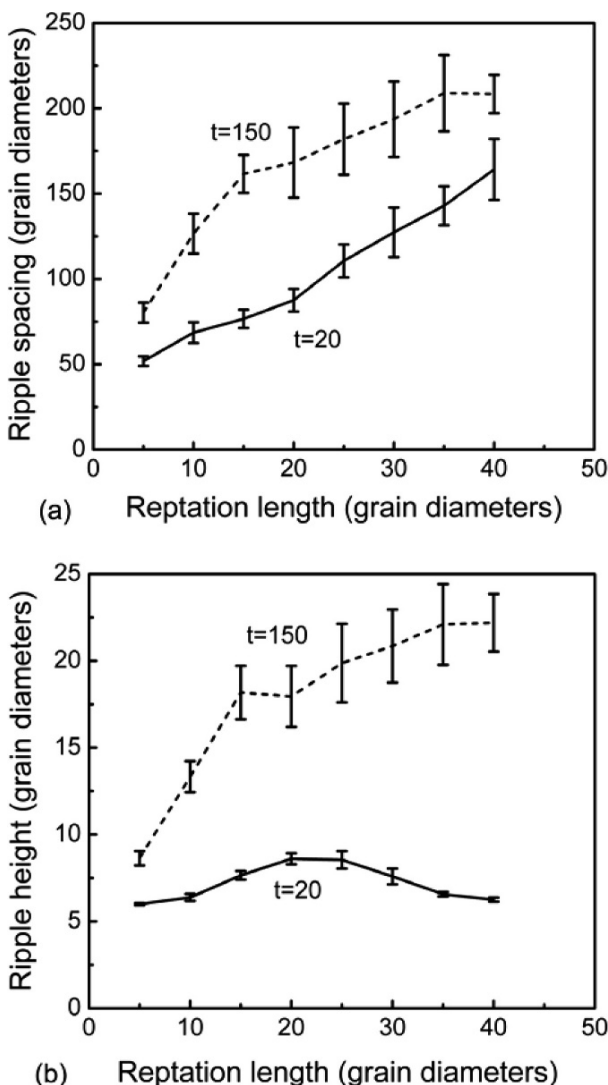


Fig. 6.14. The influence of reptation length to the scale of an aeolian sand ripple, (a) ripple spacing and (b) ripple length (from Landry and Werner 1994)

movement, and then back to the surface ('straight ahead' algorithm). A target particle is given 5 units of pseudo-momentum when it is dropped to the sand bed. Each time the particle moves one particle diameter upslope, it loses 2 units of pseudo-momentum, each time it moves downslope, it gains 1 unit of pseudo-momentum, and each time it moves one lattice spacing without gaining or losing elevation, it loses 1 unit of pseudo-momentum. The sand movement stops until the pseudo-momentum is zero ('rolling' algorithm).

Step 4: Stipulating the number of operation steps. One operation step is finished till all the reptating and the creeping sand particles stay on the bed surface. If the current number of operation steps is less than the stipulating number of operation steps, then return to the step 2, and carry on the next operation step computation. The resulting bed surface is used as the initial bed surface for the next operation step, until the number of operation step is equal to the stipulation.

The Landry-Werner model (1994) can also obtain the asymmetrical shape of sand ripple. Compared with the cellular automaton model, its advantage lies in investigating the influence of the reptation length to the scale of an aeolian sand ripple, namely, with the increase of reptation length the scale of the aeolian sand ripple increases (including height and spacing, see Fig. 6.14). Moreover, this model is a three dimensional model which therefore can reproduce the Y-junctions.

However, in Landry-Werner model (1994), the wavelength of the simulated aeolian sand ripples range from 1.25 cm to 5 cm, which is lower than actual values from 7 cm to 15 cm. This is possibly because it doesn't involve the actual particle-bed collision process and the surface creeping of sand particles. Similar with the Cellular Automaton Model (Anderson-Bunas discrete model (1993)), the operation step in Landry-Werner model (1994) can not correspond with the actual time, so the simulation result can not reflect the actual evolution of aeolian sand ripples, especially the development process from unsaturation to saturation.

6.3.3 Coupled Mapping Lattice Model (Nishimori-Ouchi Model)

The Coupled Mapping Lattice Model is a discrete model in space (the length and width of bed surface) and time with a continuous field variable representing the averaged bed height at each site. The simulation was realized by setting the exchange rule of sand flux, namely by setting the sand exchange between different positions to describe the sand movement. The model assumes that there are two types of sand movement, reptation and

creeping (due to the gravity action). Taking the Nishimori-Ouchi Model (1993) for example, the simulation is performed as follow:

Step 1: Generating the bed surface. This kind of model was established by discretizing the space variable. The bed surface was divided along horizontal and lateral direction into 100×100 cells, the length and width of each cell are larger than sand diameter; a continuous field variable was introduced to describe the bed height, that is, to describe the variations of the number of sand particles in each cell. The height of each cell was randomly determined satisfying the average height is zero.

Step 2: Regulating the transported sand amount and distance. In each operation step, the sand will lift off from all cells, and transport a certain distance L . In this process, the transported sand amount Q_L is identically taken as constant in each cell, the transportation distance can be determined by $L = L_0 + bh_n(x, z)$, here, L_0 is basic reptation length, which is change from 2.5 to 6.5, b is constant, $h_n(x, z)$ is the bed surface in the cell.

Step 3: Regulating rules of creep dynamics. The model determines the exchange sand amount between neighboring cells according to height difference between the nearest and the next nearest cells, so as to keep the height difference satisfying the specified value determined by the repose angle of sand particle.

Step 4: Regulating the number of the operation steps. When all sands stay on the bed surface, one operation step calculation is finished. If the operation step is less than the required operation step, then return to the step 2, and carry on the next operation step computation based on the new bed surface, until it reaches the stipulated number.

Comparing the two models introduced above, the Nishimori-Ouchi model (1993) can also present the asymmetrical shape of aeolian sand ripples and their growth processes. Moreover, it can also obtain the Y-junctions and self-reparation behavior of aeolian sand ripples in three-dimensional space. The merit of this kind of model is few computation cells are required in the simulation, and it has no need to trace every sand particle, but only need to trace the spatial positions, which together to some extent reduce the computation complexity. Besides, the influence of L_0 to the scale of aeolian sand ripples can also be investigated (see Fig. 6.15).

However, in this model, the height of the bed surface is not discretized, which results in the simulation not being able to reflect the stratigraphic structure of aeolian sand ripples. At the same time, it is worth pointing out that each operation step in this model represents the time required for the fulfillment of all erosion and deposition processes on the bed. Due to the transportation distance and creep rule are artificially regulated, this model

can not reflect the corresponding relationships with the real time. In addition, the erosion and deposition of sand particles are not identical everywhere during the formation of aeolian sand ripples.

In summary, although the three kinds of discrete models mentioned above can to some extent reflect the splash, transportation and deposition of reptating sands during the formation of aeolian sand ripples, but they generally resort to some artificial rules or hypotheses which to a large extent limit the accuracy and validity of their simulations. The rules in above

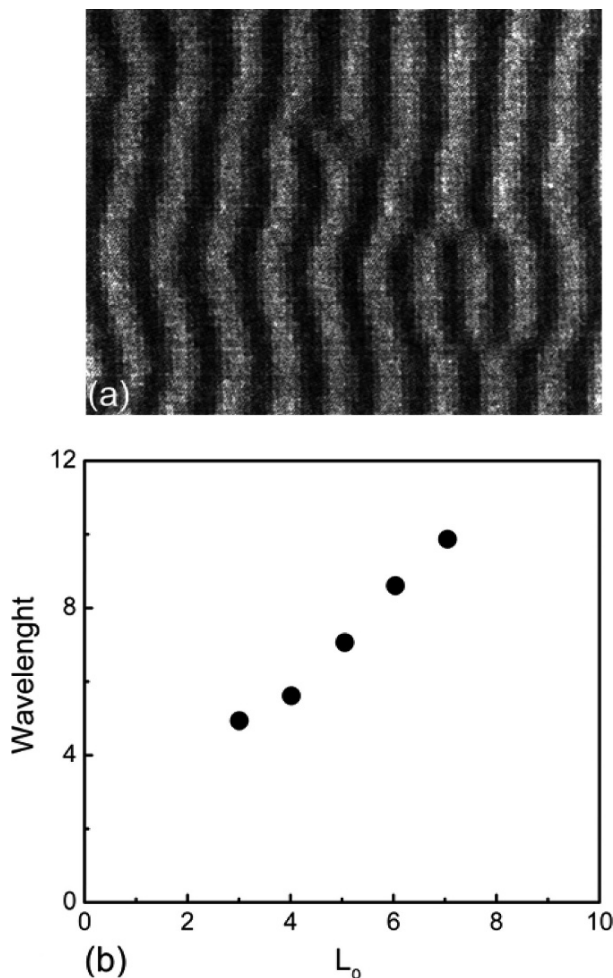


Fig. 6.15. (a) The asymmetrical shape of aeolian sand ripples simulated by Nishimori-Ouchi model, and (b) the influence of L_0 to wavelength (from Nishimori and Ouchi 1993)

models are generally given by simplifying the actual physical process, so it can not reflect the physical mechanism of sand movement in formation of aeolian sand ripples objectively and comprehensively. In addition, the simulation results are very difficult to correspond with the real time scale which also makes their simulation results do not agree with the actual aeolian sand ripples in quantity, and not be unable to effectively forecast the entire evolution process of aeolian sand ripples, i.e. the coarsening, the merge and the saturation of aeolian sand ripples. Besides, it is unable to effectively investigate the influences of wind velocity and sand particle size to the formation and evolution of aeolian sand ripples with these models, which makes them impossible to forecast the threshold wind velocity and the development of the Y-junctions in three-dimensional space, such as the change of the number of Y-junctions with wind velocity, time and particle diameter, and the migration of Y-junctions mentioned in Sect. 6.1.1.

6. 4. Discrete Particle Tracing Method (DPTM) Model

6.4.1 Basic Method

In this model, three main factors relevant to the formation of the aeolian sand ripples are considered. They are the wind-blown sand flux above the sand bed formed by sand particles with different diameters, the particle-bed collision and the rebound and ejection of sand particles after collision, as well as the saltation of high-speed sand and the creep of low-speed sand (transportation and deposition of creeping sand), respectively. The model main simulation steps are as follows:

Step 1: Establishment of initial sand bed which is similar with actual natural sand bed surface. This model is different from the Cellular Automaton model and the Coupled Mapping Lattice model, but is the same as the Discrete Element model, namely, the basic task of this model is to trace the motion of sand particles in the sand bed. The simulation sand bed is generated by the cooling method (see in Sec 3.5.1). It is composed of three particle sizes: fine (0.2 mm), middle (0.3 mm) and coarse (0.4 mm) with a ratio of 2:5:3. It is about 60 cm in length and 1.5 cm in width. Particle size is chosen statistically from lognormal distribution which is the same as natural sand particle distribution.

Step 2: Taking the time step as 1 s, the model uses the statistical coupled model (see in Sect. 5.2.1) to calculate the steady wind-blown sand flux. It can obtain the particle concentration and the distribution of sand particles' velocities changing with height above the sand bed under a given friction wind velocity, and further the number of incident sand particles and their

incident velocities and angles. Based on the concentration of sand particles and the distribution of sand particles' velocities per height cell, the incident sand particles will be inputted into the simulation system from the left boundary according to certain spacing and time interval. Here, periodic boundary is employed, namely, if the reptating sand departs from the right boundary, then it renters into the computation region again from the left boundary.

Step 3: Distinguishing the reptation and creep of bed surface sand according to the soft-sphere collision model (see in Sect. 3.3.2). Since the sands taking part in the formation of aeolian sand ripples are mainly composed of the reptating sands ejected from bed surface, so after obtaining the impacting speed and angle of saltating sands, we adopt the soft-sphere collision model to determine the number, position, speed and angle of ejected sands, then discriminate the type of sand movement (creep or reptation) according to the vertical speed of ejected sand.

Step 4: Determining the transportation and deposition of reptating sands according the movement of reptating sands. For the reptating sands, their trajectories can be calculated by solving saltation trajectory Eq. 5.12. Then, we compute the local wind field around aeolian sand ripples so as to introduce the influence of bed fluctuation on the local wind field and further on the formation of aeolian sand ripples. The creeping sands particles can't fly away from the sand bed but only roll over the other sand particles on the bed. Therefore, these particles lose their energies and finally stop due to friction work, and their final settling positions are determined by considering the friction and gravity during their creeping. Assuming a creeping sand particle rolls over another n sand particles to stop on bed surface, in which n_1 sand particles belong to the stoss slope α_{ss} , n_2 particles belong to the lee slope (angle of lee slope α_{ls}), this process satisfies the follow inequation:

$$0 \leq W_s + W_g + nW_f < m_s g D_s \left(1 + \frac{\mu}{4} \right), \quad (6.8)$$

where, the kinetic energy W_s , the gravity work W_g and friction work W_f of the creeping sand particle can be respectively expressed as follow:

$$W_s = \frac{m_s}{2} [\dot{x}^2 + \dot{z}^2],$$

$$W_g = -n_1 D_s \sin \alpha_{ss} + n_2 D_s \sin \alpha_{ls},$$

$$W_f = - \int_{-\pi/6}^{\pi/6} m_s g \mu \frac{D_s}{2} \cos \theta_c d\theta_c = - \frac{1}{2} m_s g \mu D_s .$$

θ_c is the angle between the line connecting the centroid of two contacting particles and perpendicular.

Step 5: Determining the computational time steps according to the pattern of bed surface. After all saltating sands entered into the system, and all reptating sands completed their movements (maybe more than once), we define one computational time step is completed. If the scale of aeolian sand ripple obtained in this time step is the same with that in the previous time step, which means the aeolian sand ripple achieves saturation, then stop inputting sands into the system, and the simulation is end. Otherwise return to the step 2, and carry on the next computation step, the bed surface obtained in this step serves as the initial bed surface for the next computational time step.

Obviously, the difference between the discrete particle tracing method (DPTM) and the above models is that the DPTM traces the reptation and creeping motion of every ejected sand particle, which reflects the discreteness of wind-blown sand system. At the same time, through computing the wind-blown sand flux, the local wind field around aeolian sand ripples and the particle-bed collision process, it can reflect the interaction between wind field and sand movement and the integral behavior of wind-blown sand movement. Besides, the operation step in this model is taken as the real time (for example, in Zheng et al. (2008), the time step was taken as 1s, which can be further subdivided or extended according to the required precision), so it can realize the time correspondence between the simulation results and the actual states, furthermore it can realize the reproduce the formation and evolution of natural aeolian sand ripples, and obtain the threshold time when the aeolian sand ripples reaching saturation.

6.4.2 Major Simulation Results

The discrete particle tracing method (DPTM) is not only able to simulate the basic shape and the characteristic of an aeolian sand ripple in the ‘mixed’ sand case, such as particle size segregation of ripple, but also to reproduce the development process of aeolian sand ripples from unsaturation to saturation. In addition, it can predict the propagation velocities of the saturated aeolian sand ripples, the influence of wind velocity and diameter to the scale and saturation time, and the threshold wind velocity when ripple appear and disappear (Werner et al. 1986). Fig. 6.16 is the pattern of a simulated aeolian sand ripple, and the shape is asymmetric,

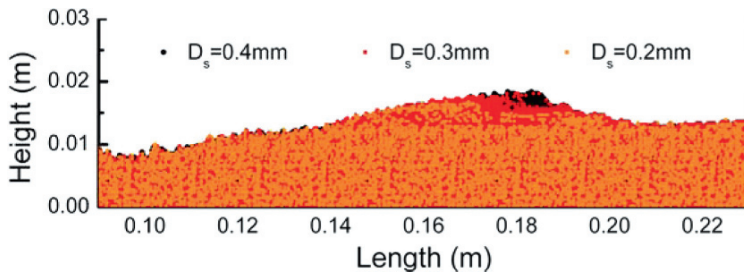


Fig. 6.16. The aeolian sand ripple in ‘mixed’ sand case simulated by the DPTM, the incoming friction wind velocity is taken as $0.5 \text{ m}\cdot\text{s}^{-1}$, the sand bed is composed of three particle sizes, fine (0.2 mm), middle (0.3 mm) and coarse (0.4 mm) with a ratio of 2:5:3, which is 60 cm in length and 1.5 cm in height including about 10^5 sand particles (from Zheng et al. 2008)

Table 6.1. Simulated results ($u_* = 0.5 \text{ m}\cdot\text{s}^{-1}$) and experimental results (from Zheng et al. 2008)

| Particle diameter [mm] | λ [cm] | H [cm] | RI | α_{ss} | α_{ls} |
|----------------------------------|----------------|---------|-------|---------------|---------------|
| 0.3 (with creep) | 12.62 | 0.715 | 17.65 | 9° | 17.32° |
| ‘Mixed’ sands (with creep) | 11.52 | 0.54 | 21 | 7.3° | 19.3° |
| 0.3 (without creep) | 12.05 | 0.5 | 24.1 | 8.44° | 8° |
| ‘Mixed’ sands (without creep) | 9.7 | 0.4 | 24.25 | 7.8° | 11° |
| Experiments | 7–14 | 0.5–1.0 | 15–20 | 8°–10° | 20°–30° |

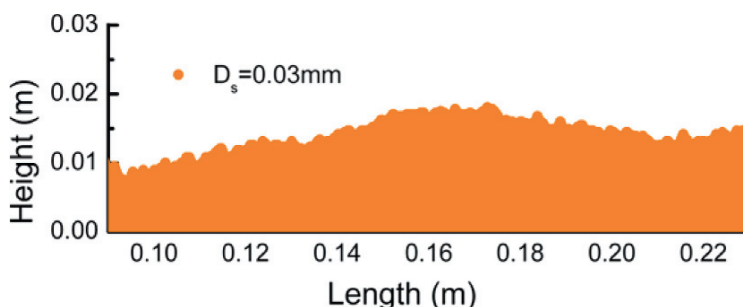


Fig. 6.17. The aeolian sand ripple in the ‘uniform’ sand case without considering the creeping sand, friction wind velocity is $0.5 \text{ m}\cdot\text{s}^{-1}$, sand diameter is 0.3 mm, the sand bed is 60 cm in length and 1.5 cm in height including about 10^5 sand particles (from Zheng et al. 2008)

with convex upwind (stoss) slopes, and concave lee slopes, which agree with experimental observation result of Anderson and Bunas (1993) as well as Werner et al. (1986) etc. (see Table 6.1 for comparisons in detail). Moreover, it can also present the stratification structure, that is, coarse particles are accumulated on the crest, and fine particles are in the trough of the ripple. At the same time, the simulation results also demonstrate that if the influence of

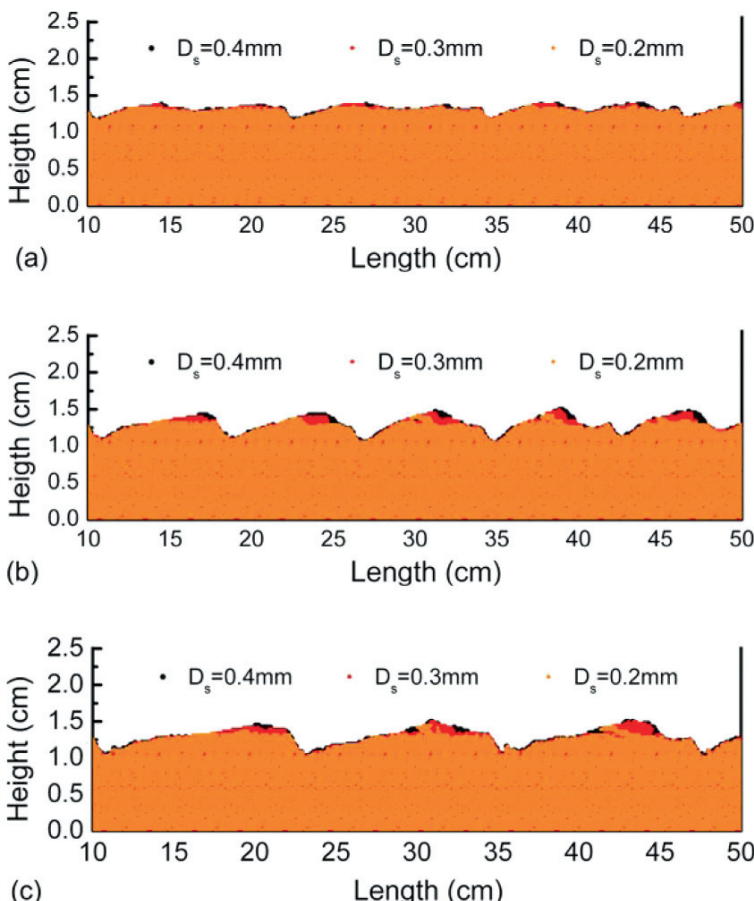


Fig. 6.18. Evolution of aeolian sand ripples: **(a)** tiny structure at $t = 80$ s, **(b)** merging of tiny structure at $t = 180$ s and **(c)** saturated aeolian sand ripples at $t = 440$ s; the friction wind velocity is taken as $0.5 \text{ m}\cdot\text{s}^{-1}$; the sand bed is composed of three particle sizes, fine (0.2 mm), middle (0.3 mm) and coarse (0.4 mm) with a ratio of 2:5:3, which is 60 cm in length and 1.5 cm in height including about 10^5 sand particles (from Zheng et al. 2008)

the surface creeping is not considered in the ‘uniform’ sand case, the surface of the simulated aeolian sand ripples are rough and symmetrical in shape (see Fig. 6.17) and the wavelength is clearly smaller than the real one. It indicates that it is necessary to consider the surface creeping in the simulation of the aeolian sand ripples.

The simulated results can also replay the formation process of aeolian sand ripples, that is, the initial flat sand bed starts deforming and tiny structures are observed (see Fig. 6.18a), and then these tiny structures started merging so that the pattern exhibits coarsening (see Fig. 6.18b), and finally the pattern tends to be saturated (see Fig. 6.18c). This is completely consistent with the results of field observations and wind-tunnel experiments. It is worth pointing out: the saturation time in the ‘mixed’ sand case is shorter than that in the ‘uniform’ sand case. The simulations also show that: the scale of saturated sand ripple is related with the incoming friction wind velocity and sand diameter (see Fig. 6.19). During the formation and evolution of sand ripple, it always moves forward along wind direction associated with the increase of ripple scale before achieving saturation, after that, the sand ripple maintains its shape and scale moving along wind direction. In addition, the migration velocity of saturated ripple is also related with the incoming shear wind velocity and sand diameter, for

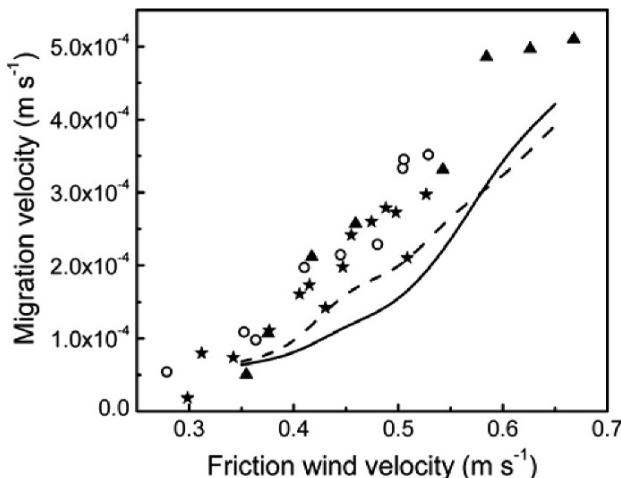


Fig. 6.19. The variations of propagation velocities of aeolian sand ripples with wind velocity. ★ measured results of field observation by Andreotti et al. (2006); ○ measured results in the Badain Jaran Desert by the author et al.; ▲ measured results in the multi-function environmental wind tunnel of Lanzhou University by the author et al.; — and —— represent the simulated results by the DPTM (Zheng et al. 2008) in the ‘uniform’ sand and the ‘mixed’ sand cases, respectively

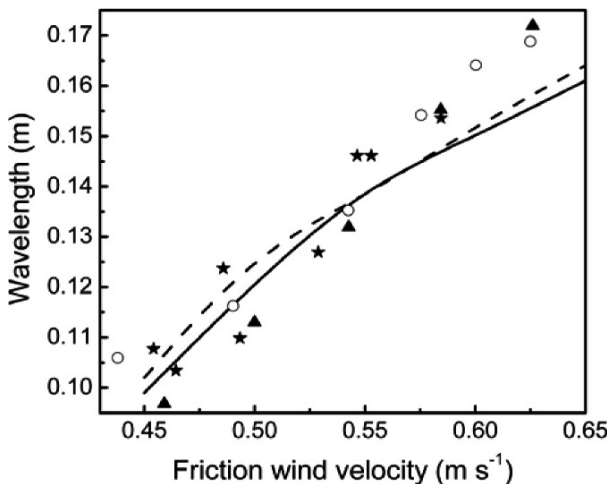


Fig. 6.20. The variations of the wavelengths of aeolian sand ripples with friction wind velocity. ★ measured results of field observation by Andreotti et al. (2006); ○ measured results in the Badain Jaran Desert by the author et al.; ▲ measured results in the multi-function environmental wind tunnel of Lanzhou University by the author et al.; — and - - - represent the simulated results by the DPTM (Zheng et al. 2008) in the ‘uniform’ sand and the ‘mixed’ sand cases, respectively

example, the migration velocity increases with friction wind velocity increasing (see Fig 6.20). When the friction wind velocity is $0.5\ m\cdot s^{-1}$, the migration velocities of the saturated aeolian sand ripples are $1.454 \times 10^{-4}\ m\cdot s^{-1}$ and $1.885 \times 10^{-4}\ m\cdot s^{-1}$, respectively for the ‘uniform’ sand case (0.3 mm) and the ‘mixed’ sand case, which agree with the observed value ($2.586 \times 10^{-4}\ m\cdot s^{-1}$) in the wind tunnel experiment (Bagnold 1941) in magnitude. Moreover, we obtain the threshold friction wind velocity for the appearance and disappearance of the aeolian sand ripples with our simulations. For both the ‘mixed’ sand case and the ‘uniform’ sand case ($D_s = 0.3\ mm$), the threshold friction wind velocities are $0.3\ m\cdot s^{-1}$ and $0.7\ m\cdot s^{-1}$, which means that when the friction wind velocity is less than $0.3\ m\cdot s^{-1}$, the wind field is too weak to form aeolian sand ripples. However, when the wind velocity is larger than $0.7\ m\cdot s^{-1}$, the deposition of sand becomes so difficult that the wind ripples can not be formed.

Extending this model to simulate sand ripples in three dimensional space ($1.6\ m \times 1.2\ m$), it can reproduce the formation of the Y-junctions and their development process. From Fig. 6.21a, we can see that in the initial stage, the length of the crest-line of aeolian sand ripples are short and different everywhere. During the merging stage, these ripples interconnect each other forming many Y-junctions (see Fig. 6.22a). Afterwards, during

the development stage from unsaturation to saturation, as the ripples moving forward, the Y-junctions are gradually separated from the upwind ripples, and connected with the downwind ones. This kind of migration of Y-junctions to a certain extent promotes the enlargement of the aeolian sand

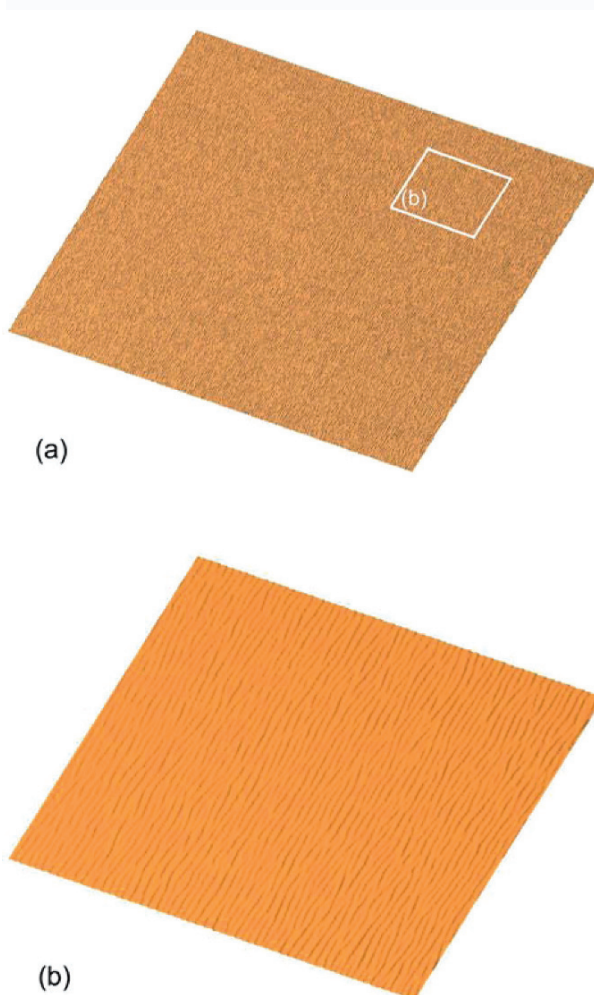


Fig. 6.21. The formation and evolution of Y-junctions simulated by the DPTM, **(a)** The tiny structures occur on bed surface at $t=22$ s; **(b)** locally enlarged drawing of a part of bed surface of (a); the sand diameter is 0.3 mm; the simulation area is $1.2\text{ m}\times 1.2\text{ m}$, the depth of the sand bed is 2 cm, which includes about 2.5×10^7 particles (by the author et al.)

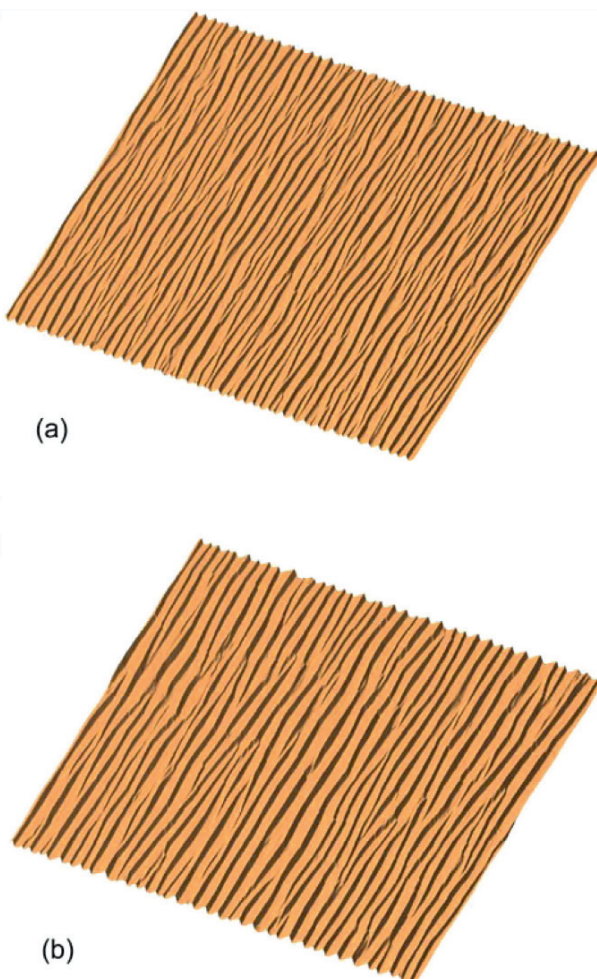


Fig. 6.22. The formation and evolution of Y-junctions simulated by the DPTM, **(a)** tiny structures start merging at $t=268$ s; **(b)** the aeolian sand ripples are mature (saturated) at $t=536$ s; the friction wind velocity is $0.5 \text{ m}\cdot\text{s}^{-1}$; the sand diameter is 0.3 mm ; the simulation area is $1.2 \text{ m} \times 1.2 \text{ m}$, the depth of the sand bed is 2 cm , which includes about 2.5×10^7 particles (by the author et al.)

ripple's scale. However, when the sand ripples are saturated, the number of Y-junctions obviously decreases (see Fig. 6.22b). From our simulations, we found that the wavelength of upwind junction is less than that of downwind, and their difference firstly decreases and then increases with the friction wind velocity (shown in Fig. 6.23), which agree with the results given

by field observations (shown in Fig. 6.5). Besides, our simulation results also reveal that the number of Y-junctions decreases with incoming friction wind velocity increasing.

If we efface a part of the saturated sand ripple in three dimensional space (see Fig. 6.24a), then new sand ripples will reappear in the effaced area under the action of wind field in our simulation (see Fig. 6.24b). After that, these new ripples will gradually connect with their neighboring undestroyed ripples until reaching saturation (see Fig. 6.25a). The initially destroyed traces are eliminated so completely that it seems the same as the state before effacement. However, comparing the same region with and without effacement (see Fig. 6.25b), we find the number of Y-junctions increases after self-reparation.

The difference between the discrete particle tracing method and the continuous models is that the former reflects the discreteness of sand particles; it connects the reptation of sand particles with wind velocity and sand diameter through the particle-bed collision model, the trajectory equation of saltating sand and the computation of surface creeping. The main physical processes of wind-blown sand movement can be described by the existing

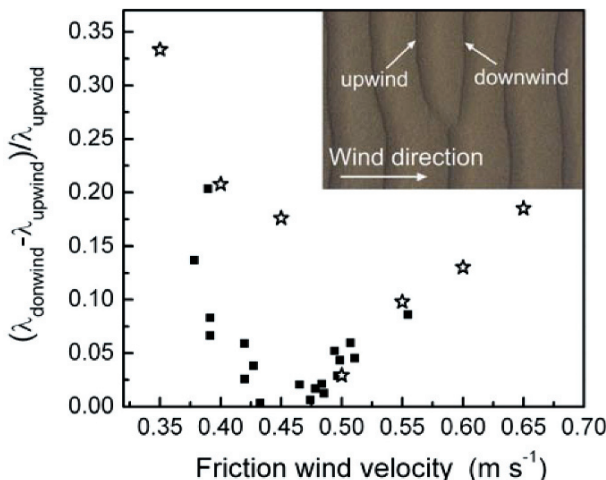


Fig. 6.23. The difference between the downwind wavelength ($\lambda_{\text{downwind}}$) and the upwind wavelength (λ_{upwind}) of Y-junctions for different friction wind velocities. \star – the simulated results by the DPTM (the friction wind velocity is $0.5\ m\cdot s^{-1}$; the sand diameter is $0.3\ mm$; the simulation area is $1.2\ m \times 1.2\ m$, the depth of the sand bed is $2\ cm$, which includes about 2.5×10^7 particles); ■ – measured results in the Badain Jaran Desert, the embedded picture is a photo of a Y-junction captured by the author et al. in the Desert

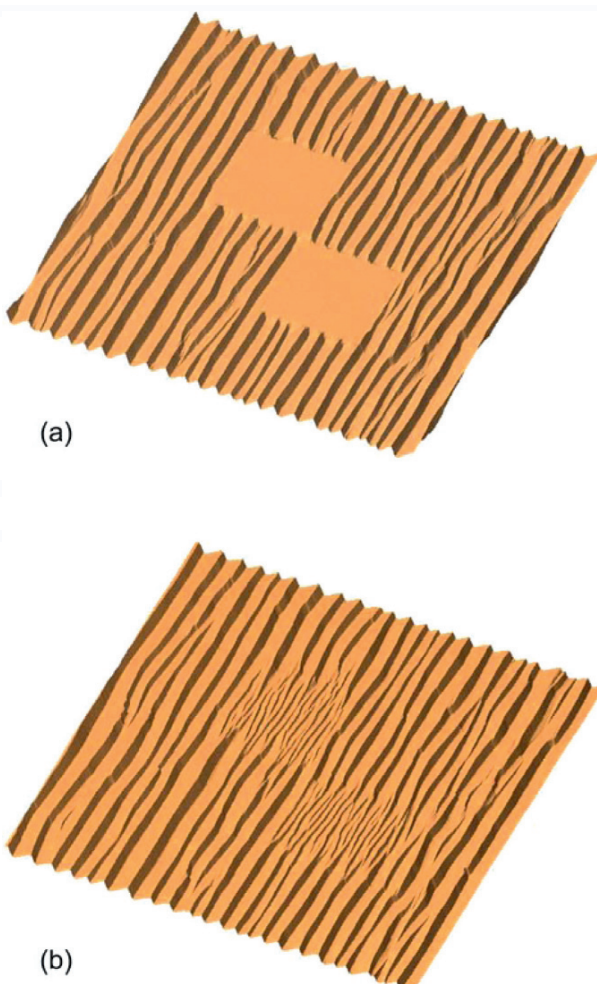


Fig. 6.24. The self-reparation behavior of aeolian sand ripples simulated by the author et al. (the friction wind velocity is $0.5 \text{ m}\cdot\text{s}^{-1}$; the sand diameter is 0.3 mm; the simulation area is $1.2 \text{ m} \times 1.2 \text{ m}$, the depth of the sand bed is 2 cm, which includes about 2.5×10^7 particles): (a) parts of the ripple surface are effaced; (b) new ripples appear in the effaced area with tiny Y-junctions at $t = 54 \text{ s}$; (by the author et al.)

theoretical model in the DPTM without introducing new model parameters. Compared with the existing discrete model, the treatment of ejection, transportation and deposition in the DPTM is more close to the actual state, such as the impacting speed and angle of saltating, the position and

speed of ejected sand, and the calculation of the reptation particles through considering friction force etc. Moreover, the scales and propagation velocities of aeolian sand ripples obtained by the DPTM agree well with the actual values in quantity. Besides, it can reproduce the developing process of

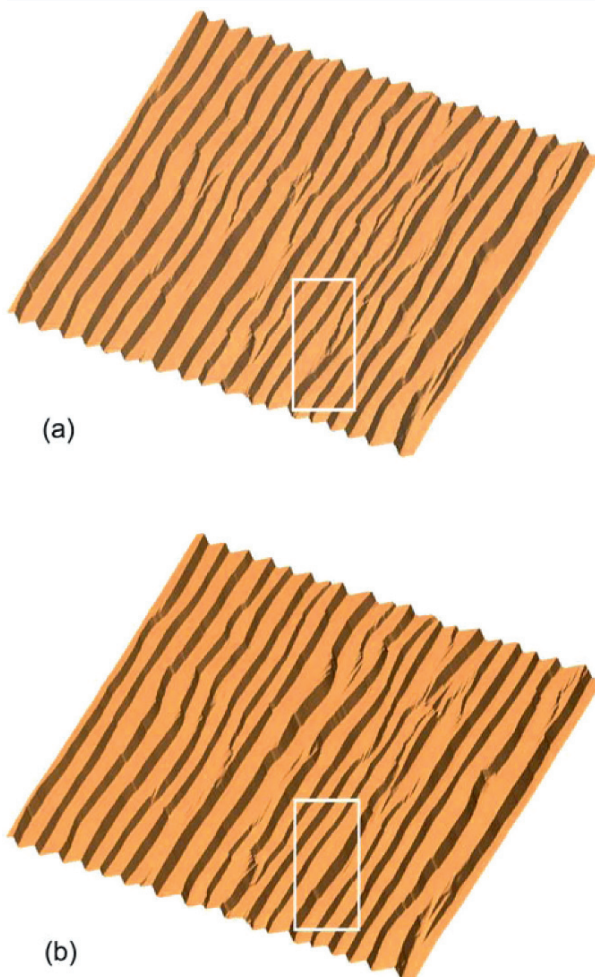


Fig. 6.25. The self-reparation behavior of sand ripples simulated by the author et al. (the friction wind velocity is $0.5 \text{ m}\cdot\text{s}^{-1}$; the sand diameter is 0.3 mm; the simulation area is $1.2 \text{ m} \times 1.2 \text{ m}$, the depth of the sand bed is 2 cm, which includes about 2.5×10^7 particles): (a) the configuration of the bed surface at $t = 220 \text{ s}$, with new junctions appearing compared with (b) the configuration of the bed surface without effacement at $t = 220 \text{ s}$ in the same area (by the author et al.)

aeolian sand ripples, and predict the influence of wind velocity and diameter to the scale and saturation time of an aeolian sand ripple, as well as the threshold wind velocity for appearance and disappearance of an aeolian sand ripple.

Chapter 7 Aeolian Geomorphology and its Simulation – Aeolian Sand Dunes

No matter from the viewpoint of occupied area or from the complexity of dynamical behavior, sand dunes and sand dune fields are the most significant manifestation of aeolian geomorphology system. Small-scale sand ripples can not grow into large-scale sand dunes, and sand dunes have distinct characteristics compared with sand ripples. The spatial and temporal scale in the formation and evolution of a sand dune is much larger than that of a sand ripple, and field observation and simulation on sand dunes are more difficult than on sand ripples. For example, the fundamental task in simulating the formation and evolution of dune field is to solve the trans-scale problem, that is, the transition from the small scale physical processes (such as the transport of sand particles) to the large scale physical processes (such as the formation and evolution of dune fields). Obviously, such trans-scale transition is not a simple linear superposition. In other words, it is impossible to characterize the formation and evolution of a dune field by modeling the process of every sand particle, which brings an infinite number of degrees of freedom into the modeling. Apart from capability limitation of present computers, the characteristics and physical mechanism of the formation and evolution of dune field are inherently different from those for sand movement and sand ripples. However, the dynamical behaviors of large-scale dune fields are definitely related with sand movement. Therefore, ignorance or complete parameterization of sand movement would possibly cause mis-reflecting the real formation and evolution physical process of dune field.

This chapter will mainly launch the discussion on aeolian sand ripples. In Sect. 7.1, the basic types of sand dunes and some observational results are introduced. Sects. 7.2 and 7.3 provide two methods used for simulating the formation and evolution of aeolian sand dunes, namely the continuum model used for the numerical calculation of single sand dune and the computer simulation methods for dune field, respectively. Sect. 7.4 devotes to a numerical simulation method and its simulation results on the formation and evolution of dune field. For the accuracy of statement, we call the approach giving the quantitative results of the formation and evolution of

sand dunes based on the differential equation solution as the numerical calculation method, while the approach presenting the qualitative results (patterns) of sand dunes by artificially defining the related rules for the underlying processes as computer simulation method, and the approach combining the above two methods as numerical simulation method.

7.1 Aeolian Sand Dunes and Observation Results

7.1.1 Classification of Sand Dunes

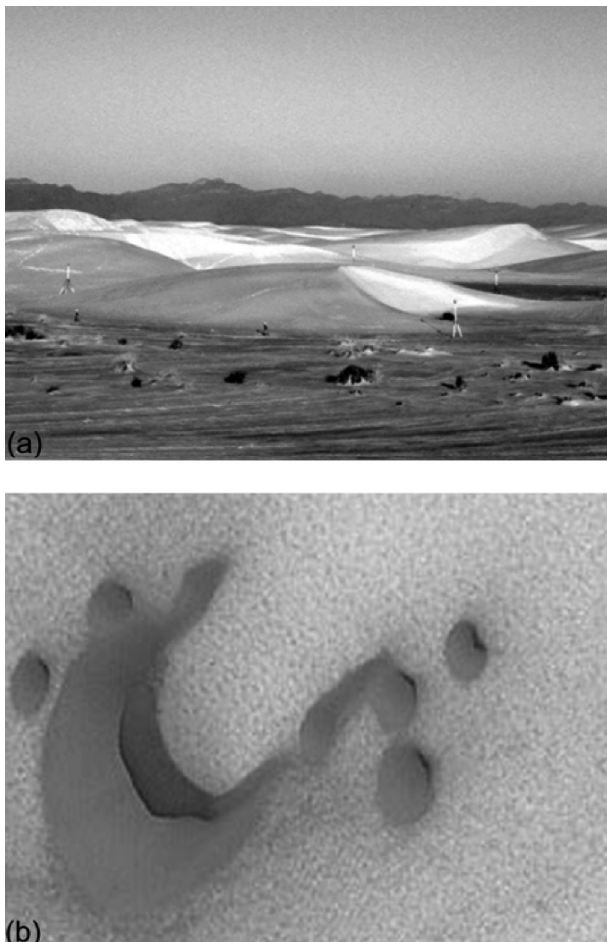


Fig. 7.1. The barchan dune: (a) barchan located in the White Sands, New Mexico (Nagihara et al. 2004), (b) barchan on Mars (Courtesy NASA/JPL)

Sand dunes can be classified by their shape, position and number of slip faces. The basic types are barchan dunes, transverse dunes, linear dunes and star dunes (see Fig. 7.1–7.4). The formation and evolution of these dunes are directly affected by the intensity of wind regime, wind direction, sand supply and vegetation coverage, etc. Generally, in areas where the wind has a prevailing direction, barchan dune formation occurs when there are insufficient sand supply; transverse dune formation occurs when there are sufficient sand supply. A barchan dune has a sickle-shaped form with

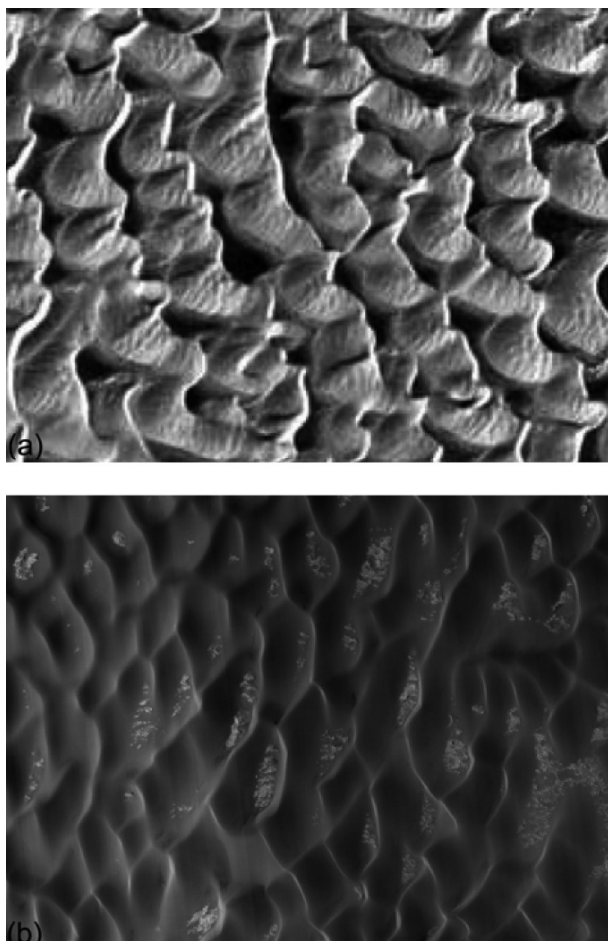


Fig. 7.2. The transverse dunes: (a) transverse dunes located in White Sands, New Mexico and (Kocurek and Ewing 2005), (b) transverse dunes on Mars (Courtesy NASA/JPL)

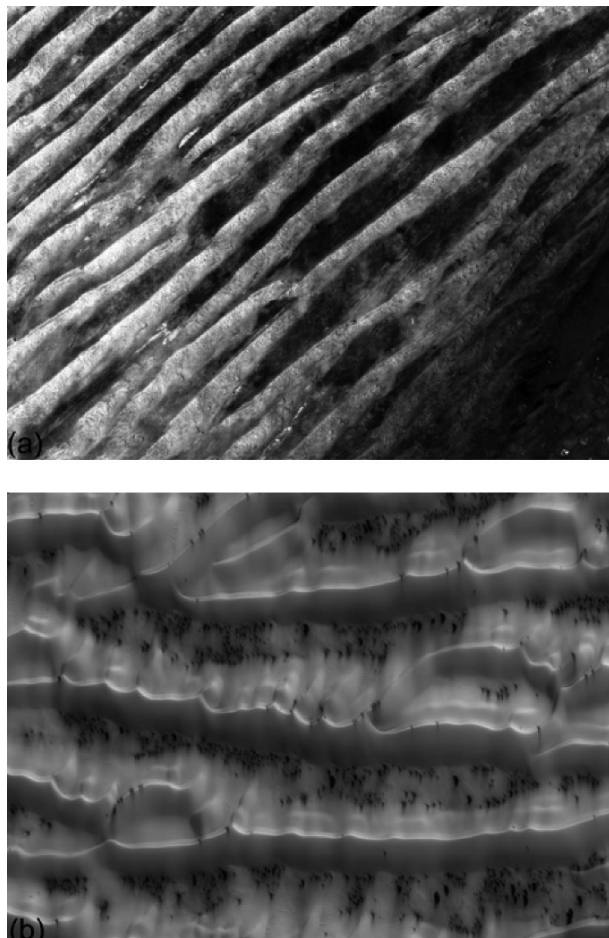


Fig. 7.3. The linear dunes: (a) linear dunes in the Rub' al Khali, Saudi Arabia, (b) linear dunes on Mars (Courtesy NASA/JPL)

two uneven arms pointing parallel to the movement direction. The height of a typical barchan dune is generally 0.3–10 m; the angle of windward slope ranges 5°–15°; the angle of leeward slope varies 30°–34°, which is close to the repose angle of sand particle. Moreover, field observations show that both the width of dune and the length of dune arms are proportional to the dune height (Finkel 1959; Hastedt and Madison 1967; Long and Sharp 1964; Sauermaier et al. 2000). The height of a transverse dune generally ranges from 10 m to 30 m and its length may reach up to several hundred meters, even to more than one kilometer in extreme case. The crest line of transverse dune is oriented perpendicular to the long-term

resultant wind direction and its windward and leeward slope are always asymmetrical.

If the wind has bi-directional or multi-directional regimes and the thickness of sand supply is sufficient, the dominant dune type in dune field changes from transverse dune to linear dune. The height of a typical linear sand dune generally is 20–50 m in height, 100 m or more in width and in length from a few hundred meters to several hundred kilometers. Most deserts in world are dominated by the linear dune type, such as the Libyan Desert in Saudi Arabia, Dasht-e-Lut Desert in Iran and those in the arid

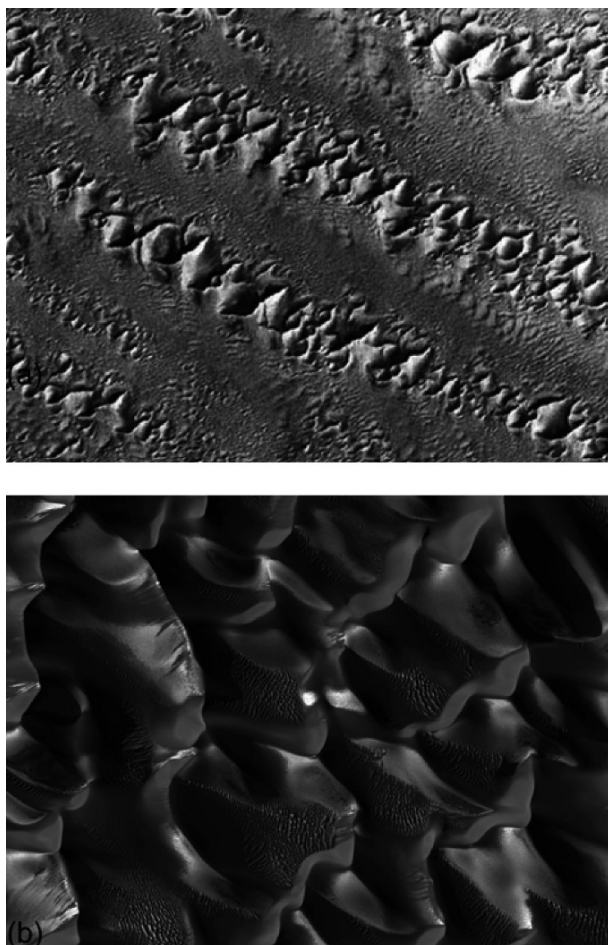


Fig. 7.4. The star dunes: (a) star dunes in the central Sahara Desert (Kocurek and Ewing 2005), (b) star dunes on Mars (Courtesy NASA/JPL)

region of Indian and Australia. The spacing between linear dunes is around 2–3 km in general.

Star dunes are formed in areas with multiple-direction wind regimes. They commonly grow upward rather than laterally and have a high central peak and slip faces on three or more arms with a slope of 25°–30°. Taking the star dunes in the south of Takla Makan Desert as an example, most of them are sporadically distributed with a height between 50 m and 100 m, although exceptional heights above 100 m are observed.

Besides the several basic types of sand dune mentioned above, dunes appear in compound and in complex forms in most sand seas. Examples of compound and complex sand dune mainly include (Fryberger et al. 1979): (1) barchan dunes coalescing; (2) star dune coalescing; (3) little barchan dunes on the arms of a large one; (4) small parabolic dunes between the arms of a large one and (5) major dunes covered by many smaller dunes.

Reports on aeolian landforms on other planets in the last several decades demonstrate that the dune patterns on the other planets have a surprising similarity with those on earth. For example, Cutts et al. (1976) reported a vast belt of dunes occupies a large area in the north polar of Mars after analyzing some 700 high-resolution images. Both linear dunes and transverse dunes were identified. Lorenz et al. (2006) have analyzed high-resolution images of Titan from Cassini orbiter and concluded that extensive areas of dark linear features are directly comparable to large linear desert dune fields on Earth. Lancaster (2006) believed the dunes on Titan have similar geometry (width, crest-to-crest spacing, and length) with linear dunes in Namibia and the Rub al Khali of Arabia (see Fig. 7.5) and showed patterns and interactions with preexisting topography that have direct parallels in terrestrial desert regions. Although current researches can not provide accurate field measurement results of saltation transport on other planets, many numerical simulations and wind tunnel experiments under Earth and Mars conditions show that the conditions on Mars are very different from on Earth. For example, Martian particles have an average diameter of about 600 μm which is much larger than 200 μm on Earth; air density on Mars is about $0.02 \text{ kg}\cdot\text{m}^{-3}$ which is much lower than $1.225 \text{ kg}\cdot\text{m}^{-3}$ on Earth; the gravity on Mars is $3.71 \text{ m}\cdot\text{s}^{-2}$ which is also much lower than $9.81 \text{ m}\cdot\text{s}^{-2}$ on Earth. All of these differences result in Martian particles saltating 100 times higher and longer in trajectories and 5–10 times higher in velocities than Earth particles do (Almeida et al. 2008). Therefore, the dune sizes (length and height) on Mars usually larger than those on Earth (Parteli and Herrmann 2007).

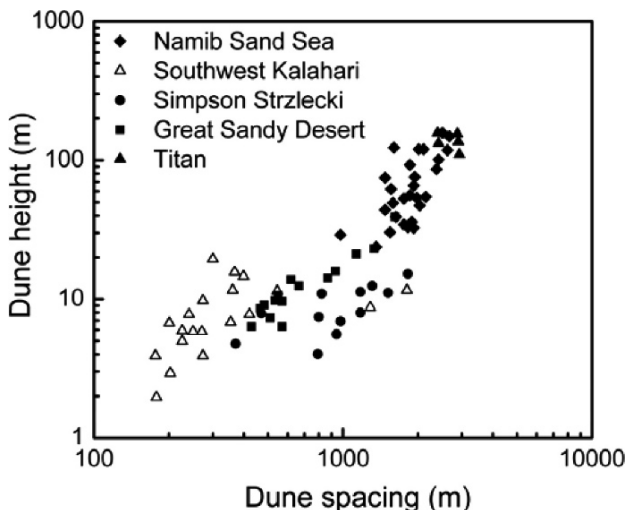


Fig. 7.5. Plot of height versus crest-to-crest spacing of linear dunes in Namibia, Kalahari, and Australia, compared to Titan dunes (from Lancaster 2006)

7.1.2 The Observation of Sand Dune Migration

As the wind velocity exceeds the threshold friction speed, sand particles on the windward slope are eroded, transported and deposited to the lee-side. The process eventually leads to the dune migrating large distances. Field observations indicate that the migration direction varies with the change of wind direction. The general migration direction is roughly consistent with the resultant wind direction in a year. The mode of migration depends on the change of wind direction and it can be divided into three types: the advancing type, which results from single-direction winds; the reciprocating advancing type, which results from two opposite uneven wind actions; and the reciprocating type, which results from two opposite wind actions but equal in strength.

To precisely measure the migration velocity of sand dunes, researchers used to compare the navigation pictures of the same area in several years continuously (e.g., Hastedrath and Madison 1967). With the development of satellite remote sensing technique, combination of the navigation picture and Global Positioning System (GPS) provides a more precise method for measurement of dune migration velocity.

The study of dune's migration mainly focuses on barchan dunes. The measurement results indicate that a barchan dune always migrates parallel to the wind direction, and the dune velocity usually has a negative exponential relationship with dune height (Fig. 7.6). Typically, a small dune in 3 m height, propagates at a velocity from 15 m·year⁻¹ to 60 m·year⁻¹, while a velocity is between 4 m·year⁻¹ and 15 m·year⁻¹ for a large dune in 15 m height. With the assumption that a barchan dune migrates forward without significantly changing its form and size, Bagnold (1941) derived that the migration velocity of a barchan is related to the rate of sand transport over the crest and inversely related to the height:

$$V_d H = \frac{Q}{\gamma}. \quad (7.1)$$

Here, V_d is the migration velocity, H is the dune height, Q is the stream-wise saltation flux over the crest. Elbelrhiti et al. (2005) measured the velocities of 140 dunes in Moroccan Sahara using global positioning system with resolution less than 4 m. They modified the Bagnold relation into $V_d \approx aQ/(H+H_0)$, where $H_0 \approx 87$ cm is a cut-off of minimal barchan height, $a \approx 2.7$ represents the increase in flux between the ground and the brink.

Besides field measurement and observation, under-water experiments are also performed to simulate dune formation and migration under atmosphere conditions. Water tanks are able to generate a strong unidirectional water flow which can shape a conical sand pile into a migrating barchan.

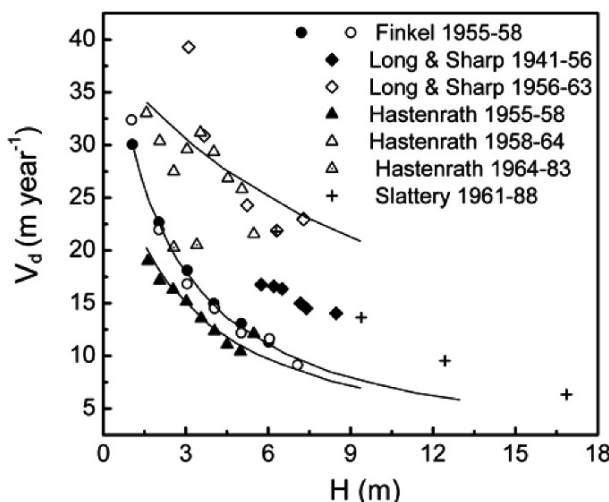
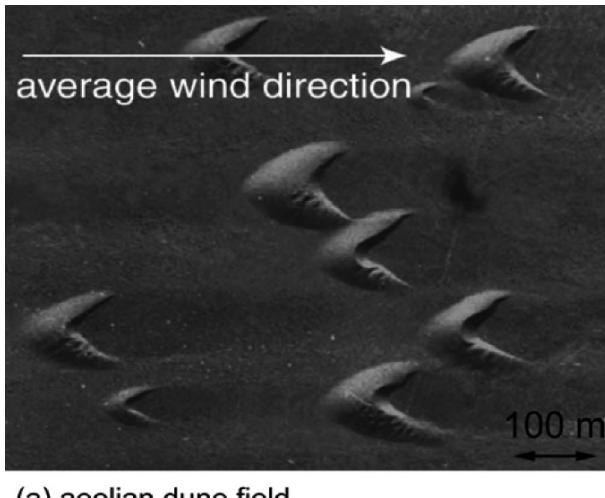
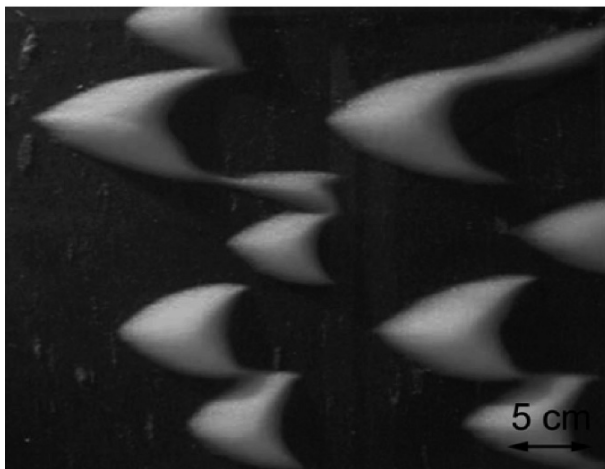


Fig. 7.6. Dune velocity versus dune height based on the measurements by Finke, Long and sharp, Hastenrath and Slattery (from Andreotti et al. 2002)

The experiments help to explore subaqueous barchans which have the similar morphology and dynamics with aeolian barchans (Figs. 7.7). The measurement data in under-water experiments are comparable with field measurements after being rescaled by the characteristic length scale (Sauerermann et al. 2001): $l_{drag} = \rho_s / \rho_f \bar{D}_s$, in which ρ_s and ρ_f represent the sand particle density and fluid density respectively; \bar{D}_s is the mean sand diameter.



(a) aeolian dune field



(b) aquatic dune field

Fig. 7.7. Comparison between (a) aeolian and (b) aquatic barchans field (from Hersen et al. 2002)

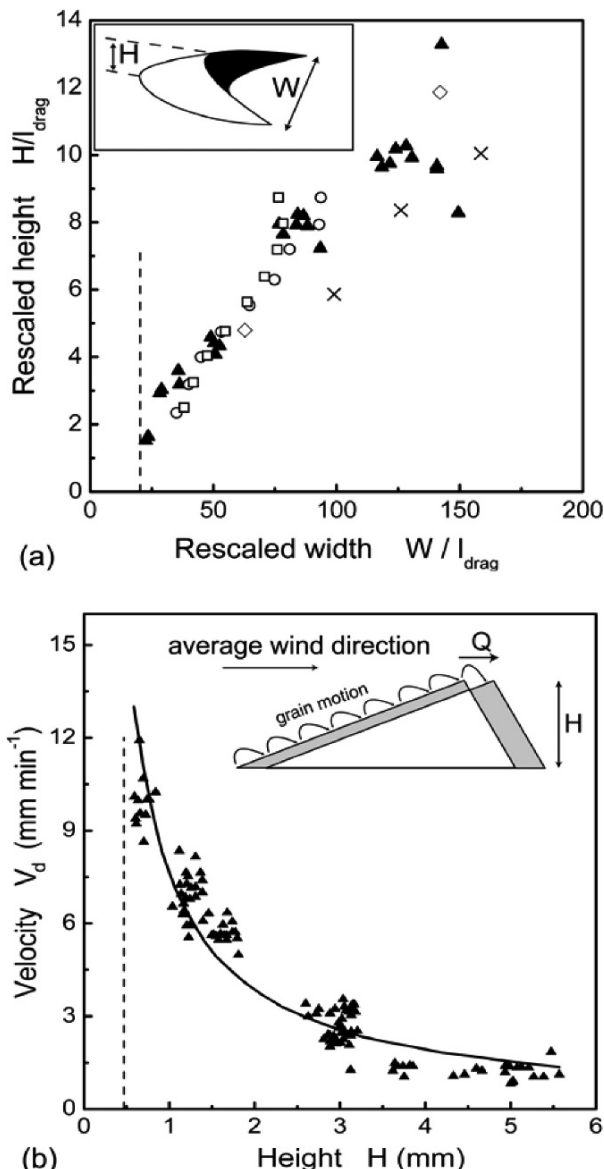


Fig. 7.8. The relationship between (a) rescaled dune width and height and (b) the velocity in under-water experiments compared with those in field measurements (from Hersen et al. 2002)

Figs. 7.8a and 7.8b show the relationship between rescaled dune width and height and the velocity in under-water experiments done by Hersen et al. (2002).

The linear sand dunes usually elongate along the crest line. Tsoar (1983) made field measurements on a linear dune in the Sinai Desert and concluded that the dune elongated at an average velocity of more than 1m per month and the peaks and saddles along the crest line formed during elongation advanced at an average velocity of 0.7 m per month. In addition, one issue rising from the study of linear dunes is whether linear dunes migrate laterally along the wind direction. Rubin and Hunter (1987) argued that few linear dunes are in symmetrical wind regimes so that linear dune has the tendency to migrate laterally when one regime dominates in the development of the dune. Bristow et al. (2000) employed the Ground-Penetrating Radar (GPR) to detect three-dimensional sedimentary structure of a linear dune in the Namib sand sea. The results showed that internal dips on a dune cross section were often predominantly in one direction. Oppositely, Livingstone (2003) argued that there had been no proof of perceptible lateral shift of the study dune in the same area in the Namib after more than two decades of field measurement. Tsoar et al. (2004) were also unable to find evidences for lateral movement in aerial photographs from Sinai taken in 1973, 1982, and 1999.

7.1.3 Observation on the Dynamical Behavior of Sand Dunes

Since the migration velocity of sand dune is related to its scale, the dunes in different size will collide with each other due to the relative differences in migration rates. Besides, changes of wind direction also play a role in destabilizing the dunes, which cause part of dunes appear or disappear. Many field observations and under-water experiments have been conducted to reveal the mechanism of these dynamical behaviors of sand dunes.

With the aid of aerial photographs and GPS, Elbelrhiti et al. (2005) performed a three-year field study of 140 barchan dunes in the Moroccan Sahara. They analyzed responses of barchan dunes to changes of wind direction and the collision between barchan dunes in detail. The results are shown in Fig. 7.9. We can see that both the windward slope face and dune trend quickly readapt to changes of wind direction, which destabilizes the dunes and generates surface waves on the barchans (in Figs. 7.9b and 7.9d). Under the affect of wind, a medium size dune is unstable and releases several small-scale barchans from the horns of the dune. The process is shown in Fig. 7.9c. Fig. 7.9f demonstrates the edging collisions between small dunes, which lead to changes of dune patterns. When two medium-sized dunes come into a coaxial collision (Fig. 7.9g), they merge into a large dune with releasing new small barchans on the tail. These released new

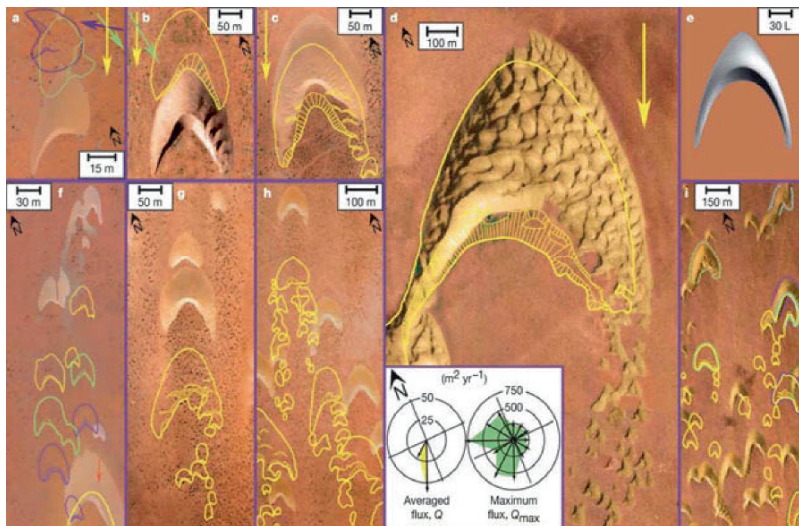


Fig. 7.9. Responses of barchan dunes to changes of wind direction and to collisions (from Elbelrhiti et al. 2005)

barchans sustain the instability of the next downwind medium-sized dunes which then release more small-scale dunes (see Fig. 7.9h). It acts like a chain destabilization of sand dunes. Fig. 7.9i presents a long-term (305 months) evolution of a barchan field. Though the largest dunes persist, many smaller dunes appear or disappear. Based on above field studies of barchans, they concluded that dune collisions and changes in wind direction play a fundamental role in the control of size selection and the development of dune patterns.

Endo et al. (2004) conducted an under-water experiment to examine the process of interaction between two moving barchans under a steady unidirectional water flow. They recognized three distinct types of interaction between barchans (see Fig. 7.10): the first type is ‘absorption’, in which the small and fast barchan catches up and is completely absorbed by the large slow barchan; the second type is ‘ejection’, in which the upstream barchan catches up with the downstream large barchan and a new barchan is born out of the lee side of the large barchan; and the third type is ‘split’, in which the downstream barchan at higher velocity than the upstream barchan is split into two barchan dunes when approaching the upstream barchan. Their experiments show that the type of the interaction is determined by both relative and absolute size of two barchans. Furthermore, Hersen and Douady (2005) conducted under-water experiments to investigate the off-center collisions between two dunes. Their results showed that when

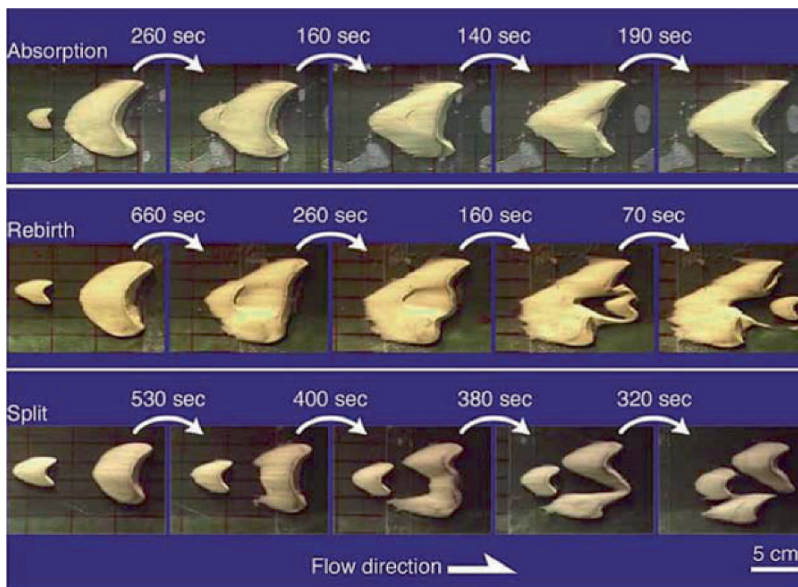


Fig. 7.10. Three distinct types of interaction between barchans observed in underwater experiment (from Endo et al. 2004)

two dunes are close enough, the eroded sand is preferentially directed through the horn of the target dune which gives rise to very small and fast barchans detaching from the target dune while the two upwind barchans merge and form a new dune.

7.1.4 Influence Factors

After observation measurements and model simulations on the dune systems in Sahel and southern African, Thomas et al. (2000) concluded that the interaction between dune surface erodibility (determined by vegetation coverage and moisture availability) and atmospheric erosivity (determined by wind energy) is critical for the activity of dune field. Their findings show that the relationship between erodibility and erosivity is susceptible to climate change and that dune fields are likely to experience significant reactivations as a consequence of global climate change in twenty-first century.

Buckley (1987) investigated the effect of sparse vegetation on the transport of dune sand in wind tunnel. Lancaster and Baas (1998) measured sand flux in sites having different vegetation coverage density at Lake Owens, California. The measurement results show that surface roughness

and threshold friction wind velocity increase with projected vegetation coverage and roughness density increasing. It results in a negative exponential decrease in sediment flux with increasing vegetation coverage density when the projected vegetation coverage is greater than 15 percent. Durán and Herrmann (2006) investigated the influence of vegetation coverage on the development process of sand dune. They introduced a fixation index FI to describe the competition between aeolian sand transport and vegetation growth. It was found that there exists a critical fixation index FI_c below which the dunes are stabilized; otherwise, the dunes remain mobile. Magnitude of FI determines the dune pattern and the barchan-like dune appears with a high FI , while a parabolic dune appears when FI is low.

Although field observation on the formation and evolution of sand dune and dune field is a necessary method to reveal the characteristic of sand dunes, due to the large time and space scale involved in the formation and evolution process of sand dune and the limitation of existing observation methods and equipments, field measurement on the sand dune and dune field is a difficult task. As a supplement, theoretical analysis and numerical simulation can to some extent reveal the mechanism of the formation and evolution of sand dune and dune field more conveniently and accurately. Existing simulation models on sand dune mainly include two types. One aims to reproduce sand dunes and their collision behaviors and another aims to simulate the dune field where a large number of sand dunes coexist. Here, we will introduce the two types of models in next section, respectively.

7.2 Continuum Sand Dune Model

The numerical simulation on the formation and evolution of one or several sand dunes has been carried on for a long time. Howard et al. (1978) and Weng et al. (1991) combined the analytical model of the flow field and sand flux over a sand dune proposed by Jackson and Hunt (1975) and gave a numerical method to simulate single dune's formation and evolution. Sauremann et al. (2001, 2003), Hersen (2004) and Hersen and Douady (2005) et al. (2004) made further improvements through considering the relationship between the change of surface flow field over a sand dune and the sand flux. This type of models was widely applied into the research of the dynamical behaviors between two dunes (Schwämmle and Herrmann 2003) and the dune formation on Mars (Parteli and Herrmann 2007). Inspired by continuum theory, the continuum sand dune model establishes

the corresponding system of differential equations by treating the incoming wind flow and the sand flow within the near-surface layer as a steady incompressible flow and a pseudo-fluid flow, respectively. During the simulation of sand dune with this model, a small sand heap $h(x, y, t=0)$, such as a sand cone, is needed to set as the initial condition (Schwämmele and Herrmann 2003). Then, the flow field over a sand dune is divided into the inner layer and the outer layer. The expressions of wind velocity and pressure after the second-order perturbation are substituted respectively into three dimensional Navier-Stokes equations of the inner layer and the outer layer. For the boundary between the inner and outer layer, the matching asymptotic technique is employed to produce an expression of surface shear stress through solving the N-S equations in the Fourier space. After that, the sand flux \mathbf{q} at different positions can be obtained according to the mass and momentum conservation equation, while the input sand flux at the entrance of the computation region is set as a constant \mathbf{q}_{in} . Through solving the following equation:

$$\frac{\partial h}{\partial t} = -\frac{1}{\rho_s} \nabla \cdot \mathbf{q}, \quad t = 0 : \quad h(x, y) = h_0(x, y), \quad (7.2)$$

we can get the new bed surface based on the initial bed surface $h(x, y, t = 0) = h_0(x, y)$. By judging whether the surface local gradient $\partial_x h$ surpasses the repose angle, stipulating the sand transport along the leeward slope under the action of gravity or not, until all surface local gradients are smaller than repose angle. Then the resulted bed is assumed as $h_1(x, y)$, and the distance l_0 between the toe of windward slope of this sand dune and the initial setting sand dune $h_0(x, y)$ is determined. If $h_1(x, y) \neq h_0(x + l_0, y)$ or the computation accuracy doesn't satisfy $|h_1(x, y) - h_0(x + l_0, y)|_{max} < \varepsilon_0$, then $h_1(x, y)$ is substituted for $h_0(x, y)$ and new bed surface based on $h_1(x, y)$ is recalculated, here, ε is defined as a computation accuracy. This process is repeated until $|h_{n+1}(x, y) - h_n(x + l_n, y)|_{max} < \varepsilon_n$ is satisfied, here l_n is the distance between the windward side feet of sand dune obtained in step $n+1$ and in step n , respectively.

The above continuum model method not only simulate one (Schwämmele and Herrmann 2005) and two (Durán et al. 2005) barchan sand dunes which are close to the actual sand dune shape, but also give the change rules of the length and width of barchan sand dune with dune height and the conclusion that the migration velocity decreases with dune height increasing (see in Sauermann et al. 2001; Andreotti et al. 2002). The results are consistent to a certain extent with the field survey result (Fig. 7.11). At the meanwhile, this method can also be used to the study of the collision

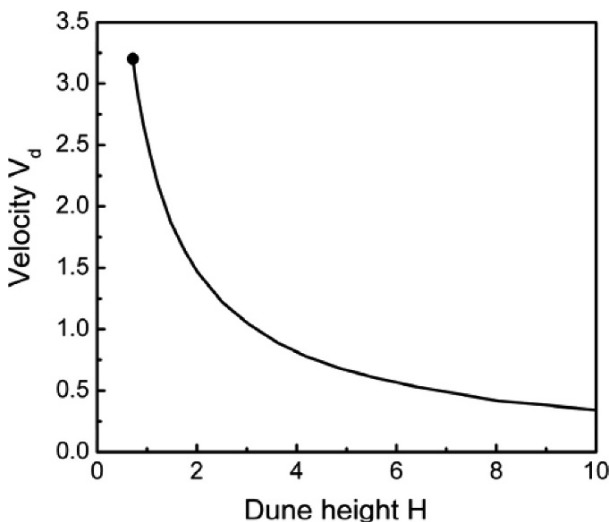


Fig. 7.11. Dune velocity as a function of dune height (edit from Andreotti et al. 2002)

behaviors between two dunes (Durán et al. 2005) and replay the behavior of two barchan dunes observed by Elbelrhiti et al.(2005), and the solitary wave behavior, that is, a sand dune passes through one another while still preserving its shape, which, however, has not been proved by field observations (Livingstone et al. 2005). Moreover, this method has been applied to simulate sand dunes on Mars vividly. The results show that the relationship between length and width of sand dunes on Mars is linear, which is similar to the one on Earth. When u^*/u_{*t} is the same, the migration velocity of sand dunes on Mars is ten times larger than the one on Earth.

However, the results simulated by continuum model to a great extent depend on the scale of the defined initial bed surface shape, such as a cone. For example, if we want to simulate a 10 m high sand dune, we firstly should suppose a 10 m high cone on the bed and the simulation is only a process in which the cone is revised to like the actual brachan dune shape. It can not show the entire process of dune formation and evolution. Meanwhile, when sand dunes in different scales exist in the sand dune field, it can not accurately simulate the flow field. So this method cannot extend to the research on the formation and evolution of a whole sand dune field.

7.3 Simulation of Sand Dune Field

7.3.1 Coupled Mapping Lattice Method

The Coupled Mapping Lattice (CML) Method applied to simulate the sand ripples (Nishimori and Ouchi 1993) is also used to simulate sand dune fields (see Sect. 6.3.3). First of all, an initial morphology composed of single-sized sands is set in a three-dimensional (3-D) sand bed, and then the sand bed is divided into grid columns. Every grid column occupies equivalent area and has the same height with the sand bed in the same position. Secondly, some rules of the transportation and deposition of sand particle in ‘grid columns’ along the wind direction are made. In detail, the quantity of sand transported from the ‘grid column’ (i' , j) to the ‘grid column’ ($i' + L_n(i', j), j$) by saltation is $q_{sn}(i', j) = a_1[-\tanh \nabla_i h(i', j) + 1 + \varepsilon]$ and the height of ‘grid column’ (i, j) changes to

$$h'_{n+1}(i, j) = h_n(i, j) + \sum_{i', j'} q_{sn}(i', j)(\delta_{i'+L_n(i', j), i} - \delta_{i', i}).$$

Considering the creeping of sand particles under gravity, it is necessary to make some modifications to the height of ‘grid column’, i.e. when the slope is too abrupt or too gentle, the corresponding rules of modifications are

$$h'_{n+1}(i, j) = h'_{n+1}(i, j) + \frac{d_{re}}{12} \left[2 \sum_{i', j' \in NN} h'_{n+1}(i', j') + \sum_{i', j' \in NNN} h'_{n+1}(i', j') - h'_{n+1}(i, j) \right]$$

$$\text{and } h'_{n+1}(i, j) = h'_{n+1}(i, j) + \sum_{i', j' \in NN} q_{cn}^{NN}(i', j': i, j) + \sum_{i', j' \in NNN} q_{cn}^{NNN}(i', j': i, j).$$

The subscript ‘ s ’ and ‘ c ’ in q_{sn} and q_{cn} represent the transported quantity of sand particles by saltation and creep, respectively; Subscript ‘ n ’ stands for the n th transportation; Superscript ‘ NN ’ presents the nearest 4 neighboring grids of (i, j) and ‘ NNN ’ represents the second nearest 4 neighboring grids; d_{re} is a constant describing the gradient of adjacent positions; The transportation distance is $L_n(i', j) = a_2[\tanh \nabla_i h(i', j) + 1]$, in which $\nabla_i h(i', j) = h(i' + 1, j) - h(i', j)$ and $q_{cn}^{NNN}(i', j': i, j) = a[h_n(i', j') - h_n(i, j)]/2$, while for $i > i'$ or $i < i'$, $q_{cn}^{NN}(i', j': i, j) = a[h_n(i', j') - h_n(i, j)] \pm b\delta_{j', j}$; a_1 , a_2 and ε are constants; a and b are positive non-zero constants, δ is Kronecker Delta. When all the ‘grid columns’ have finished transportation and deposition once, the new sand bed serves as a new initial sand bed for next step. The calculation of transportation and deposition of sands continues until

the defined calculation step, for example 500th step (Nishimori et al. 1998).

Nishimori et al. (1998) applied the above method to investigate the influence of incoming wind direction, the thickness of sand supply and vegetation on the patterns of sand dunes. They presented the relationship between the migration velocity and the dune height. Their results showed that under a single prevailing wind direction, traverse sand dunes are formed with abundant sand supply, while barchan dunes are formed when the sand supply is not abundant; under two or three prevailing wind directions, most sand dunes are the linear dunes and star dunes. Under the same conditions, the vegetation would change a barchan dune into a parabolic dune. In order to discuss the migration velocity of a sand dune, they adopted the result given by the continuous model (proposed by Wippermann and Gross 1986) that it takes $t = 24 \times 18$ hours for a conical sand pile to develop into a barchan dune, and then deduced the time needed at each step of the CML method. From the result, they pointed out that the migration velocities of sand dunes decrease with the heights of sand dunes increasing, which approximately follows a negative exponential function. The migration velocities of sand dunes higher than 10 m were estimated to be $10^2\text{--}10^3 \text{ m}\cdot\text{year}^{-1}$ which were less than $30 \text{ m}\cdot\text{year}^{-1}$ measured by field observation. In addition, the simulated forms of sand dunes were also different from real forms, for example, the length of simulated sand dune was shorter than its width which is contrary to real measurements.

The main cause resulting in the difference between the simulated sand dune and the real one is that some artificial rules are used in the CML method, which are very different from what really happen in the formation of real sand dunes. For example, the artificial rules require that transportation and deposition happen on every position on the sand bed; the quantity of transported sand $q_n(i, j)$ and the transport distance $L_n(i, j)$ are only related to the partial gradient of the sand dune; the modifacaton of the height of ‘grid column’ does not reflect the difference between windward slope and leeward slope etc. Besides, there is a main reason that the real simulation time is not considered in the method. Thus the simulation is only a reflection of the ‘pattern’ of sand dune field but not a simulation of real formation and development of sand dune field.

7.3.2 Cellular Automaton Method

Some researchers (Werner 1995; Momiji et al. 2000; Bishop et al. 2002) used the Cellular Automata (CA) Method to simulate the sand dune field. The major simulation steps are as following:

Step 1: Generate the sand bed. After given thickness of sand supply and randomly defined sand bed with fluctuation, the sand bed is divided into square lattices with $1\text{ m} \times 1\text{ m}$ in size, and then the sand bed is vertically cut in unit of $1/3\text{ m}$. Thus the initial sand bed of sand dune field is divided into cuboids in same sizes, called ‘sand slabs’. Of course, the numbers of ‘sand slabs’ at different lattice sites are different, i.e., there might not be any ‘sand slabs’ in some sites, while several sand slabs in other sites. The minimum height difference of adjacent sites, if it exists, is the height of one ‘sand slab’, $1/3\text{ m}$.

Step 2: Define the erosion, transportation and deposition of sand slabs. Randomly choose a ‘sand slab’ from the simulation bed and assume this sand slab move along the wind direction with $L = 5\text{ m}$ in distance. According to the results of Bagnold (1941), sand particles rebound more easily on smooth surface than on coarse sand bed, it is assumed that the deposition rate at sites where there are not any sand slabs is $p_{ns} = 0.4$, and the deposition rate at sites where there are at least one sand slab and not in the protection area in lee side of sand dune is $p_s = 0.6$, otherwise $p_s = 1.0$. If the slab is not deposited, then it repeatedly is moved L in the transport direction until deposition.

Step 3: Consider the avalanche of sand particles. The maximum gradient of two adjacent sites on the sand bed is set to be the same as the angle of repose 30° (Bagnold 1941). If the gradient is larger than the angle of repose, sand slab at higher site moves to lower neighboring site until the gradient is smaller than the angle of repose.

Then go back to the step 2 and randomly choose another for transportation and deposition until the shape of simulated sand bed gets close to the real sand dune.

The simulated dune forms by Werner (1995) were very close to the real sand dunes in forms. For example, under single wind direction condition, traverse or banchar dune is formed depending on sand supply in simulation. The effect of wind direction on the form of sand dune is qualitatively consistent with the field observation. Linear dunes are formed under two wind directions condition; and star dunes are formed under three wind directions condition. Besides, Anderson (1996) studied the influence of the range of diversion of wind velocity on the form of sand dune field and suggested two kinds of attractors, the linear dune and the traverse dune. The former corresponds to the condition that the wind velocity has smaller deflection, and the latter corresponds to condition that the wind velocity has larger deflection.

However, the assumption that the erosion and transport distance are constants in the model which don’t respond to the real sand transportation

process. Actually the sand quantity of erosion and the transport distance have close relationship with the wind velocity and the size of sand particles. These treatments would make the simulation deviated from actual conditions quantitatively and qualitatively.

As discussed above, in the existing computer simulation methods of the formation and the evolution of sand dune field, a large gap is between man-made rules and real situation on the transportation and the deposition of sand dunes. Thus the simulated results are similar as real sand dunes only in pattern, but not in the formation and evolution of sand dune field in length-scale and time-scale. Therefore, in the following section, we will introduce a numerical simulation method applied to simulate the formation and the evolution of sand dune field. This method is better than all existing methods in dealing with corresponding time and space problems in simulation result and the scale transition problem linking the motion of sand particles to the formation and evolution of dune field.

7.4 Numerical Simulation of Sand Dune Field

7.4.1 Discrete Numerical Simulation of Sand Dune Field

The basic idea of discrete numerical method for the simulation of sand dune field is to mesh the sand bed into rectangular sand slabs, and define both microscopic and macroscopic transportation properties and erosion-deposition behavior of ‘sand slabs’. On the microscopic level, the thicknesses of ‘sand slabs’ are firstly determined by analyzing the physical process in wind-blown sand flow, then the transportation length of ‘sand slabs’ are determined based on the mechanism of entrainment, rebound and deposition of sand particles with the aid of the probability and statistics theory. On the macroscopic level, the position and quantity of eroded ‘sand slabs’ as well as the deposition of ‘sand slabs’ are determined by analyzing the deformation of sand bed. The major procedure of discrete numerical simulation of sand dune field is described as following.

Step 1: The discretization of sand bed. For a given thickness of sand supply H_s , particle diameter D_s and simulation area, the sand bed can be divided into many rectangular units with length a and width b , respectively, called ‘sand slabs’. The positions of ‘sand slabs’ can be represented by the subscript i and j . For example, for a simulation area of 3000×3000 m and $a = b = 1$ m, we get $i = 1, 2, \dots, 3000$ and $j = 1, 2, \dots, 3000$.

Step 2: Determine the real friction velocity $u_{*ij}^{(n)}$ in the n th day according to the shape of sand bed. Generally speaking, at the surface of windward side of sand dune, the acceleration increment of the downstream friction

velocity is linear to the height of sand bed $h_{ij}^{(n-1)}$ (Momiji et al. 2000). Inspired by the experimental results on wind acceleration factor given by Lancaster (1985), we can determine the friction velocity at any position in any time interval $\Delta T = T/N$ as follow:

$$u_{*ij}^{(n)} = u_{*-\infty} + \Delta u_{*ij}^{(n)}, \quad (7.3)$$

where $\Delta u_{*ij}^{(n)}$ can be expressed as a function of the slope angle $\alpha_{ij}^{(n-1)}$ and surface elevation $h_{ij}^{(n-1)}$:

$$\Delta u_{*ij}^{(n)} = \left[u_{*1top}^{(n-1)} - u_{*-\infty} - \left(u_{*1top}^{(n-1)} - u_{*2top}^{(n-1)} \right) \frac{\tan \alpha_1^{(n-1)} - \tan \varphi_{ij}^{(n-1)}}{\tan \alpha_1^{(n-1)} - \tan \alpha_2^{(n-1)}} \right] \frac{h_{ij}^{(n)}}{h_{ijtop}^{(n-1)}} \quad n=2,3,\dots, \quad (7.4)$$

in which:

$$\varphi_{ij}^{(n-1)} = \alpha_1^{(n-1)} + \ln \left[\frac{h_{ijtop}^{(n-1)} - h_{1top}^{(n-1)}}{\left(h_{2top}^{(n-1)} - h_{1top}^{(n-1)} \right) e^{\alpha_1^{(n-1)} - \alpha_2^{(n-1)}}} + \frac{h_{2top}^{(n-1)} - h_{ijtop}^{(n-1)}}{h_{2top}^{(n-1)} - h_{1top}^{(n-1)}} \right] \quad (7.5)$$

is related to the elevations $h_{1top}^{(n-1)}$, $h_{2top}^{(n-1)}$ and the windward slope angles $\alpha_1^{(n-1)}$, $\alpha_2^{(n-1)}$ of any two dunes on the $(n-1)$ th day. Initially, that is, when $n=1$, the sand bed is flat, $\Delta u_{*ij}^{(1)}=0$. In addition, in the protection area (which is an area ranging from the top of sand dune to the recovery point of wind. Its length is about four times of the dune height and the angle is normally 15 degree, see also in Fig. 6.8), the friction velocity is set as zero.

Step 3: Determine the position of the eroded ‘sand slab’ and the sand transportation rate $q_{sij}^{(n)}$ at every location. By calculating the friction velocity $u_{*ij}^{(n)}$ at any position, we can determine the eroded according to whether the friction velocity $u_{*ij}^{(n)}$ at this position exceeds the threshold value u_{*t} . After that, considering the variations of the configuration of sand bed, we need to identify the sand transportation rate $q_{sij}^{(n)}$ at each eroded position. Based on the Continuum model mentioned in Sect. 7.2, in which the saltation layer of wind-blown sand flow was treated as fluid-like granular, we can derived the sand flux $q_{sij}^{(n)}$ and steady state velocity $u_{sij}^{(n)}$ of wind-blown sand flow at different positions through solving the mass and momentum conservation equation. The resulted expressions can be written as:

$$q_{sij}^{(n)} = \frac{2}{g} \gamma \rho u_{sij}^{(n)} \left[(u_{*ij}^{(n)})^2 - u_{*t}^2 \right] \quad (7.6)$$

and

$$u_{sij}^{(n)} = \frac{1}{\kappa} \left[2u_{*ij}^{(n)} \sqrt{\frac{z_1}{z_m} + \left(1 - \frac{z_1}{z_m}\right) \frac{u_{*t}^2}{(u_{*ij}^{(n)})^2}} + u_{*t} \ln \left(\frac{z_1}{z_m} \right) - \kappa \right] - \sqrt{\frac{\rho_s D_s g}{3C_d \gamma}}, \quad (7.7)$$

where $z_m = 0.04$ m is the thickness of saltation layer, $z_1 = 0.005$ m is the reference height, and $\gamma = 0.4$ is the model parameter.

Step 4: Randomly select one of the ‘sand slabs’ on the sand bed and calculate the thickness $B_{ij}^{(n)}$ of the eroded ‘sand slab’. After obtaining the sand flux eroded during ΔT , that is, $Q_{sij}^{(n)} = q_{sij}^{(n)} \Delta Tb (1 - \Delta s)$, we can deduce the average thickness of the eroded ‘sand slab’: $B_{ij}^{(n)} = Q_{sij}^{(n)} / (\eta \rho_s S_{ij})$, in which η is the porosity of sand bed and usually is supposed to be 0.62; Δs is the coverage coefficient which is defined as the ratio between the length of the sand area covered by the deposited sands after one-time saltating and the average saltation length $L_{sij}^{(n)} = u_{sij}^{(n)} T_{sij}^{(n)}$ (see Fig. 7.12), that is:

$$\Delta s = \frac{q_{sij}^{(n)} T_{sij}^{(n)}}{\rho_s D_s L_{sij}^{(n)}} \left[1 + r_{dep} + r_{dep} (1 - r_{ero}) + \dots + r_{dep} (1 - r_{ero})^{n_t - 2} \right] \approx \frac{q_{sij}^{(n)} T_{sij}^{(n)}}{\rho_s D_s L_{sij}^{(n)}} \frac{r_{ero} + r_{dep}}{r_{ero}}, \quad (7.8)$$

where r_{dep} and r_{ero} are the deposition and erosion rate of sand particles; $T_{sij}^{(n)} = 1.7 u_{*ij}^{(n)} / g$ is the average saltation time (Nalpanis et al. 1993); $n_t = |\Delta T / T_{sij}^{(n)}|$ saltation and deposition times of sands within ΔT ; $|\cdot|$ is the integral function.

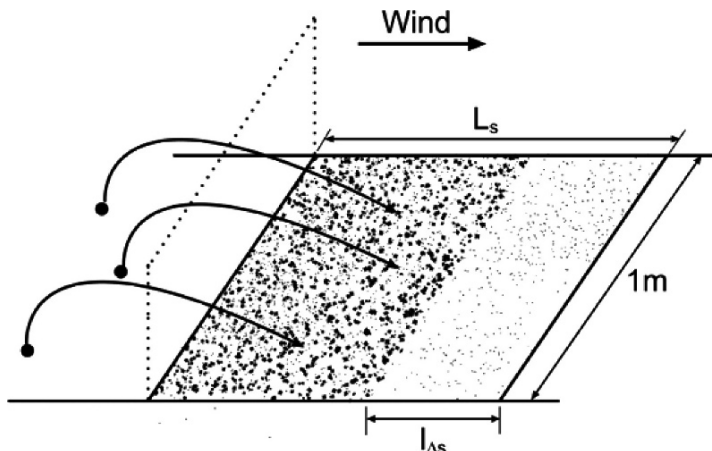


Fig. 7.12. Schematic illustration of the meaning of the coverage coefficient (Δs); $L_s \times 1 \text{ m}^2$ is the area sand particles deposit within; $l_{\Delta s} \times 1 \text{ m}^2$ is corresponding to the area covered by the sand amount after one-time saltating; the coverage coefficient can be expressed as $\Delta s = l_{\Delta s} / L_s$ (as Eqs. 7.8)

Step 5: Determine the transportation length $l_{ij}^{(n)}$ of the eroded ‘sand slab’. We assume the mass of the ‘sand slab’ in site (i, j) , $M_{ij}^{(n)} = a \times b \times B_{ij}^{(n)} \times \rho_s$, is eroded for n_t times during ΔT , and the time required for each erosion is $T_{sij}^{(n)}$; sand mass eroded each time is $M_{ij}^{(n)} / n_t$; Considering the momentum conservation of wind-blown sand flow at steady state, and the sum of the average momentum of the sand deposited into the area with unit width and $n_t L_{sij}^{(n)}$ in length, namely, $\sum_{n'=1}^{n_t} m_{ij}^{(n')} \cdot v_{ij}^{(n')}$ is supposed to be equal to the momentum of the ‘sand slab’, $M_{ij}^{(n)} l_{ij}^{(n)} / \Delta T$ (see Fig. 7.13), therefore, we can get the average transportation length $l_{ij}^{(n)}$ of the slab S_{ij} by

$$l_{ij}^{(n)} = \sum_{n'=1}^{n_t} m_{ij}^{(n')} \cdot v_{ij}^{(n')} \frac{\Delta T}{M_{ij}^{(n)}} = \sum_{n'=1}^{n_t} m_{ij}^{(n')} \cdot n' \cdot \frac{L_{sij}^{(n)}}{M_{ij}^{(n)}} \quad (7.9)$$

where $m_{ij}^{(n')}$ represents the whole sand mass deposited at location $(i + n' L_{sij}^{(n)}, j)$ which can be expressed as:

$$m_{ij}^{(n')} = \sum_{j'=1}^{n_t+1-n'} \Delta M_{j'}(i + n' L_{sij}^{(n)}, j) \quad (7.10)$$

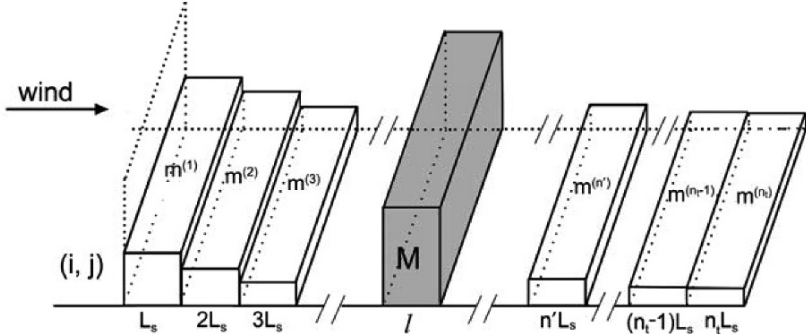


Fig. 7.13. Schematic illustration of the momentum conservation during the transportation process; M is the total sand mass leaving from (i, j) within ΔT ; $m^{(n')}$ is the sand mass leaving from (i, j) and depositing at n' ; the momentum conservation during the transportation process means that the sum of the momentum of the sand mass depositing at every position, $\sum_{n'=1}^{n_t} m^{(n')} (n' L_s / \Delta T)$, should be equal to the momentum of the total sand mass traveling along the wind direction, $ML/\Delta T$

where $\Delta M_{j'}(i + n'L_{sij}^{(n)}, j)$ represents the sand mass that leaves from (i, j) and deposits at $(i + n'L_{sij}^{(n)}, j)$ at the j' th time step. It can be deduced as follows: according to the times that the sand mass depositing to $(i + L_{sij}^{(n)}, j)$ at the j' th time step required to be eroded, the sand mass that deposits at $(i + L_{sij}^{(n)}, j)$ can be determined as

$$\Delta M_{j'}(i + L_{sij}^{(n)}, j) = \begin{cases} \frac{M_{ij}^{(n)}}{n_t} \alpha (1 - \beta)^{n_t - (j'+1)} & j' = 1, \dots, n_t - 1 \\ \Delta M_{n_t}(i + L_{sij}^{(n)}, j) = \frac{M_{ij}^{(n)}}{n_t} & j' = n_t \end{cases} \quad (7.11)$$

Since the sand mass that leaves from $(i + L_{sij}^{(n)}, j)$ and deposits at $(i + 2L_{sij}^{(n)}, j)$ can be determined from the sand mass that leaves from (i, j) and deposits at $(i + L_{sij}^{(n)}, j)$ from the $(j'+1)$ th time step to the n_t th time step, we get:

$$\Delta M_{j'}(i + 2L_{sij}^{(n)}, j) = \sum_{k=2}^{n_t - j'} [r_{dep} (1 - r_{ero})^{k-2} - r_{dep} (1 - r_{ero})^{k-1}] \cdot \Delta M_{j'+k}(i + L_{sij}^{(n)}, j) + (1 - r_{dep}) \Delta M_{j'+1}(i + L_{sij}^{(n)}, j) \quad j' = 1, \dots, n_t - 1 \quad (7.12)$$

Accordingly, the sand mass that leaves from $(i + L_{sij}^{(n)}, j)$ and deposits at $(i + n'L_{sij}^{(n)}, j)$ can be determined from the sand mass that leaves from (i, j) and deposits at $(i + (n'-1)L_{sij}^{(n)}, j)$ from the $(j'+1)$ th time step to the $(n_t + 2 - n')$ th time step:

$$\Delta M_{j'}(i + n'L_{sij}^{(n)}, j) = \sum_{k=2}^{n_t + 2 - n' - j'} [r_{dep} (1 - r_{ero})^{k-2} - r_{dep} (1 - r_{ero})^{k-1}] \cdot \Delta M_{j'+k}(i + (n'-1)L_{sij}^{(n)}, j) + (1 - r_{dep}) \Delta M_{j'+1}(i + (n'-1)L_{sij}^{(n)}, j) \quad j' = 1, \dots, n_t + 1 - n' \quad (7.13)$$

It is worth noting that, in natural wind-blown sand flow, the property of sand bed is heterogeneous which results in the inconsistency of the erosion probability r_{dep} and deposition probability r_{ero} in the whole field. For simplicity, we randomly let some positions are of deposition probability r'_{dep} according to a certain proportion, and the transportation lengths of the corresponding ‘sand slabs’ in these positions are identically set as $l_{ij}^{(n)}/2$. Besides, if a ‘sand slab’ is transported into the protection area (see Fig. 6.8), we let it deposit directly.

Step 6: Modification of the configuration of sand bed. Due to the collapse behavior of sand (Momiji et al. 2000), we need to set the maximum gradient of adjacent positions to be same as the angle of repose Θ after the eroded ‘sand slab’ is transported and deposited. That means, if the gradient

of sand bed is larger than Θ then the ‘sand slab’ at the higher position moves to the adjacent lower position. The thickness of the ‘sand slab’ moved is taken as $(\Delta h - \sqrt{S_{ij}} \tan \Theta)/2$, in which Δh is the height difference of two adjacent positions.

After that, another eroded ‘sand slab’ within time ΔT is randomly selected to repeat the above 5 step of simulation until all of the eroded ‘sand slabs’ are treated. The configuration of sand bed obtained in this period ΔT then serves as the initial sand bed for the next period ΔT to determine the friction velocity at different positions in the whole field. The whole simulation ends until $n = N$, that is, the simulation time reaches to the required time T .

7.4.2 Simulation Results

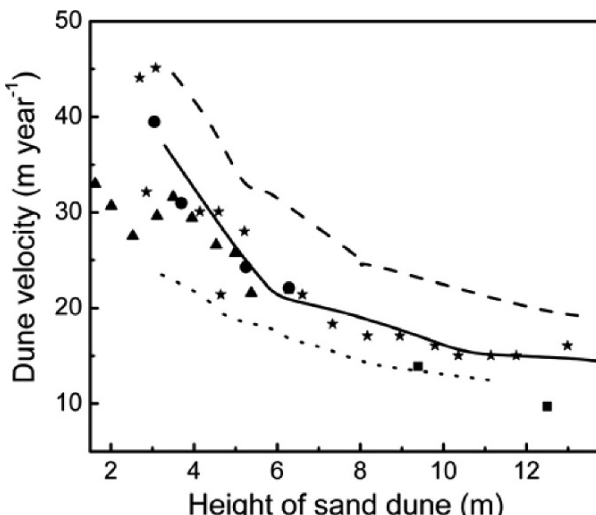


Fig. 7.14 Comparisons between the results of the field observation and simulation results (by the author et al.) on dune velocity versus dune height, ★ the measured results in the deserts of Moroccan (Elbelrhiti et al. 2005); ■ the measured results by Slattery in Namibia, South African, ▲ the measured results by Hasternrath in Peru, ● the measured results in field by Long and Sharp in the imperial valley, California (Andreotti et al. 2002); — — — the simulation results for $u_* = 0.5 \text{ m}\cdot\text{s}^{-1}$, $D_s = 0.3 \text{ mm}$; — — the simulation results for $u_* = 0.55 \text{ m}\cdot\text{s}^{-1}$, $D_s = 0.3 \text{ mm}$; the simulation results for $u_* = 0.5 \text{ m}\cdot\text{s}^{-1}$, $D_s = 0.25 \text{ mm}$; the simulation area S is $3000 \text{ m} \times 3000 \text{ m}$

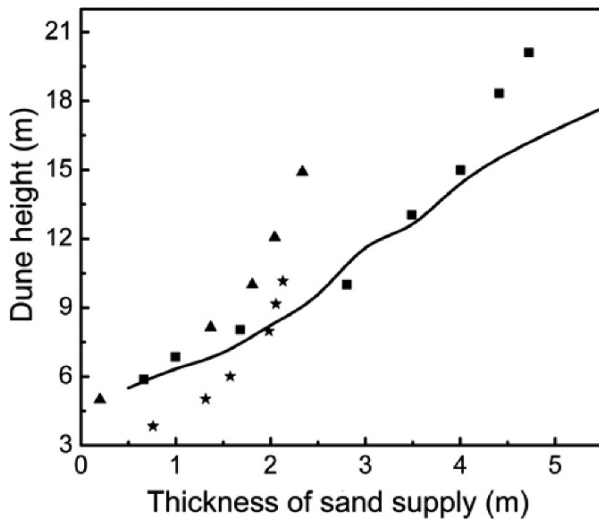


Fig. 7.15 Comparisons between the results of the field observation and simulation results (by the author et al.) on dune height versus thickness of sand supply, ■ the measured results in the Simpson-Strzelecki Desert, ▲ the measured results in the Great sandy Desert, ★ the measured results in the Great Victoria (Wasson and Hyde 1983), — the simulation results for $u^* = 0.55 \text{ m}\cdot\text{s}^{-1}$, $D_s = 0.3 \text{ mm}$; the simulation area S is $3000 \text{ m} \times 3000 \text{ m}$

With the discrete numerical method introduced above, Zheng et al. (2008) fulfilled the quantitative simulation of the formation and evolution of dune field. Through the simulations of a sand dune field with an area of $3 \times 3 \text{ km}^2$, we can get the change laws of dune velocity and dune height as well as variations of the average dune height with the thickness of sand supply, which are all consistent with field observation results qualitatively and quantitatively (shown in Figs. 7.14 and 7.15). For example, the dune velocity for a 22 m high dune in our simulation for $u^* = 0.5 \text{ m}\cdot\text{s}^{-1}$ and $D_s = 0.3 \text{ mm}$ is $12 \text{ m}\cdot\text{year}^{-1}$ which agrees well with $14 \text{ m}\cdot\text{year}^{-1}$ given by Elbelrhiti et al (2005); For the case that the thickness of sand supply is 2 m, the average dune height of our simulation is 8.35 m, and the experiment result is 8 m (Wasson and Hyde 1983), the dune velocity decreases as the dune height increases and the scale of dune increases as the thickness of sand supply increases. With the discrete numerical method, the whole formation and evolution of sand dune field is replayed, shown in Figs. 7.16–7.19. In the initial development stage of sand dune field, like the second year, under the wind blowing, a large number of small irregular sand piles are formed on the flat sand bed, shown in Fig. 7.16, the highest sand pile is 2.86 m in height. As time goes, the number of sand piles decreases and the

sizes of sand piles increase due to the interaction between sand piles (see Fig. 7.17).

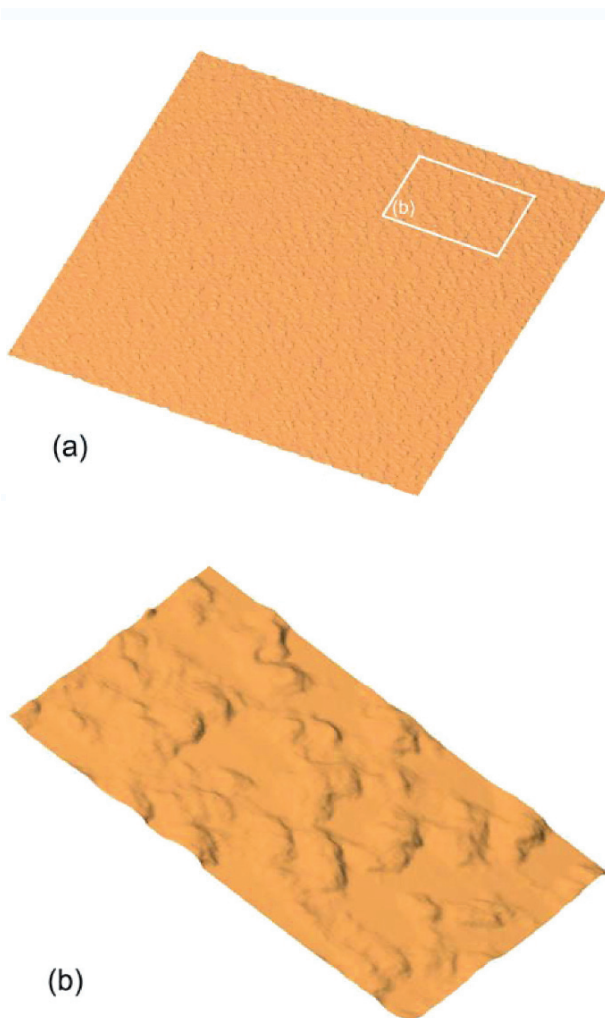


Fig. 7.16. The formation and evolution of barchans field obtained by simulations ($u_* = 0.5 \text{ m}\cdot\text{s}^{-1}$, $D_s = 0.3 \text{ mm}$, $H_s = 0.8 \text{ m}$, $S = 3000 \text{ m} \times 3000 \text{ m}$); **(a)** the global view of the whole dune field in the 2nd, year; **(b)** the local view of part of the dune field in 2nd year (by the author et al.)

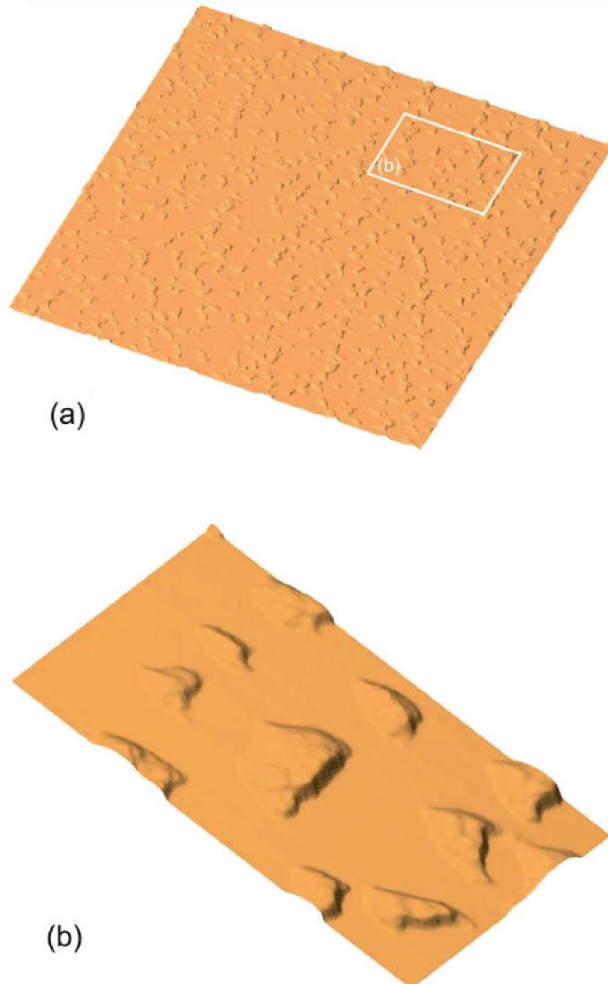


Fig. 7.17. The formation and evolution of barchans field obtained by simulations ($u_* = 0.5 \text{ m}\cdot\text{s}^{-1}$, $D_s = 0.3 \text{ mm}$, $H_s = 0.8 \text{ m}$, $S = 3000 \text{ m} \times 3000 \text{ m}$); **(a)** the global view of the whole dune field in the 5th year; **(b)** the local view of part of the dune field in 5th year (by the author et al.)

In the fifth year, the highest sand pile reaches 4.21 m in height and barchan-like sand dunes are forming. In the eighth year, most of the sand piles grow up to large sand dunes in a certain major form, such as barchans. Shown in Fig. 7.18, the highest sand dune reaches 6.84 m in height. Afterwards, although the forms and the scales of sand dunes keep varying,

for example, in the 13th year, some dunes chains are formed, but the increment of the height of individual sand dune is slowed down, the maximum height can be 7.47 m (see in Fig. 7.19).

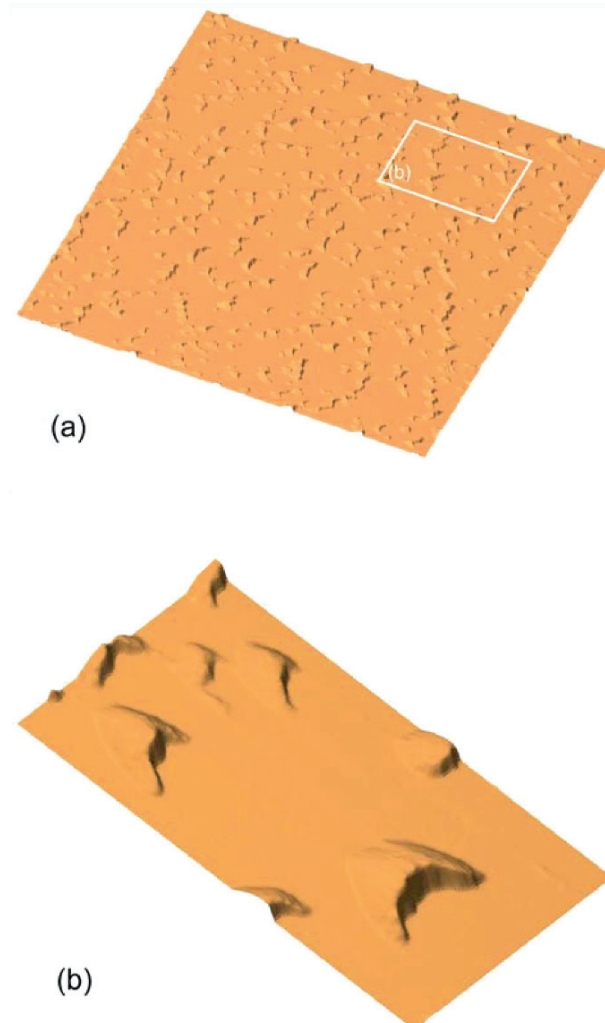


Fig. 7.18. The formation and evolution of barchans field obtained by simulations ($u_* = 0.5 \text{ m}\cdot\text{s}^{-1}$, $D_s = 0.3 \text{ mm}$, $H_s = 0.8 \text{ m}$, $S = 3000 \text{ m} \times 3000 \text{ m}$); **(a)** the global view of the whole dune field in the 8th year; **(b)** the local view of part of the dune field in 8th year (by the author et al.)

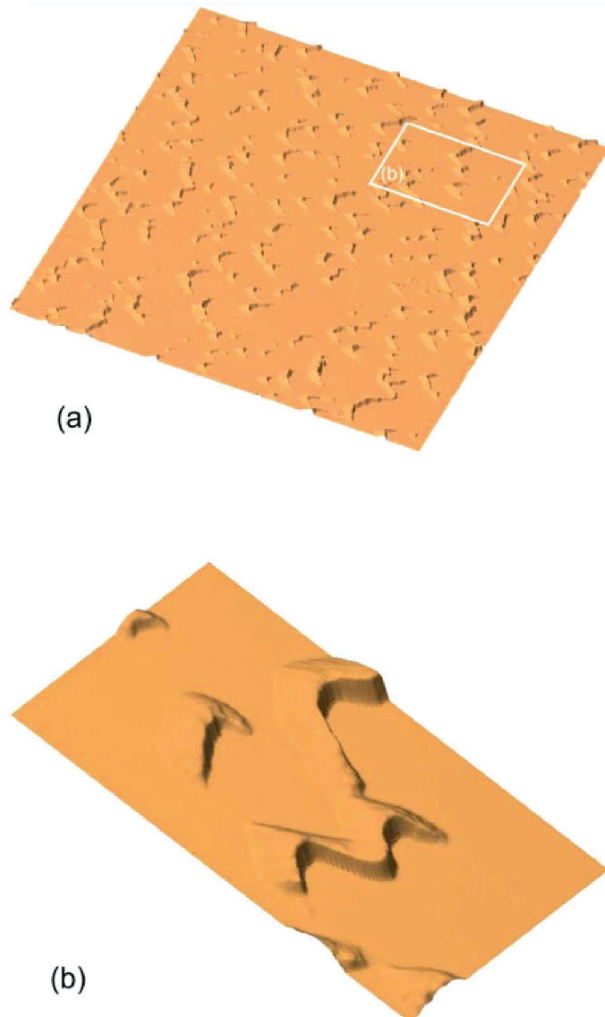


Fig. 7.19. The formation and evolution of barchans field obtained by simulations ($u_* = 0.5 \text{ m:s}^{-1}$, $D_s = 0.3 \text{ mm}$, $H_s = 0.8 \text{ m}$, $S = 3000 \text{ m} \times 3000 \text{ m}$); **(a)** the global view of the whole dune field in the 13th year; **(b)** the local view of part of the dune field in 13th year (by the author et al.)

The thickness of sand supply has obvious influences on the formation and evolution of a sand dune field. When the thickness of sand supply is $H_s = 3 \text{ m}$, the major form of sand dune is traverse dune instead of barchan. In the 2nd year, shown in Fig. 7.20, the sand dune field is formed by small traverse dunes with the maximum height 5.54 m. In the 5th year, the forms

of sand dunes are still traverse dunes, shown in Fig. 7.21, but the dune sizes increase and the highest dune reaches up to 6.69 m in height. In the 10th year, the form of sand dune field remain unchanged, shown in Fig. 7.22, the increment of dune sizes is slowed down and the maximum dune height is 9.72 m.

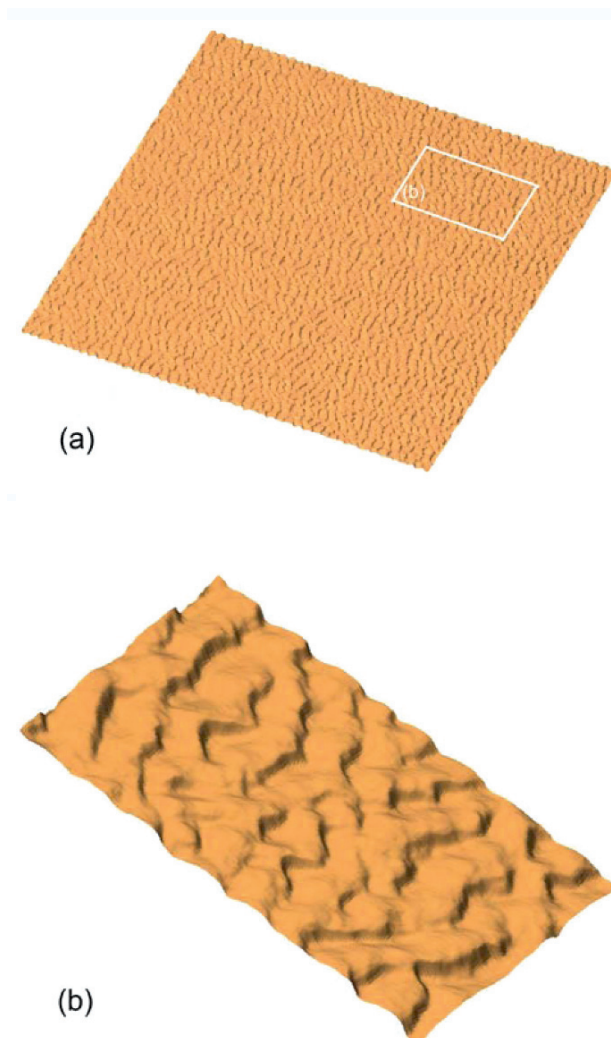


Fig. 7.20. The formation and evolution of transverse dunes field obtained by simulations ($u_* = 0.5 \text{ m}\cdot\text{s}^{-1}$, $D_s = 0.3 \text{ mm}$, $H_s = 3 \text{ m}$, $S = 3000 \text{ m} \times 3000 \text{ m}$); **(a)** the global view of the whole dune field in the 2nd year; **(b)** the local view of part of the sand dune field in 2nd year (by the author et al.).

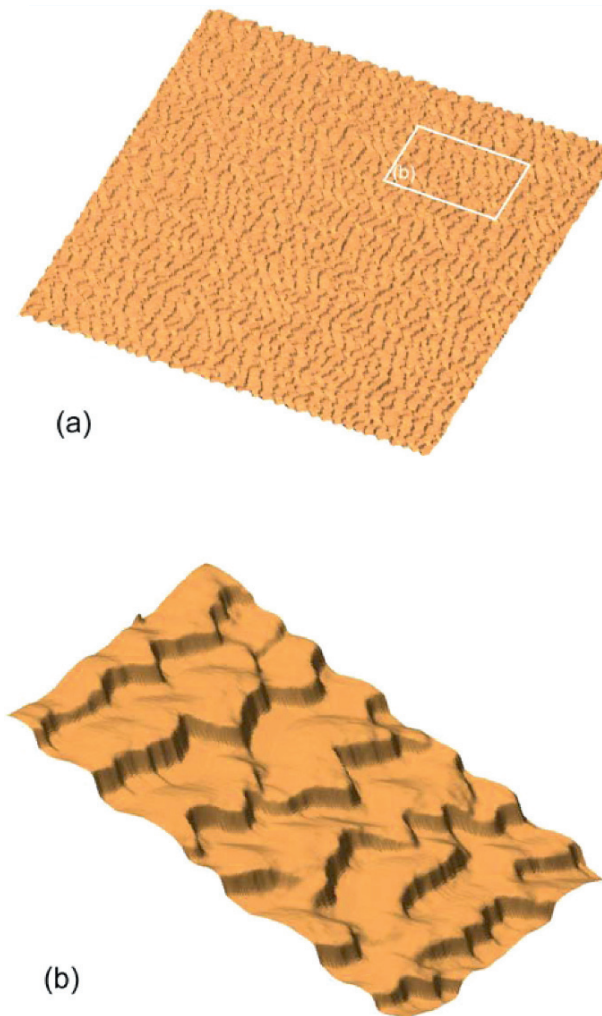


Fig. 7.21. The formation and evolution of transverse dunes field obtained by simulations ($u_* = 0.5 \text{ m}\cdot\text{s}^{-1}$, $D_s = 0.3 \text{ mm}$, $H_s = 3 \text{ m}$, $S = 3000 \text{ m} \times 3000 \text{ m}$); **(a)** the global view of the whole dune field in the 5th year; **(b)** the local view of part of the sand dune field in 5th year (by the author et al.)

Another conclusion from the simulation is that there is a threshold thickness of sand supply determining the dune pattern and the mode of the formation and evolution of a dune field. For instance, the threshold thickness is about 1.4 m when the incoming friction wind velocity is $0.5 \text{ m}\cdot\text{s}^{-1}$ and the sand diameter is 0.3 mm.

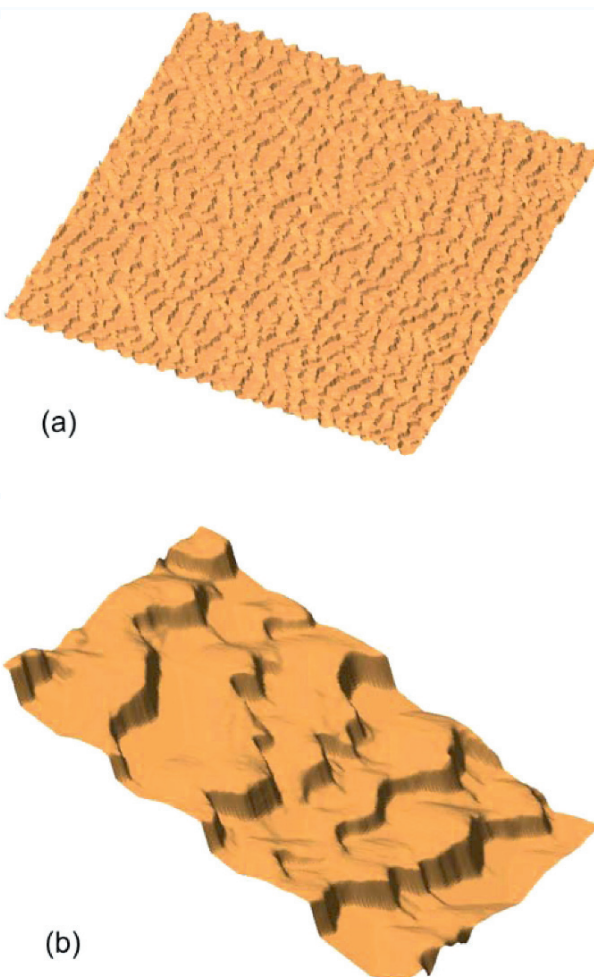


Fig. 7.22. The formation and evolution of transverse dunes field obtained by simulations ($u_* = 0.5 \text{ m}\cdot\text{s}^{-1}$, $D_s = 0.3 \text{ mm}$, $H_s = 3 \text{ m}$, $S = 3000 \text{ m} \times 3000 \text{ m}$); **(a)** the global view of the whole dune field in the 10th year; **(b)** the local view of part of the sand dune field in 10th year (by the author et al.)

Sand diameter and wind velocity have strong effect on the number and the scale of sand dunes. For given friction wind velocity and thickness of sand supply, the increase of sand diameter would result in the decrease of the maximum and average dune height, shown in Fig. 7.23(a). Increase of incoming friction wind velocity would results in the increase of the maximum and average dune height shown in Fig. 7.23(b).

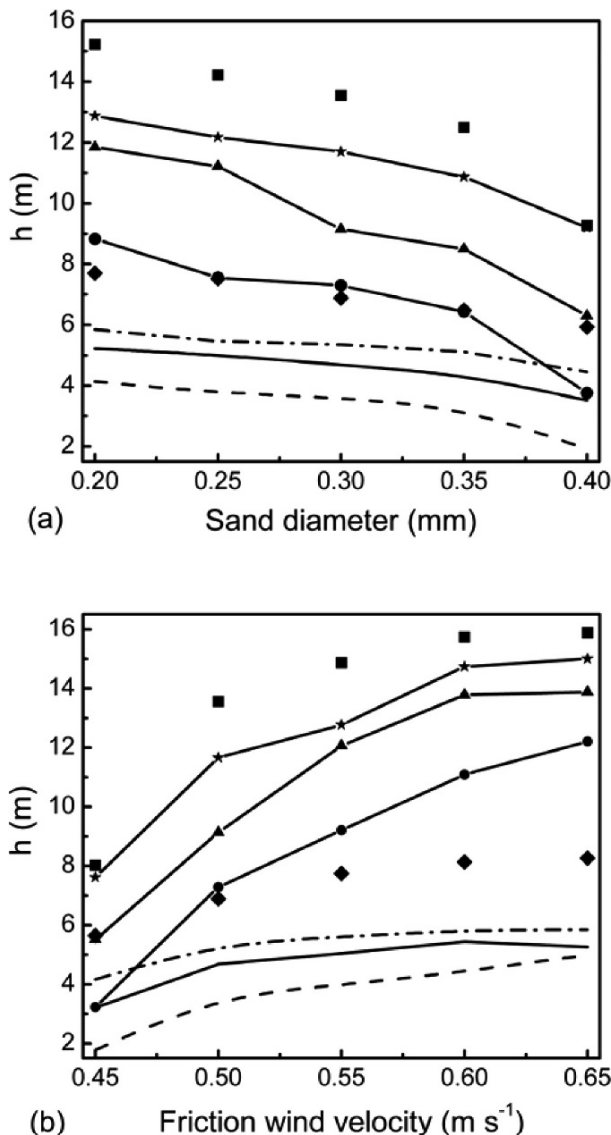
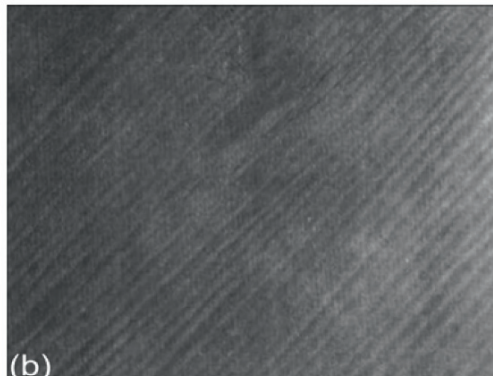


Fig. 7.23. Variations of the maximum dune height (h_{max}) and average dune height (h_{avg}) in the dune field with (a) sand diameter and (b) wind velocity; ■ and ◆ are simulation results of h_{max} and h_{avg} in the 10th year for $H_s = 4$ m; the others are simulation results for $H_s = 0.8$ m, in which ●, ▲ and ★ are the simulation results of h_{max} in the 5th, 10th and 15th year respectively; —, - - -, and - · - · - are the simulation results of h_{avg} in the 5th, 10th and 15th year, respectively (by the author et al.)



(a)



(b)

Fig. 7.24. Dune patterns in the dune field under two prevailing wind direction; **(a)** are the simulation results for $u_* = 0.5 \text{ m}\cdot\text{s}^{-1}$, $D_s = 0.3 \text{ mm}$, $H_s = 0.8 \text{ m}$ (by author et al.); **(b)** are aerial images (from Fryberger et al. 1979)

The prevailing wind direction also has a strong influence on the forms of sand dunes. Figs. 7.24–7.26 illustrate the sand dune fields formed under two, three and four prevailing wind directions conditions, respectively. If there are two opposite prevailing wind directions, the form of sand dunes is mainly linear dunes shown in Fig. 7.24a. If there are three or four prevailing wind directions, the forms of sand dunes are mainly star dunes shown in Fig. 7.25a and dome dune shown in Fig. 7.26a, respectively. The simulated results by the discrete numerical simulation are consistent with

the results of field observation (Fryberger et al. 1979) shown in Figs. 7.24–7.26b.

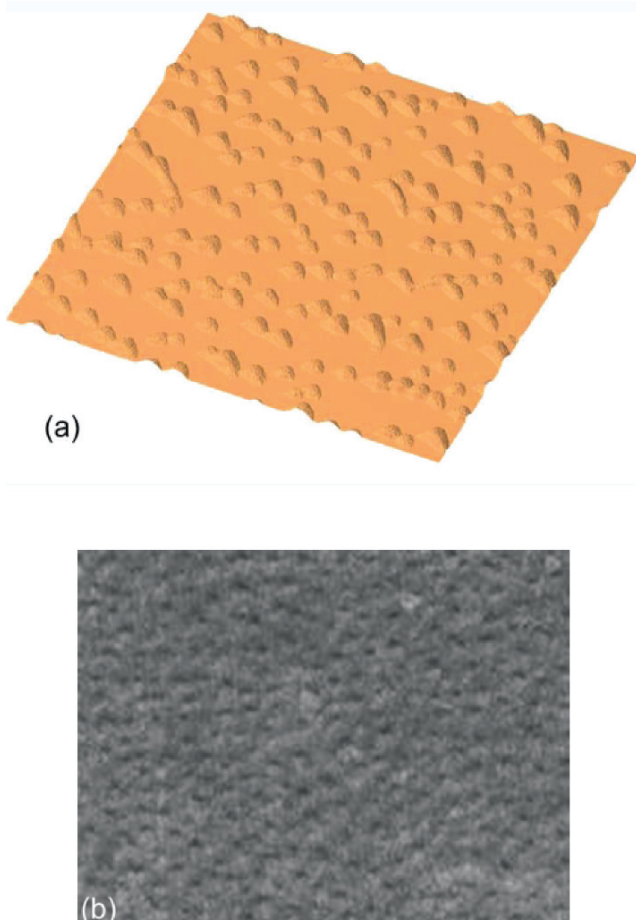


Fig. 7.25. Dune patterns in the dune field under three prevailing wind direction; (a) the simulation results for $u_* = 0.5 \text{ m}\cdot\text{s}^{-1}$, $D_s = 0.3 \text{ mm}$, $H_s = 0.8\text{m}$ (by author et al.); (b) aerial images (from Fryberger et al. 1979)

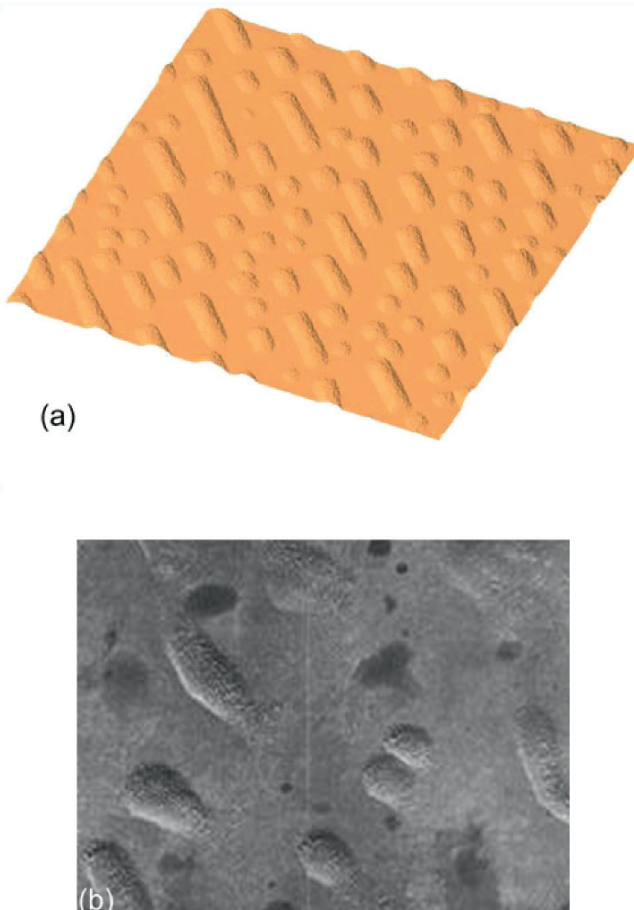


Fig. 7.26. Dune patterns in the dune field under four prevailing wind direction; **(a)** the simulation results for $u_* = 0.5 \text{ m}\cdot\text{s}^{-1}$, $D_s = 0.3 \text{ mm}$, $H_s = 0.8 \text{ m}$ (by author et al.); **(b)** aerial images (from Fryberger et al. 1979)

Some dynamic behaviors of sand dunes observed in field are also able to be replayed by the discrete numerical simulation of the formation and evolution of sand dune field given in this chapter, shown in Fig. 7.27–7.31. For example, for $u_* = 0.5 \text{ m}\cdot\text{s}^{-1}$ and $H_s = 0.8 \text{ m}$, two dunes with similar sizes, marked by ‘○’ would have a lateral collision in the 12th year and start merging in the 15th year; it becomes a larger dune than parent dunes in the 18th year. Moreover, in the 11th year, a smaller dune marked by ‘☆’ is unstable, and it would become smaller in the 12th year and vanish

in the 13th year. The ‘solitary wave’ behavior of sand dunes obtained by Schwämmle and Herrmann (2003) is also discovered in our simulations (see Fig. 7.32). Besides, the dune chain are expected to be unstable in our simulation, that is, under the action of wind field, the configuration of the dune chain varies as it advances forward, sometimes, and some parts of the dune chain will break away from the main body, and then form new dunes.

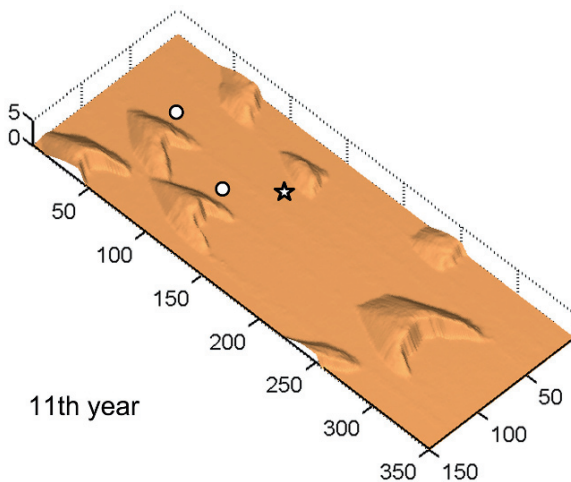


Fig. 7.27. The Coalescent and unstable behaviors of sand dunes obtained by simulations ($u_* = 0.5 \text{ m}\cdot\text{s}^{-1}$, $D_s = 0.3 \text{ mm}$, $H_s = 0.5 \text{ m}$); the configuration of dune field in the 11th year (by the author et al.)

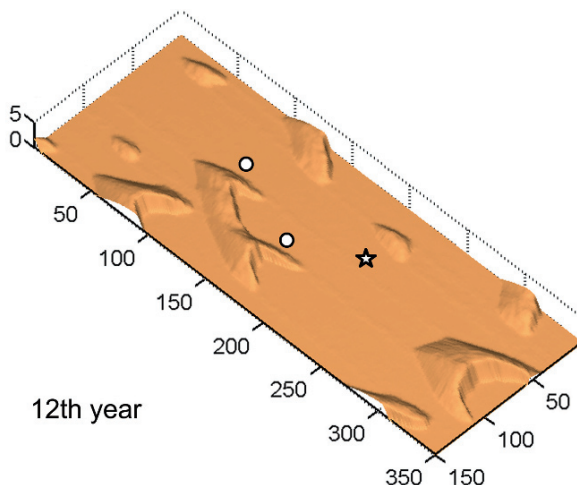


Fig. 7.28. The Coalescent and unstable behaviors of sand dunes obtained by simulations ($u_* = 0.5 \text{ m}\cdot\text{s}^{-1}$, $D_s = 0.3 \text{ mm}$, $H_s = 0.5 \text{ m}$); the configuration of dune field in the 12th year, a small dune marked by ‘☆’ in the 11th year is unstable which becomes smaller in the 12th year (by the author et al.)

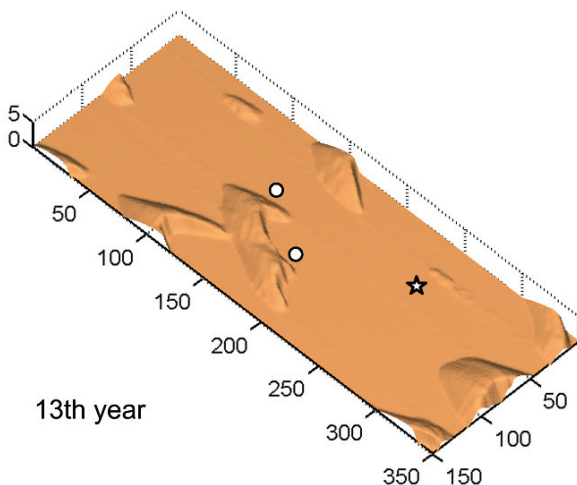


Fig. 7.29. The Coalescent and unstable behaviors of sand dunes obtained by simulations ($u_* = 0.5 \text{ m}\cdot\text{s}^{-1}$, $D_s = 0.3 \text{ mm}$, $H_s = 0.5 \text{ m}$); the configuration of dune field in the 13th year, a small dune marked by ‘☆’ vanishes in the 13th year (by the author et al.)

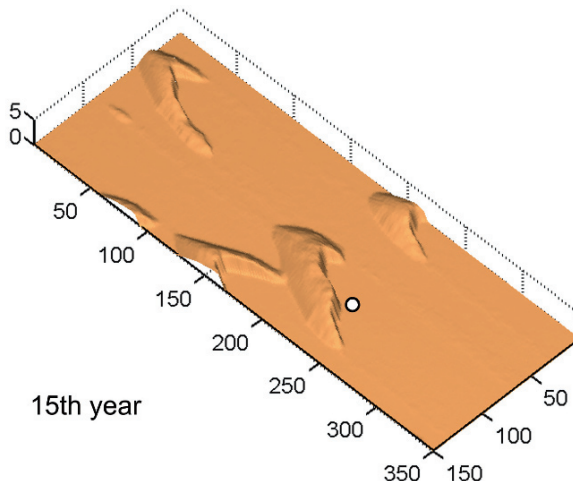


Fig. 7.30. The Coalescent and unstable behaviors of sand dunes obtained by simulations ($u_* = 0.5 \text{ m}\cdot\text{s}^{-1}$, $D_s = 0.3 \text{ mm}$, $H_s = 0.5 \text{ m}$); the configuration of dune field in the 11th year, two dunes in the 11th year marked by ‘o’ have a lateral collision in the 12th year, start merging in the 15th year (by the author et al.)

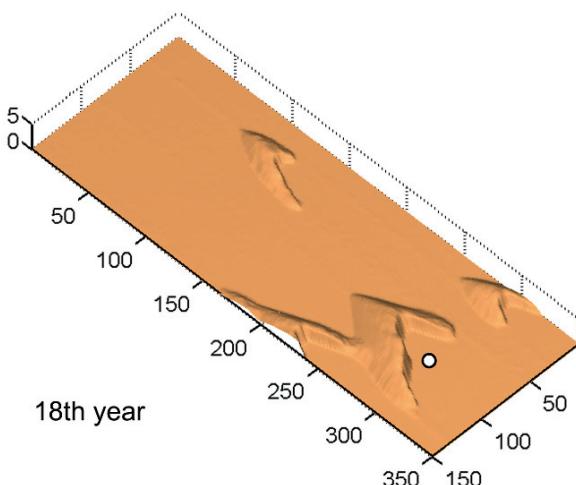


Fig. 7.31. The Coalescent and unstable behaviors of sand dunes obtained by simulations ($u_* = 0.5 \text{ m}\cdot\text{s}^{-1}$, $D_s = 0.3 \text{ mm}$, $H_s = 0.5 \text{ m}$); the configuration of dune field in the 11th year, two dunes in the 11th year marked by ‘o’ become a larger dune than parent dunes in the 18th year (by the author et al.)

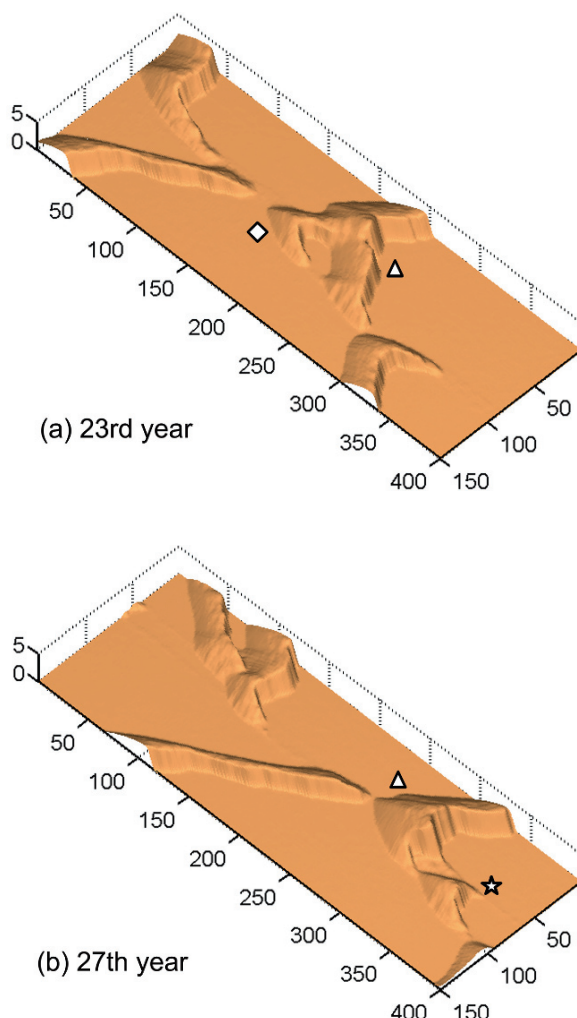


Fig. 7.32. ‘Solitary wave’ behavior of sand dunes obtained by the simulations ($u_* = 0.5 \text{ m}\cdot\text{s}^{-1}$, $D_s = 0.3 \text{ mm}$, $H_s = 0.5 \text{ m}$); two dunes collide with each other in the 23rd year, and then one dune (\star), which is similar with the dune marked by \diamond in size, is released from the tail in the 27th year (\star) (by the author et al.)

Chapter 8 Mechanical Analysis on the Efficiency of Sand Prevention Methods

Besides sandstorm, wind erosion and desertification, the deflation, transport and sediment of sand (dust) materials initiated by wind also lead to abrasion to structures, destruction to crops, and burying to roads and railroads, and so on. So the key of sand prevention is to lower the wind velocity in order to cut down the intensity of wind-blown sand flux and to increase the consolidated soil surface crusts so as to decrease the sand concentration in the air. The techniques of anti-desertification engineering could be classified into two categories, mechanical techniques and biological techniques. The former mainly include sand fence, straw checkerboard barrier and sand fixation by chemical adhesive. All of these techniques are designed to fix, block, or help transporting the sand flux. The latter mainly include establishing man-made plantations, recovering natural vegetation and building the protection forest so as to fix sand dunes and protect oasis.

The design, construction, and efficiency evaluation of sand prevention projects highly depend on desert control experiences, wind tunnel experiments, and field observations. However, all of these are complex mechanical problems. The combination of the theory and quantitative analysis of sand prevention projects and the long-term accumulated practical experiences is an effective approach to design sand prevention projects economically and effectively. Such combination also makes it possible to create design handbooks, construction codes, and evaluation standards for different sand prevention requirements as what people did in civil engineering. The content of this chapter is arranged as follows, Sect. 8.1 provides the simulation results and quantitative analysis on the effect of sand fences; Sect. 8.2 devotes to a theoretical model for the design of the checkerboard barrier; Sect. 8.3 presents some experimental results on the mechanical properties of crust and a theoretical model for the destruction of crust.

8.1 Sand Fence

Sand fence (see Fig. 8.1) can prevent the sand flux advancing and reduce the wind-blown damage. It works in two ways. First, it can directly intercept sands which would drop to the ground or deposit on barrier after sand-barrier collisions; second, it can weaken the wind-blown sand flux by changing the flow field.

At present, there have been some quite valuable empirical conclusions. For example, the field observations confirmed that the horizontal wind penetration fences are better than the vertical ones (Wu 1987). The wind tunnel experiments (Liu 1995) showed that the fence porosity (ratio of the area of fence pore to the total area) plays a key role in the efficiency of the protection range. Liu (1995) studied the flow structures of different sand fences and the influence of porosities on their protection effects by plume method in the wind tunnel. In their experiments, the sand fences were made by triple-ply board. The fence height was 8 cm and the length was roughly the same as the width of wind tunnel. The sand fence mould was fixed in the wind tunnel, and perpendicular to the incoming wind direction. Using smoke pattern photography and flow field measurement, they found that the flow field in the leeside of the sand fence is obviously different for

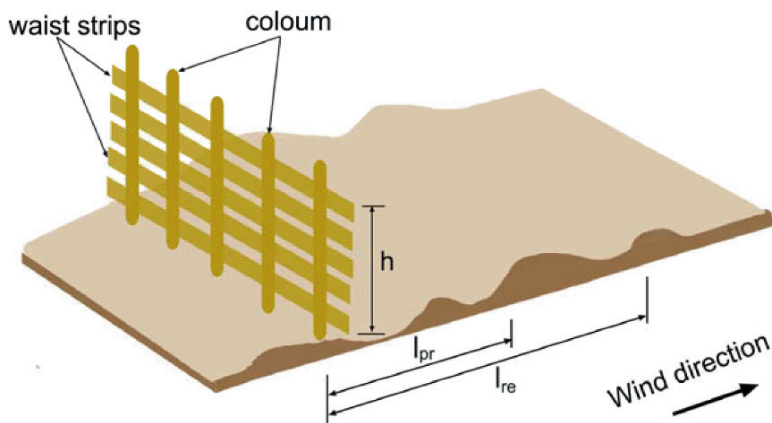


Fig. 8.1. Schematic illustration of a horizontal penetration fence, the openings between two neighboring waist strips is the pores of the sand fence; the ratio of the area of all pores to the total area of the sand fence is defined as the fence porosity η , in which l_{pr} , l_{re} and h represent the effective protection range, the distance required to recover the wind velocity to the reference value and the fence height, respectively

the compact fence (porosity $\eta = 0$) and the loosen fence ($\eta = 0.5$). In the leeside of the compact fence (porosity $\eta = 0$), a large vortex region was formed. Above the region existed a high-speed area, which caused a large velocity gradient and the momentum transferred downward strongly. All of these result in a quick recovery of the wind velocity in the leeside, thus the protection distance was reduced. While in the leeside of the loosen fence ($\eta = 0.5$), it didn't form such a vortex region. The high-speed area and the velocity gradient were small and the momentum transferred downward slowly which together caused the wind velocity of the leeside being slowly recovered. Therefore, the protection distance was increased. In addition, they also discovered that the effective protective range and the velocity recovering distance, that is, the length of the leeside region where the velocity of the leeside was 80% and 100% of the incoming wind velocity measured at 0.5 cm above the surface, increased as the porosity increased.

However, there still exist problems such as the long-term periodicity and lots of interference factors in field observations and wind tunnel experiments for measuring the flow field or the protective region around the sand fence. The quantitative research on the wind prevention effect of the sand fence based on the existing empirical experiences is not only beneficial to explain how the fence's geometry size affects its protection effectiveness but also meaningful to provide an optimum design for sand fence. We adopted the simplified two-dimensional K - ε equation (see Sect. 2.2.5) describing the actual wind field around a sand fence.

Since the influences of the wind tunnel's width and the fence's length to the wind field in front of and behind a sand fence are generally neglected in wind tunnel experiments, we adopted a two-dimensional model in the numerical simulation to describe the wind field around a sand fence in wind tunnel experiments. Namely, x direction is along the prevailing wind direction, and z direction is along the height of the wind tunnel section. The simulation region is $60\text{ cm} \times 710.5\text{ cm}$ to satisfy the inlet and outlet wind tunnel conditions because of the obvious influence of the sand fence to the flow field. Since the distribution of the wind velocity in the leeside of the fence is the key to analyze the effectiveness of the sand fence, the sand fence with the height being $h = 8\text{ cm}$ was set at $x = 20.625h \approx 165\text{ cm}$ and the length of the leeside region was set as $68.125h = 545\text{ cm}$, longer than the front region. The initial wind velocities in front of and behind the sand fence are zero, so are the wind velocities on wind tunnel walls. Besides, at the initial time ($t = 0$), the initial relative pressure is zero ($p = 0$) at the tunnel outlet. The initial wind velocity at tunnel inlet is assumed to fol-

low a symmetric logarithmic profile, then the initial-boundary conditions of two-dimensional K - ε equation (see Sect. 2.2.5) are

$$u = 0, \quad w = 0, \quad (8.1)$$

$$\begin{aligned} t = 0 : \quad u|_{x=0} &= 5.75u_* \lg \frac{z}{z_0} & 0 \leq z \leq \frac{1}{2}h_{tun} \\ u|_{x=0} &= 5.75u_* \lg \frac{h_{tun} - z}{z_0} & \frac{1}{2}h_{tun} \leq z \leq h_{tun} \end{aligned} . \quad (8.2)$$

Where h_{tun} is the wind tunnel's height; u_* is the friction wind velocity; $u_* = 0.371 \text{ m}\cdot\text{s}^{-1}$ when the axial wind velocity at wind tunnel inlet is $u_{ax} = 10 \text{ m}\cdot\text{s}^{-1}$; z_0 is the roughness length, assumed as $6 \times 10^{-4} \text{ m}$.

The calculating region is meshed with the quadrilateral element and the finite element method was adopted (Clough 1960) to solve the flow field. The shape function in the finite element method is taken as the following form:

$$\phi = \frac{1}{4} [\phi_i(1-s)(1-t) + \phi_j(1+s)(1-t) + \phi_k(1+s)(1+t) + \phi_l(1-s)(1+t)], \quad (8.3)$$

where ϕ can represent average velocity \bar{U}_i , average pressure \bar{p} or turbulent Kinetic energy K in every element; s and t are local coordinates. The viscosity coefficient is $\mu_t = 15.13 \times 10^{-6} \text{ m}^2\cdot\text{s}$ and the fluid density is $\rho = 1.22 \text{ kg}\cdot\text{m}^{-3}$ in simulation. The node value in calculations must meet the precision requirement:

$$\frac{\sum_{i=1}^N |\phi_i^k - \phi_i^{k-1}|}{\sum_{i=1}^N |\phi_i^k|} \leq \varepsilon_0, \quad (8.4)$$

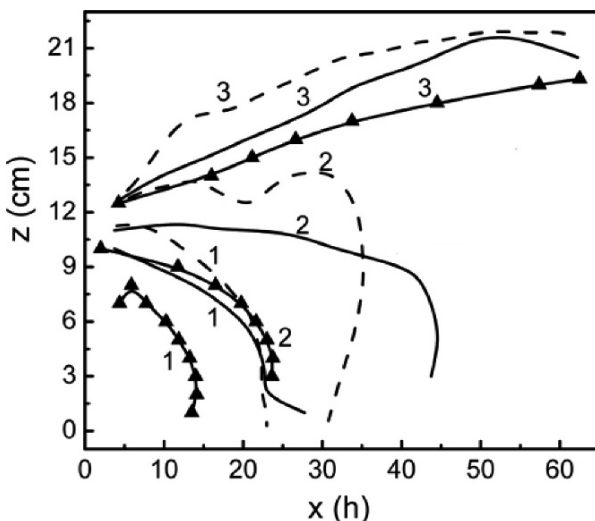
in which, $\varepsilon_0 = 0.001$ when ϕ_i represents u , w and p respectively; $\varepsilon_0 = 0.01$ when ϕ_i represents K and ε respectively.

Table 8.1 and Fig. 8.2 are comparisons between the calculated wind velocities with the experiment results (Liu 1995). We can see that the average relative errors are all within 10%, which suggests that both the mesh method and the assumption that wind velocity satisfies the symmetric logarithmic profile at wind tunnel inlet are feasible in the numerical simulation. Through our simulations, we find that the wind field around the sand fence is very complicated. There is a backflow region from 0 to 2 cm above the ground. That means there is a vortex formed in the leeside of fence.

Table 8.1. The comparison of the protective effect of a sand fence with different porosities between simulation results (SR) and experimental results (ER)

| η | l_{pr} | | $h_1=2.0$ | | l_{re} | | $h_1=2.0$ | |
|--------|-----------|----|-----------|----|----------|----|-----------|----|
| | $h_1=1.0$ | SR | ER | SR | ER | SR | ER | SR |
| 0.0 | 21.000 | 19 | 22.625 | 21 | 27.750 | 27 | 36.750 | 35 |
| 0.1 | 22.625 | 21 | 25.000 | 22 | 39.000 | 35 | 43.500 | 41 |
| 0.2 | 21.875 | 21 | 24.500 | 23 | 38.875 | 36 | 44.125 | 44 |
| 0.3 | 21.875 | 22 | 25.875 | 24 | 42.250 | 40 | 52.125 | 47 |
| 0.4 | 27.000 | 27 | 33.000 | 29 | 41.875 | 43 | 57.250 | 56 |
| 0.5 | 29.625 | 30 | 33.375 | 30 | 61.250 | 59 | 65.875 | 63 |
| 0.6 | 26.000 | 27 | 31.875 | 30 | 51.125 | 54 | 62.500 | |

$h = 8 \text{ cm}$, the axial wind velocity $u_{ax} = 10 \text{ m} \cdot \text{s}^{-1}$, the number of pores $n = 4$. In which l_{pr} and l_{re} represent the effective protection range and the distance required to recover the wind velocity to the reference value respectively; η is the porosity; h_1 (cm) is the measured height.

**Fig. 8.2.** Comparisons of the wind velocity field obtained in wind tunnel experiments by Liu (1995) and in simulations by the author et al.; ——— and —▲— are simulation results for the cases that the incoming wind velocity (u_{ax}) follows a logarithmic profile and a uniform profile respectively; line 1, 2 and 3 are wind velocity contours which are equal to 60%, 80% and 100% of the incoming values respectively; the horizontal distance is scaled by the height of sand fence (h) ($h = 8 \text{ cm}$, $u_{ax} = 10 \text{ m} \cdot \text{s}^{-1}$, $\eta = 0.4$ and the number of pores $n = 4$)

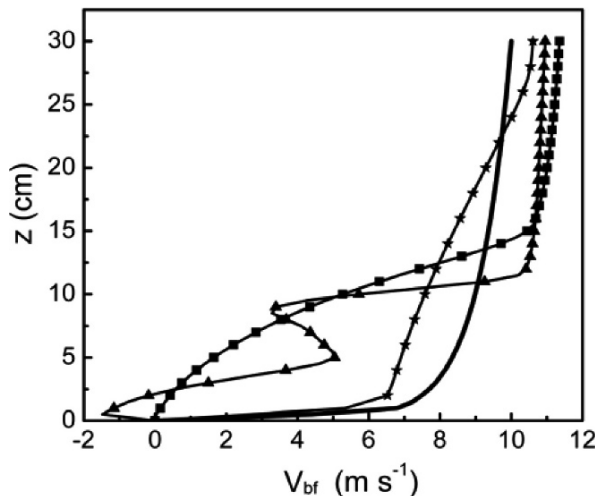


Fig. 8.3. Wind profiles along the height around the sand fence obtained in simulations: ——— at the incoming entry of wind tunnel; —▲— at $1 \times h$ behind the fence; —■— at $5 \times h$ behind the fence; —★— at $35 \times h$ behind the fence ($u_{ax} = 10 m \cdot s^{-1}$, $\eta = 0.4$, $n = 4$) (by the author et al.)

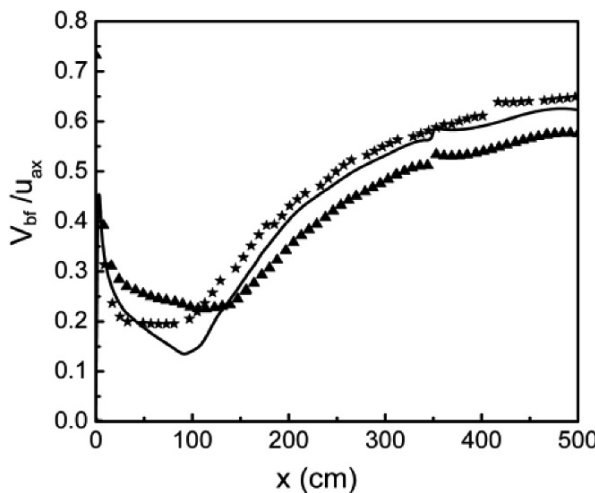


Fig. 8.4. The influences of the height of sand fence (h) to the wind velocity (collected at a height of 1 cm) behind the fence obtained in simulations, characterized by the ratio between the wind velocity (V_{bf}) and the incoming wind velocity (u_{ax}) behind ★ a 8 cm high sand fence, ——— a 10 cm high sand fence, ▲ a 12 cm high sand fence ($n = 4$, $\eta = 0.5$, $u_{ax} = 10 m \cdot s^{-1}$) (by the author et al.)

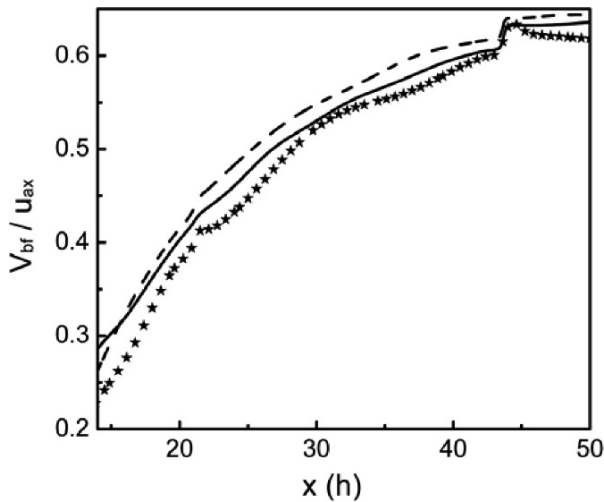


Fig. 8.5. The influences of the porosity (η) to the wind velocity (collected at a height of 1 cm) behind the sand fence obtained in simulations, characterized by the ratio between the wind velocity behind a sand fence and the incoming wind velocity with $--\cdot--$: $\eta = 0.4$, \star : $\eta = 0.5$, $---$: $\eta = 0.6$ ($n = 5$, $h = 8$ cm, $u_{ax} = 10 \text{ m}\cdot\text{s}^{-1}$) (by the author et al.)

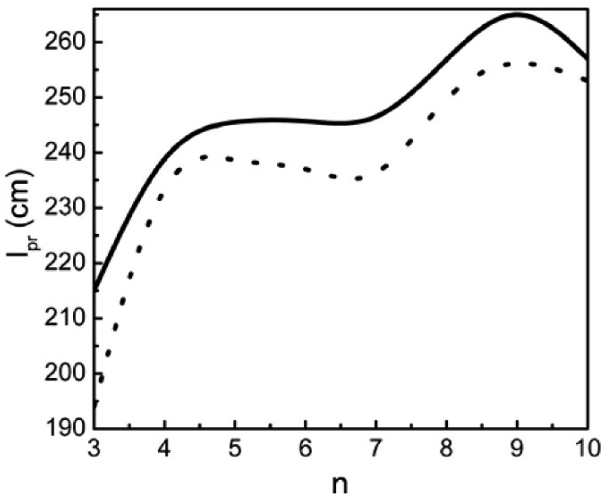


Fig. 8.6. The variations of the length of protective region (l_{pr}) with the number of pores (n); $---$ for $\eta = 0.5$; $--\cdot--$ for $\eta = 0.6$; ($h = 8$ cm, $u_{ax} = 10 \text{ m}\cdot\text{s}^{-1}$) (by the author et al.)

Based on this numerical simulation method, we can design specified fence height, porosity and the number of opening for different objects and requirements conveniently and effectively. This is much easier than the wind tunnel experiment and field observation.

8.2 Straw Checkerboard Barriers

Straw checkerboard barrier (see Fig. 8.7) was introduced to China by former soviet scholar Petrov. This kind of barrier was first successfully applied to the experimental subgrade of Baotou-Lanzhou railway cross the Tengger Desert, China and has been widely used in sand fixation projects since then. Soft materials, such as rice straw, wheat straw, and reed are inserted into the sand layer of dunes vertically and form semi covert straw checkerboard as sand barrier. The straw height and the side length of the checkerboard are the key design factors directly influencing its effect of sand fixation.

The wind action from any direction on straw checkerboard barrier can be approximately treated as the superposition of the actions from two orthogonal wind fields. Therefore, only the action from one wind direction is necessary to be discussed in wind tunnel experiments. The straw checkerboard barrier can be separated into orthogonal straw belts. The straw belts against the wind are more easily to be buried by sand than the straw belt in the other direction, so this situation is of more interest. In the wind tunnel experiment (Liu 1995), a 1:10 straw checkerboard barrier mould made by



Fig. 8.7. The wheat straw checkerboard barriers equipped on either side of a road to protect it from sand-burying (photo by the author et al. in Dunhuang, China)

single-layer sparse sacking whose diameter is about $2 \text{ mm} \times 2 \text{ mm}$ was used as a supplement for the real barrier. The sparse degree were able to be adjusted by pulling out some sacking or changing the number of sacking layers. The experiment straw belts were fastened by wooden triangle strips and fixed on the sand surface. Experimental results showed that there were vortexes between straw belts when windblown sand flux passed the barrier. After a sufficient time, the sand surface between straw belts would be smooth and concave. Thus, there are few sands leaving from the surface even strong air flow passes the barrier. That is how the barrier help sand fixation.

It's a quit complicated mechanical problem to analyze the wind field around the barrier. Under the effect of wind, the exposed parts of straw checkerboard barriers are probably deformed and swing. Even if we don't consider the irregular shapes and interaction between straws and we only consider the exposed part as a whole, the coupled effect of the barriers and the wind-blown sand flow field still makes the theoretical analysis on sand fixation of straw checkerboard barrier very complicated. In order to give theoretical results for practical application, appropriate assumptions are made. From the ideal single-row vortex model (Wang and Zheng 2002), the relationship between the distance of straw check board barriers and the exposed height are derived.

Since the size of each grid of straw checkerboard barrier is much smaller than the size of straw checkerboard barrier, the straw belt in x axis along the wind direction could be treated as being infinitely long. So the flow field around straw grid can be analyzed as a two-dimensional problem. The idea of the design is that sand stay in the grid even under air flow condition, thus it can be assumed that the sand concentration in wind flow is zero in each grid during the formation of the sand bed. The incoming wind is assumed as an inviscid and unimpressible net air fluid. Also, it is assumed that when the surface of sand bed is stable, it is in a streamline shape. The condition physically means the wind streamline follows the sand bed shape and the drag force between that air fluid and the sand bed is equal to zero. Obviously, all above assumptions are based on the situation that the sand fixation effect of straw checkerboard barrier is ideal. The actual flow field is simplified as two-dimensional laminar flow of ideal fluid without applied stress flows in semi-infinite space.

To describe such a flow field in mathematic, ideal vortices with vortex intensity Γ are placed in the center of every two neighboring straw belts $(x, z) = (\pm nl, 0)$, $n = 0, \pm 1, \pm 2, \dots$. As shown in Fig. 8.8, they form a single vortex row. Sand surface in grids is a continuous streamline that extents to infinity in both positive and negative directions, written as $z = z(x)$. Thus, the incompressible fluid's continuity equation is

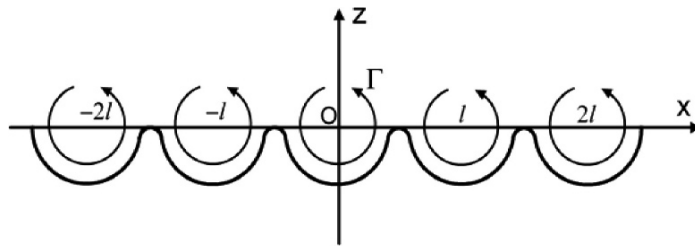


Fig. 8.8. Schematic illustration of the wind flow over checkerboard barriers; Γ is the vortex intensity; l is the distance of two neighboring straw belts

$$\frac{\partial u}{\partial x} + \frac{\partial w}{\partial z} = 0. \quad (8.5)$$

where u and w are velocity components of x and z directions respectively. It is considered that the idea vortex row forms an irrotational field, so the potential function Φ , the dual stream function Ψ and the complex potential W_{cp} are introduced into the calculation. By the complex function method of fluid mechanics, we get:

$$W_{cp} = \Phi + i\Psi, \quad (8.6)$$

$$\frac{dW_{cp}}{dz} = \frac{\partial \Phi}{\partial x} + i \frac{\partial \Psi}{\partial x} = u - iw, \quad (8.7)$$

where $i = \sqrt{-1}$, and $Y = x + iz$.

From fluid mechanics theory, the complex potential of the single ideal vortex row with vortex stress of Γ is:

$$W_{cp} = \frac{\Gamma}{2\pi i} \left[\ln \frac{\pi Y}{l} + \sum_{n \neq 0} \ln \left(1 - \frac{Y}{nl} \right) \right] = \frac{\Gamma}{2\pi i} \ln \prod_{n=1}^{+\infty} \frac{\pi Y}{l} \left[1 - \left(\frac{Y}{nl} \right)^2 \right] = \frac{\Gamma}{2\pi i} \ln \left(\sin \frac{\pi Y}{l} \right). \quad (8.8)$$

Taking conjugate of Eq. 8.6 and then substituting it into Eq. 8.8, we get

$$\Psi = \frac{\Gamma}{4\pi} \ln \left[\frac{1}{2} \left(ch \frac{2\pi z}{l} - ch \frac{2\pi x}{l} \right) \right]. \quad (8.9)$$

Thus, the streamline function passing point (x_0, z_0) is:

$$ch \frac{2\pi z}{l} - ch \frac{2\pi x}{l} = ch \frac{2\pi z_0}{l} - \cos \frac{2\pi x_0}{l}. \quad (8.10)$$

Substituting Eq. 8.7 into Eq. 8.8 and supposing $z \rightarrow +\infty$, we get $\Gamma = -U_\infty l$, where U_∞ is wind velocity far above from the ground. It shows that at certain incoming wind velocity, the vortex strength Γ in the barrier is proportional to the distance between neighboring straw belts. That means that the vortex between neighboring straw belts is more intensive and sand is blown more easily with longer distance l between straw belts. Thus in the practical construction of straw checkerboard barriers, l should not be too large. On the other hand, if the l is too small, the vortex is weak, which would cause the sand particle in the air flow not being able to pass. Then sand burial and deposition would happen. To find a proper value of l , The characteristic parameter of straw checkerboard barrier is defined $\lambda_0 = h_0/l$, here h_0 is height of exposed straw. Assuming that the mass of sand soil in a grid is constant, and the volume density does not change, we have:

$$\lambda_0 = \frac{1}{l^2} \left| \int_{-l/2}^{l/2} z(x) dx \right|. \quad (8.11)$$

Eq. 8.10 gives two kinds of streamlines with different geometric characteristics: one is the closure curves surrounding vortex centre; another is continuous curve extending from the origin to the positive and negative infinite along x axis separately. The transition curve of these two kinds streamlines is parameter $(\lambda_0)_{\min}$. Thus input $(x_0 = l/2, z_0 = 0)$ into Eq. 8.10, we can obtain the equation of this streamline:

$$ch \frac{2\pi z}{l} - \cos \frac{2\pi x}{l} = ch \frac{2\pi 0}{l} - \cos \frac{2\pi l}{2l} = 2. \quad (8.12)$$

At the interception point between the streamline and the z axis, $h = 0.28l$. From Eqs. 8.11 and 8.12 we can get:

$$(\lambda_0)_{\min} = \frac{2}{l^2} \left| \int_0^{-l} \frac{l}{2\pi} \arcsin \left[-2 + ch \frac{2\pi z}{l} \right] dz \right| = 0.1856. \quad (8.13)$$

Therefore, the maximum distance of two adjacent straw grids is $l_{\max} = h_0 / (\lambda_0)_{\min} = 5.338h_0$ from the definition of λ_0 . In the practical applications, the exposed straw height in the barrier is determinate by the straw material size, so the corresponding maximum distance l_{\max} for straw height h_0 could be calculated easily, shown in Table 8.2. In the sand protection project of the highway of the Tarim desert, China (Wang and Chen 1996), when the height of reed in sand barrier is $h_0 = 18\text{--}20$ cm, the spacing is

Table 8.2. The relation between the straw height h_0 (cm) and the maximum distance of two adjacent straw grids l_{max} (cm)

| h_0 | l_{max} | h_0 | l_{max} | h_0 | l_{max} | h_0 | l_{max} |
|-------|-----------|-------|-----------|-------|-----------|-------|-----------|
| 1.0 | 5.4 | 9.0 | 48.5 | 17.0 | 91.6 | 25.0 | 134.7 |
| 2.0 | 10.8 | 10.0 | 53.9 | 18.0 | 97.0 | 26.0 | 140.1 |
| 3.0 | 16.2 | 11.0 | 59.3 | 19.0 | 102.4 | 27.0 | 145.5 |
| 4.0 | 21.5 | 12.0 | 64.7 | 20.0 | 107.8 | 28.0 | 150.9 |
| 5.0 | 26.9 | 13.0 | 70.0 | 21.0 | 113.1 | 29.0 | 156.2 |
| 6.0 | 32.3 | 14.0 | 75.4 | 22.0 | 118.5 | 30.0 | 161.6 |
| 7.0 | 37.7 | 15.0 | 80.8 | 23.0 | 123.9 | | |
| 8.0 | 43.1 | 16.0 | 86.2 | 24.0 | 129.3 | | |

$l = 100$ cm according to long-term practical experience. Our calculation result gives the maximum l between 97 cm and 108 cm based on the height of barrier and is consistent with practical result. It is confirmed the theoretical model and analysis method for the straw checkerboard sand barrier design and construction in this chapter are basically feasible. In the further research, the air coherent influence (equal to Reynolds number that is infinitely large) and distortion and movement of sand barrier material are needed to be considered to find quantitative relationship between the straw checkerboard sand barrier size and the wind velocity, the best material parameter, the actual sand erosion and sand deposition in the straw grids and expiration date of straw checkerboard barriers and so on.

8.3 The Mechanical Properties of Crust

The crust on the sand surface can cause the surface roughness to increase, the anti-wind erosion ability to enhance and prevents the migration of wind-drift sand effectively. The soil crust is classified into three kinds: physical crust, biological crust and chemistry crust. The latter two kinds are introduced here with emphasis.

The biological crust is the micro natural feature in arid region. It is one kind of crustose body formed by organic materials (for example, moss, lichen, algae, fungus and so on) or their metabolites and the soil particles. The average thickness of crusts is less than 0.4 cm after 2 to 3 years it is formed, shown in Fig. 8.9a. Electron microscope image (Fig. 8.9b) shows the microscopic structure of biological crust's undersurface, where sand and the organic materials as well as their metabolite are combined compactly.

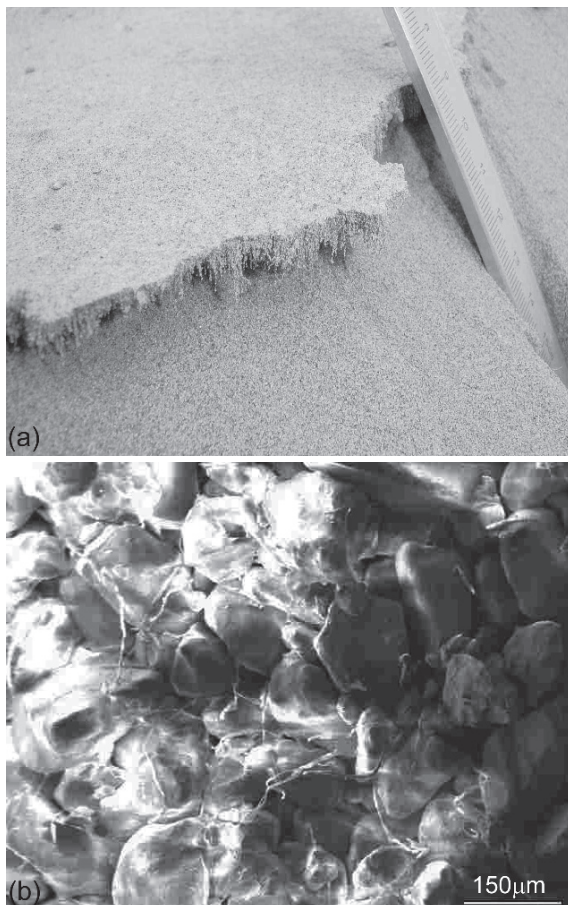


Fig. 8.9. Natural biological crust in eastern edge of the Tengger Desert **(a)** natural biological crust which is less than 0.4cm in depth and **(b)** the electron microscope image of the crust in (a); (photo by the author et al.)

The advantage of the biological crust is that the composition material including algae, moss, lichen etc., not only can grow and reproduce in the seriously drought arid environment but also can affect and change the environment by its metabolism. It plays a significant role in sand fixation and improving the moisture content of soil. However, the distribution of biological crust formed in nature is not continuous. The exposed sand surface on crust's edge can be easily eroded by wind and form wind erosion pits, which cause the biological crust to collapse and thus activate the fixed sand. Therefore, to maintain the integrity of the biological crust is the pre-

mise to increase its ability of sand fixation. Chemistry crust is firmly formed by spraying chemical sand-fixation agents on loose bed surface.

There are a lot of chemical sand-fixation agents for choice. The construction of chemistry sand fixation crust could be mechanized, which is simple, fast and efficient. The method is suitable for the areas where the construction sand fixation materials are lacking or the areas where the environment is severe, the precipitation is little, and the biological sand fixation technology is not easy to be applied. But, the effect of chemical sand-fixation is poor and it does not have protection height. The human activities including herd etc. might destroy the integrity and continuity of the crust. Wind-blown sand can also destroy the crust by impact and erosion. Therefore, both the biology crust and chemistry crust can only fix sand effectively for a certain time.

8.3.1 The Survey on the Mechanical Properties of Crust

Neuman et al. (1996) and Neuman and Maxwell (1999) carried on the preliminary discussion on the stress-strain relationship of crust by bending experiment. Because the important mechanical parameters, such as elastic modulus of crust were not given, the quantitative description for distortion, collapse and destruction process of the crust is difficult. In addition, the ability of the crust to resist against sand impact and wind erosion and its efficiency of sand prevention cannot be estimated accurately.

In order to investigate the mechanical properties of biology crust, we sampled a natural crust from the eastern edge of the Tengger Desert, China. The surface of the sampled crust was flat and its thickness was uniform. We cut it into several $15 \times 10 \text{ cm}^2$ rectangular blocks which were loaded into the shock-proof box and was shipped to the laboratory. The water-soluble SH polyer binder is mixed with the natural sand taken from the same area (the distribution of sand diameter is shown in Fig. 3.1) in different weight ratios to form different chemistry crust. Because the crust is very fragile, conventional universal testing machines are not suitable for the crust test. Tensile and bending experiments are designed as shown in Figs. 8.10a and 8.10b. In the tensile experiment, the dune sands were added into the hanging basket as shown in Fig. 8.10a to slowly increase the external load, and then the sand mass was measured by balances to measure the pulling force acted on the crust. At the same time, the vertical displacement of crust fixed on the horizontal metal rod was measured by the laser displacement sensor (LDS).

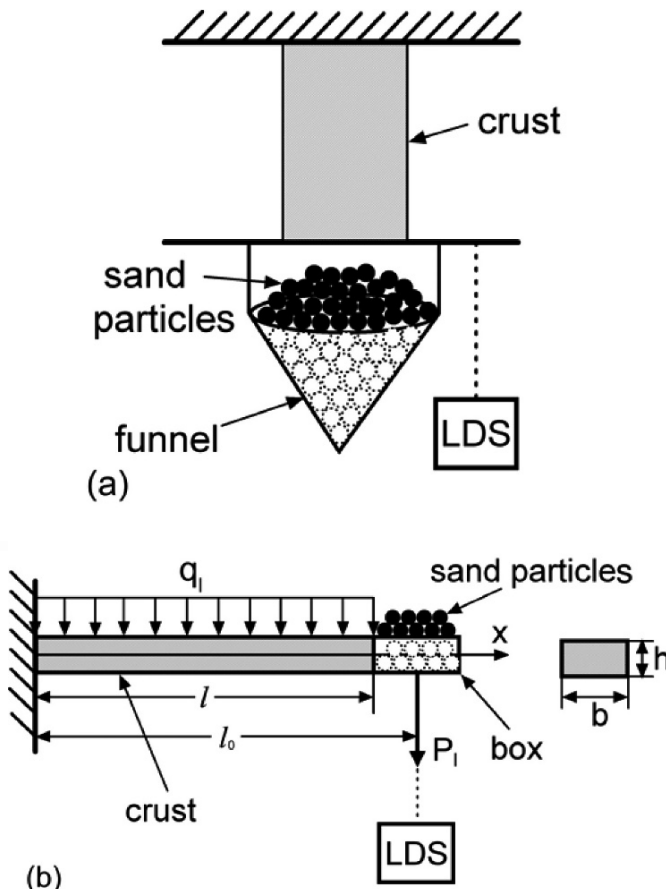


Fig. 8.10. The schematic illustration of the tensile and bending experiment; the crust sample is fixed with one fixed end and one free end; LDS is the laser displacement sensor; l , b and h are the length, width and depth of the crust sample respectively; q_l and P_l are the dead weight and the external load of the sample respectively; l_0 is the distance from the fixed end to the position of external load

The results obtained from the tensile and bending experiment for biology crust (Fig. 8.11) showed that the stress-strain relationship is fairly linear, however, some samples presents a non-linear stress-strain relation near their break. Due to the difficulty to observe the mechanical behavior of the biological crust when unloading, it is hard to determine if the nonlinear deformation is elastic deformation or the plastic deformation. The Young's modulus E of the crust measured in our experiment is about 1.596×10^7 Pa. The range of maximum stress $\sigma_{l\max}$ is 30.0–42.8 kPa with average value

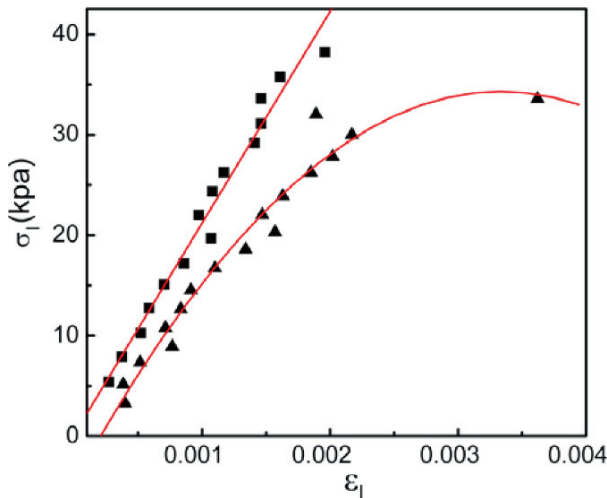


Fig. 8.11. The stress (σ_l) and strain (ε_l) curves given by the single-direction tensile experiment; it's close to a linear relationship (■), however, some samples presents a non-linear stress-strain relation near their break (▲) (by the author et al.)

$\sigma_{lav} = 36.4$ kPa. The Young's modulus and the average of maximum stress obtained by this experiment are consistent with the results gotten by Neuman and Maxwell (1999) in magnitude, but the range of our results is much smaller.

For the chemistry crust formed in two kinds of weight ratios between adhesives and sands, the deflection data were recorded when there is no creep deformation occurring in the middle point of the crust in our experiments. Using the deflection formula for the unmovable simply-supported beam under a concentrated load P_l and a dead weight q_l (Sun et al. 1994):

$$w_e = \frac{1}{144EI_l} q_l x (5l^3 + l^2 x - 12lx^2 + 6x^3) + \frac{1}{48EI_l} P_l x (3l^2 - 4x^2), \quad (0 \leq x \leq l). \quad (8.14)$$

where, w_e is the elastic deflection; I_l is the moment of inertia of its cross-section; $l = 6$ cm is the length of beam, we can derived the elastic modulus E of the crust. The results are shown in Tables 8.3 and 8.4.

From Tables 8.3 and 8.4, we find that the elastic modulus is about 0.240–0.279 GPa and 0.240–0.268 GPa for two crust samples with adhesive-sand ratio 3:100 and 5:100 respectively. The elastic modulus of crusts could be regarded as a constant and it is far smaller than the elastic modulus of structure material. Although the weight ratio between adhesive and

Table 8.3. The experiment result of the crust which has adhesive-sand weight ratio 3:100

| P _l | m | l | b | h | w _e | E |
|----------------|--------|-----|--------|--------|----------------|---------|
| 1.0 | 0.9703 | 8.0 | 1.2790 | 0.0895 | 0.3336 | 0.26393 |
| 1.5 | 0.9864 | 8.0 | 1.2640 | 0.0825 | 0.5433 | 0.27918 |
| 2.0 | 1.0473 | 8.0 | 1.284 | 0.0890 | 0.6261 | 0.23973 |

P_l (g) is the external load; m (g) is the mass of the crust; l (cm), b (cm) and h (cm) are the length, width and depth of the crust sample respectively; w_e is the elastic deflection; E (GPa) is the Young's modulus

Table 8.4. The experiment result of the crust which has adhesive-sand weight ratio 5:100

| P _l | m | l | b | h | w _e | E |
|----------------|--------|-----|--------|--------|----------------|---------|
| 1.0 | 1.3087 | 8.0 | 1.2765 | 0.1015 | 0.2526 | 0.26814 |
| 1.5 | 1.1740 | 8.0 | 1.2840 | 0.0970 | 0.3588 | 0.26883 |
| 2.0 | 1.1850 | 8.0 | 1.2625 | 0.1010 | 0.4395 | 0.24456 |

P_l (g) is the external load; m (g) is the mass of the crust; l (cm), b (cm) and h (cm) are the length, width and depth of the crust sample respectively; w_e is the elastic deflection; E (GPa) is the Young's modulus

sand have a great effect on the thickness of crust, its influence on the elastic modulus is small.

The distortion of the crust with time under the action of force is called the creep deformation of crust which is an important parameter reflecting the performance of crust and there have been very few discussions about it. Through wind tunnel experiments, Neuman and Maxwell (2002) found that if the wind-blown sand flow lasts enough time even with the wind velocity only slightly larger than the threshold, the biological crust will be destroyed by saltating sands. However, the hardness test for the same biological crust showed that the crust couldn't be destroyed by saltating sands. These results indicated that if the continuous impact on crust by saltation sand is regarded as a kind of steady static load, crust creep deformation possibly is a noticeable reason to the destruction of crust. Therefore, the creep deformation behavior of crust plays an important role in the research of crust life and crust destruction.

Fig. 8.12 gives the experiment results of the deflection of the free end of the crust $W(l_0)$ varying with time. The results showed that the creep deformation process of crust can be divided into three typical stages, namely, rapid deflection increment, gentle deflection increment, and repeating rapid deflection increment. It generally takes several hours for the crust to be destroyed.

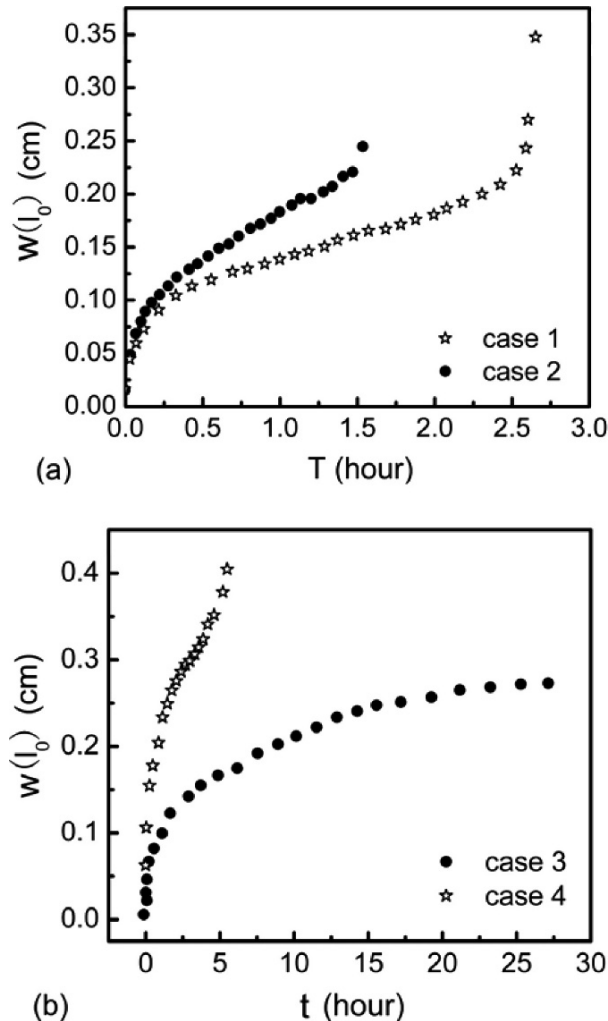


Fig. 8.12. The variations of the deflection of the free end of the crust $W(l_0)$ to time; case 1: $l = 5.326$ cm, $b = 1.44$ cm, $h = 0.271$ cm, $l_0 = 5.886$ cm, $q_l = 0.47814$ N·m $^{-1}$, $P_l = 0.01455$ N; case 2: $l = 4.582$ cm, $b = 1.475$ cm, $h = 0.241$ cm, $l_0 = 5.4$ cm, $q_l = 0.45831$ N·m $^{-1}$, $P_l = 0.01878$ N; case 3: $l = 5.324$ cm, $b = 1.488$ cm, $h = 0.256$ cm, $l_0 = 6.18$ cm, $q_l = 0.44292$ N·m $^{-1}$, $P_l = 0.01593$ N; case 4: $l = 5.566$ cm, $b = 1.653$ cm, $h = 0.243$ cm, $l_0 = 5.95$ cm, $q_l = 0.46822$ N·m $^{-1}$, $P_l = 0.01496$ N (by the author et al.)

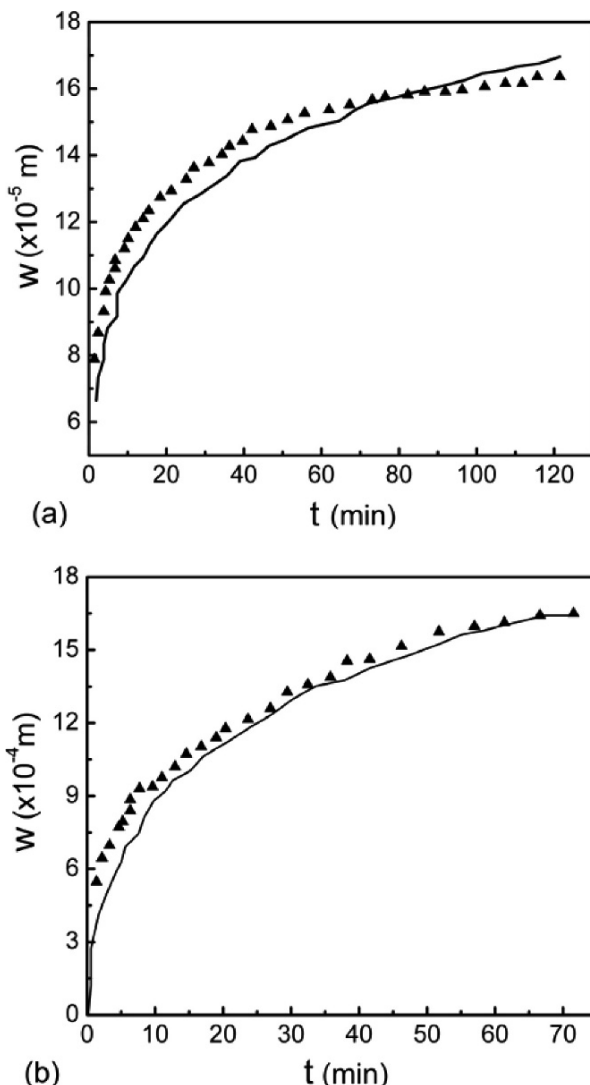


Fig. 8.13. The comparison of the variations of the deflection (W) of the crust with time between theoretical prediction values and the experimental data: —■— the theoretical prediction values calculated by Eq. 8.15; ▲ the measured results obtained by the author et al. for (a) $l = 6 \text{ cm}$, $b = 1.273 \text{ cm}$, $h = 0.0905 \text{ cm}$, $m = 0.9685 \text{ g}$, $P_l = 1.5 \text{ g}$ and (b) $l = 7 \text{ cm}$, $b = 1.308 \text{ cm}$, $h = 0.1027 \text{ cm}$, $m = 1.268 \text{ g}$, $P_l = 1.0 \text{ g}$ (the constant term in Eq. 8.16 $a_2 = 0.00265$), m is the mass of crust (by the author et al.).

Using the variable separation method and considering the bending moment and the strain of the crust beam, we gave the creep deformation func-

tion $g(t)$ and the function of deflection W with respect to time as following:

$$W = \frac{1}{144EI_l w_{e0}} x \left[q_l (5l^3 + l^2 x - 12lx^2 + 6x^3) + 3P_l (3l^2 - 4x^2) \right] \\ \cdot \left[w_{e0} - a_2 \left(\frac{t}{72} \right)^{0.515} \right] \left[1 + \left(\frac{t}{72} \right)^{0.515} \right]^{-1}, \quad (8.15)$$

$$g(t) = \frac{7.153}{E \times 10^3} \frac{w_{e0} - a_2}{w_{e0}} \left(\frac{t}{72} \right)^{0.485} \left[1 + \left(\frac{t}{72} \right)^{0.515} \right]^{-1}. \quad (8.16)$$

Here, w_{e0} is the deflection in middle point of the crust beam; a_2 is a constant which can be taken from 0.001 to 0.003 depending on the uniformity of the crust. To validate the forecasting results, we calculated the deflection in the middle point of crust for two different groups of test samples using the same value of a_2 . The calculation results are compared with the experimental results, shown in Fig. 8.13. The theory forecasting results given in this section are basically consistent with the actual experimental results. Except for the initial several points, the smallest relative errors between theoretical results and minutes experiment results are 7.13% and 1.97% respectively from 21 min to 80 min.

8.3.2 The Destruction of Saltating Sand to Crust

If the crust is very thin like new born crust, that is, the length and width of crust are much longer than its thickness, then the crust can be regarded as a semi-infinite elasto-plastic plate. It is supposed that a sand particle A whose mass is m_s and diameter is D_s , impacts on crust; the angle between sand impacting direction and wind direction is φ_0 , the impacting speed is V_{im} , the impact angular speed is ω_0 , and the impact angle is θ_0 and collision happens at point J , all shown in Fig. 8.14. The hard sphere collision model introduced in Chap. 3 is used here and it is assumed that the diameter of sand particle being impacted tends to infinite in Eqs. 3.19–3.24, then three velocity components and three angular speed components of the sand particle after colliding with the crust can be gotten as following.

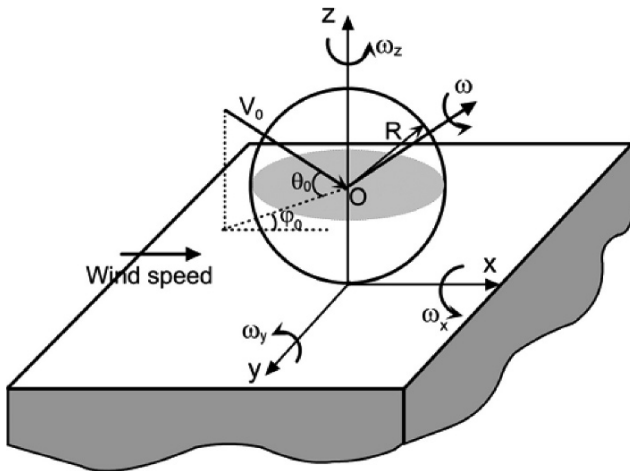


Fig. 8.14. The schematic illustration of the collision between sand particle (sphere) and crust (plate); J is the impact point; φ_0 is the angle between sand impacting direction and wind direction; θ_0 is the impact angle; V_{im} is the impacting speed; ω_0 is the impact angular speed (ω_{x0} , ω_{y0} , ω_{z0} are the horizontal, lateral and vertical components, respectively)

$$U_{xt} = \frac{1}{3} \left[(k+5)V_{im} \cos \theta_0 \cos \varphi_0 - \frac{1}{2}(k+2)\omega_{y0} D_s \right], \quad (8.17)$$

$$U_{yt} = \frac{1}{3} \left[(k+5)V_{im} \cos \theta_0 \sin \varphi_0 - \frac{1}{2}(k+2)\omega_{x0} D_s \right], \quad (8.18)$$

$$U_{zt} = -kV_{im} \sin \theta_0, \quad (8.19)$$

$$\omega_{xt} = -\frac{2}{3D_s} \left[\frac{1}{2}(2.5k+2)\omega_{x0} D_s - 5(0.5k+1)V_{im} \cos \theta_0 \sin \varphi_0 \right], \quad (8.20)$$

$$\omega_{yt} = -\frac{2}{3D_s} \left[\frac{1}{2}(2.5k+2)\omega_{y0} D_s - 5(0.5k+1)V_{im} \cos \theta_0 \cos \varphi_0 \right], \quad (8.21)$$

$$\omega_{zt} = \omega_{z0}. \quad (8.22)$$

Supposing that only the vertical impact force on the crust is considered, the vertical speed reduces at a constant acceleration and the crust largest dis-

placement is d_{max} , the impacting force F_{imz} acting on the crust can be expressed as

$$F_{imz} = \frac{1}{2d_{max}} m_s V_{im}^2 \sin^2 \theta_0. \quad (8.23)$$

For a single sand particle, the collision range is so small that the distortion process of crust impacted by sand particle can be approximately regarded as a distortion process of a circular plate pressed by an equivalent static force F_{imz} . From the theory of plate and shell, the largest deflection of the crust is

$$w_{e\max} = \frac{3}{4\pi Eh^3} F_{imz} l^2 (1 - \nu^2), \quad (8.24)$$

where, l , h , ν , E are the radii of crust, the thickness of crust, the possion ratio and the Young's modulus, respectively. Substituting Eq. 8.24 into Eq. 8.23, the impacting force F_{imz} of a single sand particle on the crust is

$$F_{imz} = \frac{h}{l} V_{im} \sin \theta_0 \sqrt{\frac{2\pi h E m_s}{3(1-\nu^2)}}. \quad (8.25)$$

From the yield line distribution mode of a thin regular polygon plate under a central concentrated force (shown in Fig. 8.15), the threshold force to crash the crust by one sand particle could be calculated. Therefore, the threshold impacting speed V_{im}^* of a single sand particle to crash the crust is

$$V_{im}^* = \frac{l \sigma_y}{\sin \theta_0} \sqrt{\frac{3\pi(1-\nu^2)h}{2m_s E}}, \quad (8.26)$$

where, σ_y is crust strength. The threshold impacting speed is related with crust's size, crust material properties and the impacting angle. Fig. 8.16 shows the rule of threshold impacting speed change with crust thickness in different biological crusts. The mass of the sand particle is $m_s = 3.75 \times 10^{-5}$ g; the possion ratio is $\nu = 0.4$; the side length of crust is $l = 1$ mm and the impacting angle is $\theta_0 = 15^\circ$. Fig. 8.16 shows that the threshold impacting speed rapidly increases with crust thickness. For example, the threshold impacting speed needs to be about $2 \text{ m}\cdot\text{s}^{-1}$ in order to destroy a crust of 0.1 mm thickness. But to destroy a crust of 4 cm thickness, the threshold impacting speed rise to about $20 \text{ m}\cdot\text{s}^{-1}$, which is not possible.

The results indicated that it is not enough to only consider one single sand particle's impact in the analysis of crust destruction. Besides the

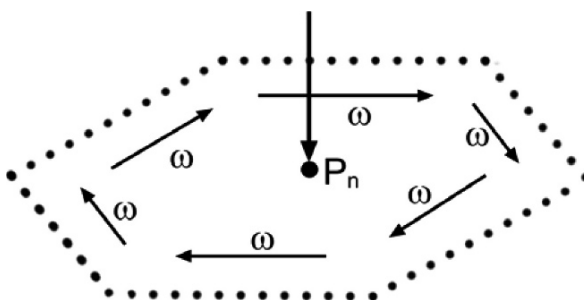


Fig. 8.15. A schematic illustration of the distribution model of regular polygon thin steel plate's yield line when it bears a concentrated load in central point; P_n is the critical central concentrated load; ω is the angular speed of the rigid part; - - - is the yield boundary

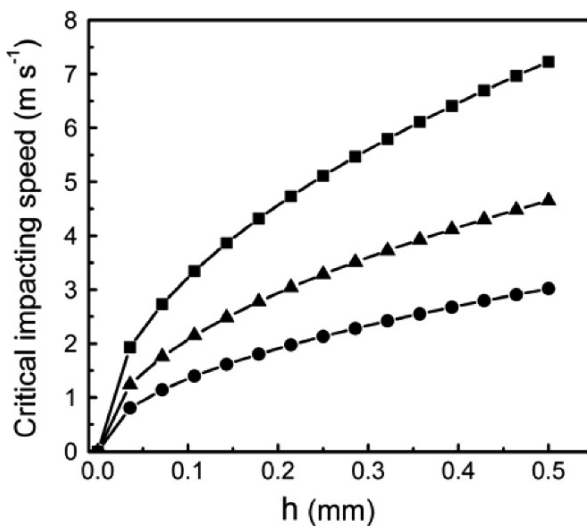


Fig. 8.16. The variations of the critical impacting speed to the thickness of crust (h) predicted by Eq. 8.26; —■— the results based on the elastic modulus of crust $E = 19.97 \text{ MPa}$, the crust intensity $\sigma_y = 36.4 \text{ KPa}$ measured in eastern edge of the Tengger Desert (by the author et al); —▲— the results based on $E = 21 \text{ MPa}$, $\sigma_y = 24 \text{ KPa}$ of man-made biological crust (Neuman et al. 1996); —●— the results based on $E = 25 \text{ MPa}$, $\sigma_y = 17 \text{ KPa}$ of man-made biological crust (Neuman et al. 1996) (the mass of the sand particle $m_s = 3.75 \times 10^{-5} \text{ g}$, possion ratio $\nu = 0.4$, the side length of crust $l = 1 \text{ mm}$, the impacting angle $\theta_0 = 15^\circ$) (by the author et al.)

creep deformation of the crust, the repeated impact and erosion effect of a large amount of sand particles on the crust must be considered.

Here, we start from the viewpoint of energy and give a preliminary result by analyzing the energy change during crust destruction process. Considering the velocity change of the sand particle before and after collision, we can get the energy loss ΔE_s of the sand particle

$$\begin{aligned}\Delta E_s = & \frac{1}{2}m_s V_{im}^2 + \frac{1}{2}I_s(\omega_{x0}^2 + \omega_{y0}^2 + \omega_{z0}^2) - \frac{1}{2}m_s(U_{xt}^2 + U_{yt}^2 + U_{zt}^2) - \frac{1}{2}I_s(\omega_{xt}^2 + \omega_{yt}^2 + \omega_{zt}^2) \\ & - \frac{1}{2}m_s V_{im}^2 \left[\frac{1}{9}(14k^2 + 40k + 35)\cos^2 \theta_0 + 4k^2 \sin^2 \theta_0 - 1 \right] \\ & + \frac{7}{9}(k+1)^2 m_s D_s V_{im} \cos \theta_0 (\cos \varphi_0 + \sin \varphi_0)(\omega_{x0}^2 + \omega_{y0}^2) \\ & - \frac{1}{36}(7k+1)(k+1)m_s D_s^2 (\omega_{x0}^2 + \omega_{y0}^2)\end{aligned}, \quad (8.27)$$

Due to the randomness of the impacting speed V_{im} , the angular speed ω_0 , the impacting angle θ_0 and the angle with wind direction φ_0 of sand particles. By applying the random variable probability density analysis introduced in Chap. 3 and the probability density of φ_0 which follows a negative exponent function (see in Sect. 3.4), the average energy loss $\bar{\Delta E}_s$ of sand particle before and after collision per unit area per unit time can be expressed as:

$$\begin{aligned}\bar{\Delta E}_s = & N_s m_s \left[-\frac{1}{36}(50k^2 + 40k + 17) - \frac{5}{8\pi}(40k + 35 - 22k^2) \sin \frac{2\pi}{45} \cos \frac{2\pi}{15} \right] M_2(V_{im}) \\ & + (k+1)^2 \frac{35m_s D_s N_s}{2\pi(e^\pi - 1)} \sin \frac{\pi}{45} \cos \frac{\pi}{15} (1 + e^\pi) M_1(V_{im}) [M_1(\omega_y) + M_1(\omega_x)] \\ & + \frac{1}{36}m_s N_s D_s^2 (7k+1)(k+1) [M_2(\omega_y) + M_2(\omega_x)]\end{aligned}, \quad (8.28)$$

where, $M_n(\cdot)$ is a random variable, such as the moment of V_{im} and ω_{x0} ; Subscript '1', '2' represent the order of the moment; N_s is the number flux of salvation particles. From the collision theory, part of the energy of the sand particle is absorbed by the crust during collision and another part of the energy is lost in form of heat. Generally the energy absorbed by the crust can be expressed as $E_c = \eta_s \bar{\Delta E}_s$, where η_s is the proportional coefficient and $0 \leq \eta_s < 1$. The energy absorbed by the crust is related with not only wind velocity but also impacting angle of sand particle. Assuming that the collision duration is Δt , the average impacting force \bar{F}_{im} on crust by impacting sand particles per unit area per unit time can be calculated as following

$$\bar{F}_{imx} = \frac{3N_s}{2(k+1)m_s\Delta t} \left[\frac{1}{2} D_s M_1(\omega_{y0}) + \frac{45}{8\pi} M_1(V_{im}) \sin \frac{\pi}{45} \cos \frac{\pi}{15} \right], \quad (8.29)$$

$$\bar{F}_{imy} = \frac{3N_s}{2(k+1)m_s\Delta t} \left[-\frac{1}{2} D_s M_1(\omega_{x0}) + \frac{45}{8\pi} M_1(V_{im}) \sin \frac{\pi}{45} \cos \frac{\pi}{15} \right], \quad (8.30)$$

$$\bar{F}_{imz} = \frac{45N_s}{2\pi\Delta t} m_s (2k+1) M_1(V_{im}) \sin \frac{\pi}{45} \sin \frac{\pi}{15}. \quad (8.31)$$

From the above formulas, we can find that for given incoming wind velocity and sand diameter, the horizontal force and lateral impacting force on crust are related with the impacting angular speed. They increase much more quickly than the vertical impacting force when the impacting angular speed increases. This leads to the conclusion that the abrasion effect of the impacting sand particles shouldn't be neglected.

Eqs. 8.29–8.31 can also be used to calculate the impacting force on the crust per unit area per time in wind-blown sand flow. It's worth noticing that the collision duration depends on the sand-bed collision process and the uniformity of the shape of the sand particle. Whether it is an important factor influencing the impacting force of sand particles on the crust should be discussed further.